096329

Final

Condor Consulting, Inc.

REPORT ON PROCESSING & ANALYSIS OF HUMMINGBIRD EM, MAGNETICS AND RADIOMETRICS DATA

QUITE LAKE, YUKON

FOR

GLACIER DRILLING LTD.

FEBRUARY 2013

NTS 105C-14,15

UTM 604993E/6754257N Zone 8N

Whitehorse Mining District

RECEIVED
FEB 27 2013
MINING RECORDER
WHITEHORSE, YT
Government of Yukon

Ken Witherly
Condor Consulting
Lakewood Colorado
USA

CONTENTS

1.SUMMARY 2

2.INTRODUCTION 3
  Hummingbird Survey 3

3.DATA QUALITY 4
  Culture and flying height 4
  Magnetic Data 4
  EM Data 4
  Radiometric Results 4
  Comments 4

4.INTREPRETATION 7
  Prior Work & Target Model 7
  Processing 8
  Magnetic Results 9
  Radiometric Results 11
  EM Results 13
  Discussion 13

5.CONCLUSIONS AND RECOMMENDATIONS 16

6.REFERENCES 17

7.APPEDNDIX 18
  APPENDIX A MultiPlots for Hummingbird Survey 19
  APPENDIX B Information on Data Processing 20

1. SUMMARY

Glacier Drilling Ltd. (Glacier) commissioned Condor Consulting, Inc. (Condor) to undertaken an assessment of airborne EM, magnetics and radiometrics data acquired over Glacier's Quiet Lake property, Yukon. The property is felt to be prospective for Ni-Cu-gold mineralization and therefore the focus of the survey was to identify targets of high conductance with possible magnetic association.

This report constitutes the final assessment of the airborne results.

Respectfully submitted

Ken E W

Ken Witherly
February 15, 2013

2. INTRODUCTION

Hummingbird Survey

A Hummingbird airborne EM, magnetic and radiometrics survey was conducted by McPhar Ltd. over the Quite Lake property in 2004. A total of 604 line km of geophysical data were acquired. An outline of the geology (provided by Glacier) and the area of the geophysical survey are shown in Figure 1.

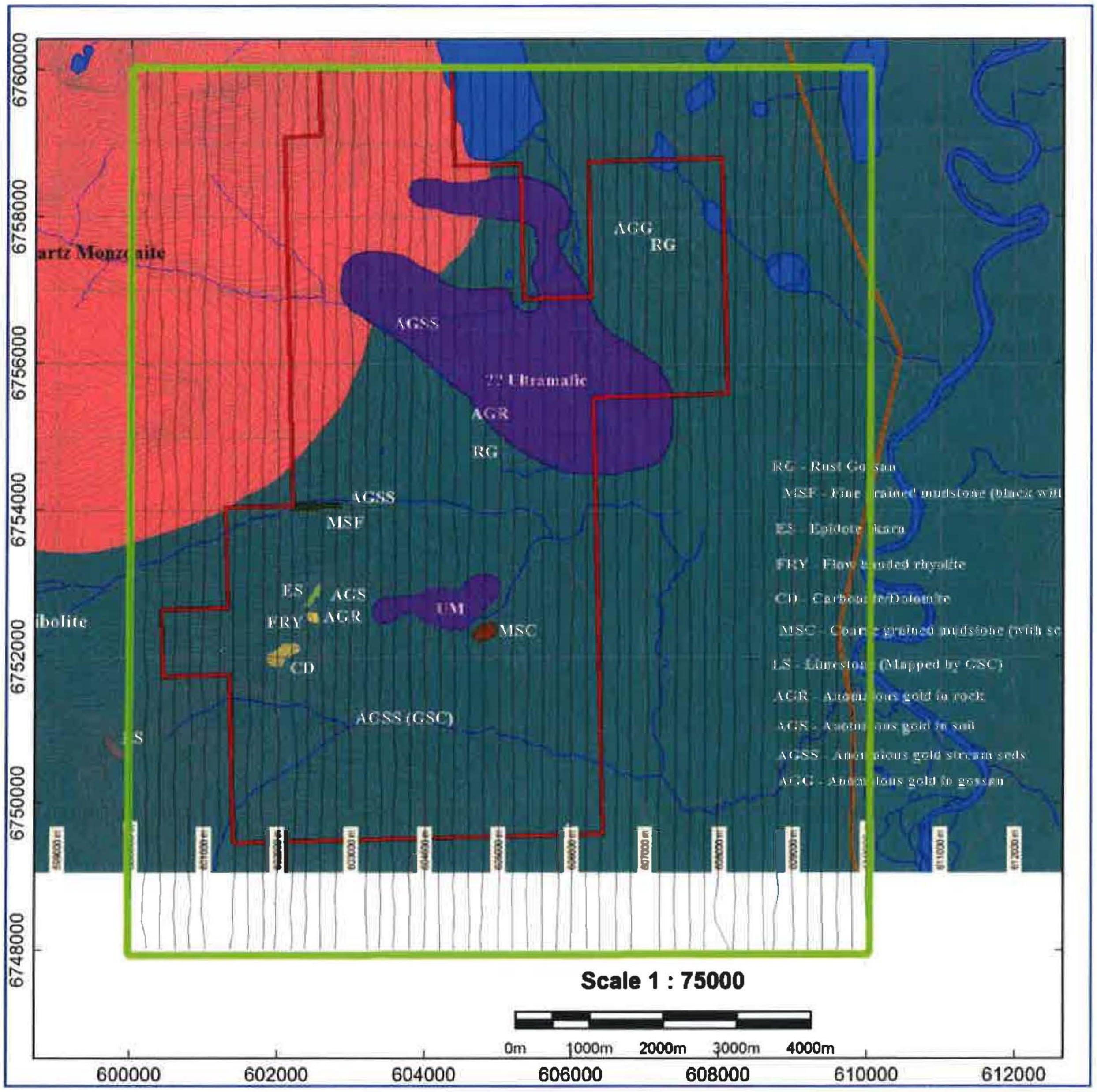

Figure 1: Location of a Hummingbird survey (green outline with flight lines), claim outline (red) and property geology, Quite Lake property, Yukon.

3. DATA QUALITY

As was noted in Condor's original examination of the QL results in 2008 (Witherly 2008), there were several issues noted with the Hummingbird survey carried out for Glacier. Condor has been able to establish independent confirmation of certain issues with the data (Rob Hearst pers. com.) but no means to correct the observed problems has been uncovered.

Culture and flying height

There were no cultural sources within the survey area during the time of the survey. The flying height looks very good; the pilot was able to maintain an excellent above ground distance for the survey.

Magnetic Data

The magnetic data was deemed to be of good quality.

EM Data

Figure 2 shows an outline of the flight lines. Starting with L1370 and going to the east there appeared to be a degradation of the EM results. The origins of this issue are not clear but this part of the survey should be considered suspect. Data from L1470 and L1510 are shown in Figures 3 and 4. Where the issue on L1470 was more random off-sets to the data; on L1510, large parts of the recorded data appears to be missing and straight line segments have been inserted.

Radiometric Results

The radiometric results look to be of good quality.

Comments

No effort has been made to 'back out' the affected EM data or modify the processing, rather the areas of problem data are defined and the final assessment provides a caveat for the results (especially EM) obtained in the area of concern.

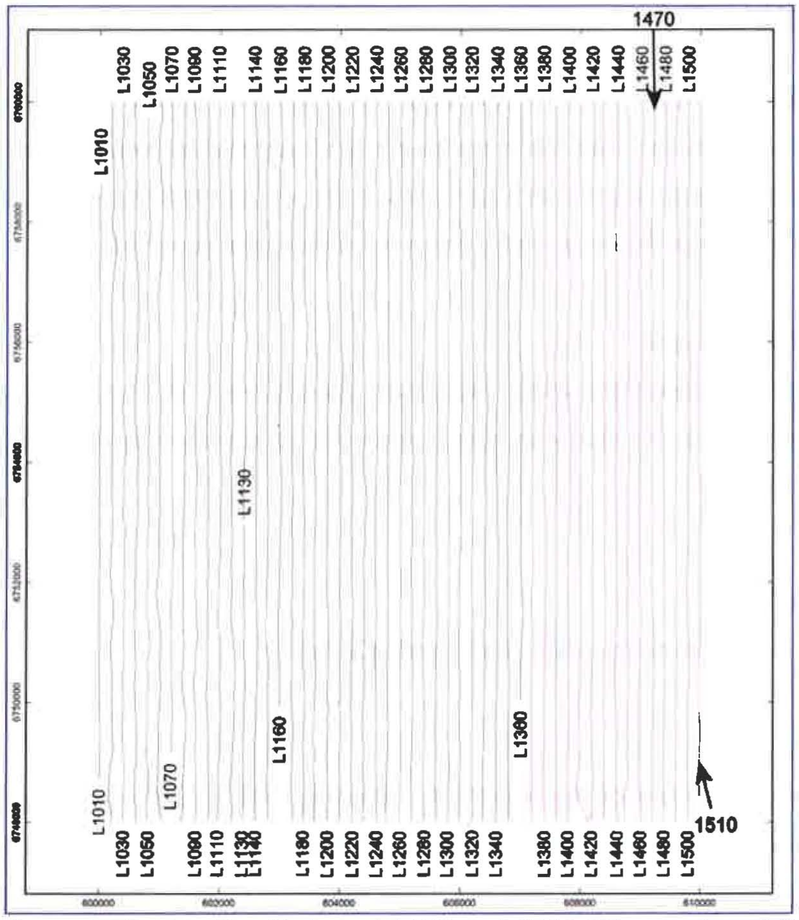

.Figure 2 Flight path with lines L1470 and 1510 (Figures 3 and 4).

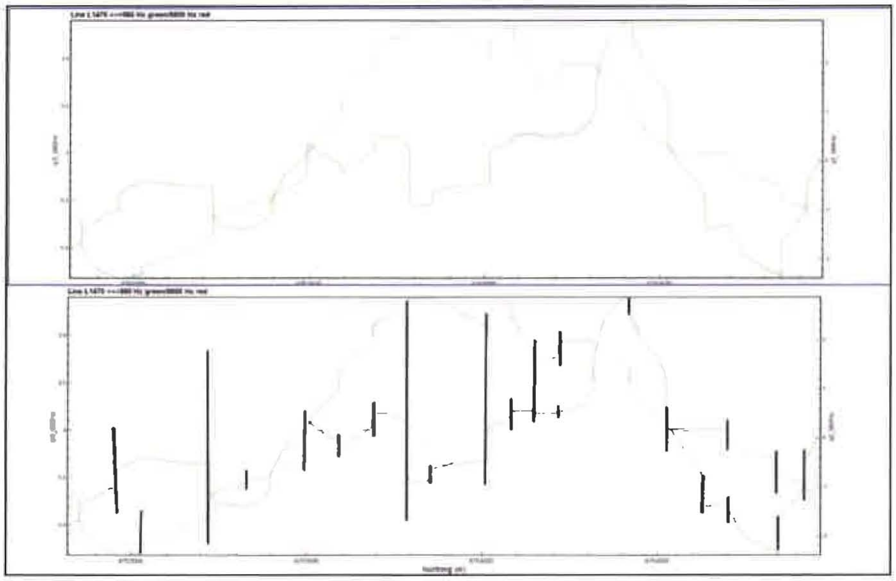

Figure 3: Segment of L1470 showing data tares (unexplained off-sets).

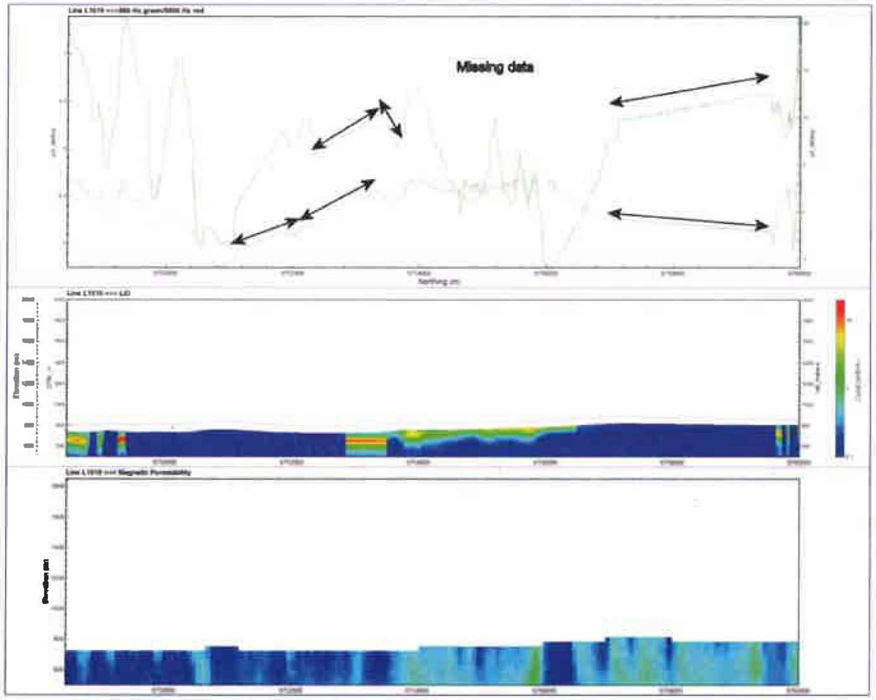

Figure 4: L1510 showing apparent missing data.

4. INTREPRETATION

Prior Work & Target Model

There has a series of ground and airborne surveys over the property, including limited drilling. Not all reviewed here but the major ones are mentioned below.

1966-Geochemical survey and ground magnetics by Newmont. Geochem was run looking for Faro-Anvil style targets (base metals rich in zinc and lead). The results were deemed negative.

1968-Waterton Airborne EM and magnetic survey. Carried out for a consultant to the Lindsey family, PH Sevensma, a consulting geologist based in Vancouver. Follow-up to the airborne survey is unclear but the major ultramafic was presumably recognized.

1969-IP surveying was conducted over a part of the ultramafic body. Two drill holes appear to have tested chargeability Zone A. Results are believed to be in hands of client.

2003-MaxMin and ground mag over location 1.4 km to 2.8 km SE of Quite Lake. One significant Max-Min conductor defined on northern grid with strike length of ~300 m. This was apparently drill tested but core lost before analysis performed. Other drilling was done to the SE of the MaxMin conductor, target unclear. No significant results known to Condor.

2004-Hummingbird Survey over was completed over claim block; the survey was undertaken by McPhar. As this survey is the major subject of this assessment, a detailed QA/QC assessment is provided (Section 3) and the results of which will be major subject of the rest of the report.

The successful use of geophysical exploration most often occurs when there is a demonstrable linkage between the target (s) of interest and the geophysical parameters being measured. That said, positive geophysical responses alone do not guarantee the presence geological target of interest. Typically this is where multiple data sets and direct geological observation are likely required along with a sensible amount of drilling to validate the various targets models being proposed.

The client provided geology is shown in Figure 5. The three major rock types are a quartz monzonite in the NW corner of the block; two outcropping areas of ultramafic and a large area of sediments and possibly volcanics. Some minor outcrops of rhyolite, dolomite and limestone are mapped as well.

The client reports that large amounts of what is believed to be iron oxide appears to the surface both in open ground and along streams. While this speaks to significant iron being weathered, the known ultramafic could be the source of this iron and does require there to be economic mineralization to be present. A more systemic assessment of the extent, chemistry and texture of the shallow iron deposits might shed light on the origins of this weathering product but at this stage, as far as a helping define a target model, this information is deemed “interesting” but not “diagnostic” for any specific deposit model/type.

To Condor's knowledge, the geochemical surveys do not pin-point a signature which can be attributed to a specific deposit style or setting.

In the absence of clear analogues to draw from, Condor has taken a data drive approach to the assessment, examining the various surveys and then deriving some ‘features of interest’ for the client’s consideration.

Processing

To assist in the assessment of the results, Condor performed the following processing to the data sets.

Magnetic data:
A suite of grid products were produced but these were deemed of limited value apart from the standard total magnetic intensity (TMI).

A Mag3D model was generated from the TMI grid. This is displayed as a sectional plot in the MultiPlots (Appendix A).

Radiometrics data:
A ternary plot was generated but was not deemed to be of value.

EM data:
The EM data were treated with several forms of processing. A Tau grid was generated. This product helps define those features of higher conductance. A layered earth inversion model was run on the data which produces a depth conductivity section along each line. Due to the marginal quality of the EM data, this outcome is deemed of limited value over grid-based products. The layered earth inversion results are displayed in the MultiPlots (Appendix A).

Further information on the processing applied to the data sets is provided in Appendix B.

Magnetic Results

Figure 5 shows the geology and total magnetic intensity (TMI). Lithologic responses dominate the image. The large zone of intrusive rock (quartz monzonite) in the NW part of the survey block appears as a zone of elevated response. A semi-circular zone of higher response appears within this area which is thought to represent some form of zonation within the intrusive body. The strongest magnetic response corresponds to a mapped ultramafic in the north-central part of the survey block. A smaller ultramafic body is noted several kms to the south. While the magnetic character is not as clear cut, the magnetic pattern suggests that the area of ultramafic rock could be much more extensive.

Figure 6 shows the geology and TMI-Tilt (Tilt enhances magnetic contacts). While this product can sometimes provide better resolution of structure, not a lot of what is thought to be structure is apparent in this result.

Figure 7 is a zoom-in around the main ultramafic body. This shows the drilling, IP survey (chargeability) and MaxMin results. The main area of drilling is SE of the MaxMin response and lies adjacent to a small magnetic body. The IP zones lie inside the main ultramafic body and the drilling appears to have tested Zone A. The MaxMin conductor was as noted earlier, tested by a drill hole whose core has been lost.

Within the magnetic results alone, there are no features what can be described a targets.

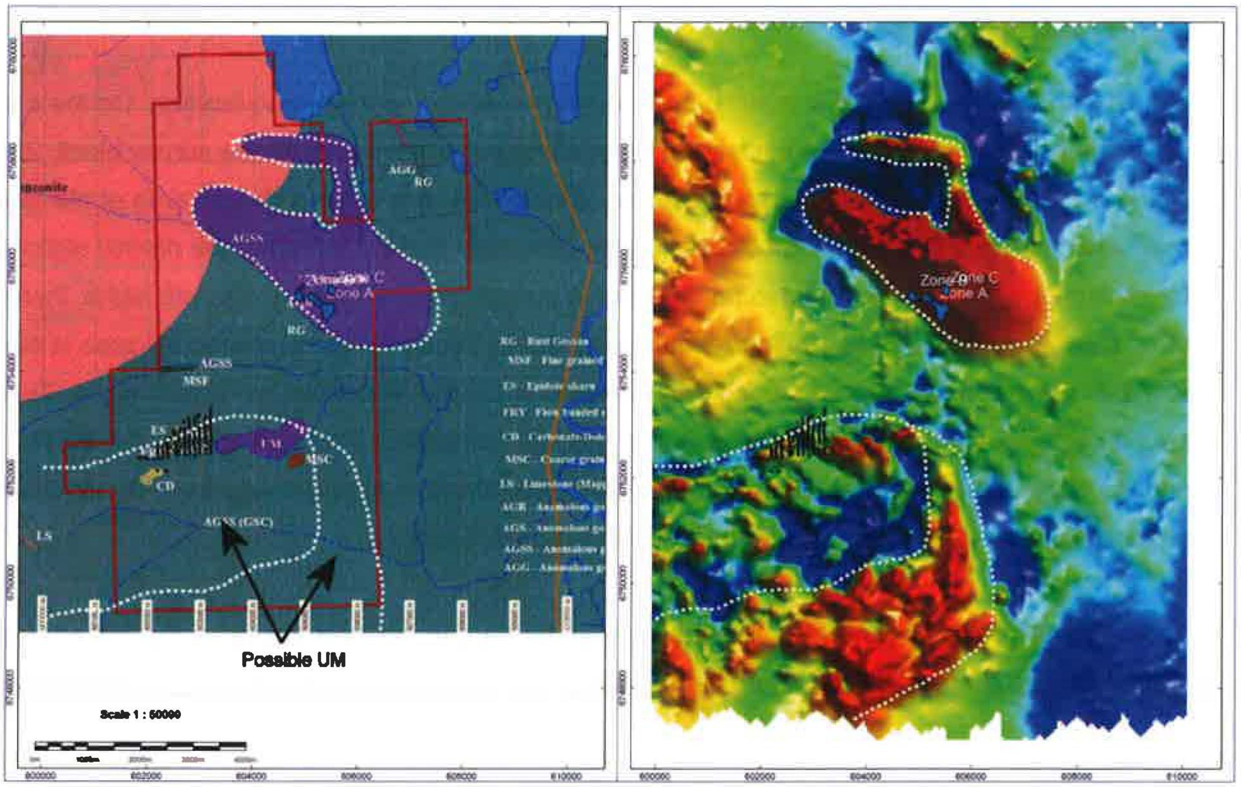

Figure 5: Geology and TMI with some contacts highlighted.

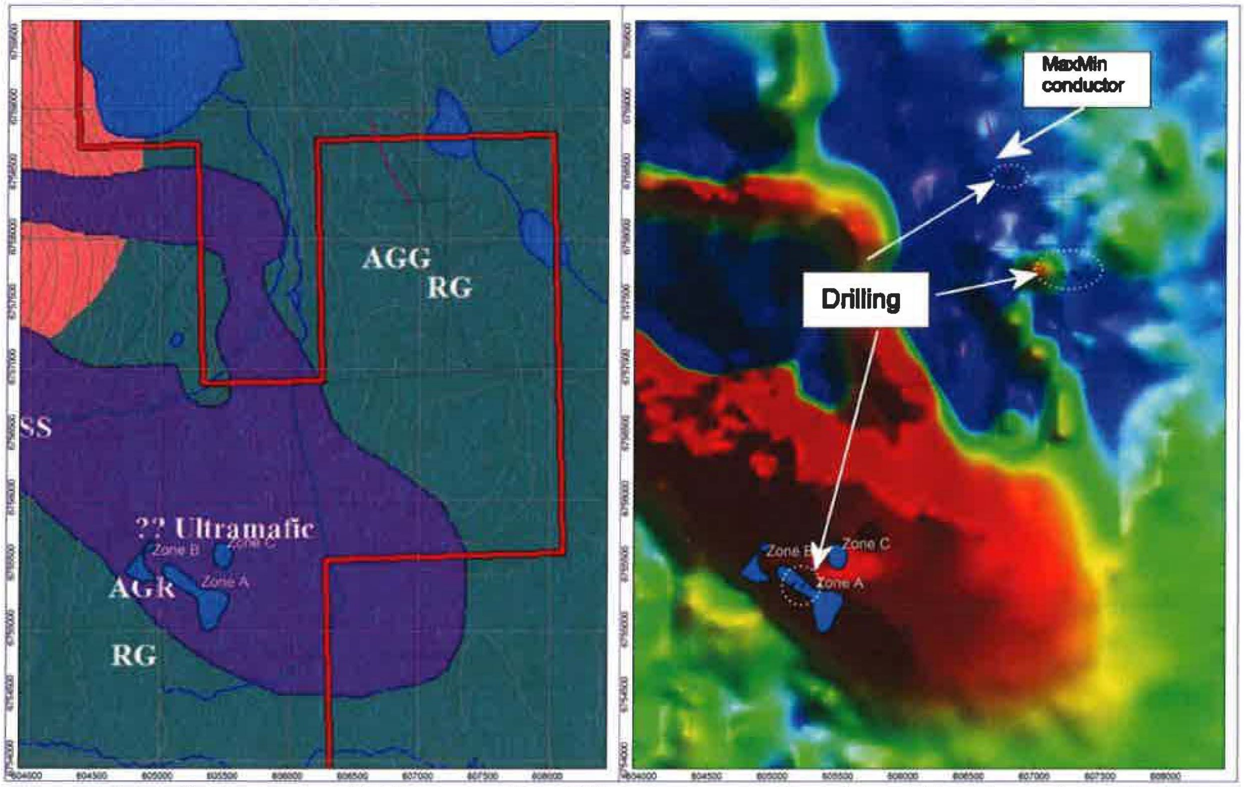

Figure 6: Geology and TMI zoomed in in NW area where drilling, IP and MaxMin performed.

Radiometric Results

Figure 8 shows the radiometric results; total count, potassium, uranium and thorium. On the total count image, there are a series of discrete highs along the western side of the survey block. Zones A and B lie over the mapped quartz monzonite. Zone C sits over what is also an area of elevated magnetic response that is thought to possibly be ultramafic rocks. This is not the normal signature for ultramafic rocks, as they tend to be depleted in potassium. Besides the discrete highs, there are three loosely defined trends running roughly north-south. Along the western side the area is elevated; in the center it is low and along the eastern margin, the responses are erratic highs. There is strong correlation between the potassium and thorium responses. This is unexpected if the response were bedrock related. Zone A (total count) also shows a strong response in the uranium channel; basically the only response noted with that radioelement.

The radiometric results produce some results that are hard to interpret based on the limited geological control. None of these features at this stage are considered economic targets.

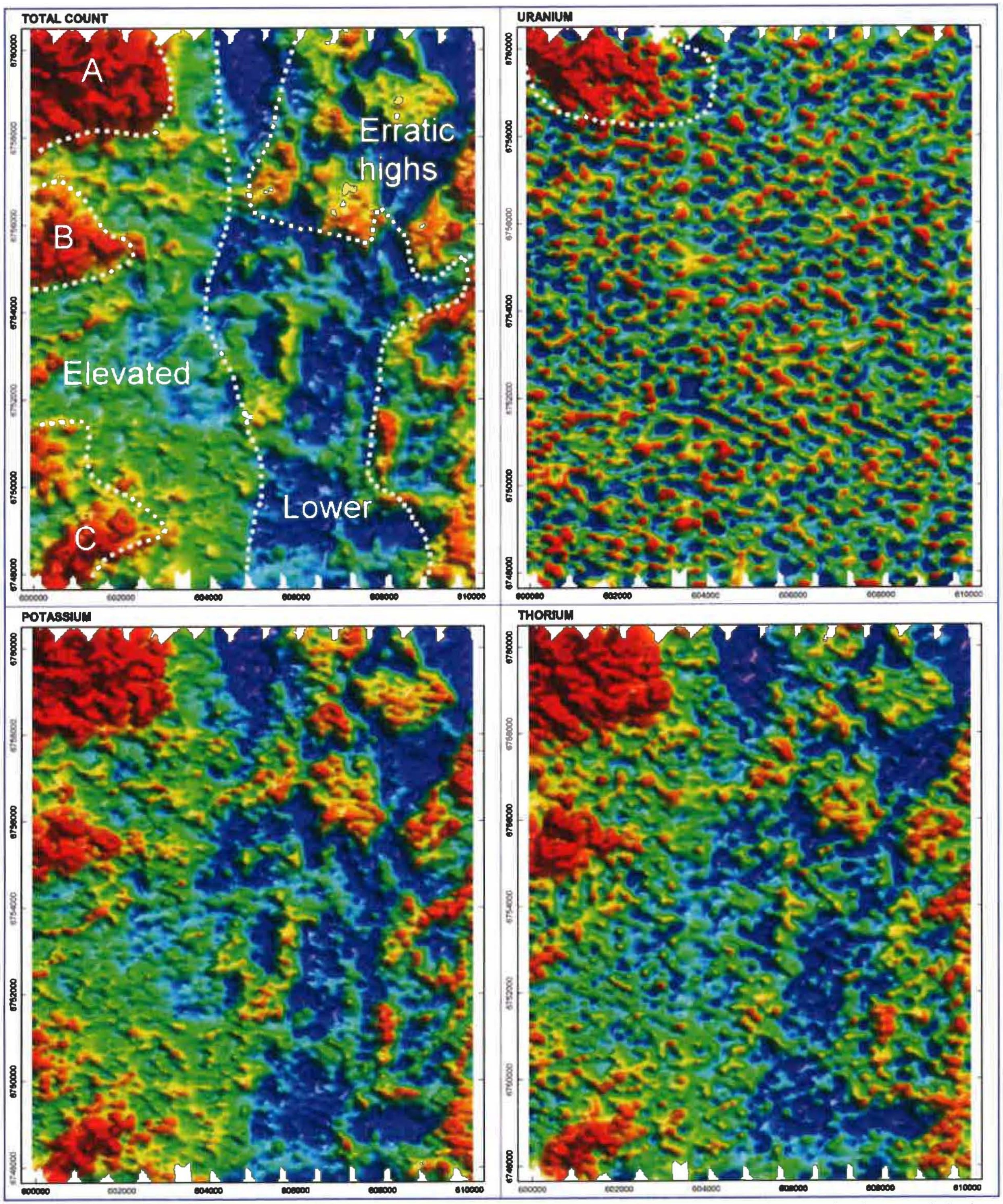

Figure 7: Total count, potassium, uranium and thorium responses; some interpretive contacts annotated.

EM Results

As discussed earlier in the report, there were obvious quality issues the EM data. While the eastern 20% of the survey has known issues, there could be issues with other parts of the survey and the only way to try and assess these is to look for non-geological (i.e. odd outcomes) in the products.

Figure 8 shows a composite image of the geology and three EM products; two generated by Condor and one taken from the EM survey directly; the In-Phase 6,600 Hz signal. The Condor parameters are the Tau and the Con [3] depth slice from the layered earth inversion models. The Tau is a more rigorous way of extracting the conductance from the EM data and the depth slice is the conductivity at a very shallow depth. The Tau result (Figure 8, lower left) produces an interesting N-S trending band that cross-cuts all the major stratigraphies. Within this trend there are some zones of higher conductance; the more intensive of which are contoured. The other two EM products both as well show an area of elevated response roughly in the center of the survey block. The geological significance of these responses is unclear. Neither appears to show any specific relationship to the mapped geology.

Figure 9 shows the geology and TMI with the major EM features annotated. The N-S trending zone is termed Res Zone 1, the central zone is Res Zone 2 and the discrete Tau highs are designated T1-T5. Of the discrete features, T2, T3 and T5 appear to line up along the contact of the inferred southern ultramafic (Figure 5) which makes these interesting features. T2-T5 all fall within Res Zone 2 which lends credence to the belief that this area does host some legitimate EM responses.

Discussion

The airborne survey produced magnetic, radiometric and EM outcomes which have been assessed following suitable processing. The magnetic results show there is a strong correlation with a mapped ultramafic and a second zone of likely ultramafic is inferred based on the magnetics.

The radiometrics showed a number of anomalous zones but it was difficult to relate these to the mapped geology. There is a strong high in the NW corner of the survey area which should be examined.

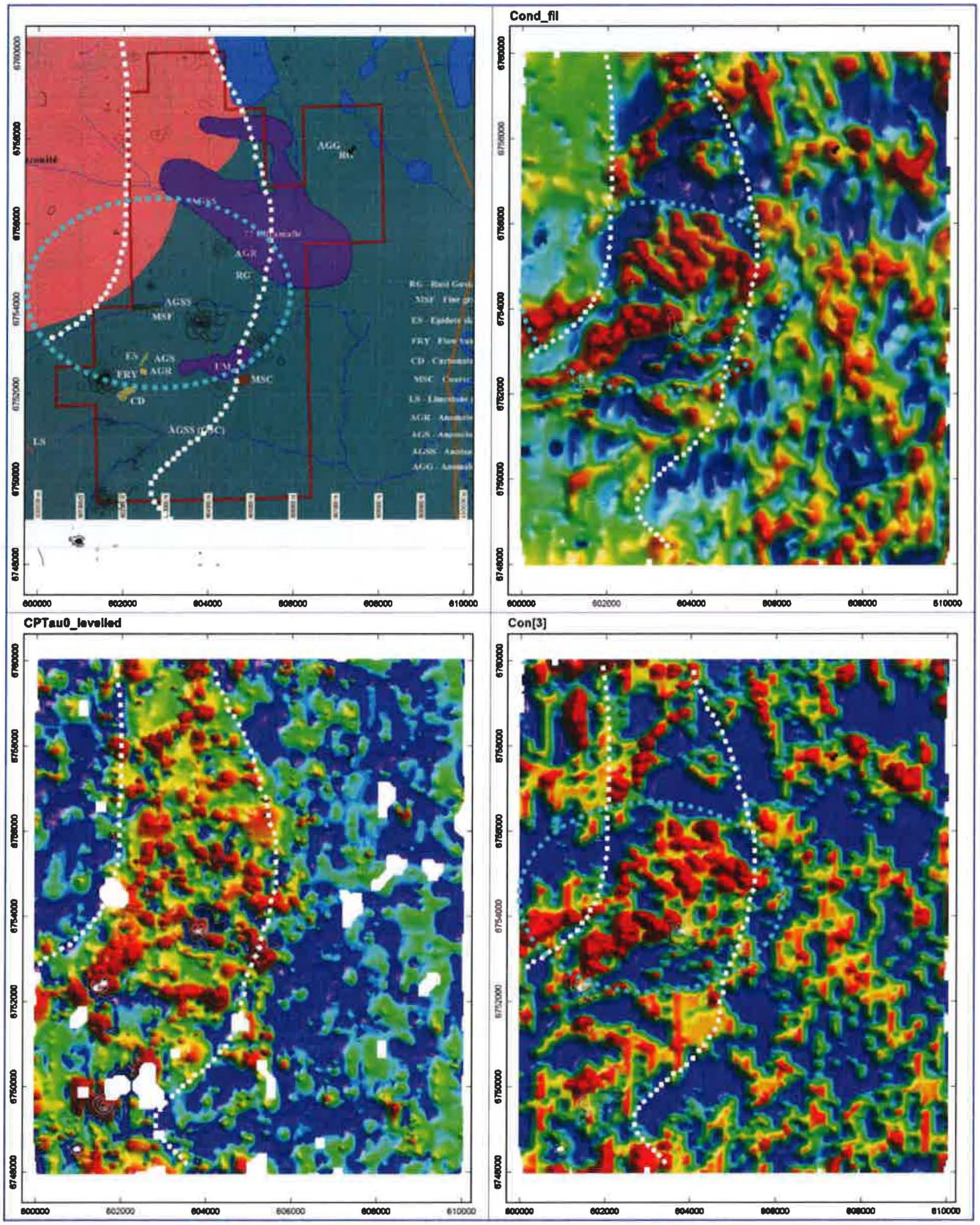

Figure 8: Geology with EM products; Tau (lower left), IP 6600 Hz (upper right) and Con [3] shallow depth slice; zone of enhanced Tau bracketed by dashed lines; zones of high Tau appear as black or white contours; elevated response in IP 6,600 Hz and Con[3] shown on as light blue dashed outline.

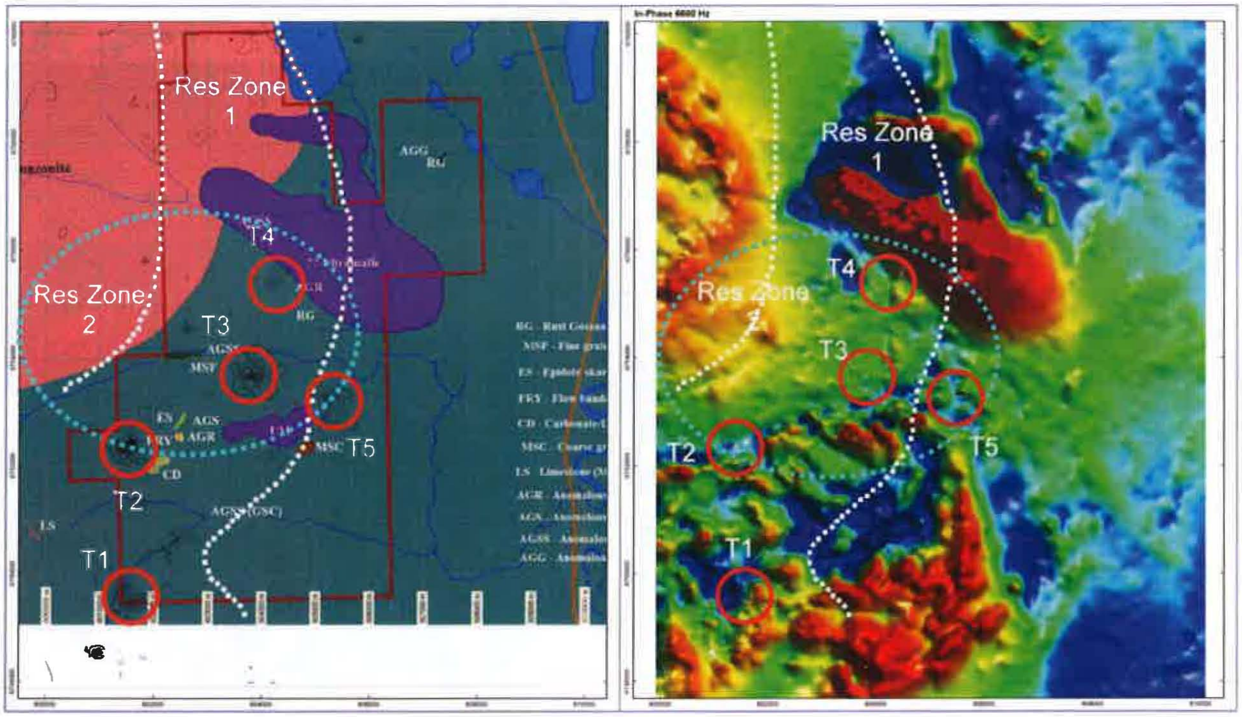

Figure 9: Geology and TMI with interpretive notes (see text for discussion).

The EM results are the most complex of the data sets. While there are significant zones elevated conductivity, it is not possible based on the geology to suggest a specific explanation. A series of discrete Tau highs (T2-T3-T5) were selected as features of interest. These appear to wrap around the northern contact of the southern ultramafic. Ground geophysics, either IP or MaxMin is suggested as follow-up over these features. T1 lies in the SW corner of the survey beside a creek; the magnetic response looks proximal. Geochemical follow-up is suggested. T4 lies adjacent the northern ultramafic, just west of the IP feature that was drilled. IP or MaxMin to define this feature is recommended.

There is a previously defined MaxMin response. Although it falls within the 'good' AEM data, its response can't be recognized in the profiles. This feature should be drill tested.

The fact that the Hummingbird survey failed to detect this strong/shallow ground EM feature indicates that the survey as a whole has likely has not evaluated the property in an effective fashion and a modern TEM style survey such as VTEM would do a superior job. This said, a sound geological rational needs to be developed as to why such a new survey should be done, since at present the geological evidence for the presence of economic deposits to be present is unclear.

5. CONCLUSIONS AND RECOMMENDATIONS

An assessment has been carried out of a Hummingbird EM, magnetic and radiometric survey over the Quite Lake property, Yukon. The magnetic and radiometric results appear to be responding to various aspects of the mapped geology but are not contributing directly to defining targets.

The EM results were more complex and there is a lack of confidence in these results due to perceived and stated issues (Hearst per. com.) However, there are three of features that appear associated with an ultramafic contact that are deemed to be worthy of follow-up.

A new airborne geophysical survey would be an improvement over the current Hummingbird survey but prior to considering such, a review of the property geology is recommended to try and better establish the over mineral prospectivity. It is felt that geochemical techniques should work fairly well in this setting but to Condor's knowledge, the surveys to date have produced results of limited encouragement.

Respectfully submitted,

Ken E W.

Ken Witherly CPG-11536

February 15, 2013

6. REFERENCES

Hearst, R., 2004 Final Report on a Helicopter-borne Geophysical Survey Canol Survey Area Yukon Territory; for Cordilleran Minerals Limited; McPhar Geosurveys Ltd. November 2004

Witherly, K. 2008 Assessment of Hummingbird Airborne EM and Magnetic Data Canol Project, Yukon; Condor Consulting report, July 2008.

Witherly, K. 2012, Preliminary Report on Processing & Analysis of Hummingbird EM, Magnetics and Radiometrics Data, Quite Lake, Yukon for Glacier Drilling Ltd. December 2012

7. APPEDNDIX

APPENDIX A MultiPlots for Hummingbird Survey

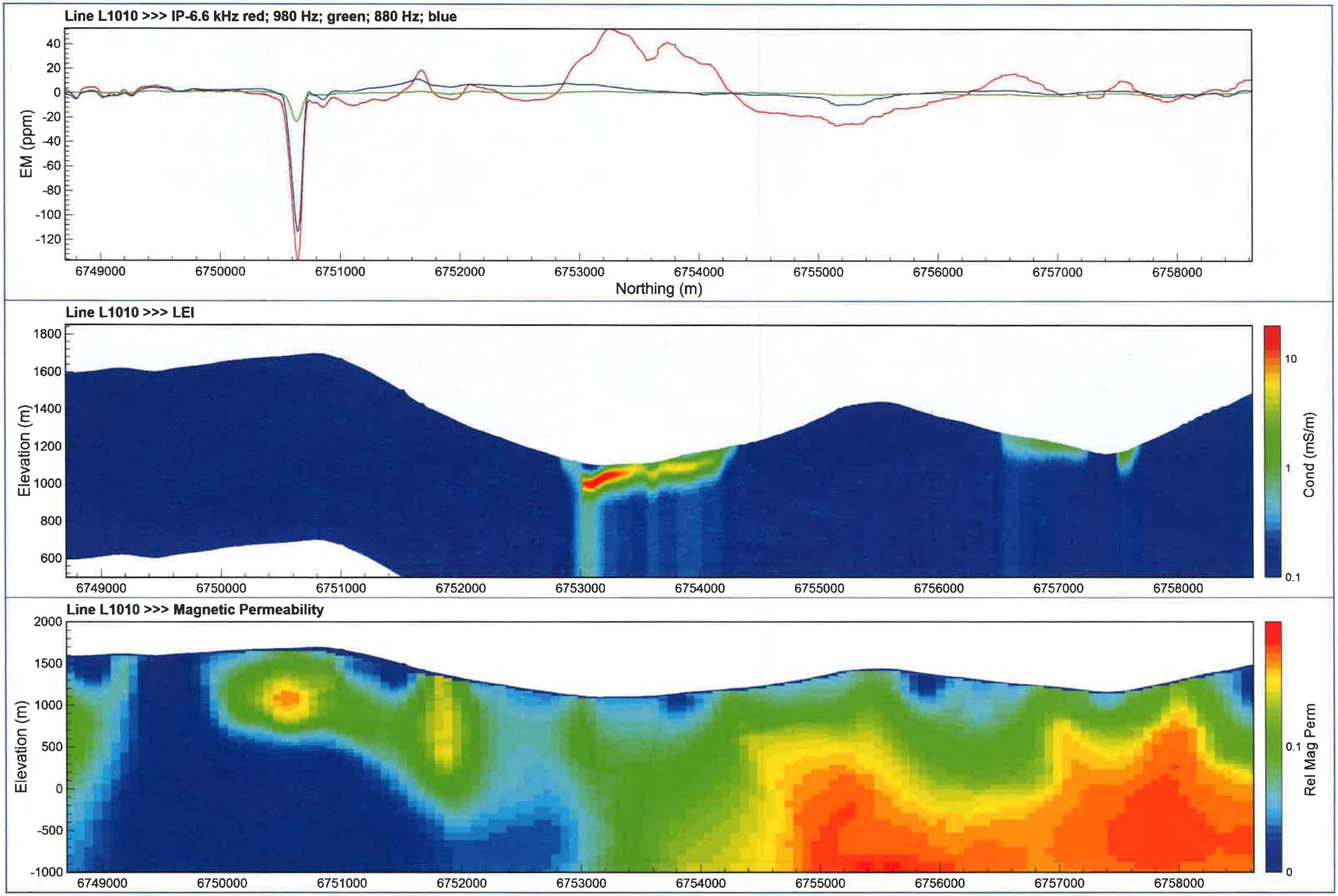
Line L1010 >>> IP-6.6 kHz red; 980 Hz; green; 880 Hz; blue
EM (ppm)
40
20
0
-20
-40
-60
-80
-100
-120
6749000
6750000
6751000
6752000
6753000
6754000
6755000
6756000
6757000
6758000
Northing (m)
Line L1010 >>> LEI
Elevation (m)
1800
1600
1400
1200
1000
800
600
6749000
6750000
6751000
6752000
6753000
6754000
6755000
6756000
6757000
6758000
Cond (mS/m)
10
1
0.1
Line L1010 >>> Magnetic Permeability
Elevation (m)
2000
1500
1000
500
0
-500
-1000
6749000
6750000
6751000
6752000
6753000
6754000
6755000
6756000
6757000
6758000
Rel Mag Perm
0.1
0

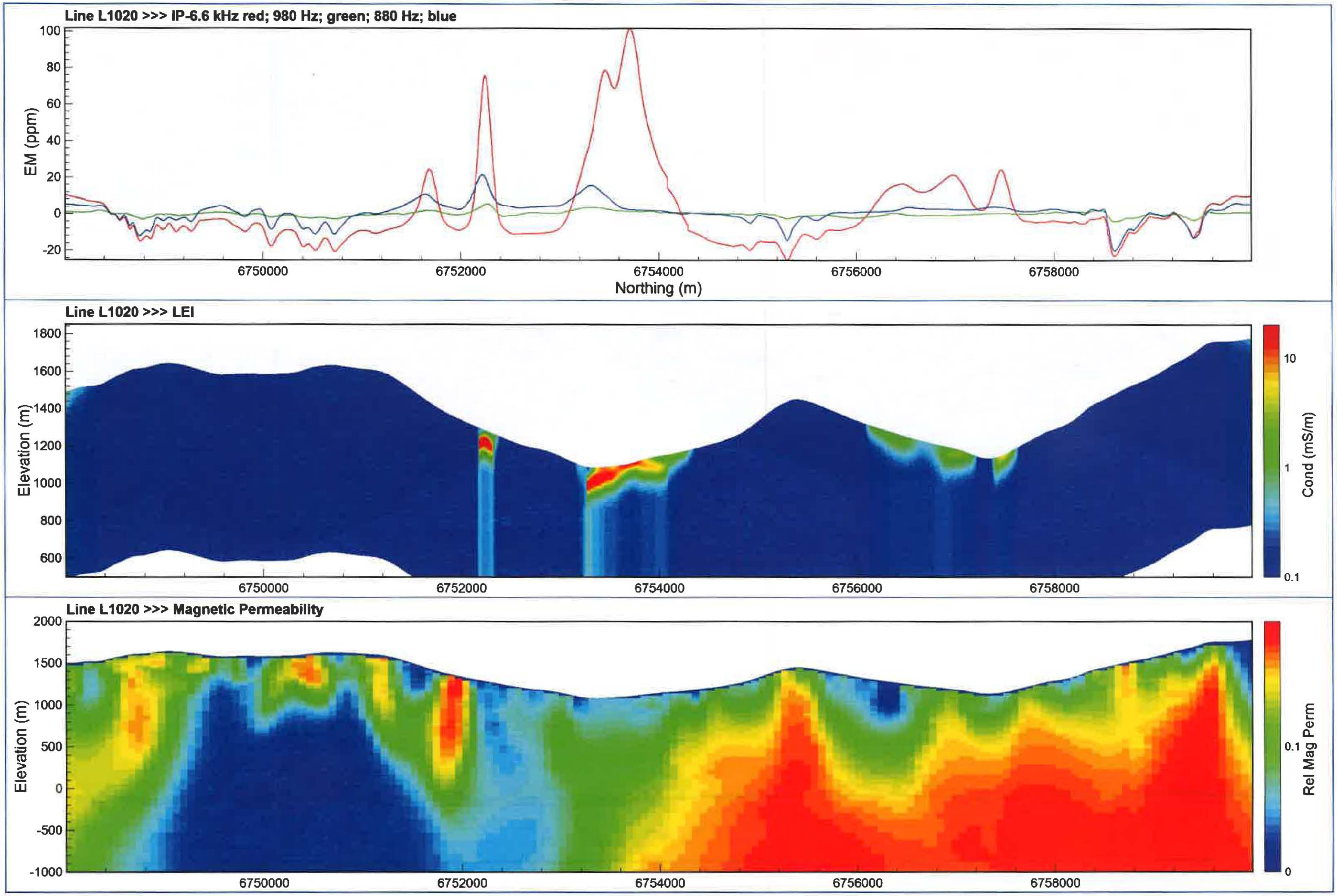
Line L1020 >>> IP-6.6 kHz red; 980 Hz; green; 880 Hz; blue

Line L1020 >>> LEI

Line L1020 >>> Magnetic Permeability

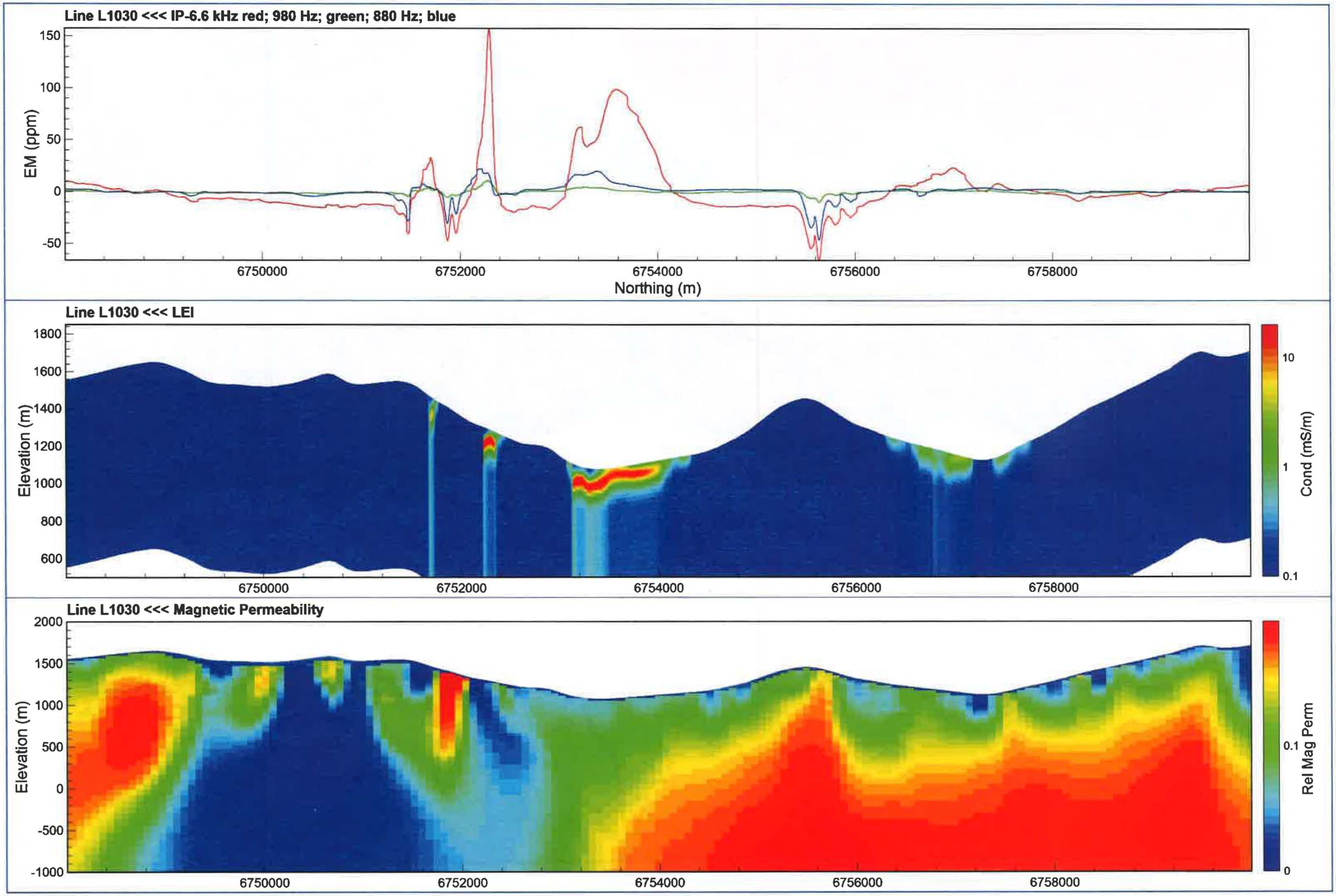
Line L1030 <<< IP-6.6 kHz red; 980 Hz; green; 880 Hz; blue
EM (ppm)
150
100
50
0
-50
6750000
6752000
6754000
6756000
6758000
Northing (m)
Line L1030 <<< LEI
Elevation (m)
1800
1600
1400
1200
1000
800
600
6750000
6752000
6754000
6756000
6758000
Cond (mS/m)
10
1
0.1
Line L1030 <<< Magnetic Permeability
Elevation (m)
2000
1500
1000
500
0
-500
-1000
6750000
6752000
6754000
6756000
6758000
Rel Mag Perm
0.1
0

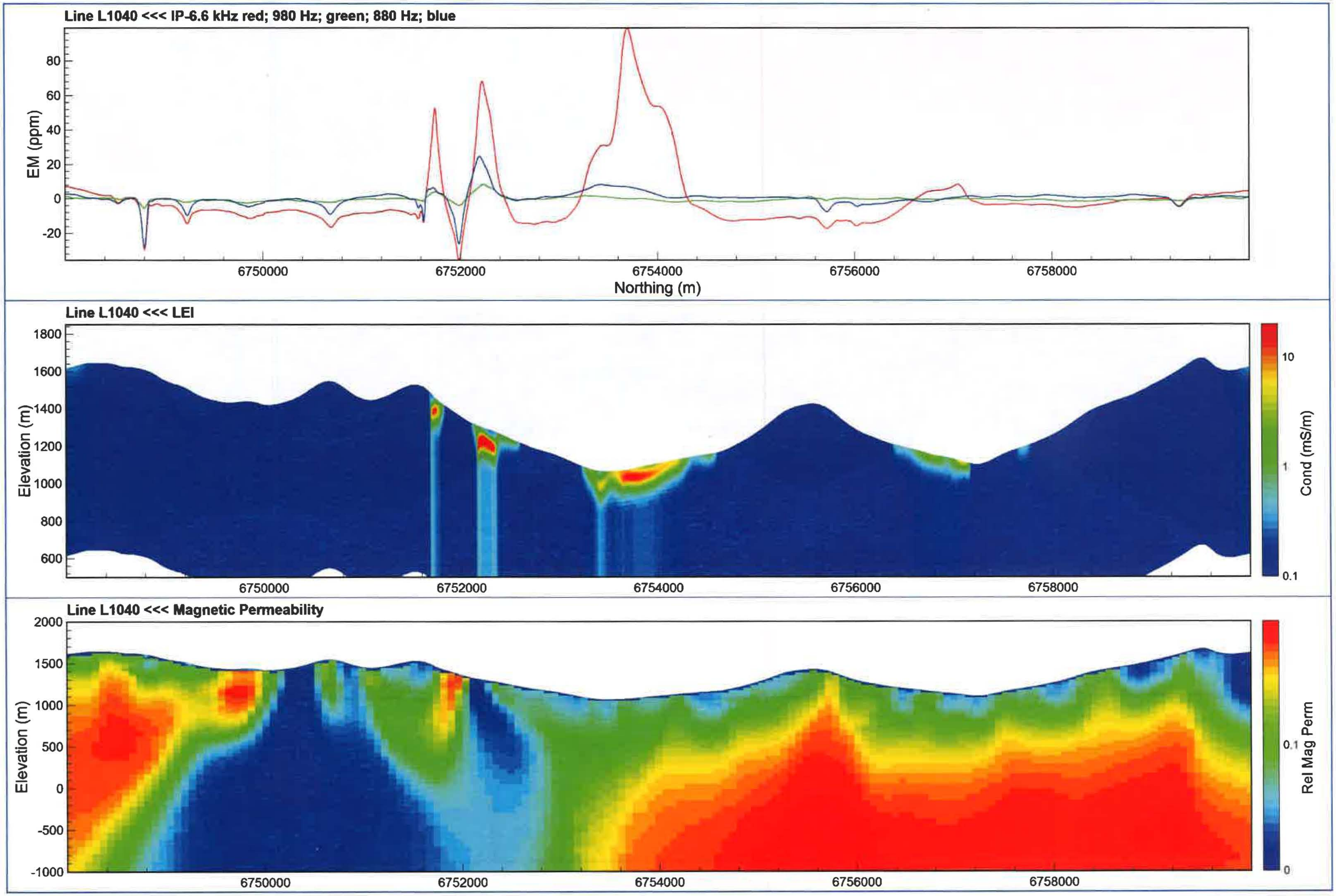
Line L1040 <<< IP-6.6 kHz red; 980 Hz; green; 880 Hz; blue

Line L1040 <<< LEI

Line L1040 <<< Magnetic Permeability

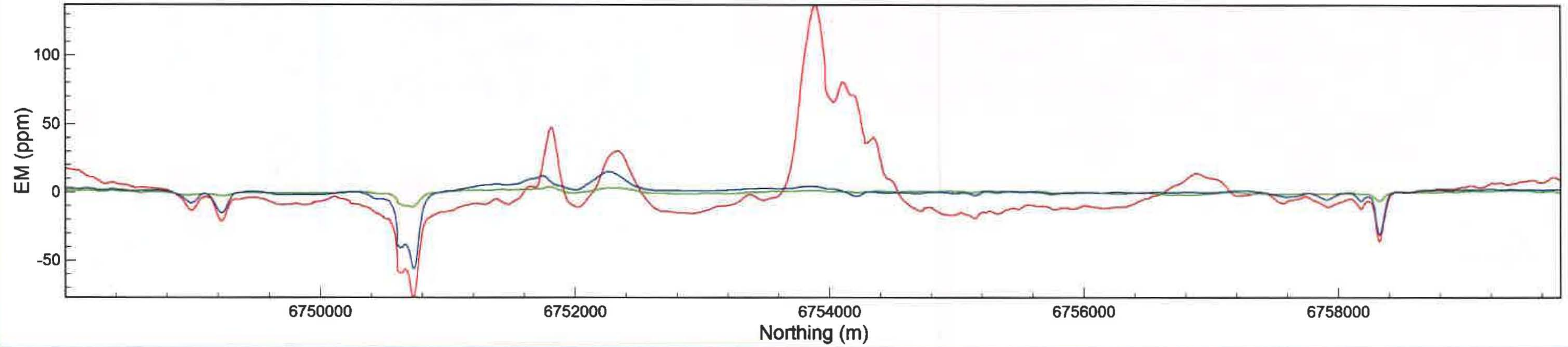

Line L1050 >>> IP-6.6 kHz red; 980 Hz; green; 880 Hz; blue

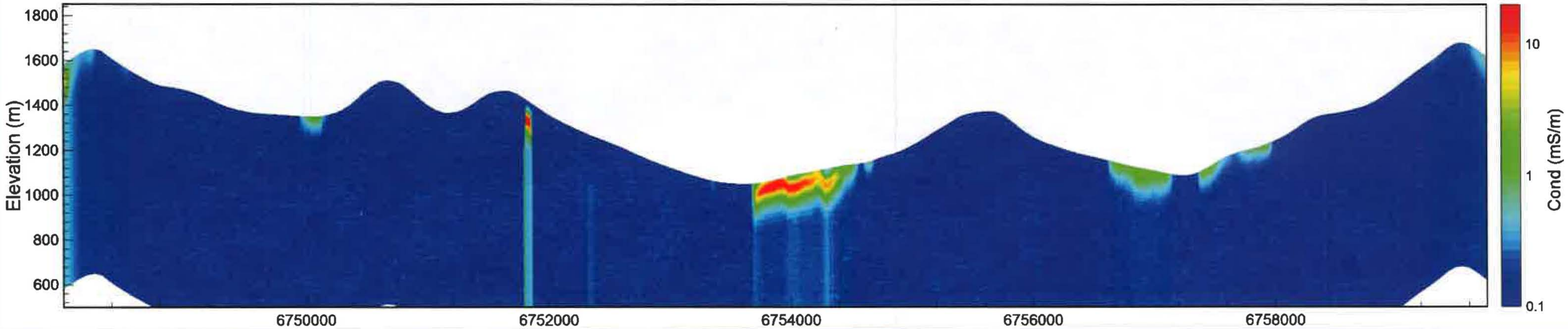

Line L1050 >>> LEI

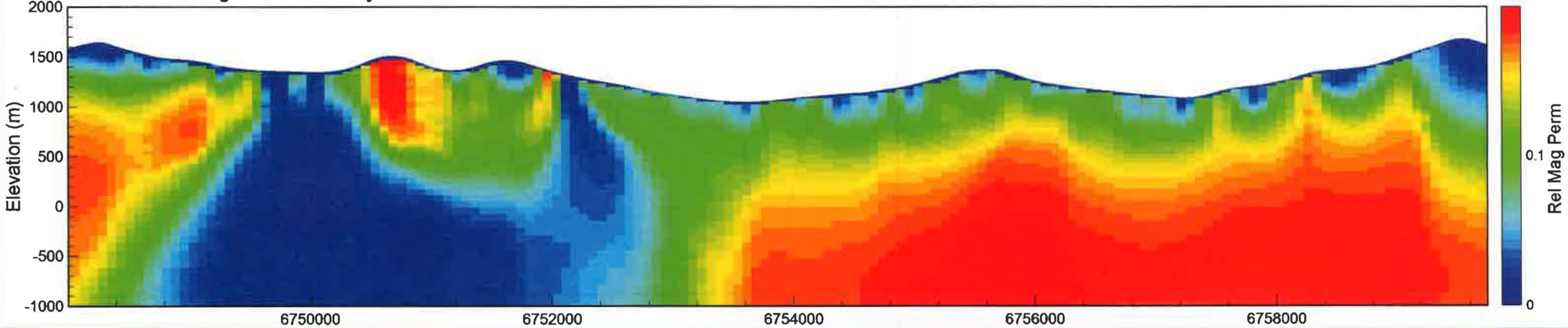

Line L1050 >>> Magnetic Permeability

Line L1060 >>> IP-6.6 kHz red; 980 Hz; green; 880 Hz; blue

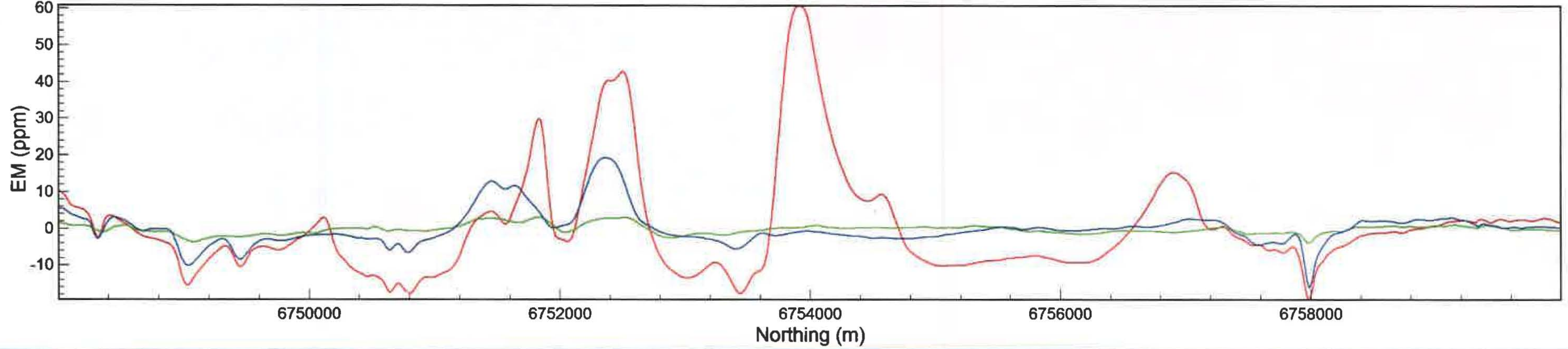

Line L1060 >>> LEI

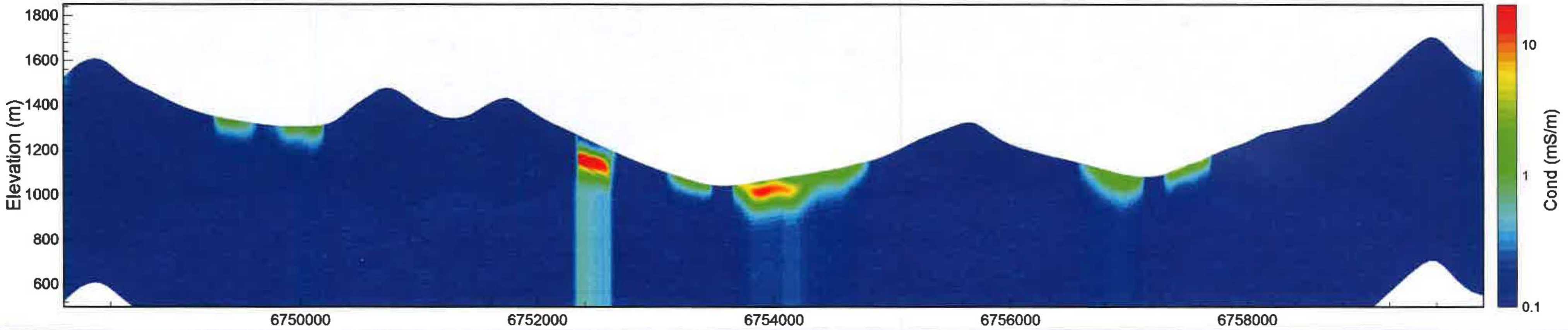

Line L1060 >>> Magnetic Permeability

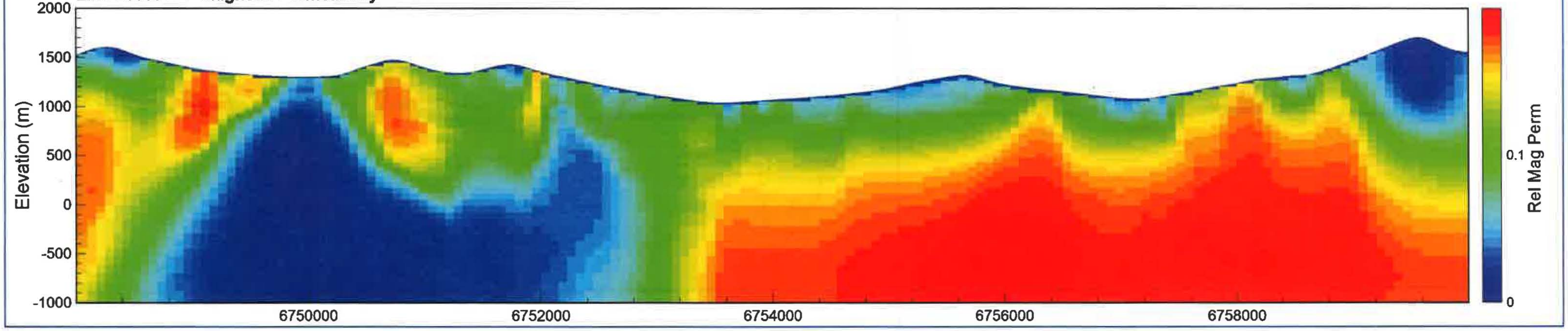

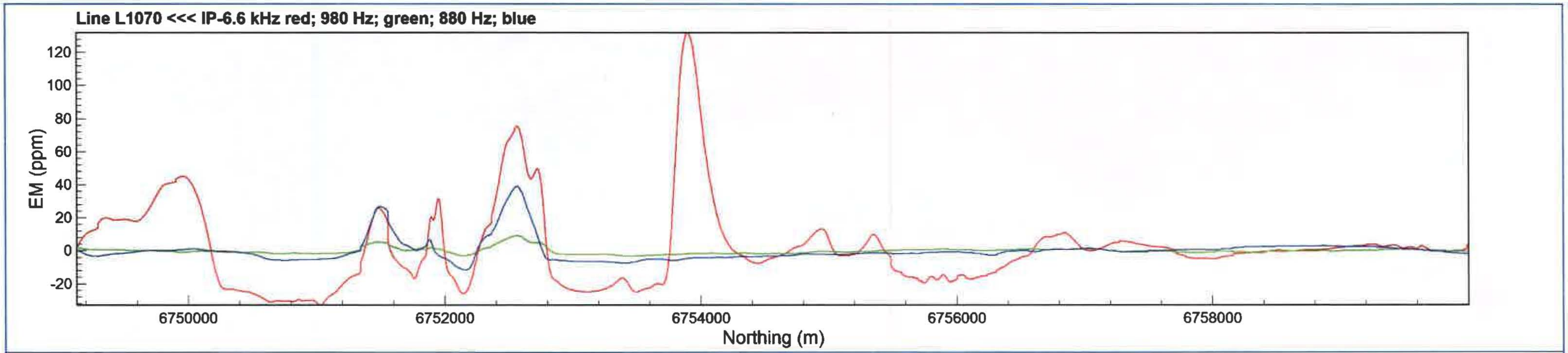
Line L1070 <<< IP-6.6 kHz red; 980 Hz; green; 880 Hz; blue

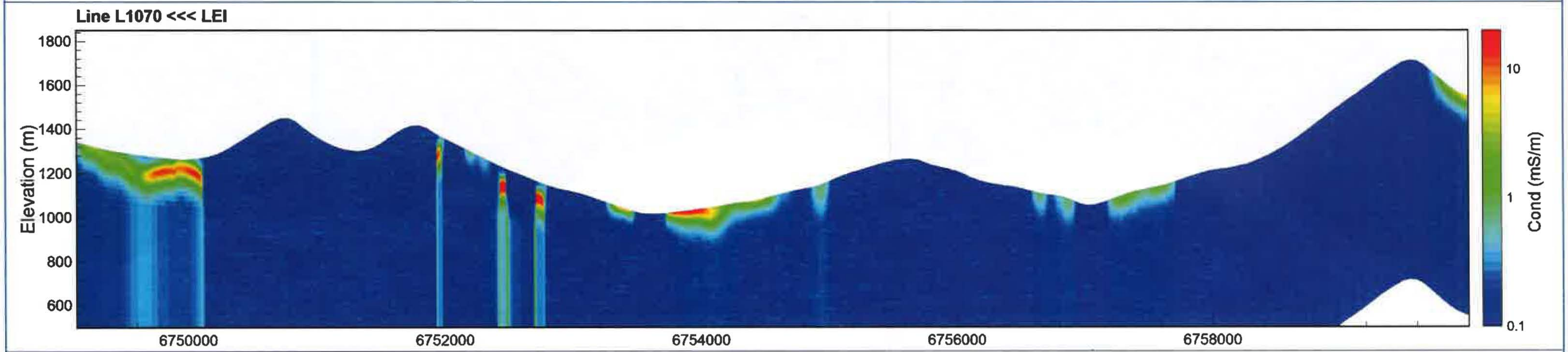
Line L1070 <<< LEI

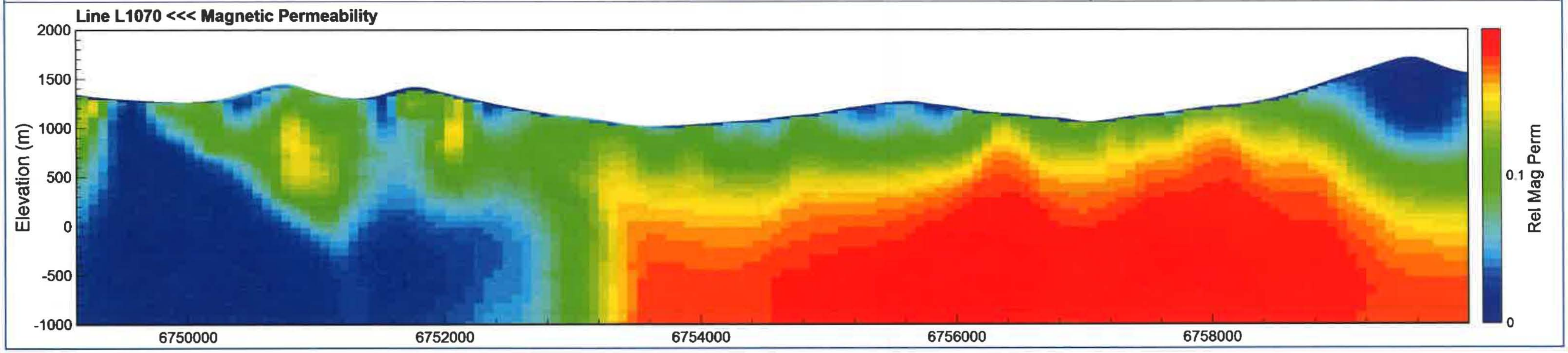
Line L1070 <<< Magnetic Permeability

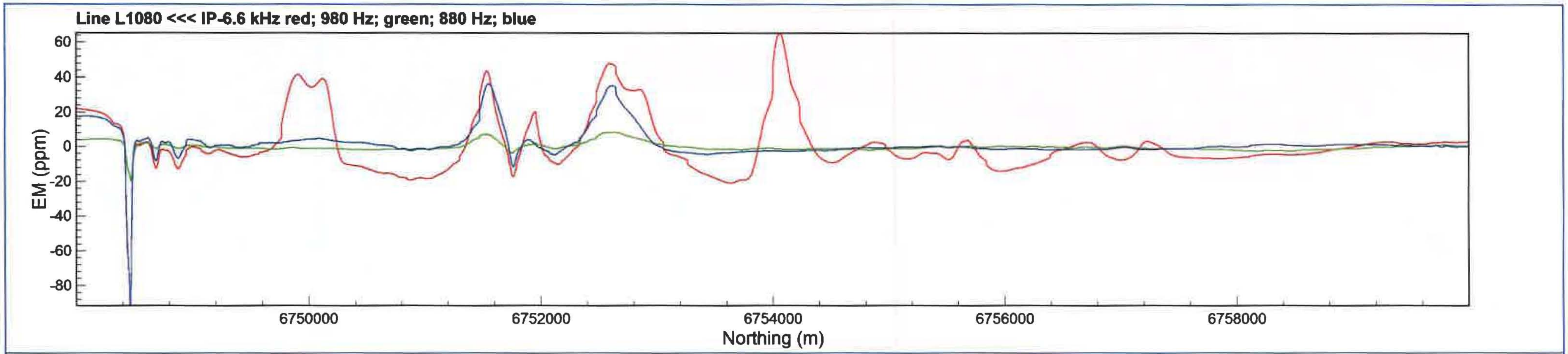
Line L1080 <<< IP-6.6 kHz red; 980 Hz; green; 880 Hz; blue

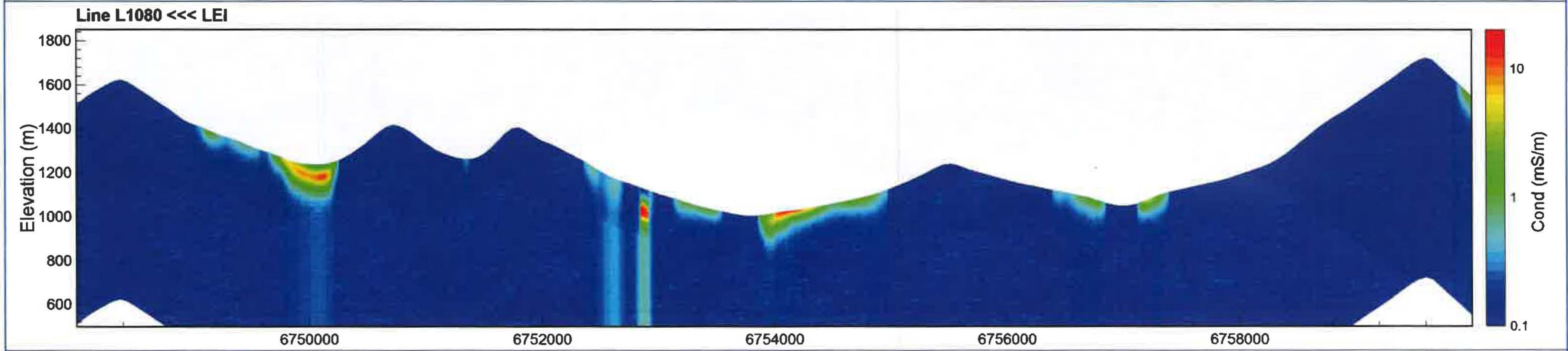
Line L1080 <<< LEI

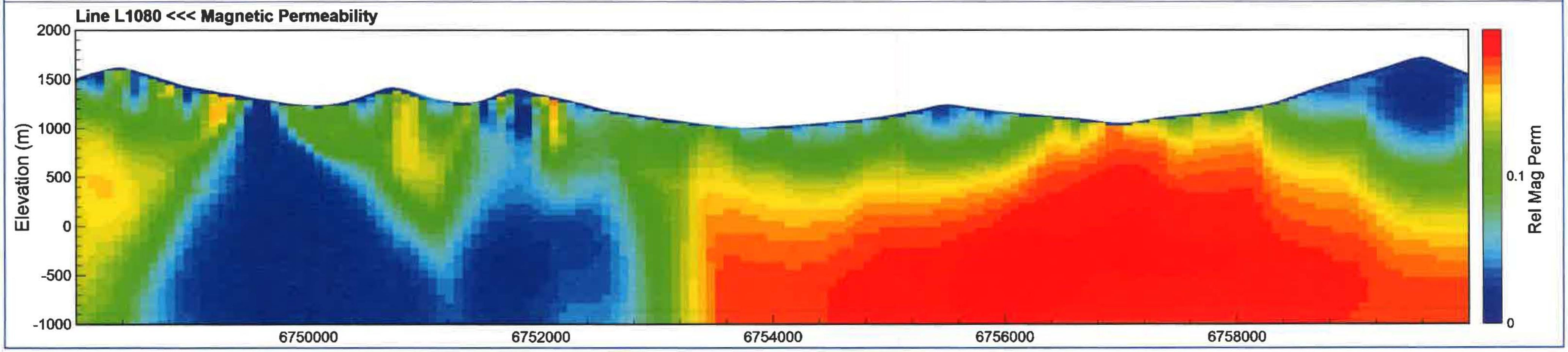
Line L1080 <<< Magnetic Permeability

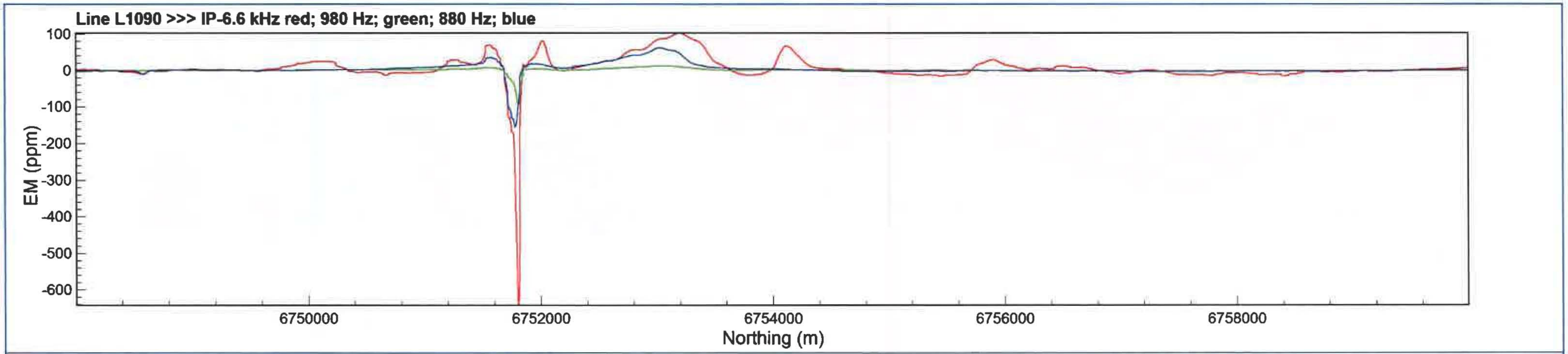
Line L1090 >>> IP-6.6 kHz red; 980 Hz; green; 880 Hz; blue

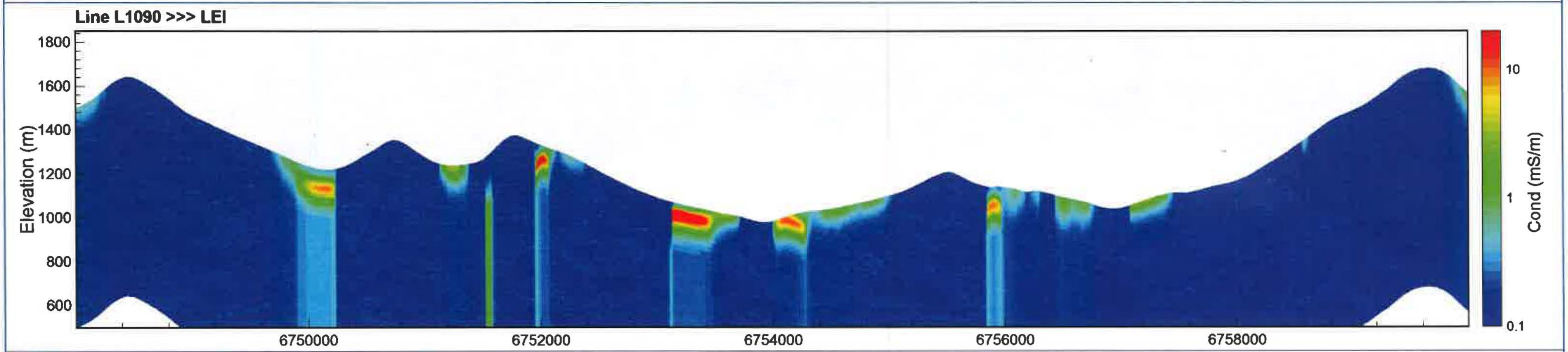
Line L1090 >>> LEI

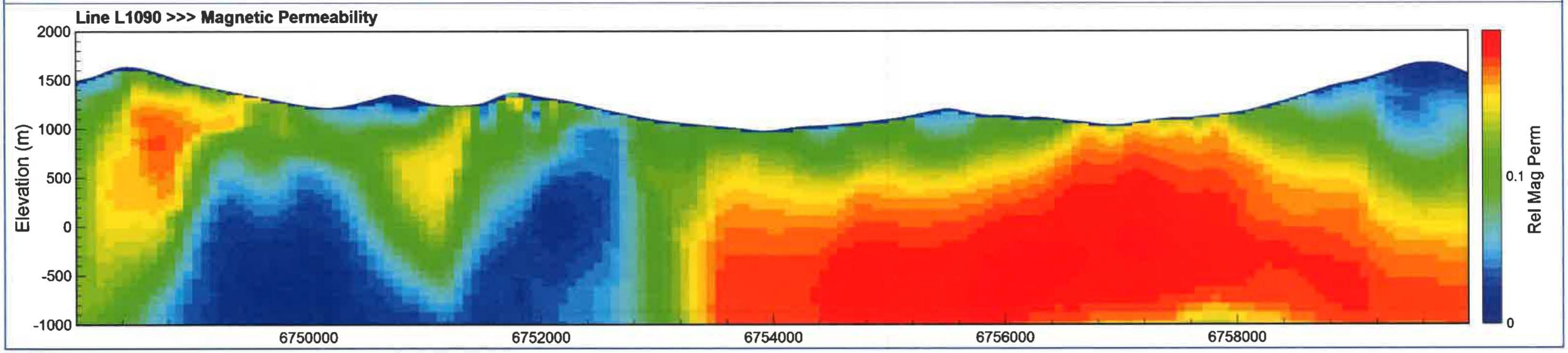
Line L1090 >>> Magnetic Permeability

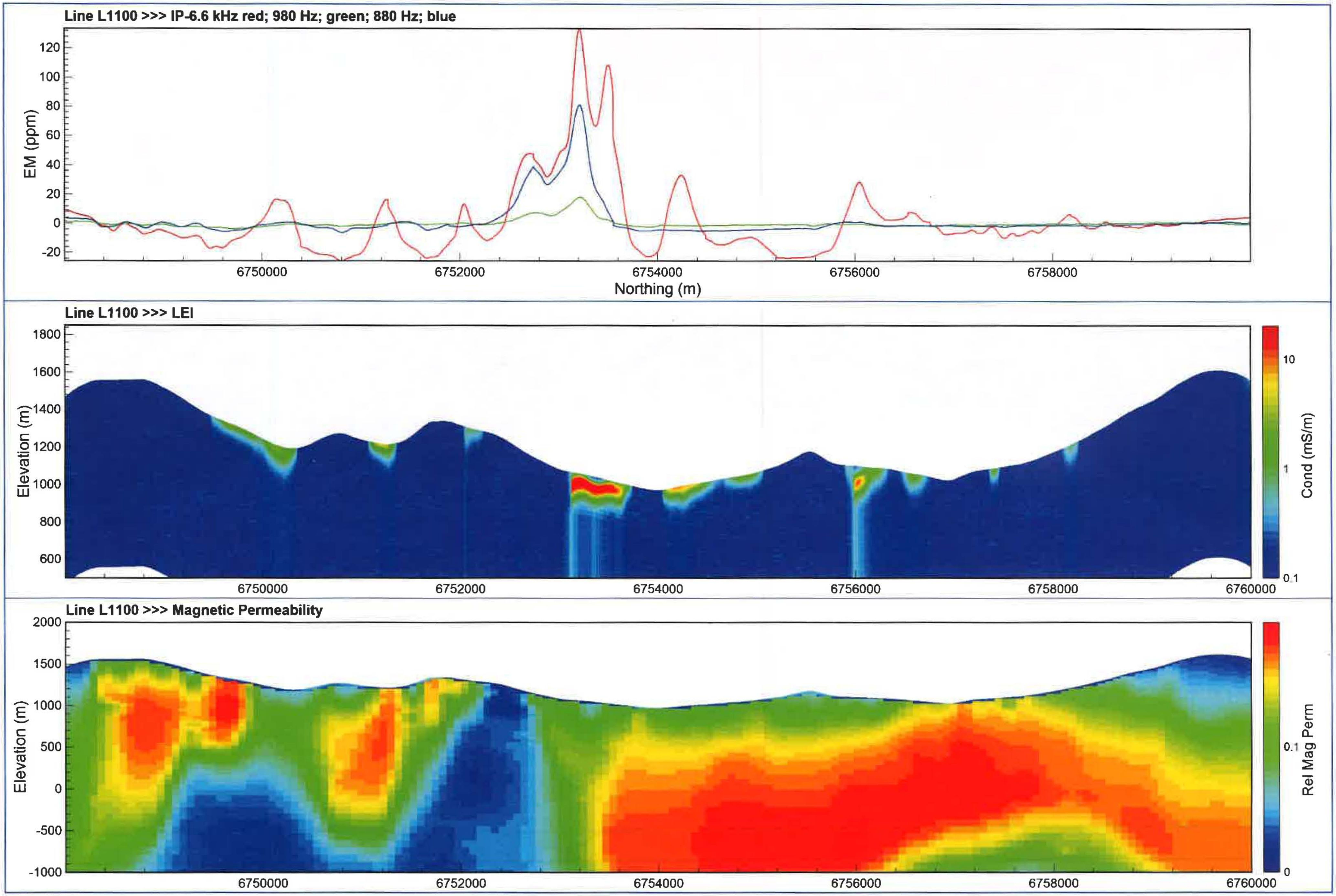
Line L1100 >>> IP-6.6 kHz red; 980 Hz; green; 880 Hz; blue
EM (ppm)
120
100
80
60
40
20
0
-20
6750000
6752000
6754000
6756000
6758000
Northing (m)
Line L1100 >>> LEI
Elevation (m)
1800
1600
1400
1200
1000
800
600
6750000
6752000
6754000
6756000
6758000
6760000
Cond (mS/m)
10
1
0.1
Line L1100 >>> Magnetic Permeability
Elevation (m)
2000
1500
1000
500
0
-500
-1000
6750000
6752000
6754000
6756000
6758000
6760000
Rel Mag Perm
0.1
0

Line L1110 <<< IP-6.6 kHz red; 980 Hz; green; 880 Hz; blue

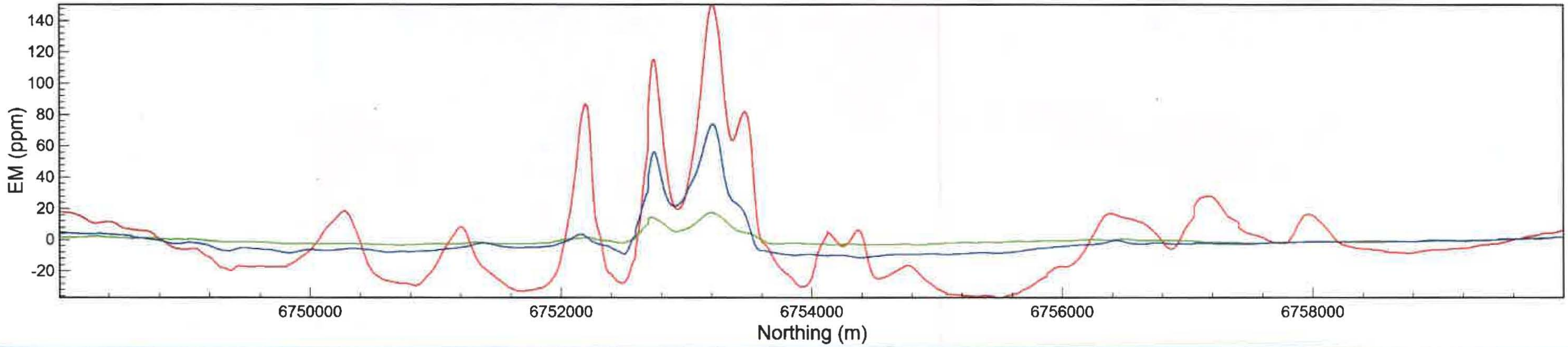

Line L1110 <<< LEI

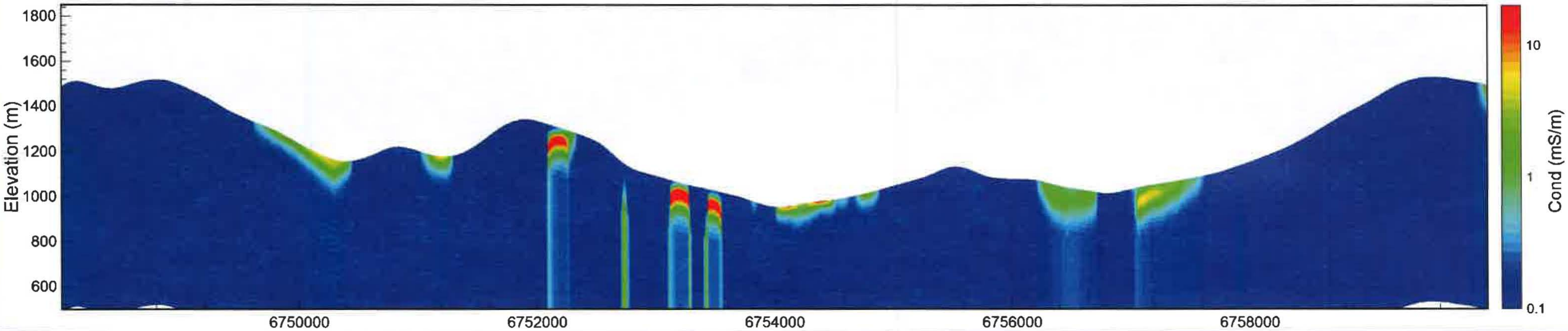

Line L1110 <<< Magnetic Permeability

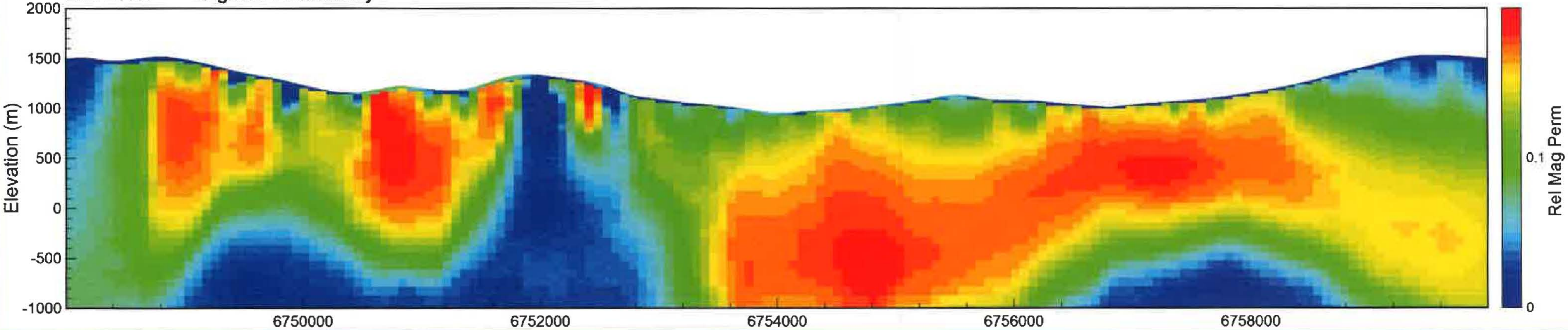

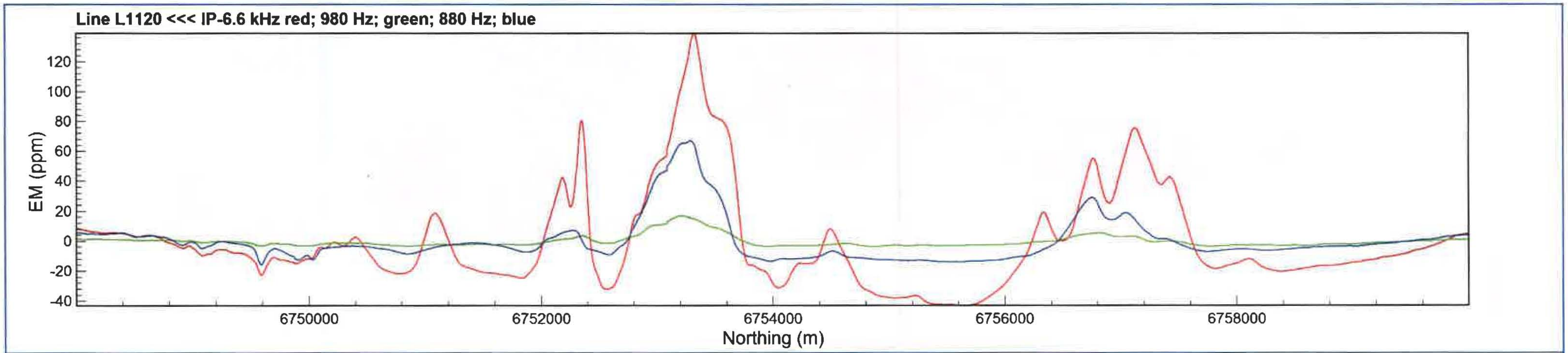
Line L1120 <<< IP-6.6 kHz red; 980 Hz; green; 880 Hz; blue
EM (ppm)
120
100
80
60
40
20
0
-20
-40
6750000
6752000
6754000
6756000
6758000
Northing (m)

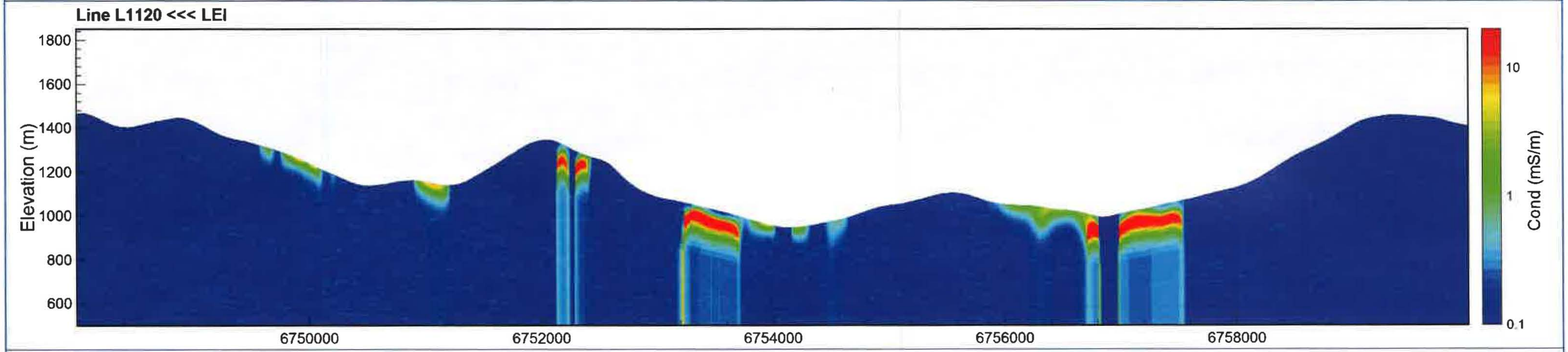
Line L1120 <<< LEI
Elevation (m)
1800
1600
1400
1200
1000
800
600
6750000
6752000
6754000
6756000
6758000
Cond (mS/m)
10
1
0.1

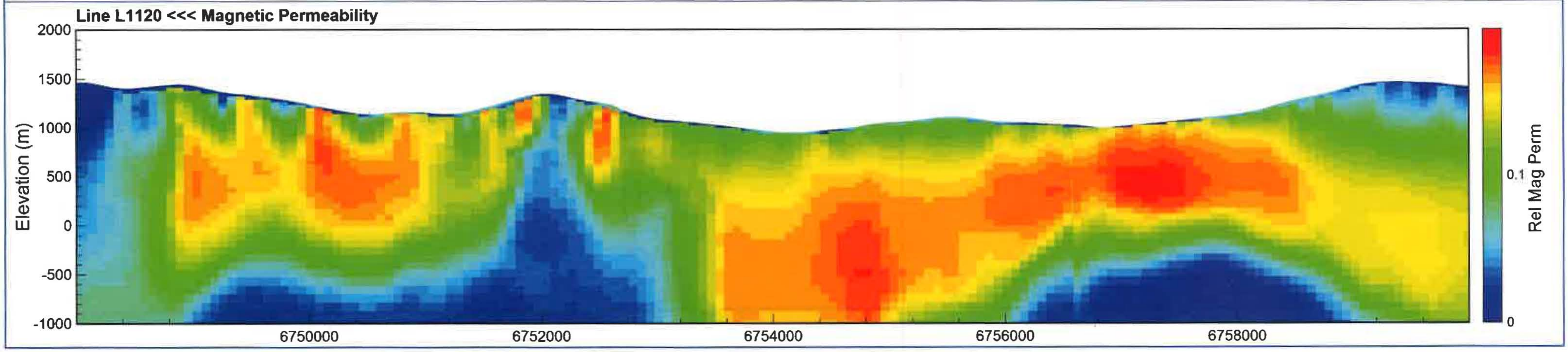
Line L1120 <<< Magnetic Permeability
Elevation (m)
2000
1500
1000
500
0
-500
-1000
6750000
6752000
6754000
6756000
6758000
Rel Mag Perm
0.1
0

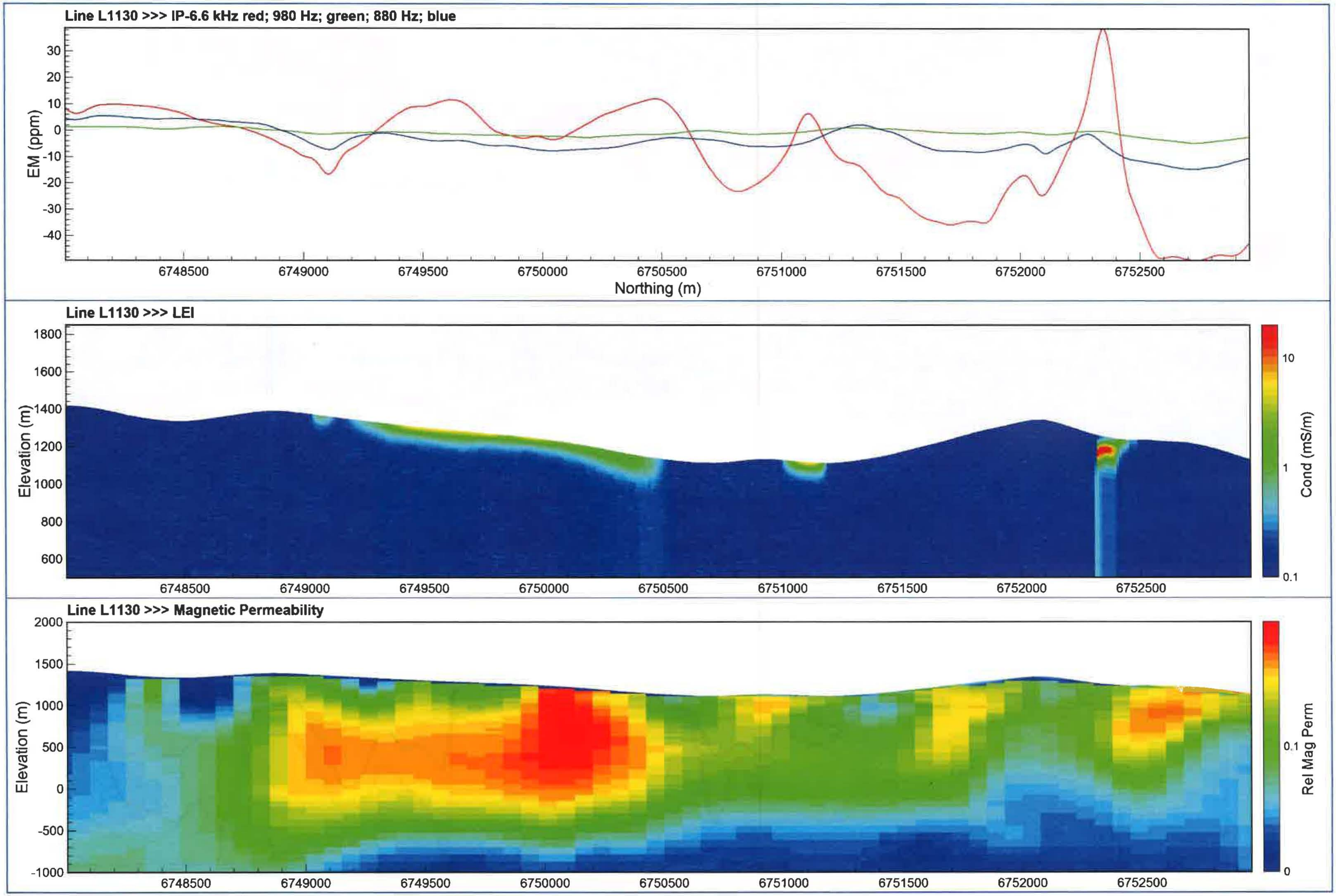

Line L1130 >>> IP-6.6 kHz red; 980 Hz; green; 880 Hz; blue
EM (ppm)
30
20
10
0
-10
-20
-30
-40
6748500
6749000
6749500
6750000
6750500
6751000
6751500
6752000
6752500
Northing (m)
Line L1130 >>> LEI
Elevation (m)
1800
1600
1400
1200
1000
800
600
6748500
6749000
6749500
6750000
6750500
6751000
6751500
6752000
6752500
10
1
0.1
Cond (mS/m)
Line L1130 >>> Magnetic Permeability
Elevation (m)
2000
1500
1000
500
0
-500
-1000
6748500
6749000
6749500
6750000
6750500
6751000
6751500
6752000
6752500
0.1
0
Rel Mag Perm

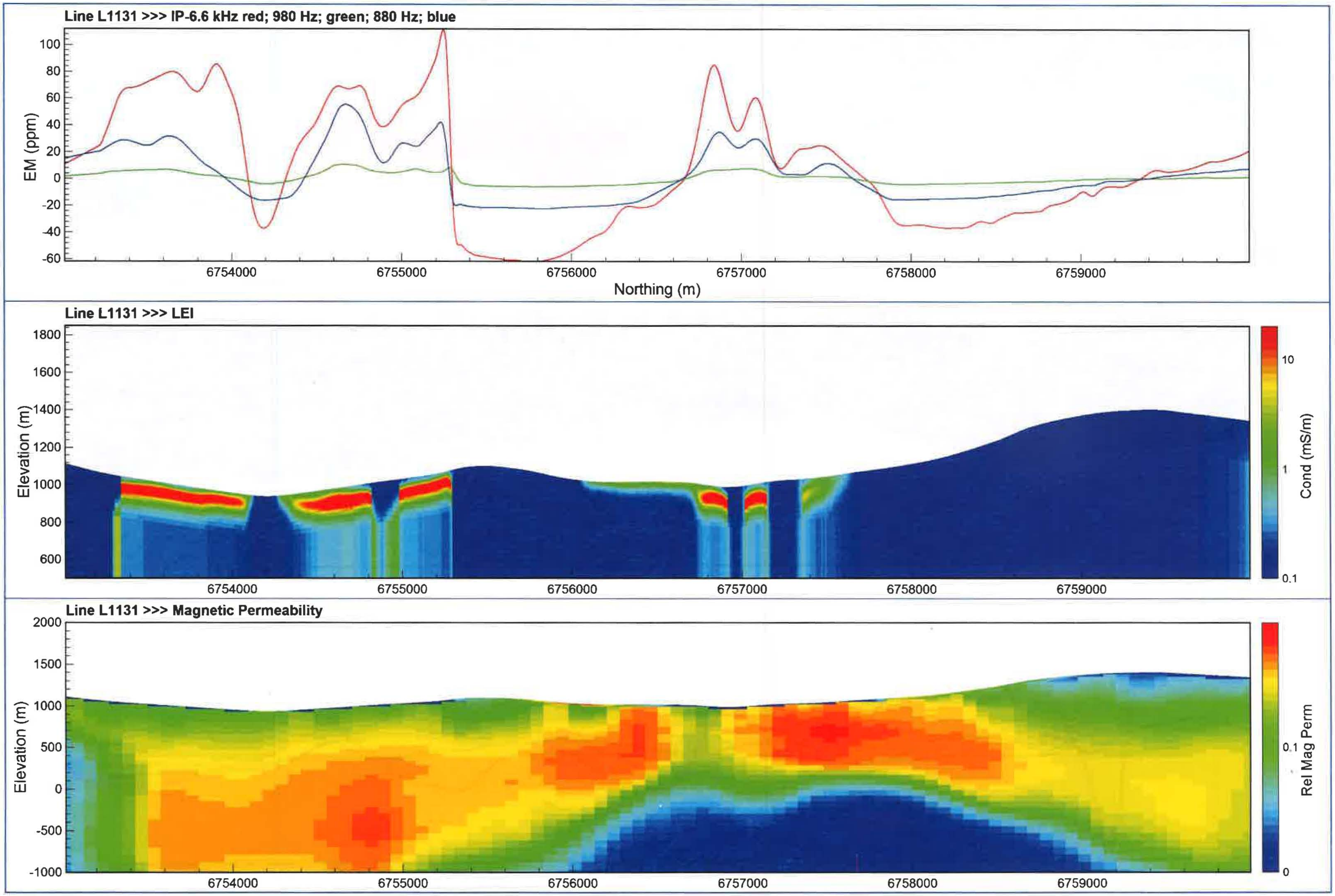

Line L1131 >>> IP-6.6 kHz red; 980 Hz; green; 880 Hz; blue

Line L1131 >>> LEI

Line L1131 >>> Magnetic Permeability

Line L1140 >>> IP-6.6 kHz red; 980 Hz; green; 880 Hz; blue

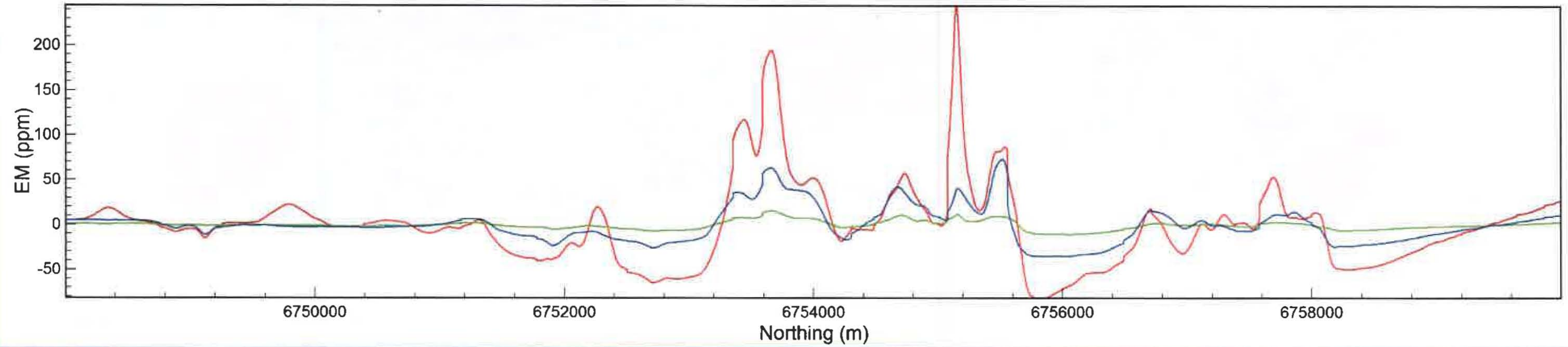

Line L1140 >>> LEI

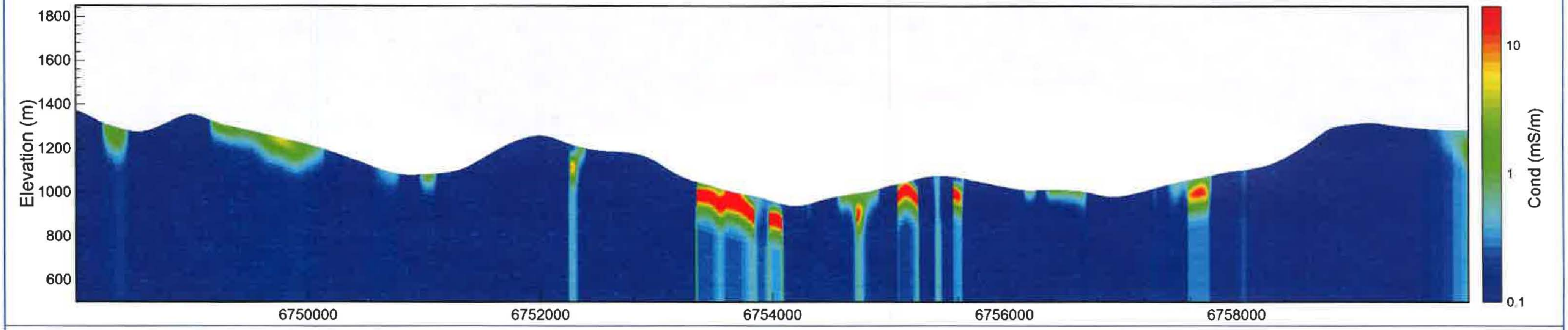

Line L1140 >>> Magnetic Permeability

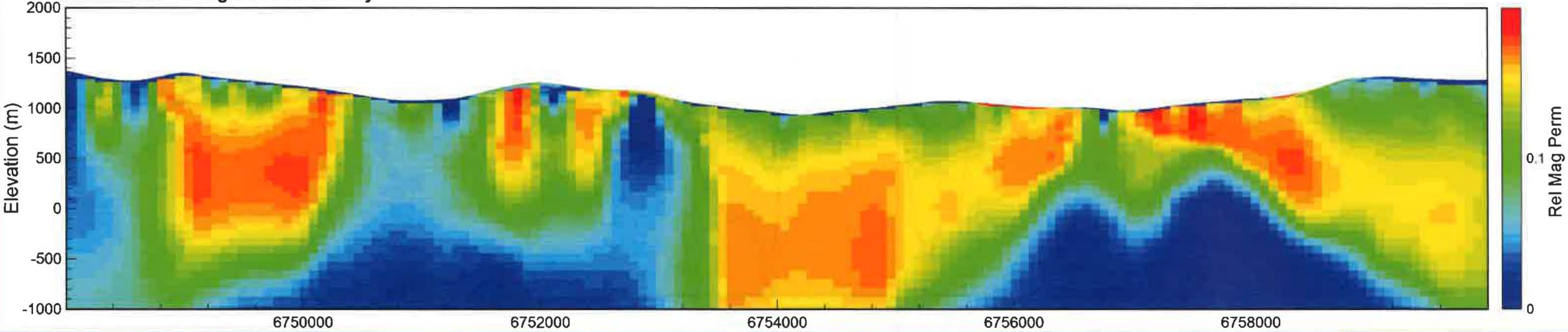

Line L1150 <<< IP-6.6 kHz red; 980 Hz; green; 880 Hz; blue

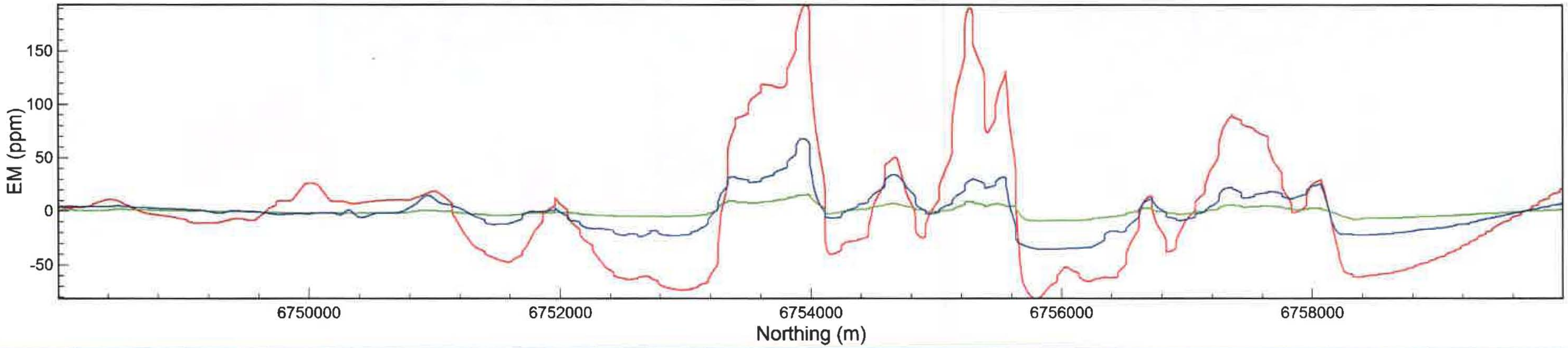

Line L1150 <<< LEI

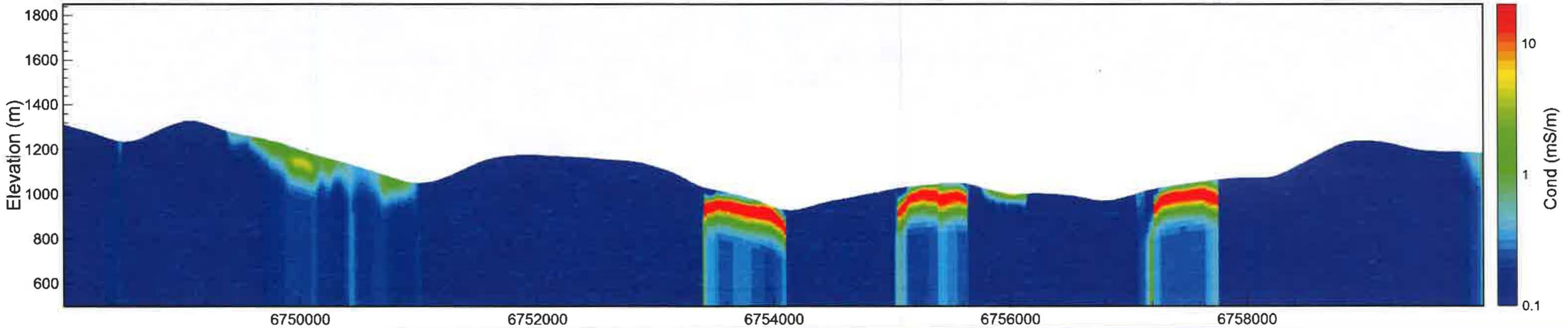

Line L1150 <<< Magnetic Permeability

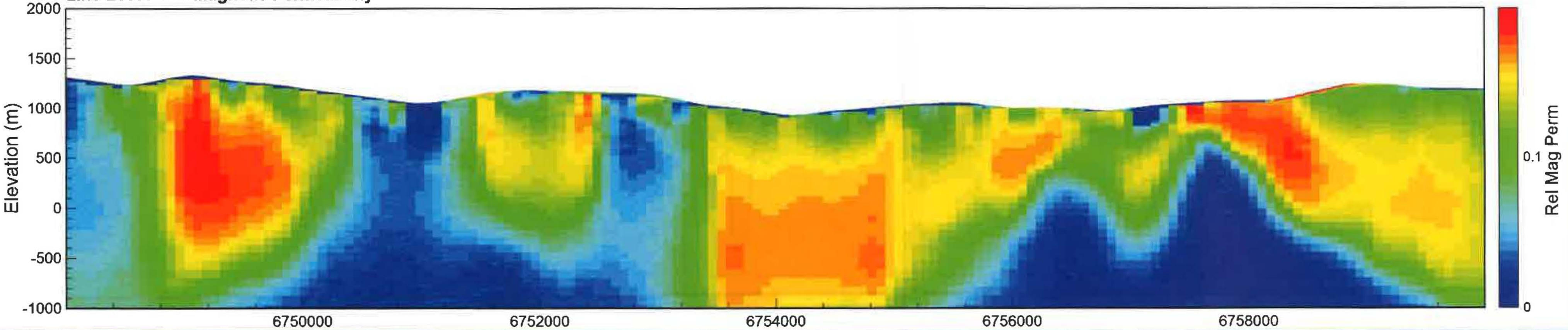

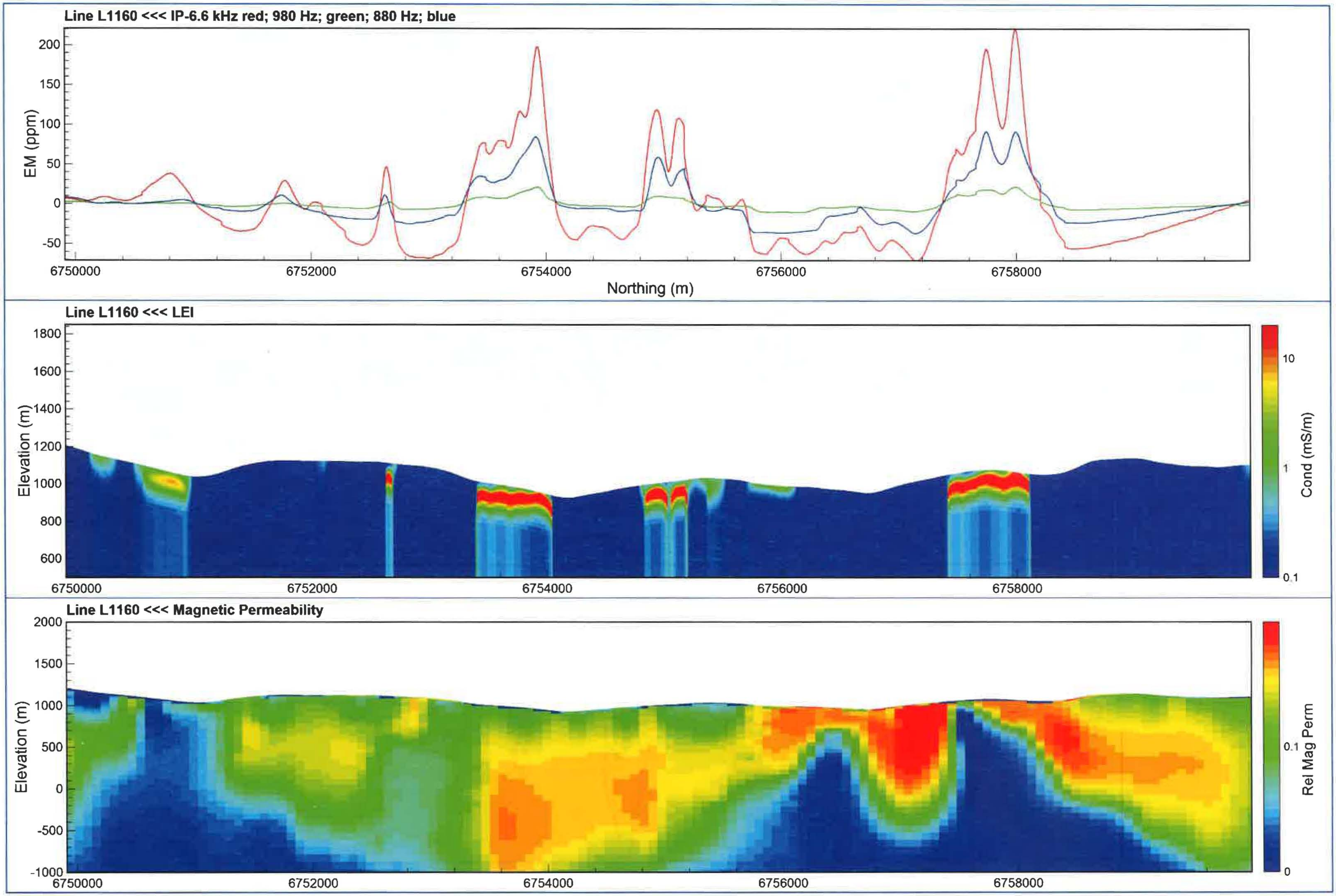
Line L1160 <<< IP-6.6 kHz red; 980 Hz; green; 880 Hz; blue
EM (ppm)
200
150
100
50
0
-50
6750000
6752000
6754000
6756000
6758000
Northing (m)
Line L1160 <<< LEI
Elevation (m)
1800
1600
1400
1200
1000
800
600
6750000
6752000
6754000
6756000
6758000
Cond (mS/m)
10
1
0.1
Line L1160 <<< Magnetic Permeability
Elevation (m)
2000
1500
1000
500
0
-500
-1000
6750000
6752000
6754000
6756000
6758000
Rel Mag Perm
0.1
0

Line L1170 >>> IP-6.6 kHz red; 980 Hz; green; 880 Hz; blue

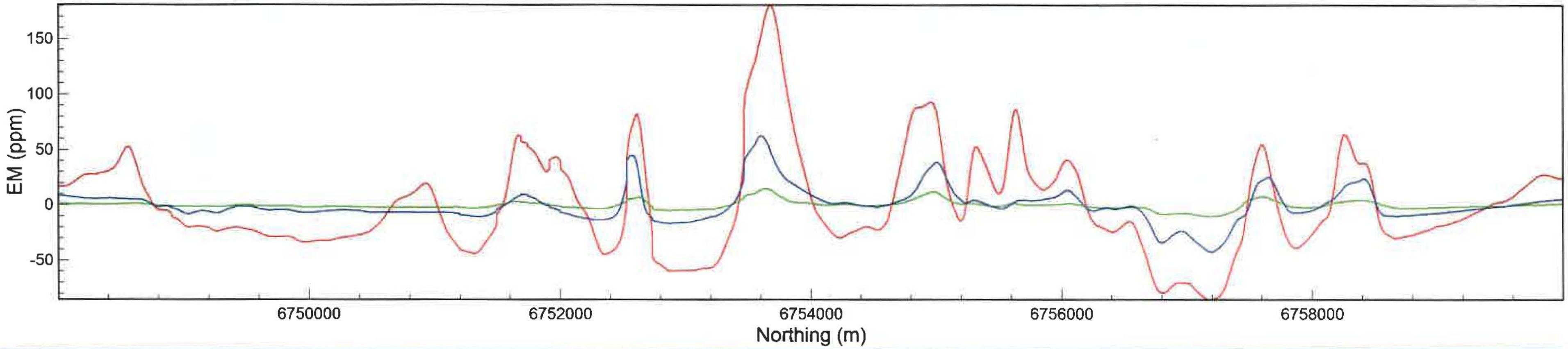

Line L1170 >>> LEI

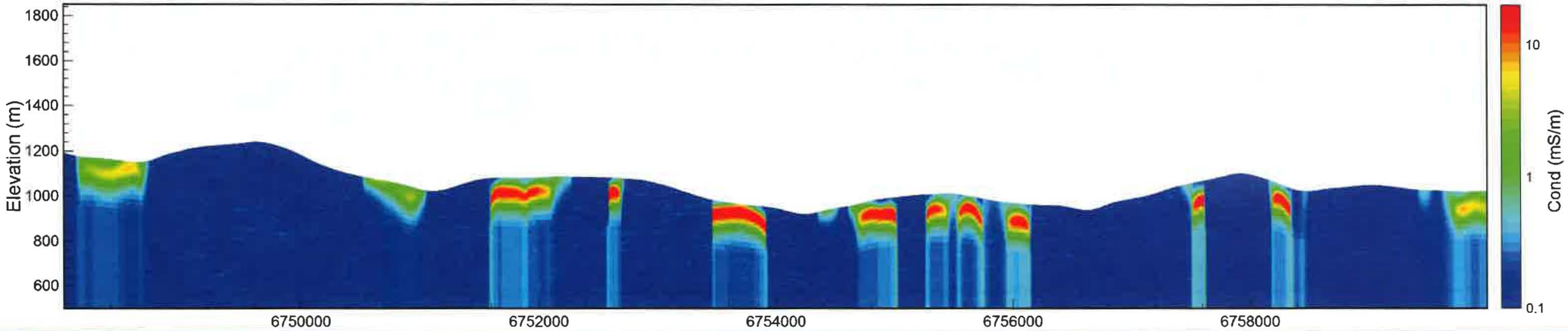

Line L1170 >>> Magnetic Permeability

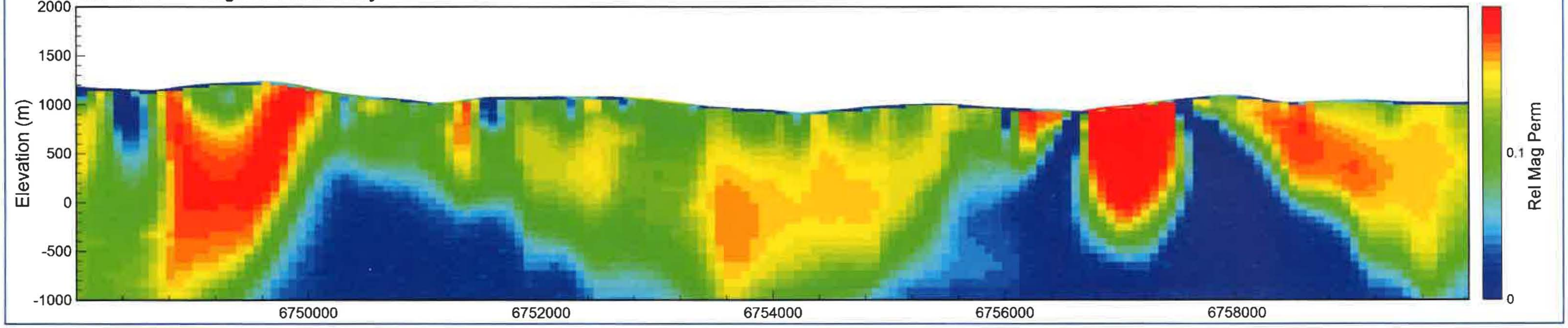

Line L1180 >>> IP-6.6 kHz red; 980 Hz; green; 880 Hz; blue

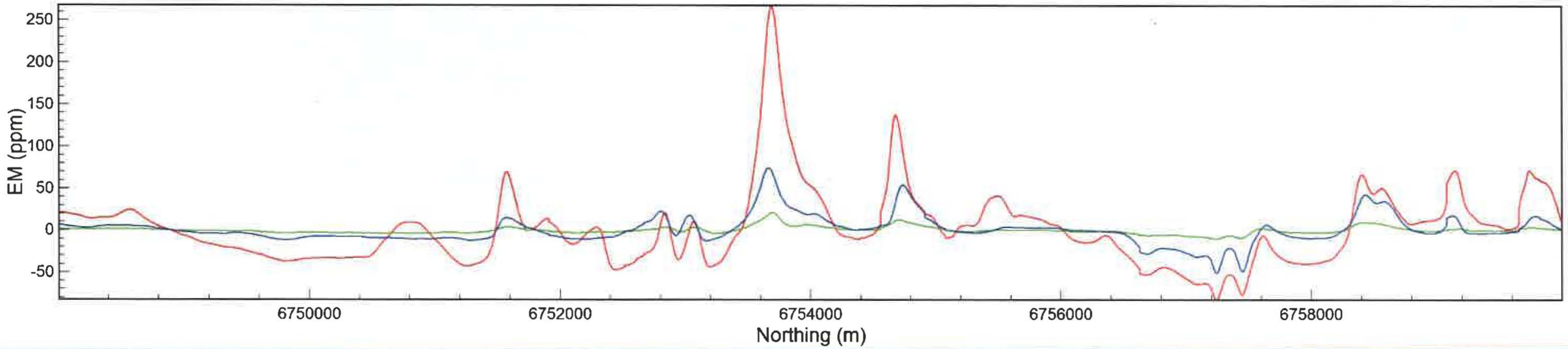

Line L1180 >>> LEI

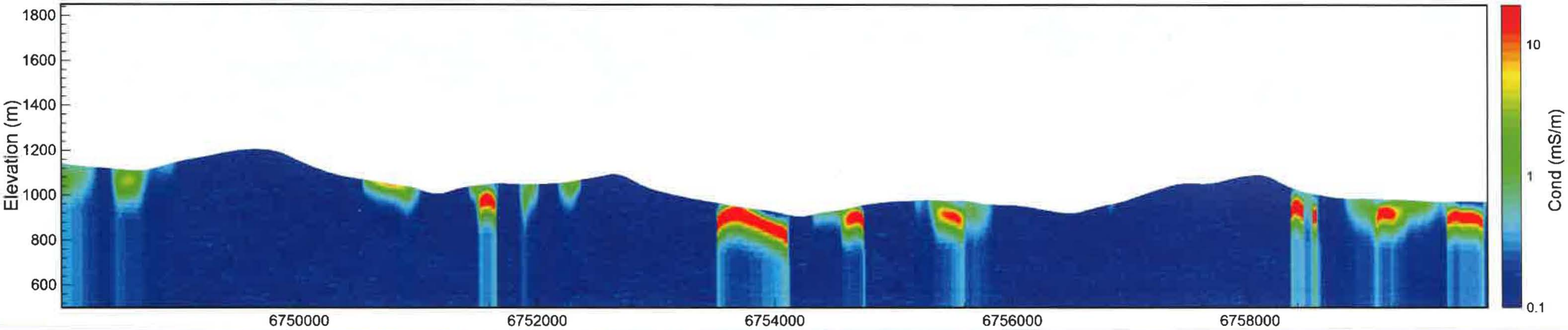

Line L1180 >>> Magnetic Permeability

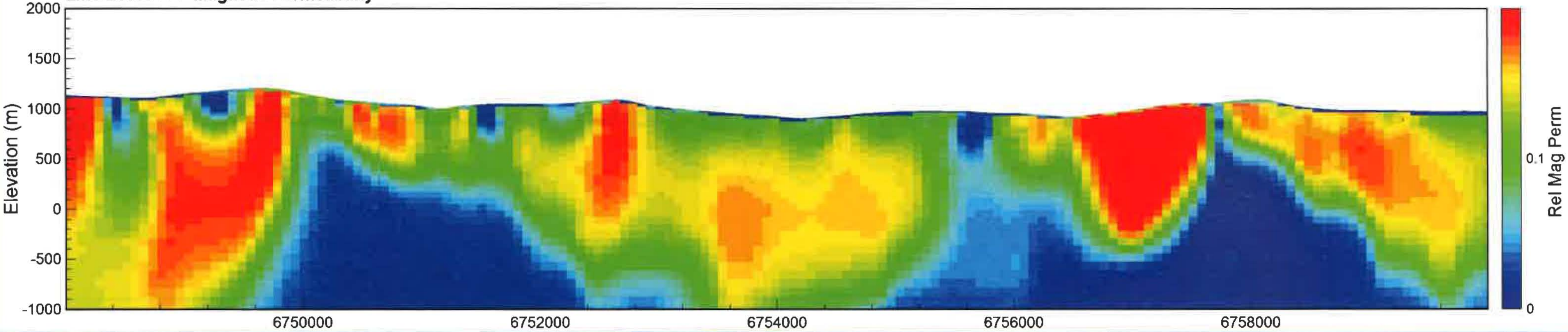

Line L1190 <<< IP-6.6 kHz red; 980 Hz; green; 880 Hz; blue

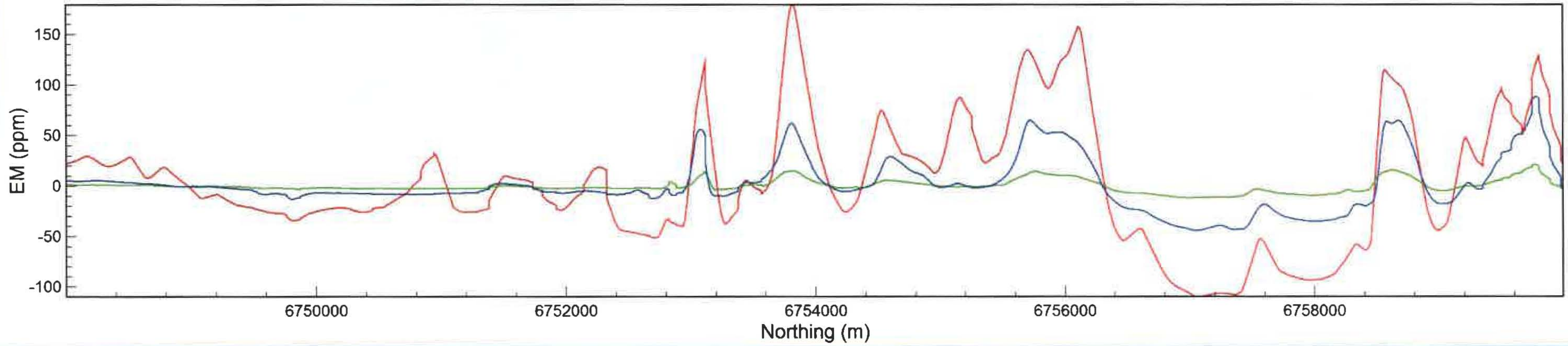

Line L1190 <<< LEI

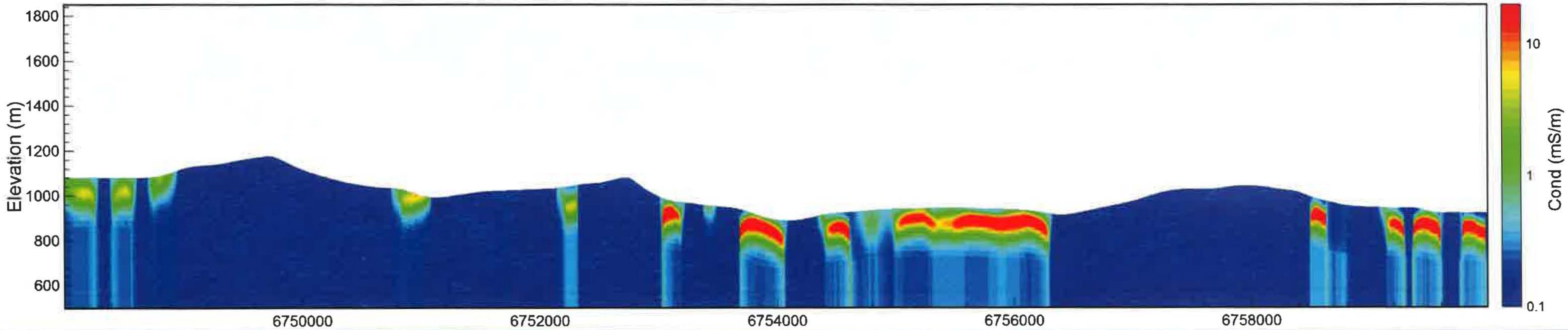

Line L1190 <<< Magnetic Permeability

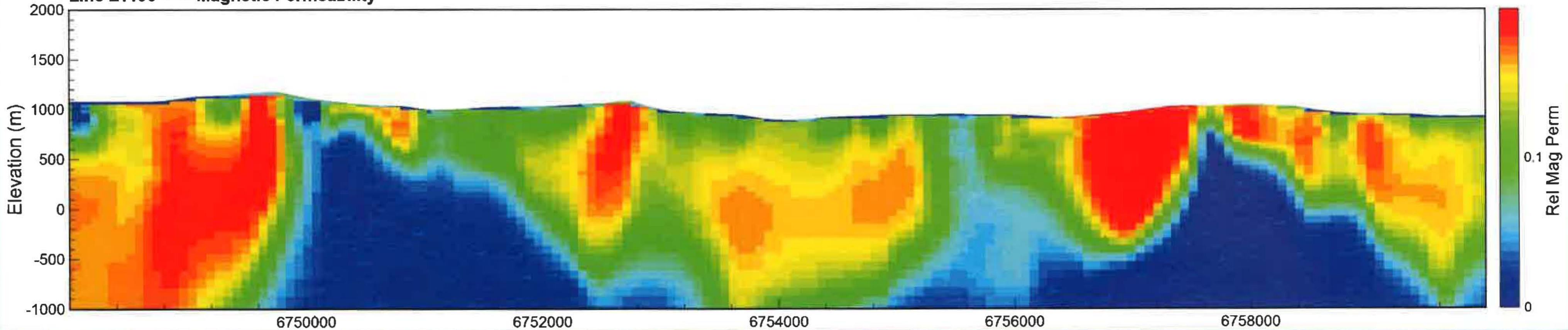

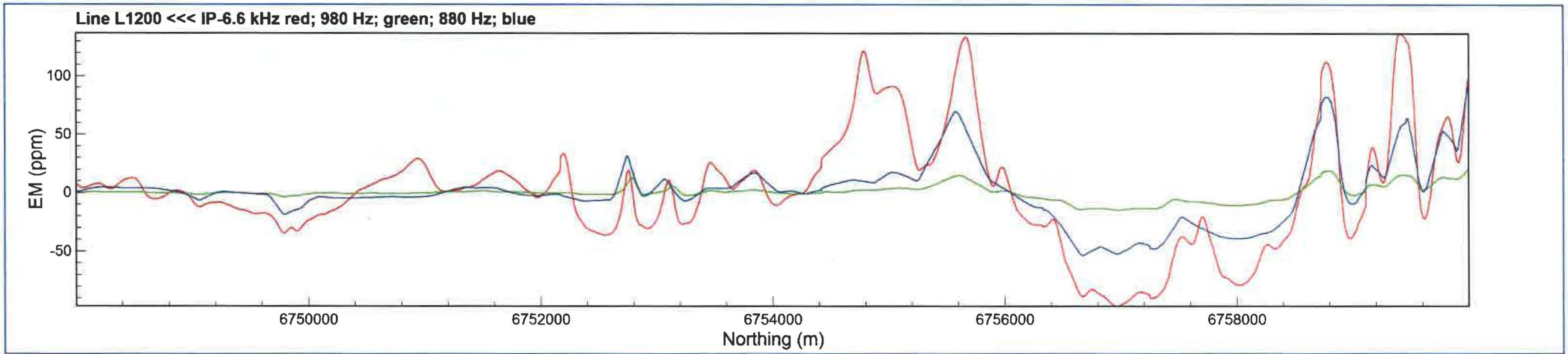
Line L1200 <<< IP-6.6 kHz red; 980 Hz; green; 880 Hz; blue
EM (ppm)
100
50
0
-50
6750000
6752000
6754000
6756000
6758000
Northing (m)

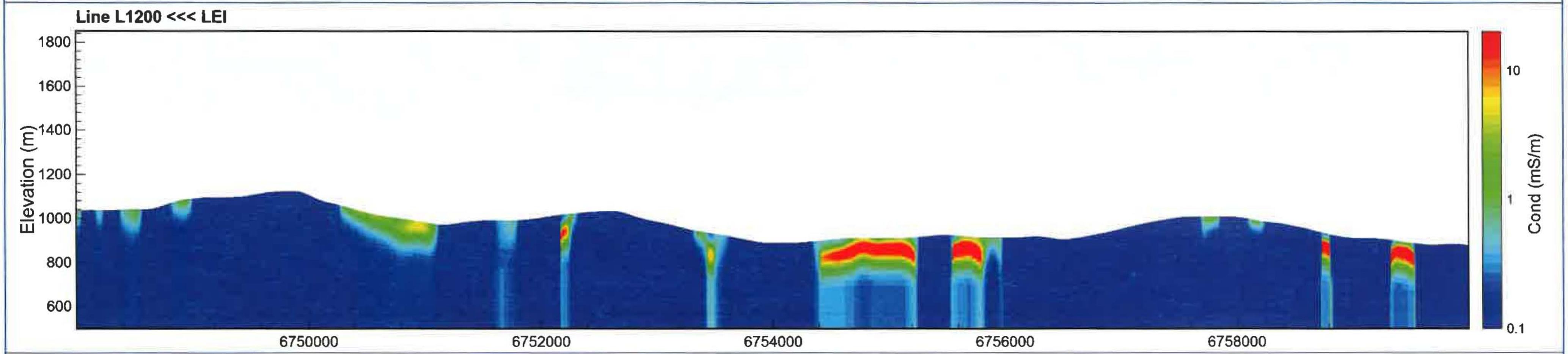
Line L1200 <<< LEI
Elevation (m)
1800
1600
1400
1200
1000
800
600
6750000
6752000
6754000
6756000
6758000
Cond (mS/m)
10
1
0.1

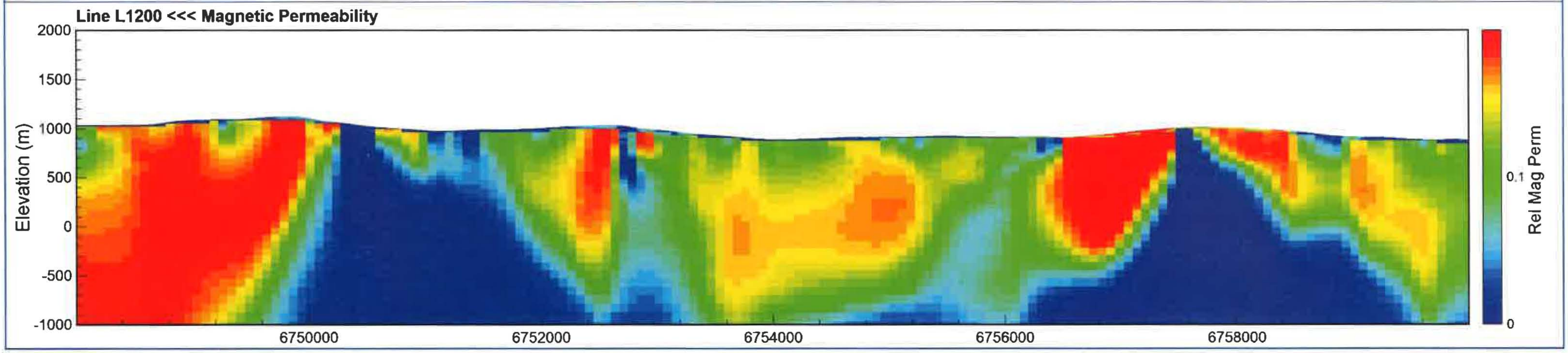
Line L1200 <<< Magnetic Permeability
Elevation (m)
2000
1500
1000
500
0
-500
-1000
6750000
6752000
6754000
6756000
6758000
Rel Mag Perm
0.1
0

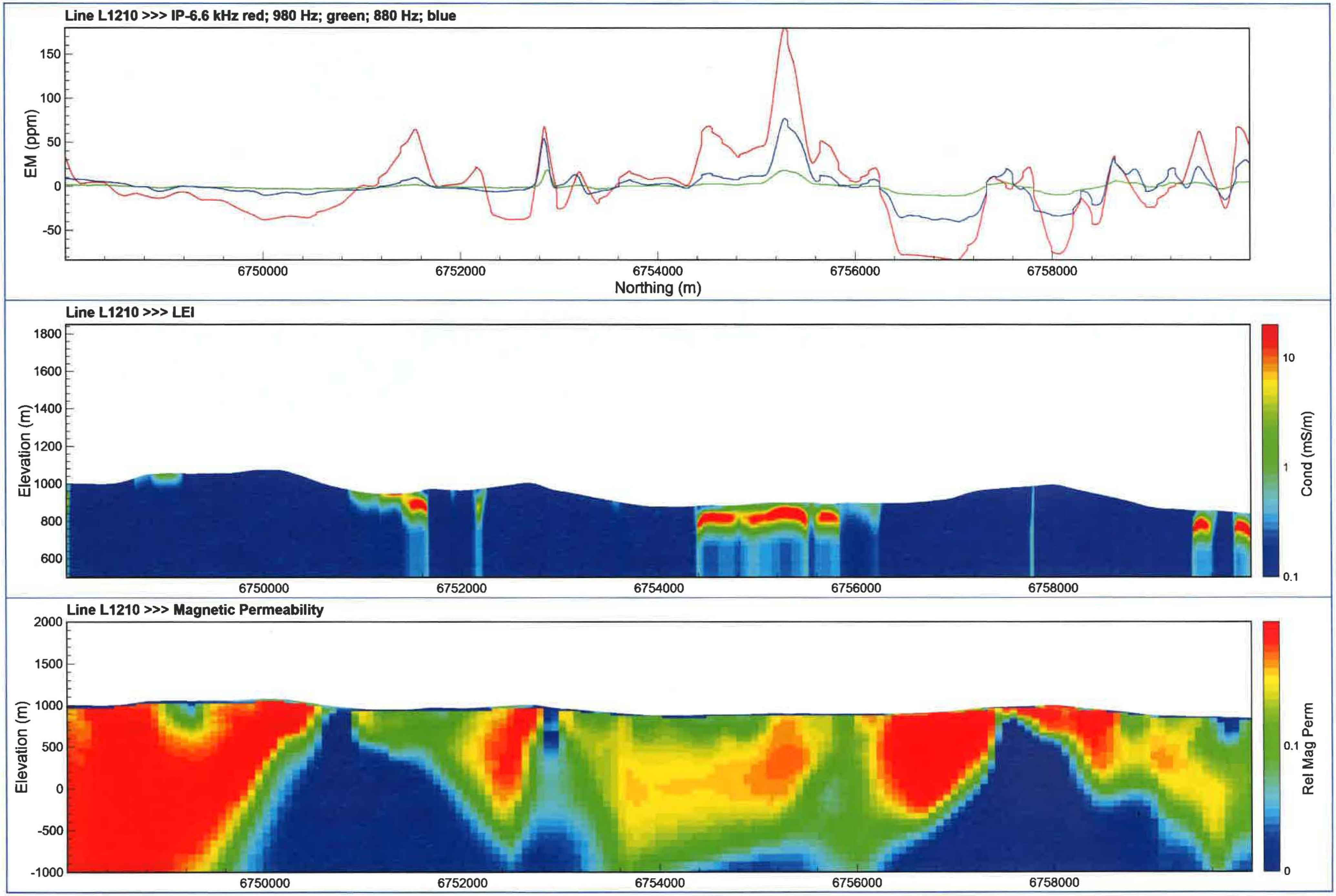
Line L1210 >>> IP-6.6 kHz red; 980 Hz; green; 880 Hz; blue

Line L1210 >>> LEI

Line L1210 >>> Magnetic Permeability

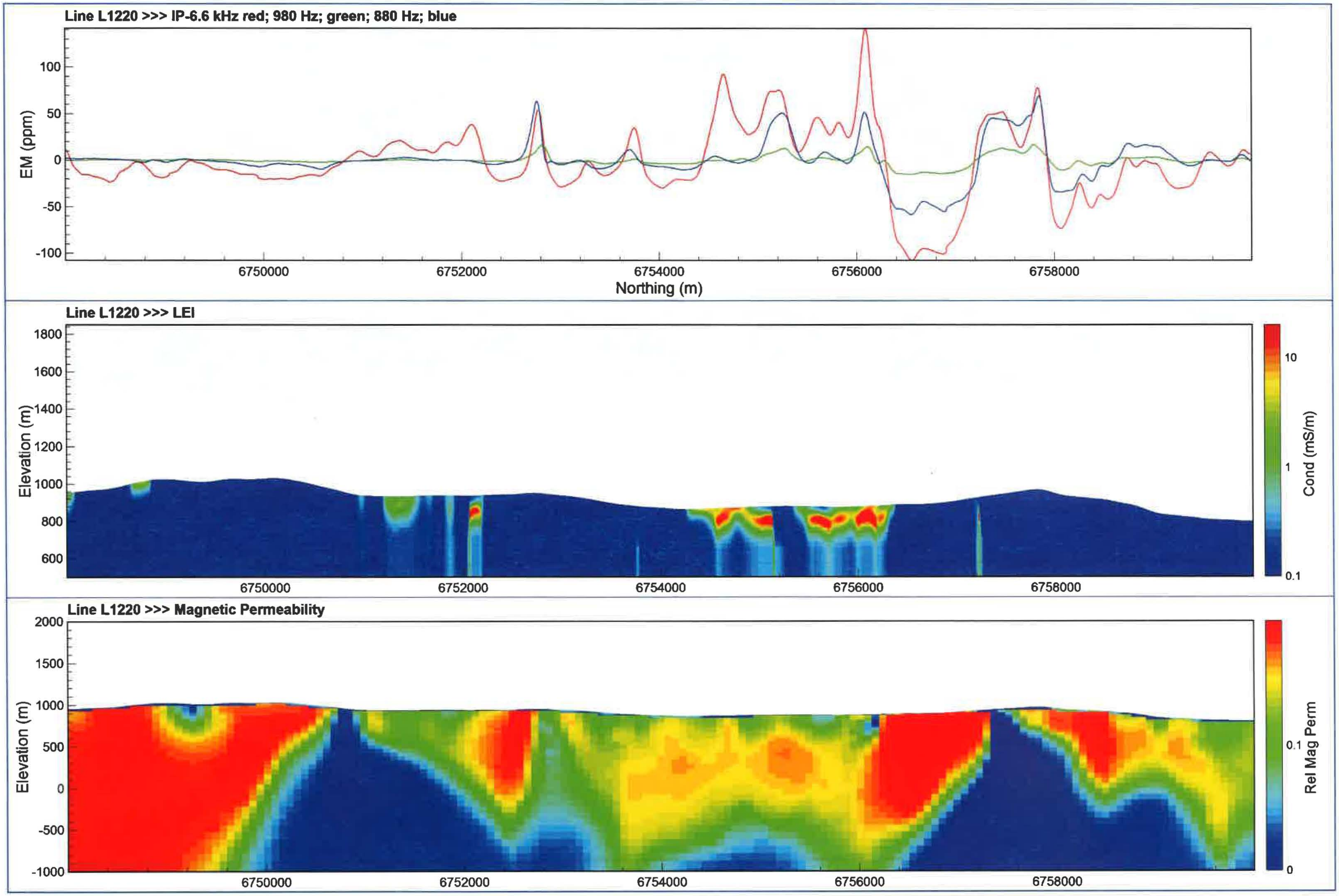
Line L1220 >>> IP-6.6 kHz red; 980 Hz; green; 880 Hz; blue
EM (ppm)
100
50
0
-50
-100
6750000
6752000
6754000
6756000
6758000
Northing (m)
Line L1220 >>> LEI
Elevation (m)
1800
1600
1400
1200
1000
800
600
6750000
6752000
6754000
6756000
6758000
10
1
0.1
Cond (mS/m)
Line L1220 >>> Magnetic Permeability
Elevation (m)
2000
1500
1000
500
0
-500
-1000
6750000
6752000
6754000
6756000
6758000
0.1
0
Rel Mag Perm

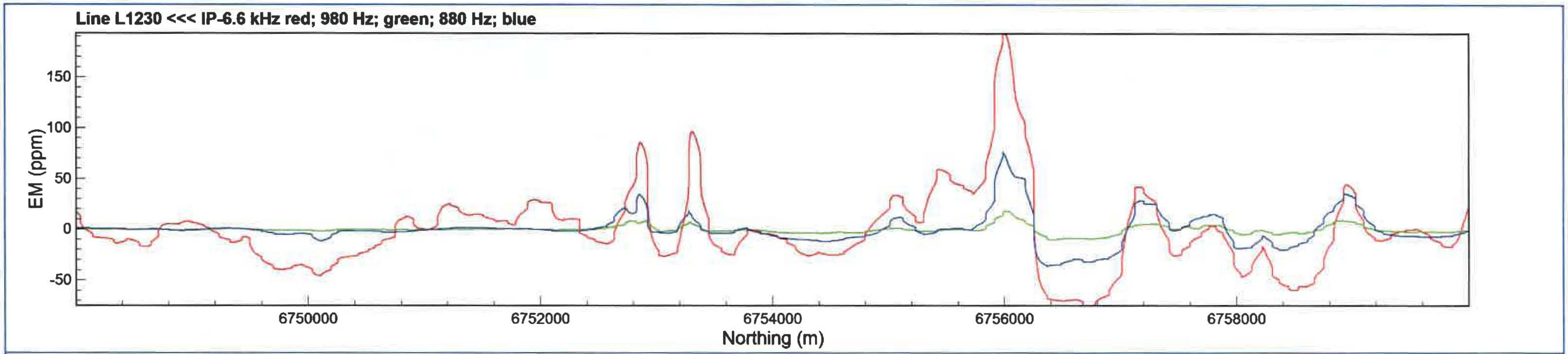

Line L1230 <<< IP-6.6 kHz red; 980 Hz; green; 880 Hz; blue

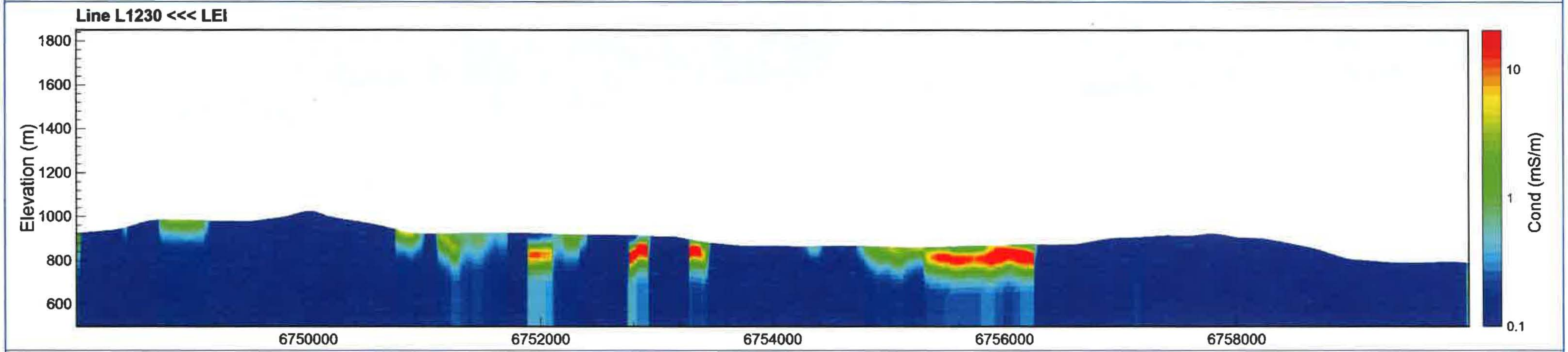

Line L1230 <<< LEI

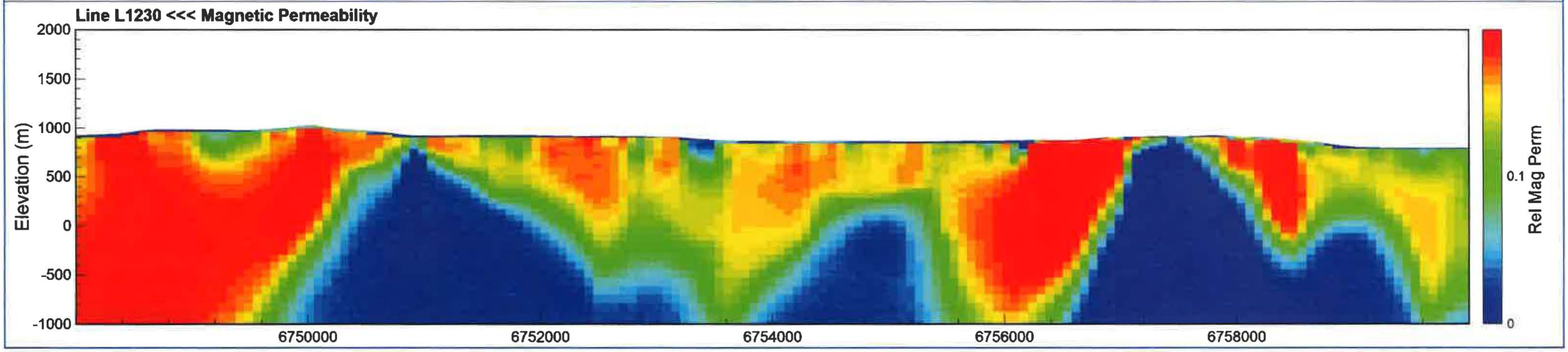

Line L1230 <<< Magnetic Permeability

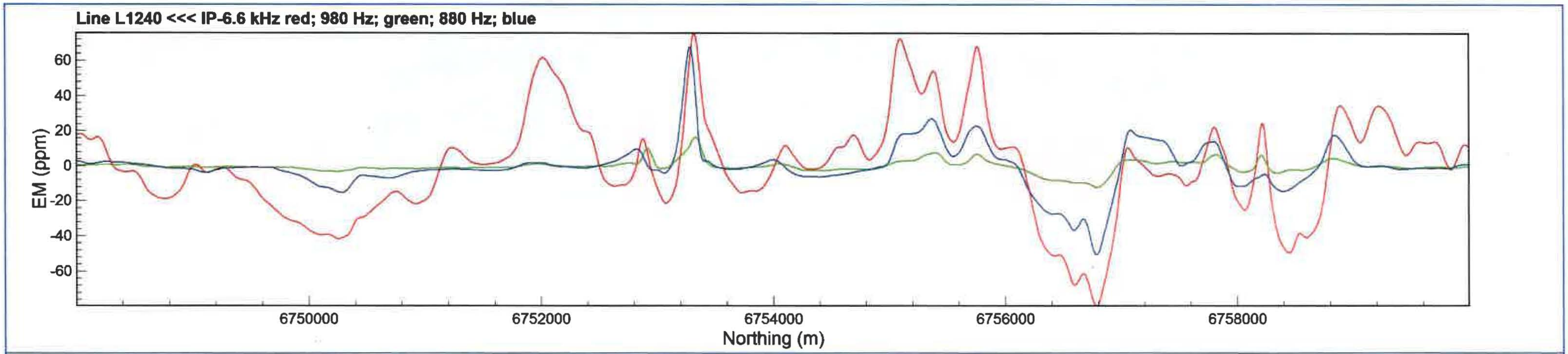
Line L1240 <<< IP-6.6 kHz red; 980 Hz; green; 880 Hz; blue

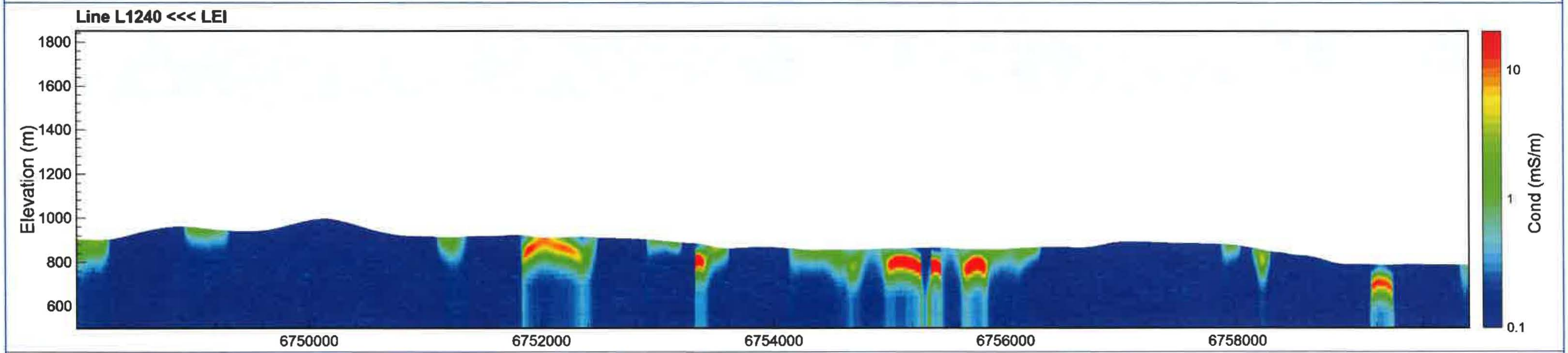
Line L1240 <<< LEI

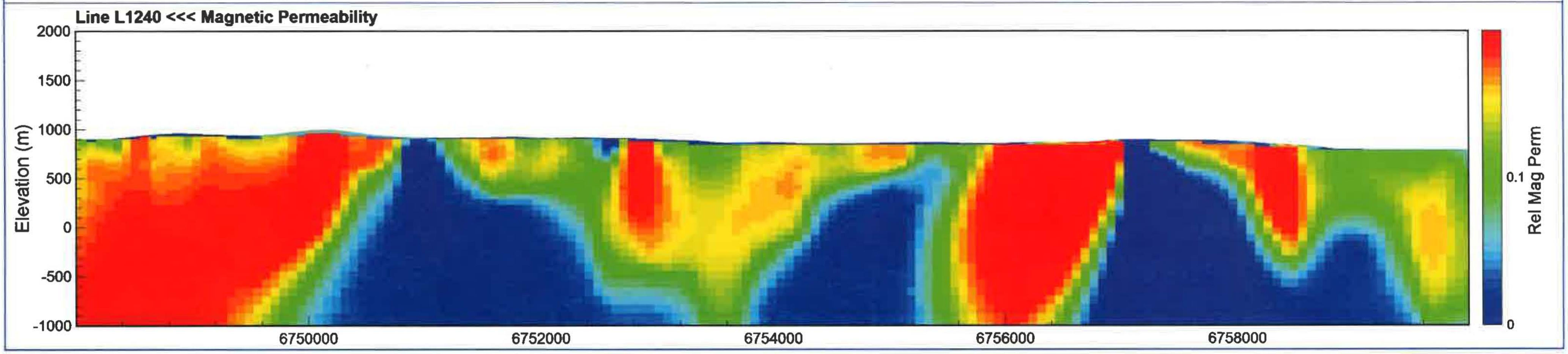
Line L1240 <<< Magnetic Permeability

Line L1250 >>> IP-6.6 kHz red; 980 Hz; green; 880 Hz; blue

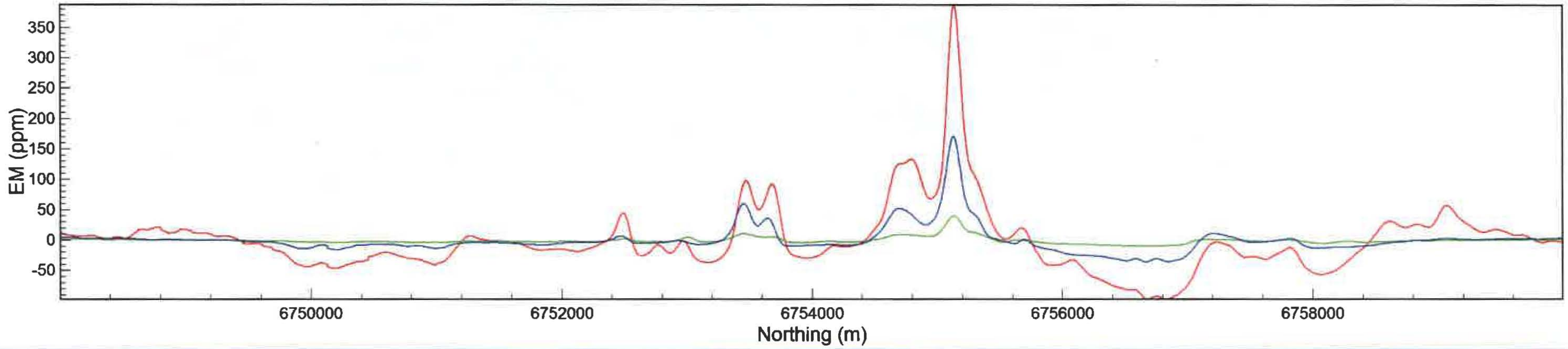

Line L1250 >>> LEI

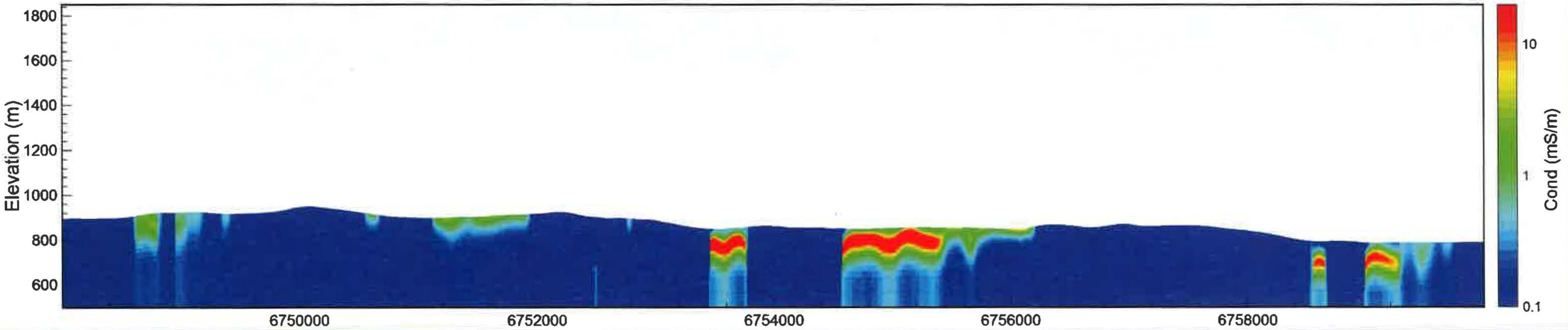

Line L1250 >>> Magnetic Permeability

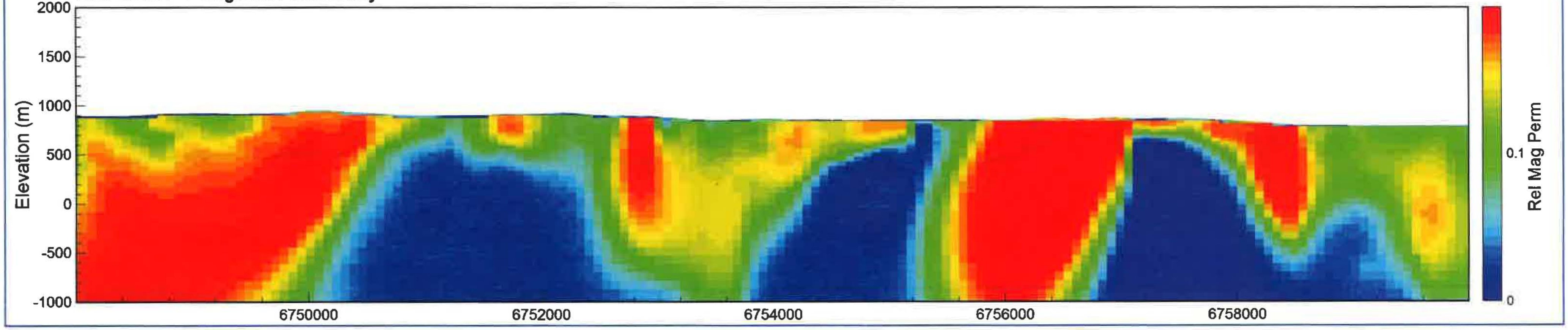

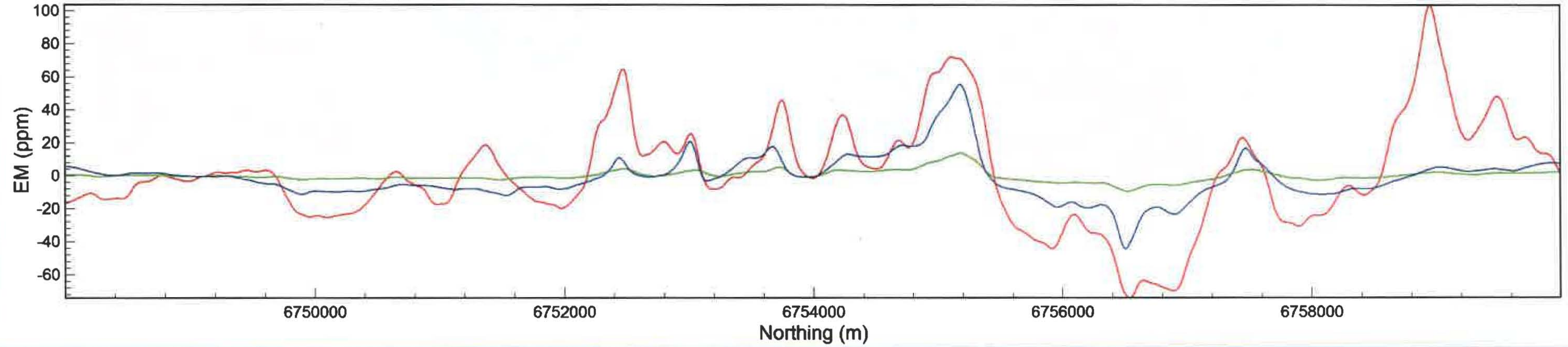
Line L1260 >>> IP-6.6 kHz red; 980 Hz; green; 880 Hz; blue

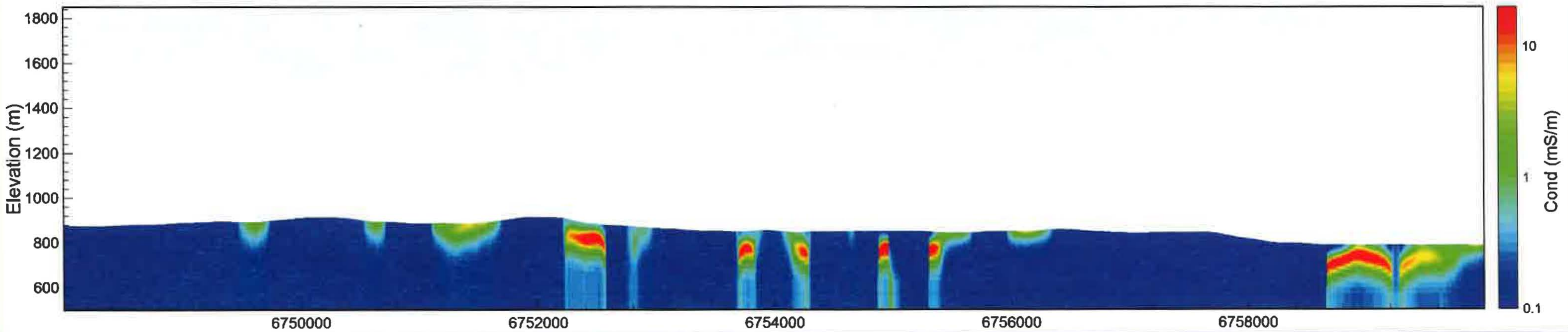
Line L1260 >>> LEI

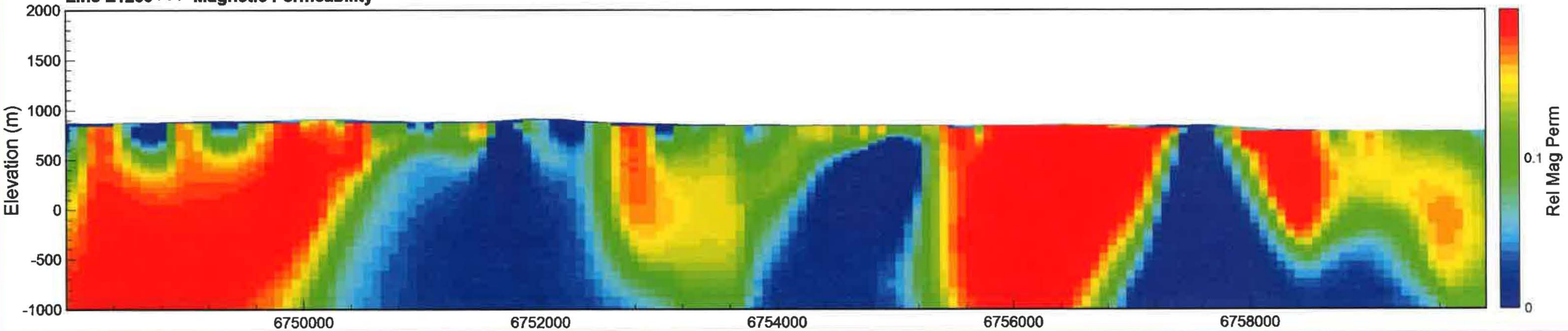
Line L1260 >>> Magnetic Permeability

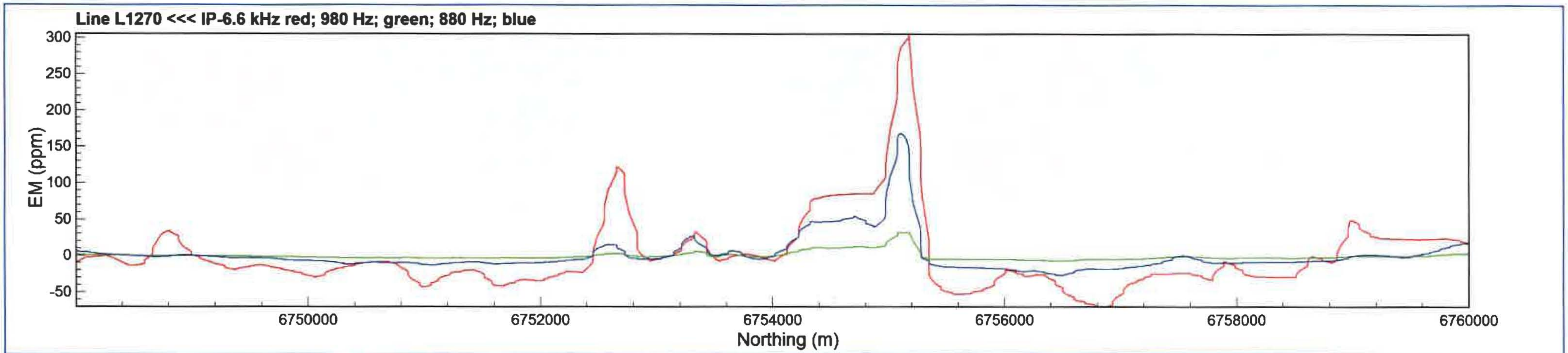
Line L1270 <<< IP-6.6 kHz red; 980 Hz; green; 880 Hz; blue

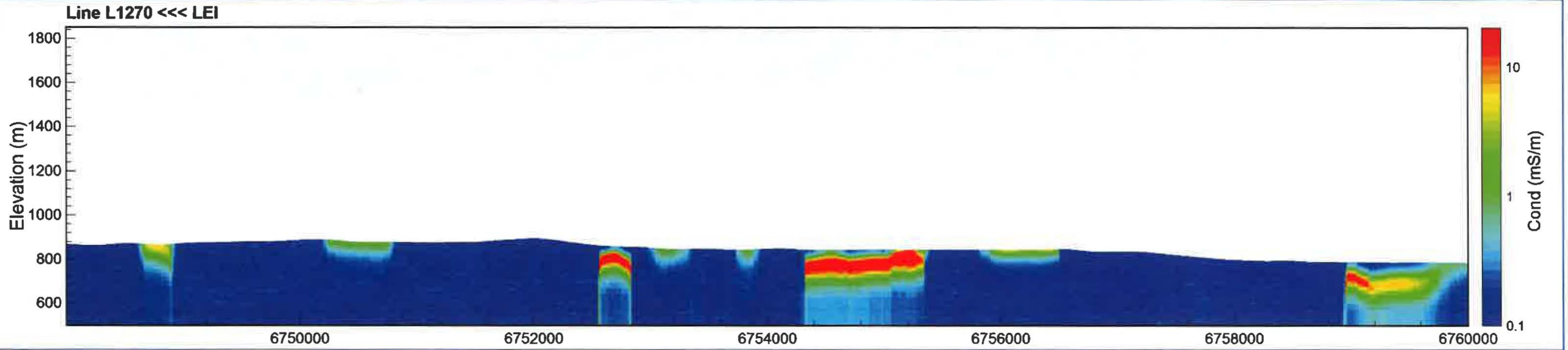
Line L1270 <<< LEI

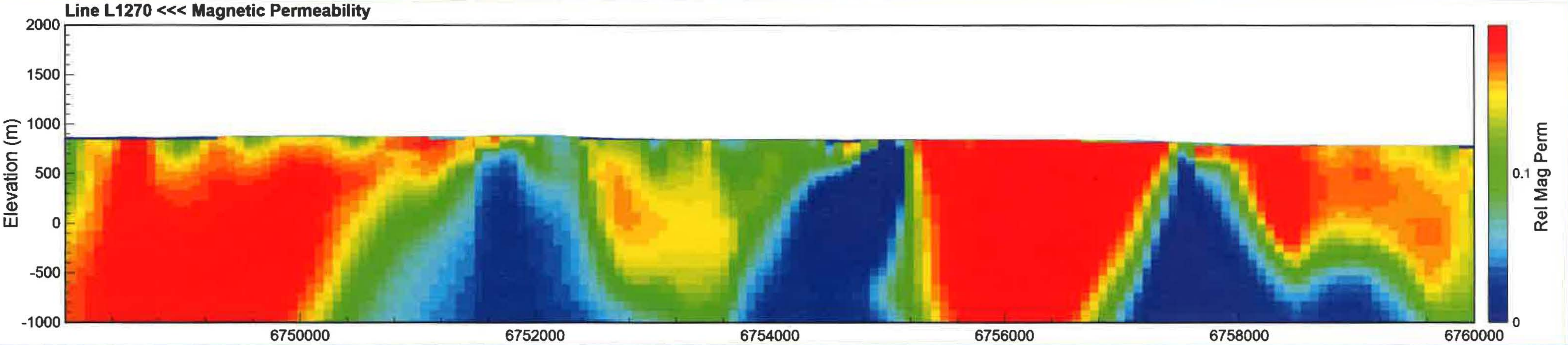
Line L1270 <<< Magnetic Permeability

Line L1280 <<< IP-6.6 kHz red; 980 Hz; green; 880 Hz; blue

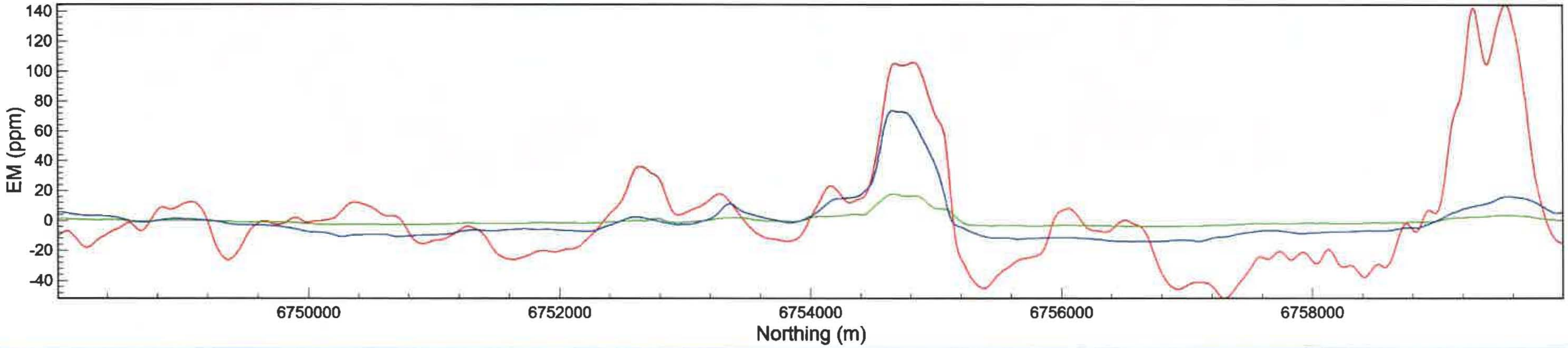

Line L1280 <<< LEI

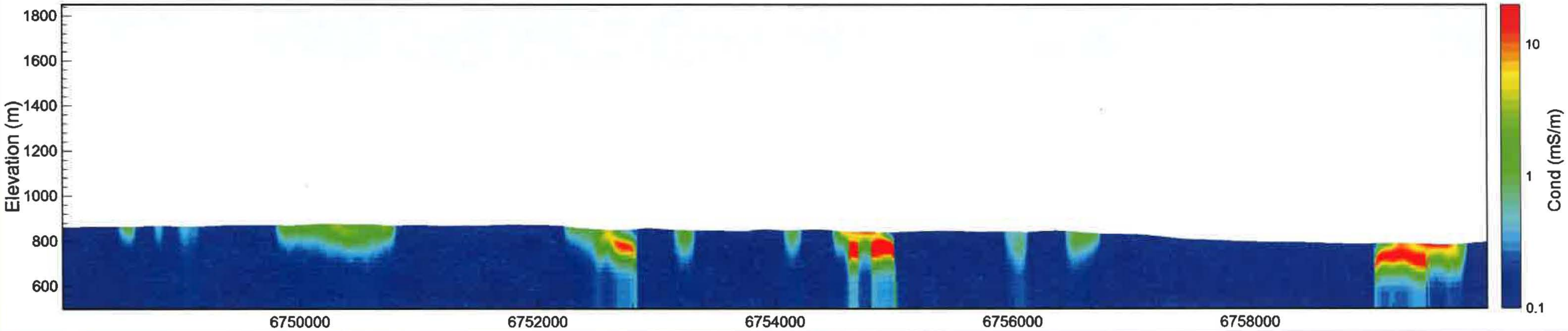

Line L1280 <<< Magnetic Permeability

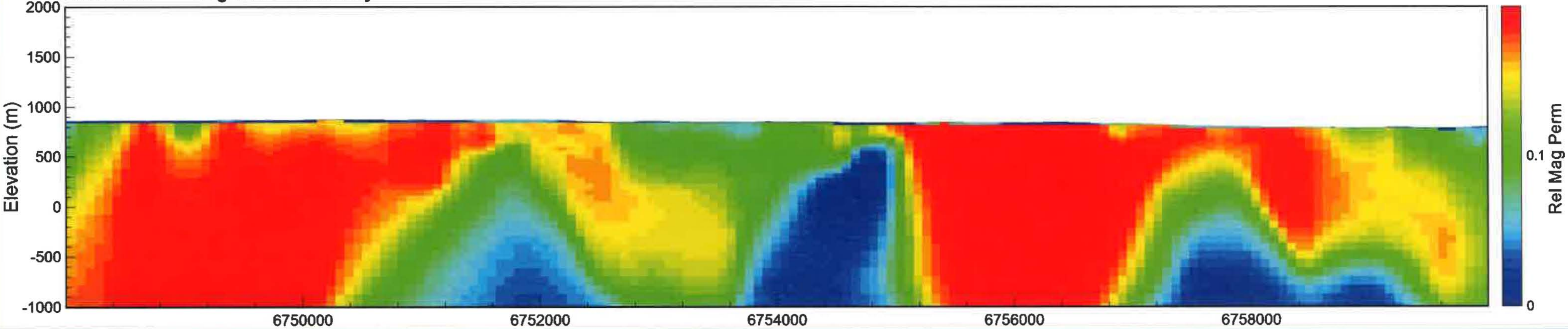

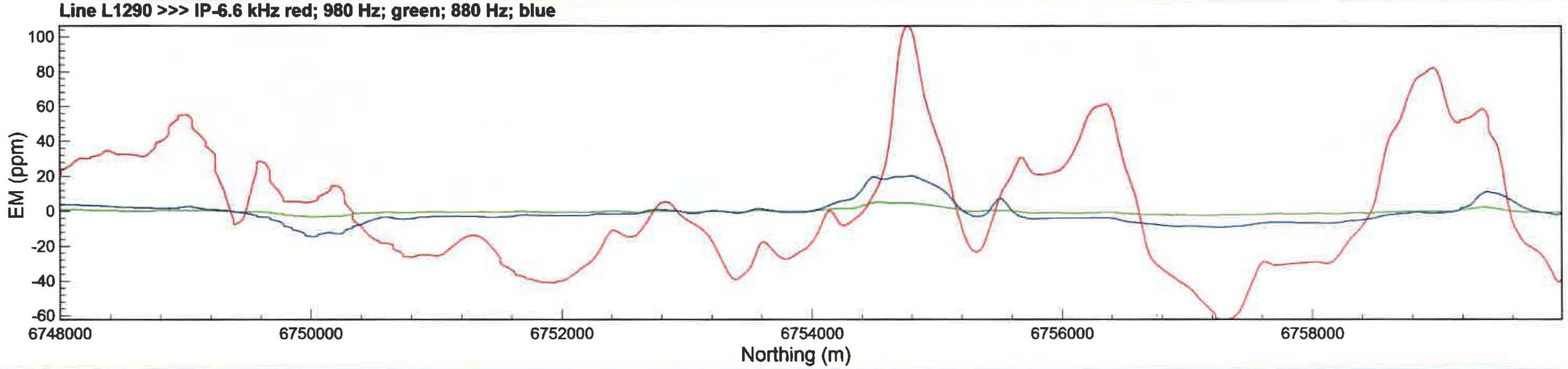
Line L1290 >>> IP-6.6 kHz red; 980 Hz; green; 880 Hz; blue

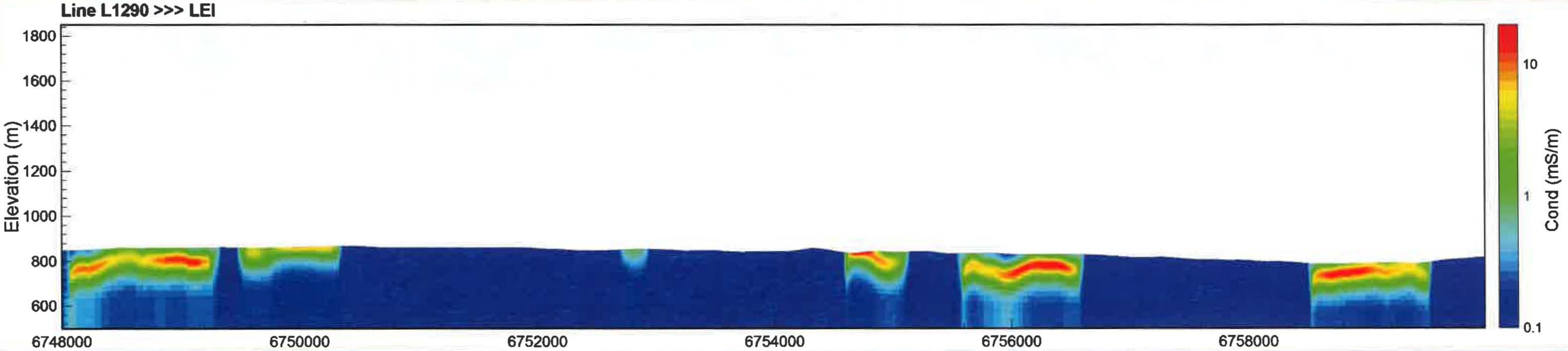
Line L1290 >>> LEI

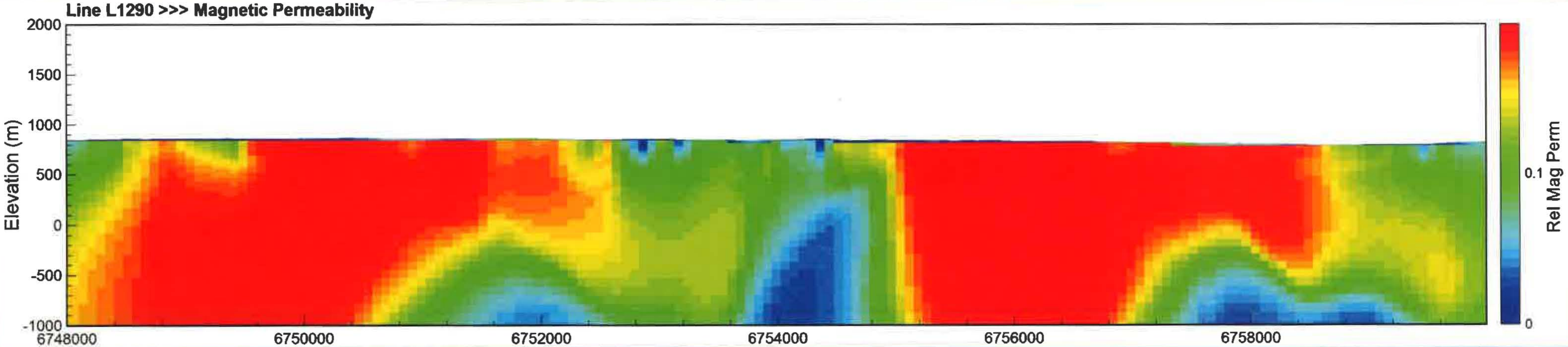
Line L1290 >>> Magnetic Permeability

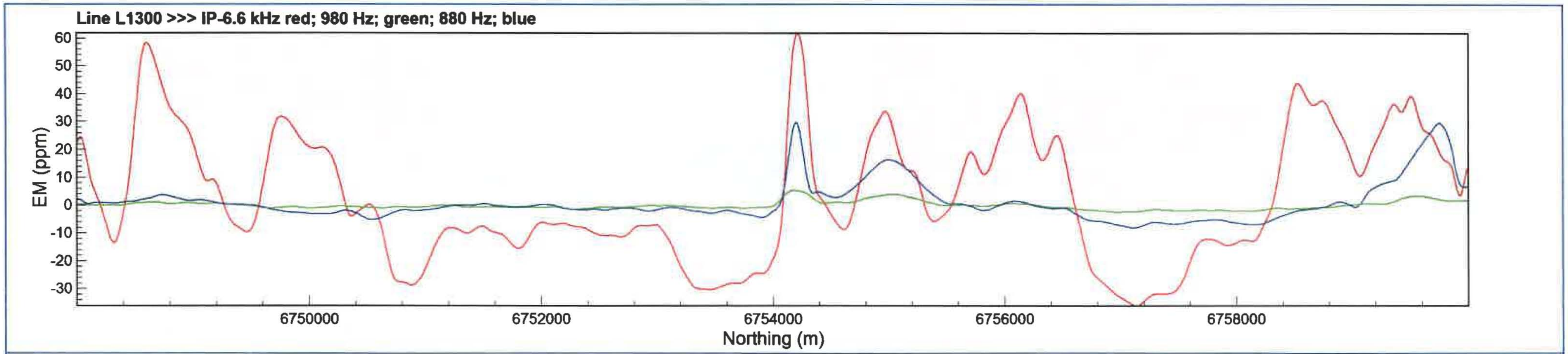
Line L1300 >>> IP-6.6 kHz red; 980 Hz; green; 880 Hz; blue
EM (ppm)
60
50
40
30
20
10
0
-10
-20
-30
6750000
6752000
6754000
6756000
6758000
Northing (m)

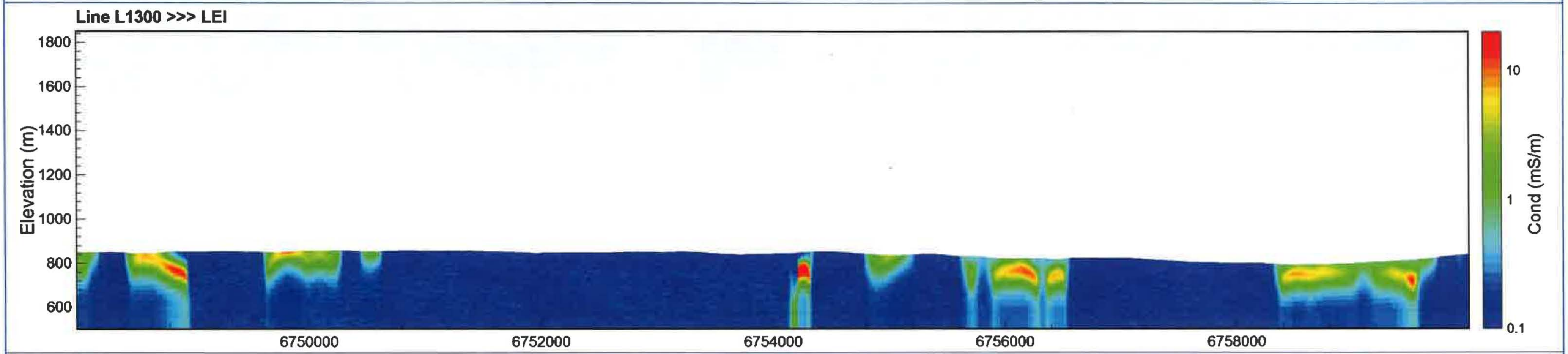
Line L1300 >>> LEI
Elevation (m)
1800
1600
1400
1200
1000
800
600
6750000
6752000
6754000
6756000
6758000
Cond (mS/m)
10
1
0.1

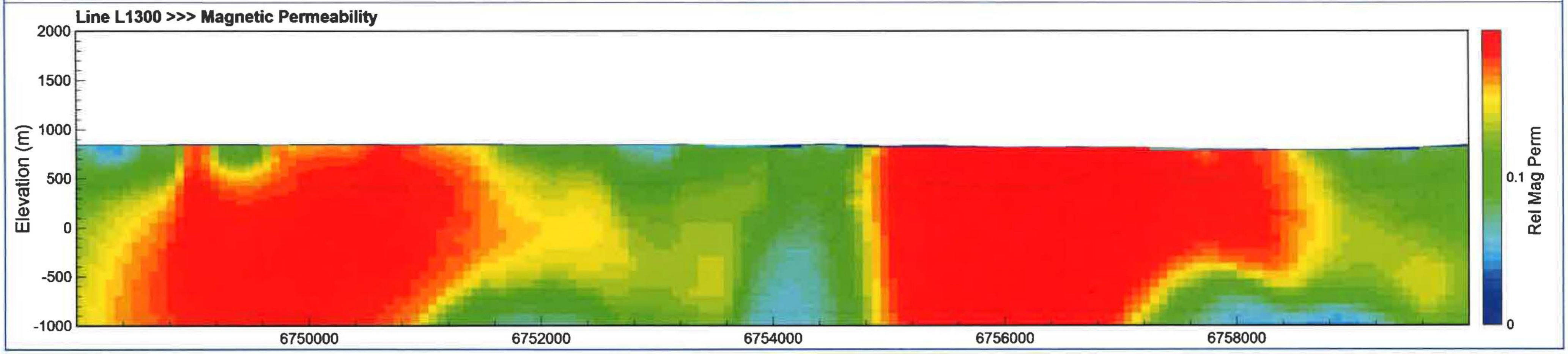
Line L1300 >>> Magnetic Permeability
Elevation (m)
2000
1500
1000
500
0
-500
-1000
6750000
6752000
6754000
6756000
6758000
Rel Mag Perm
0.1
0

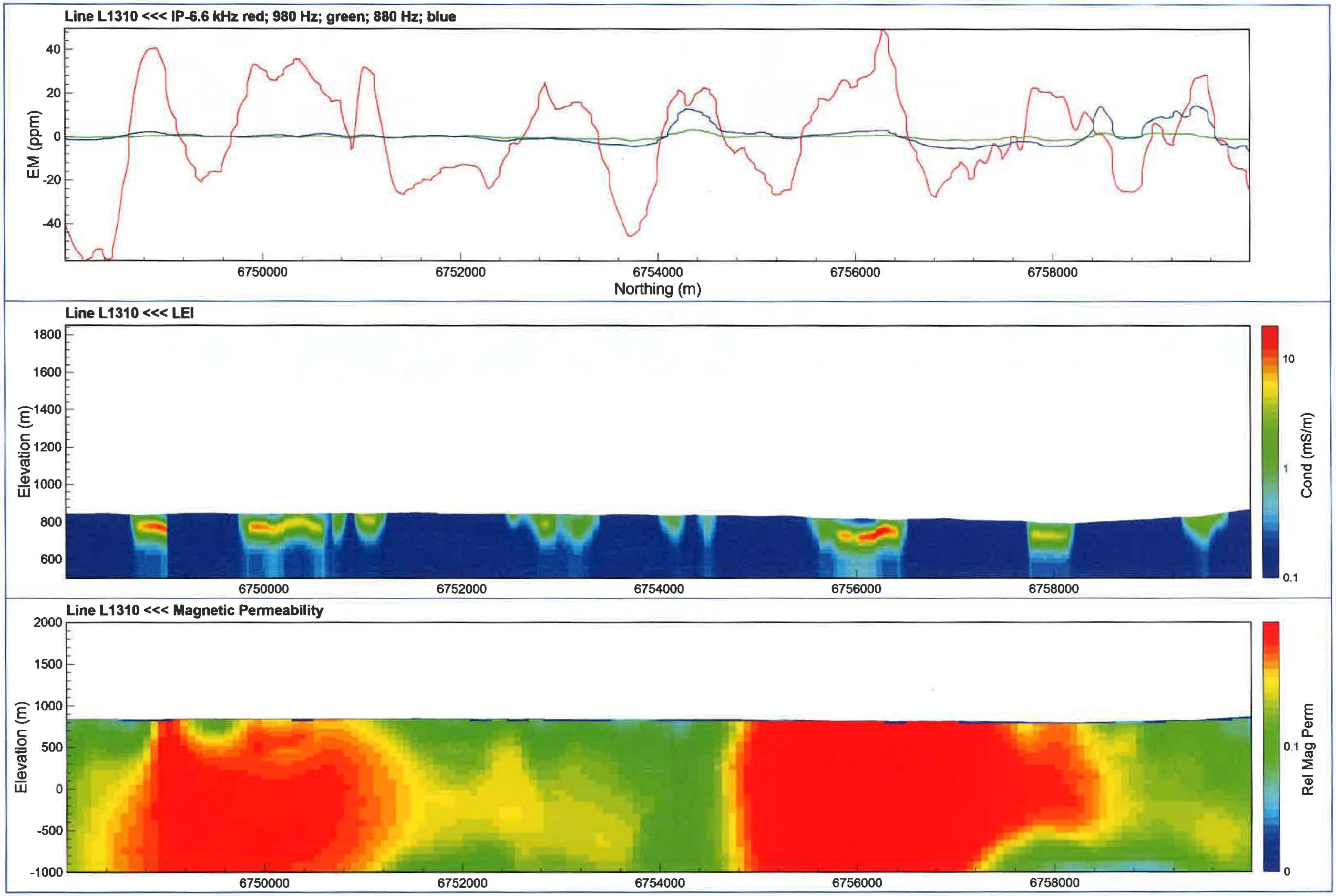

Line L1310 <<< IP-6.6 kHz red; 980 Hz; green; 880 Hz; blue

Line L1310 <<< LEI

Line L1310 <<< Magnetic Permeability

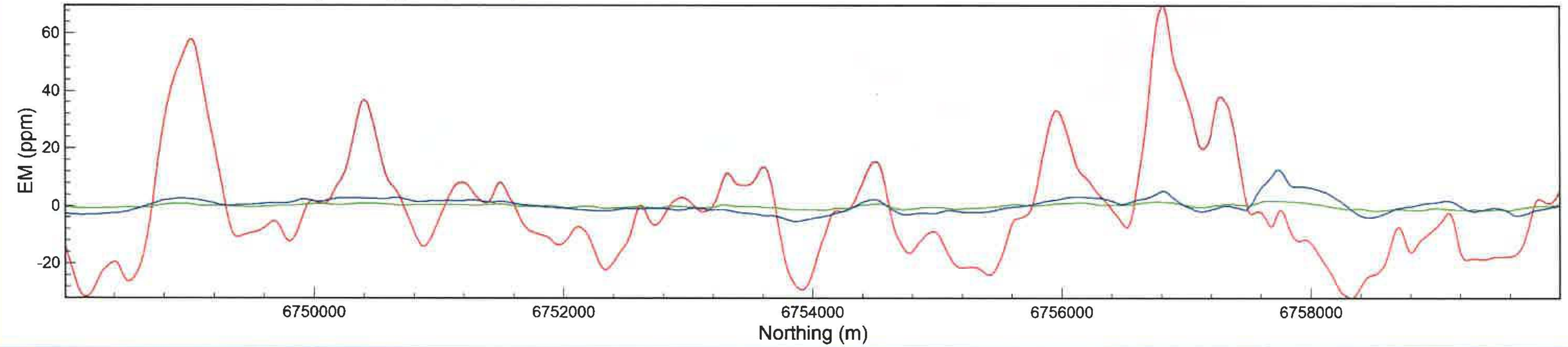

Line L1320 <<< IP-6.6 kHz red; 980 Hz; green; 880 Hz; blue

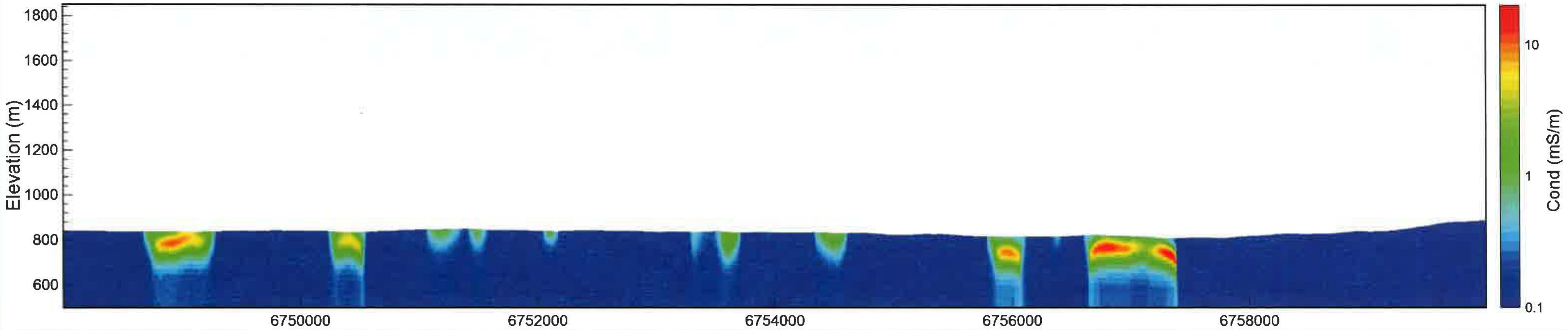

Line L1320 <<< LEI

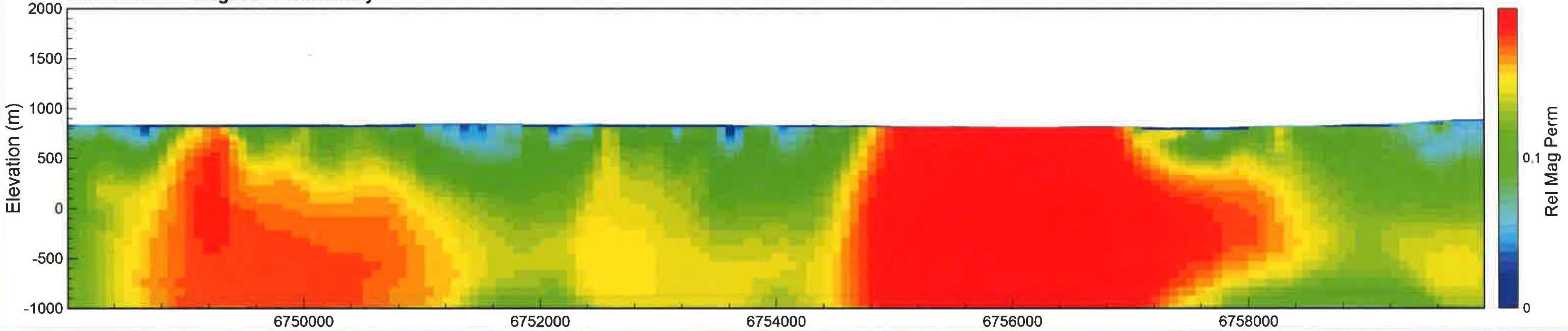

Line L1320 <<< Magnetic Permeability

Line L1330 >>> IP-6.6 kHz red; 980 Hz; green; 880 Hz; blue

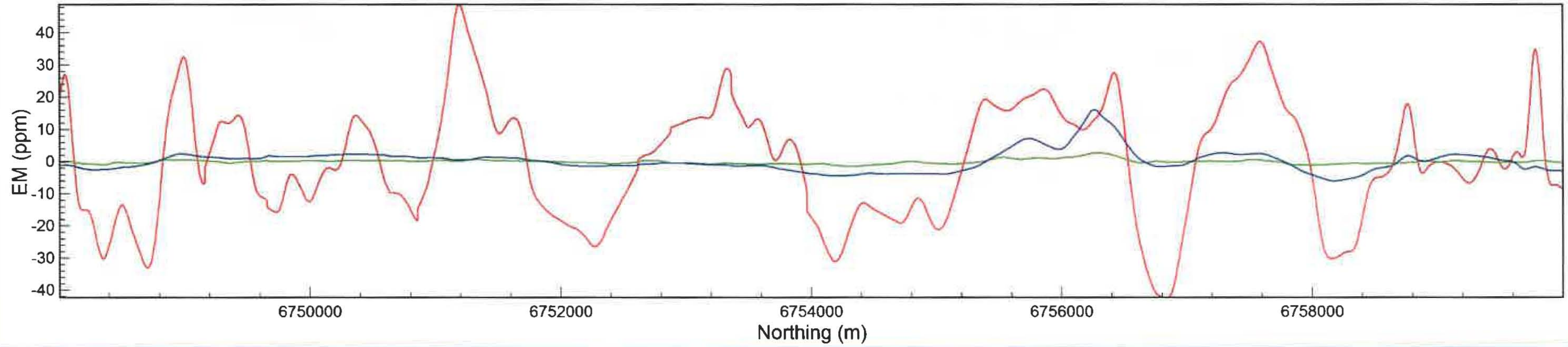

Line L1330 >>> LEI

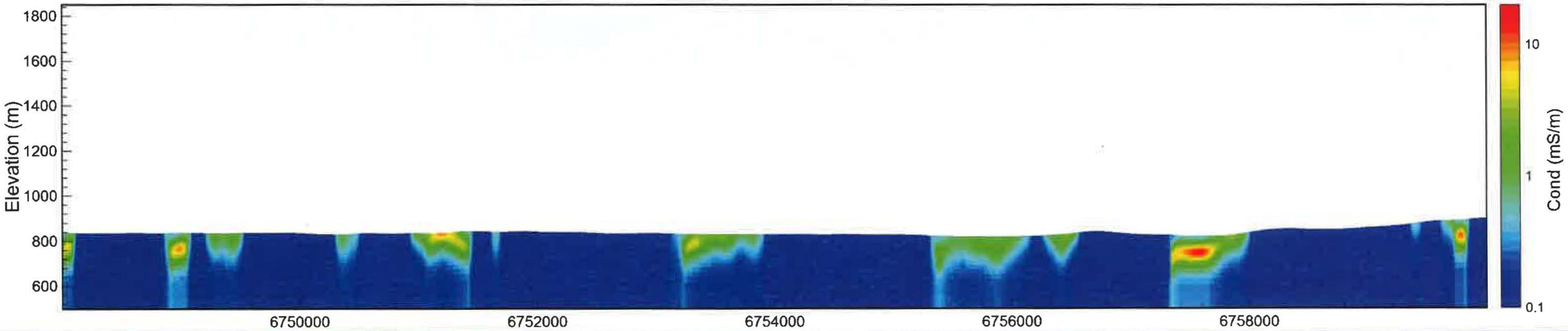

Line L1330 >>> Magnetic Permeability

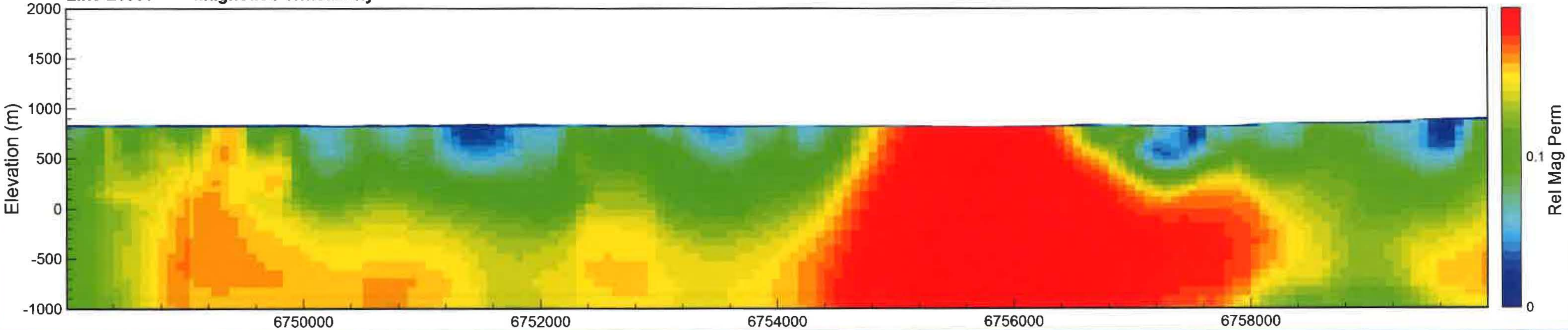

Line L1340 >>> IP-6.6 kHz red; 980 Hz; green; 880 Hz; blue

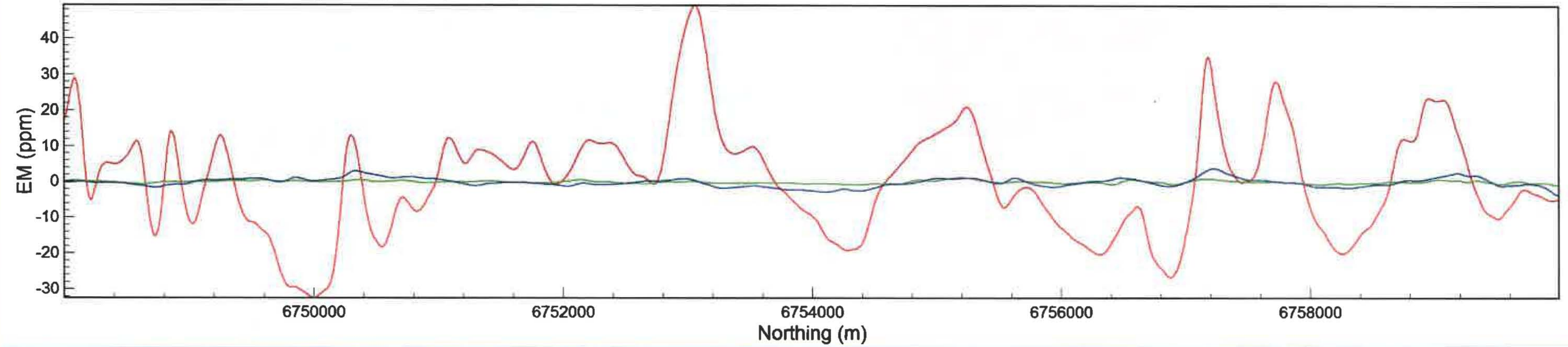

Line L1340 >>> LEI

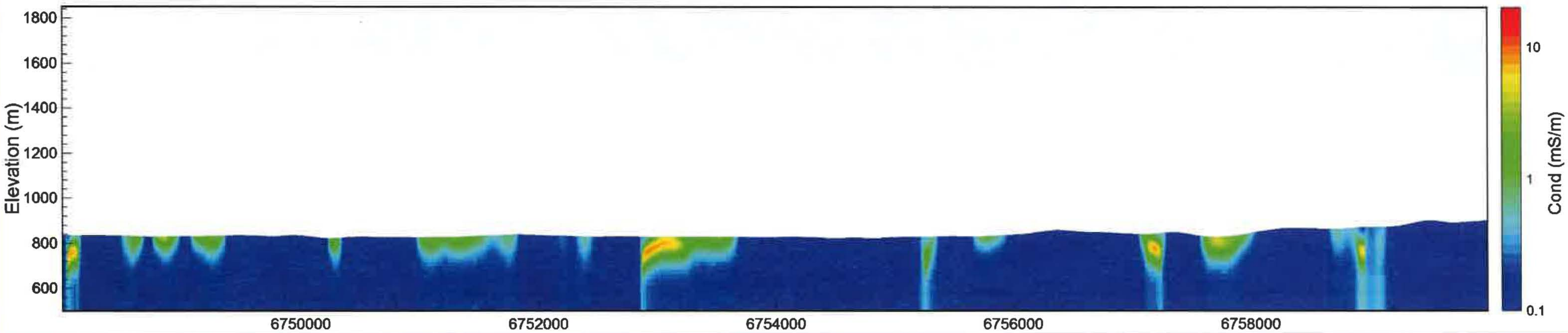

Line L1340 >>> Magnetic Permeability

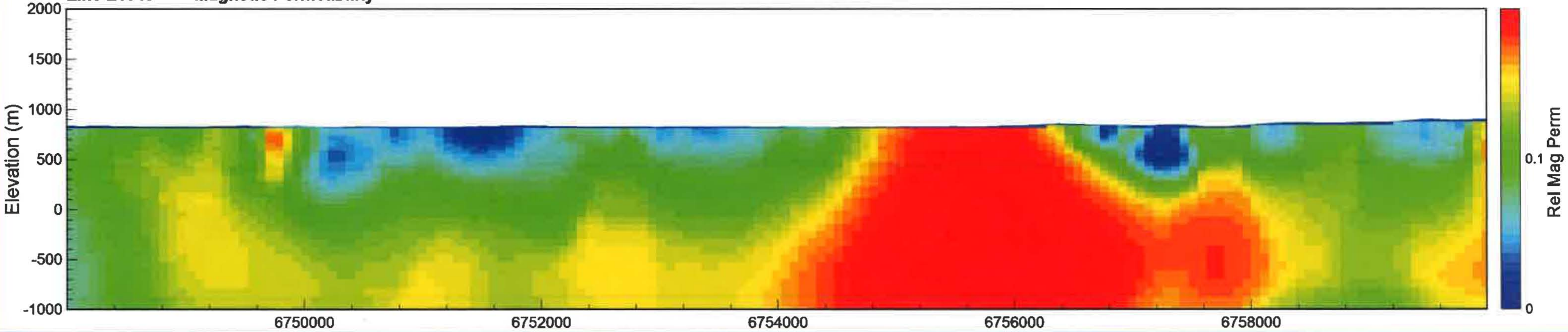

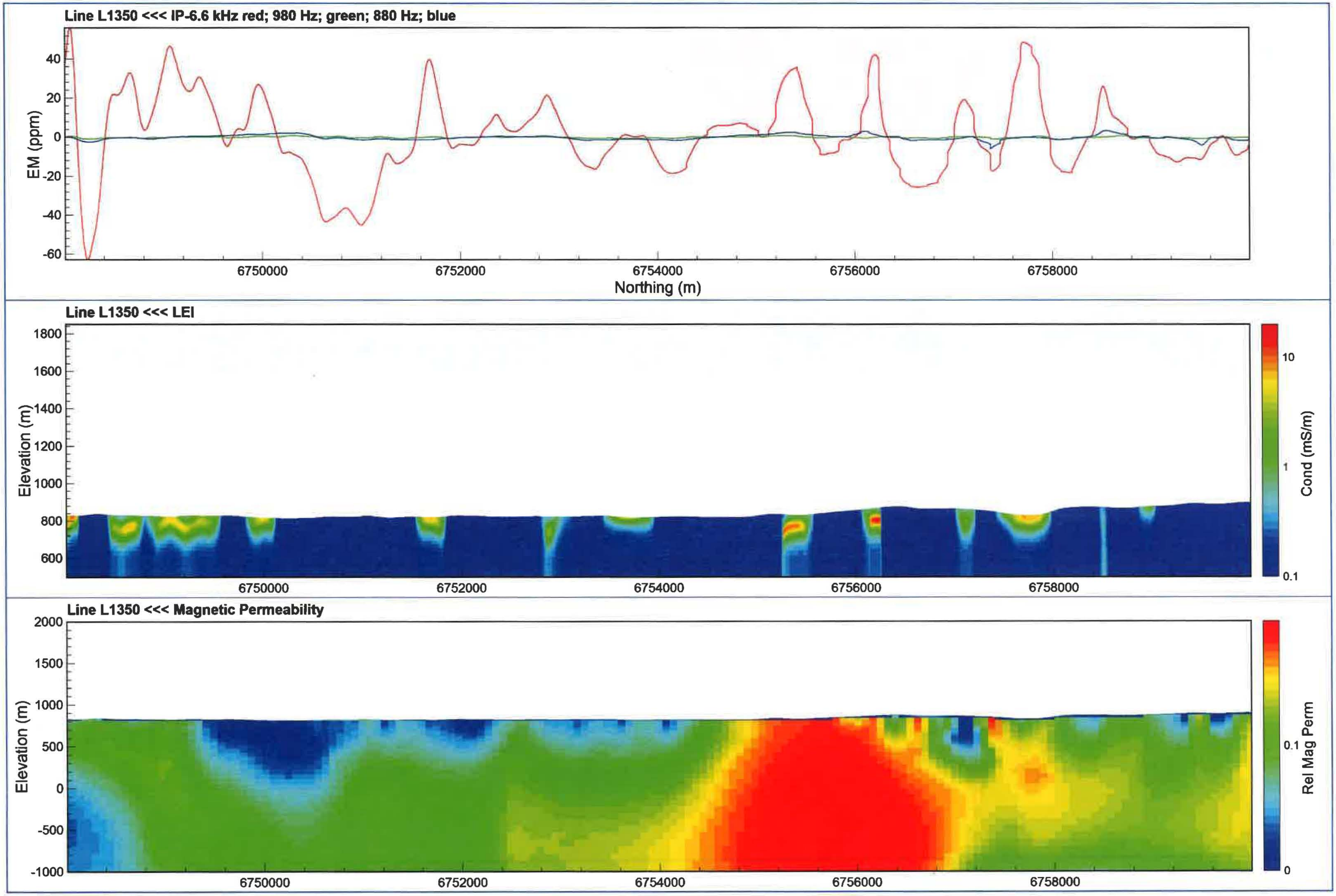
Line L1350 <<< IP-6.6 kHz red; 980 Hz; green; 880 Hz; blue

Line L1350 <<< LEI

Line L1350 <<< Magnetic Permeability

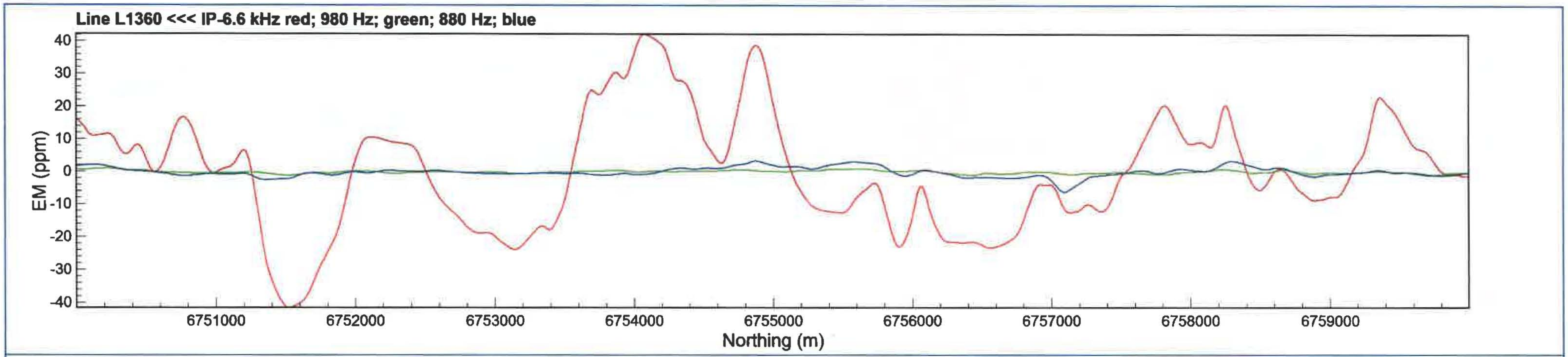
Line L1360 <<< IP-6.6 kHz red; 980 Hz; green; 880 Hz; blue
EM (ppm)
40
30
20
10
0
-10
-20
-30
-40
6751000
6752000
6753000
6754000
6755000
6756000
6757000
6758000
6759000
Northing (m)

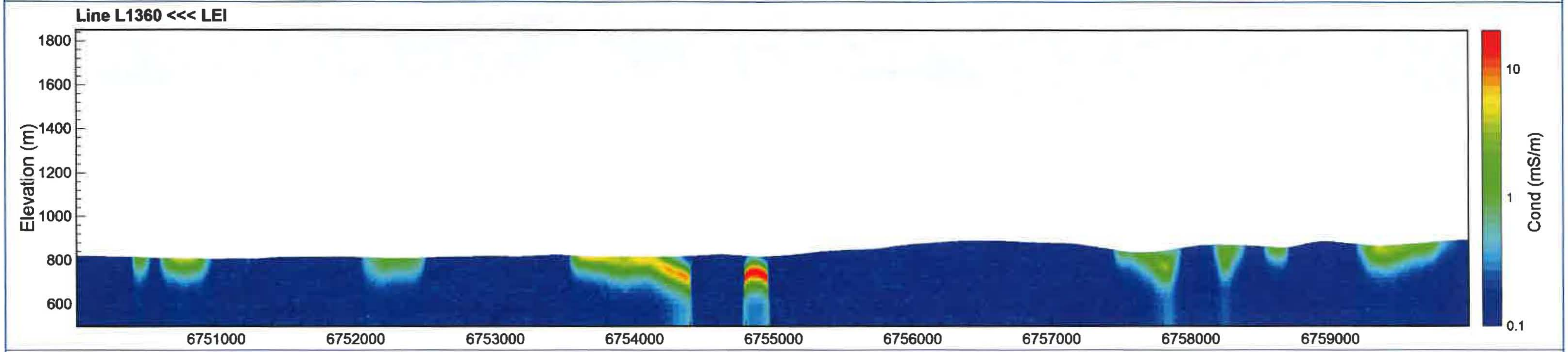
Line L1360 <<< LEI
Elevation (m)
1800
1600
1400
1200
1000
800
600
6751000
6752000
6753000
6754000
6755000
6756000
6757000
6758000
6759000
Cond (mS/m)
10
1
0.1

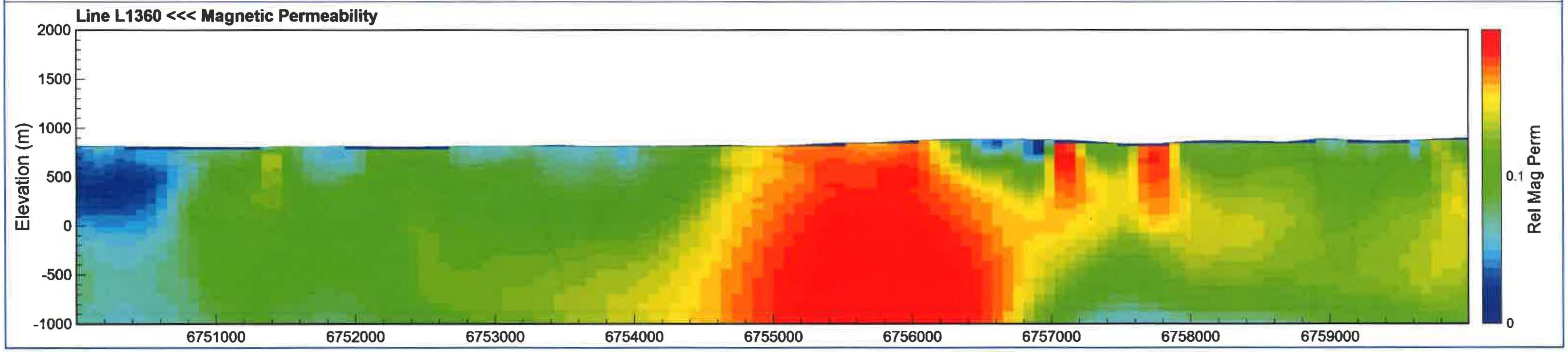
Line L1360 <<< Magnetic Permeability
Elevation (m)
2000
1500
1000
500
0
-500
-1000
6751000
6752000
6753000
6754000
6755000
6756000
6757000
6758000
6759000
Rel Mag Perm
0.1
0

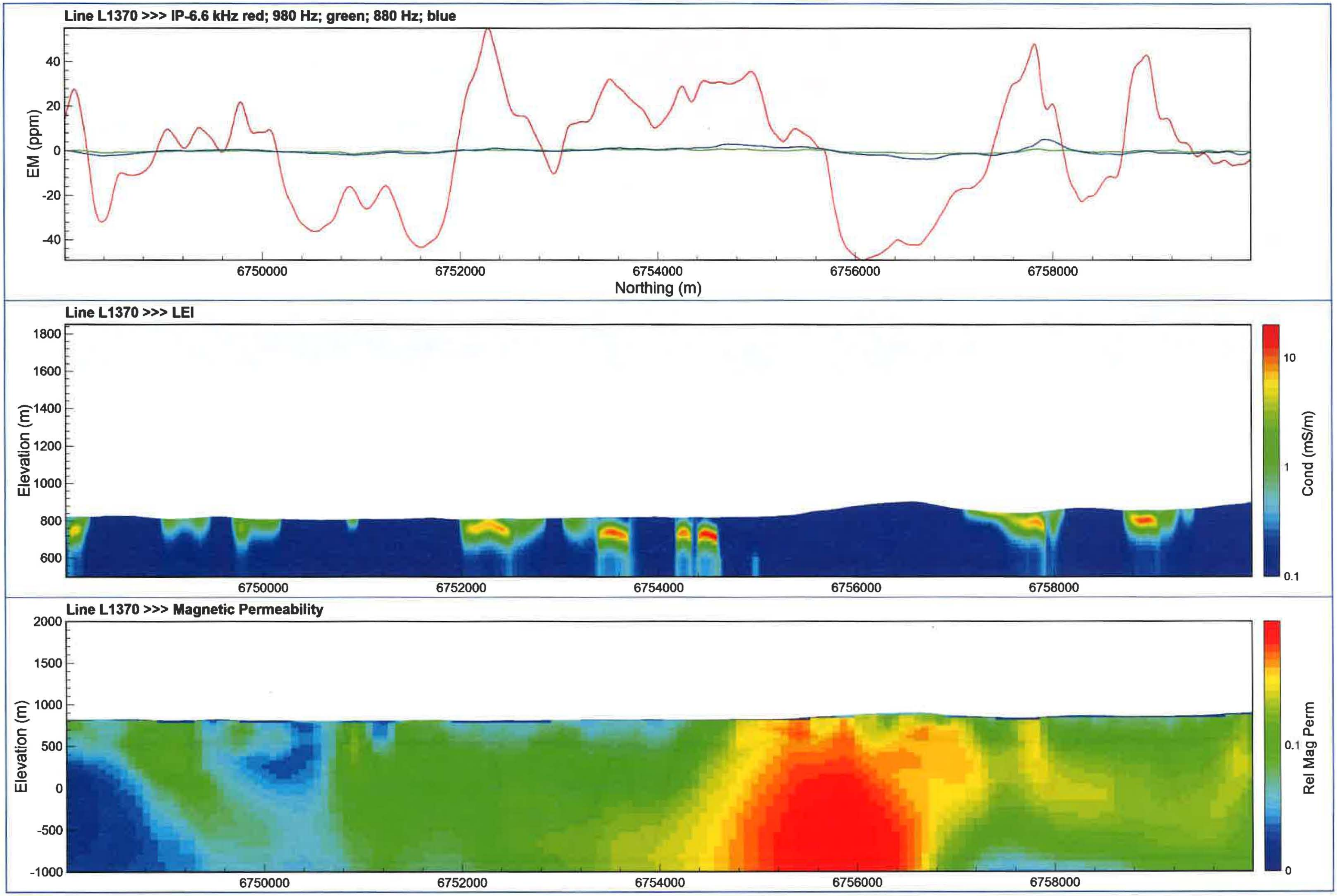
Line L1370 >>> IP-6.6 kHz red; 980 Hz; green; 880 Hz; blue
EM (ppm)
40
20
0
-20
-40
6750000
6752000
6754000
6756000
6758000
Northing (m)
Line L1370 >>> LEI
Elevation (m)
1800
1600
1400
1200
1000
800
600
6750000
6752000
6754000
6756000
6758000
Cond (mS/m)
10
1
0.1
Line L1370 >>> Magnetic Permeability
Elevation (m)
2000
1500
1000
500
0
-500
-1000
6750000
6752000
6754000
6756000
6758000
Rel Mag Perm
0.1
0

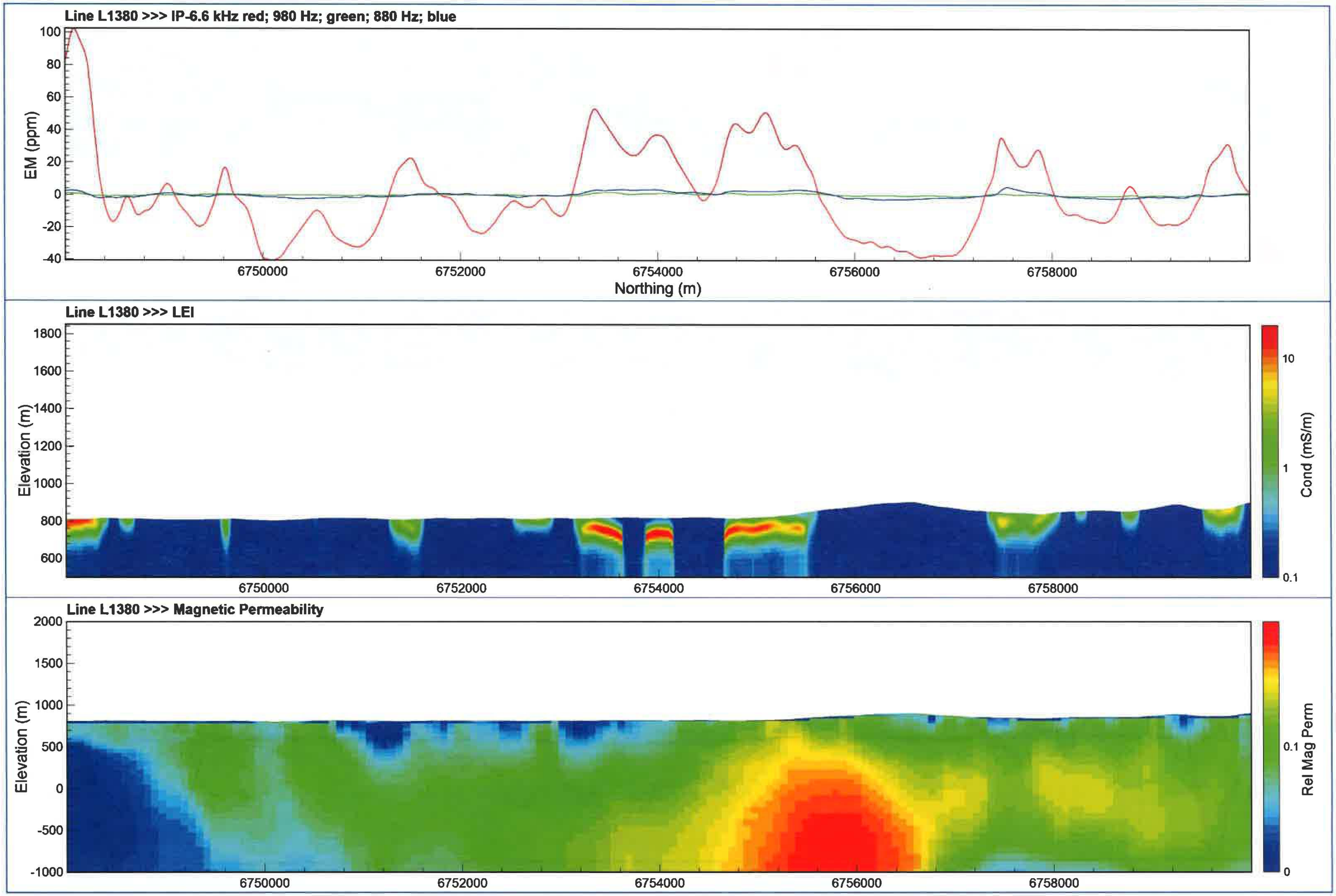

Line L1380 >>> IP-6.6 kHz red; 980 Hz; green; 880 Hz; blue

Line L1380 >>> LEI

Line L1380 >>> Magnetic Permeability

Line L1390 <<< IP-6.6 kHz red; 980 Hz; green; 880 Hz; blue

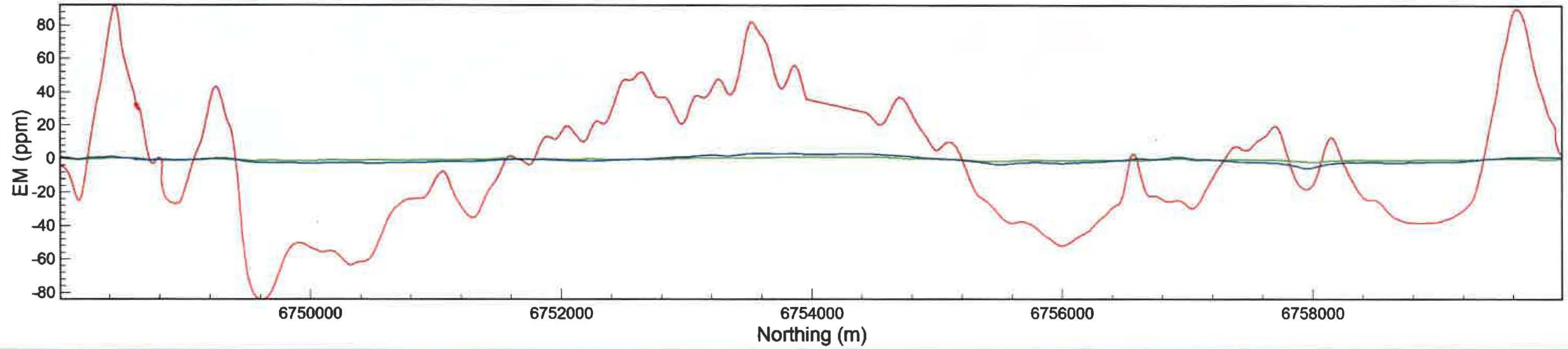

Line L1390 <<< LEI

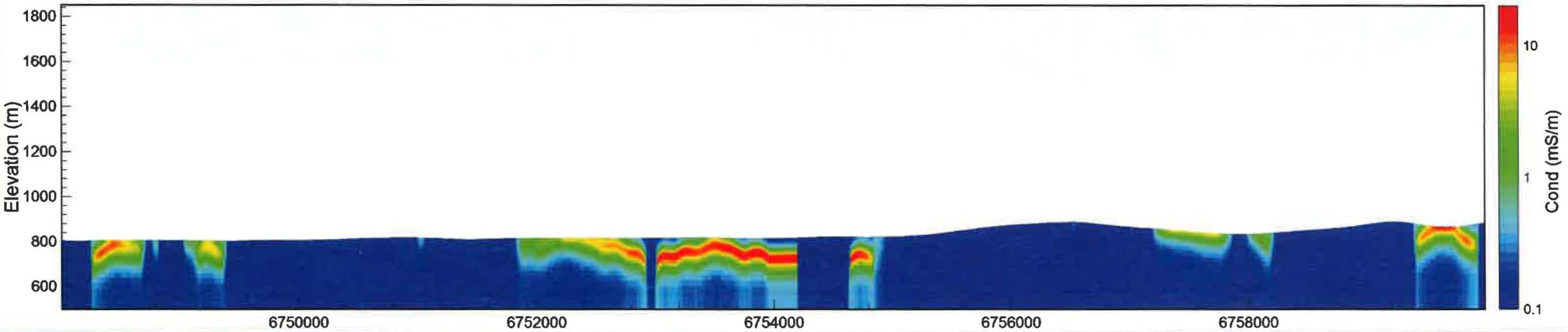

Line L1390 <<< Magnetic Permeability

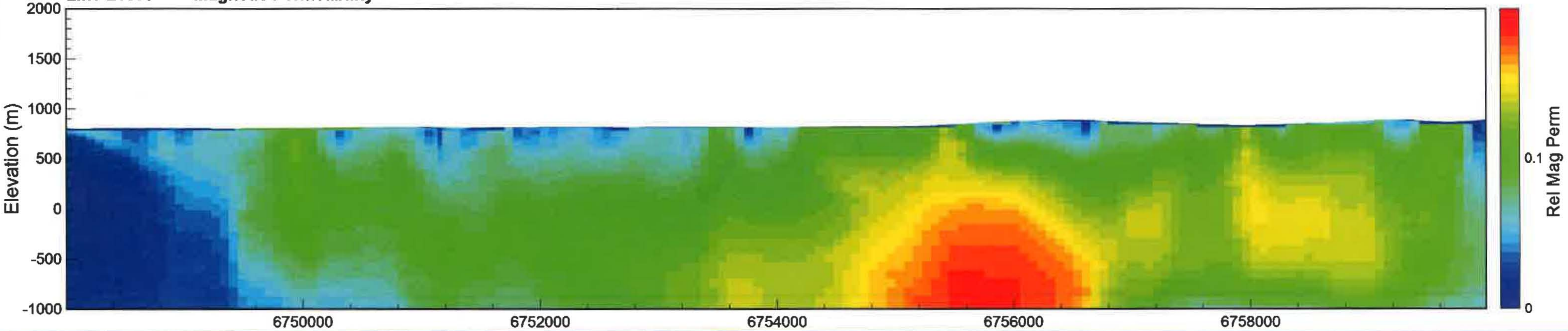

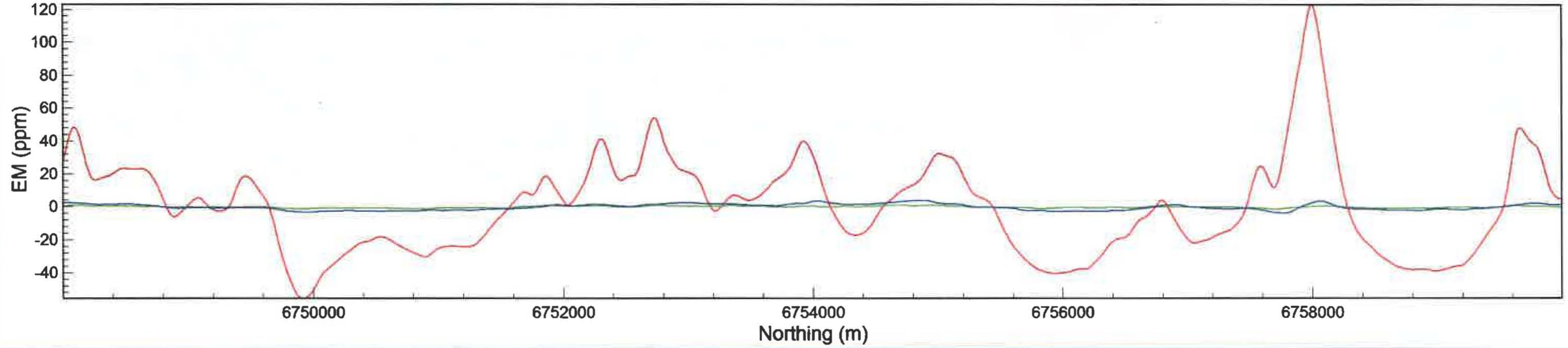
Line L1400 <<< IP-6.6 kHz red; 980 Hz; green; 880 Hz; blue

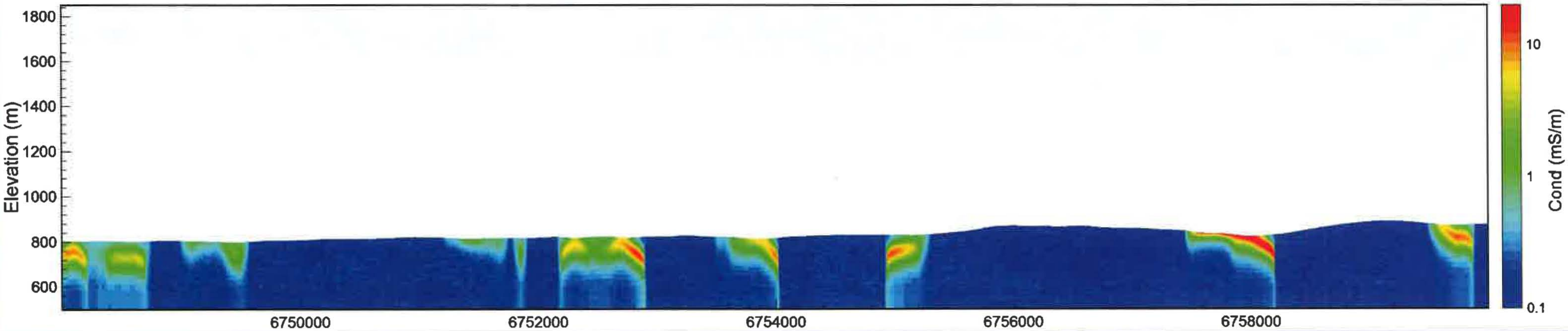
Line L1400 <<< LEI

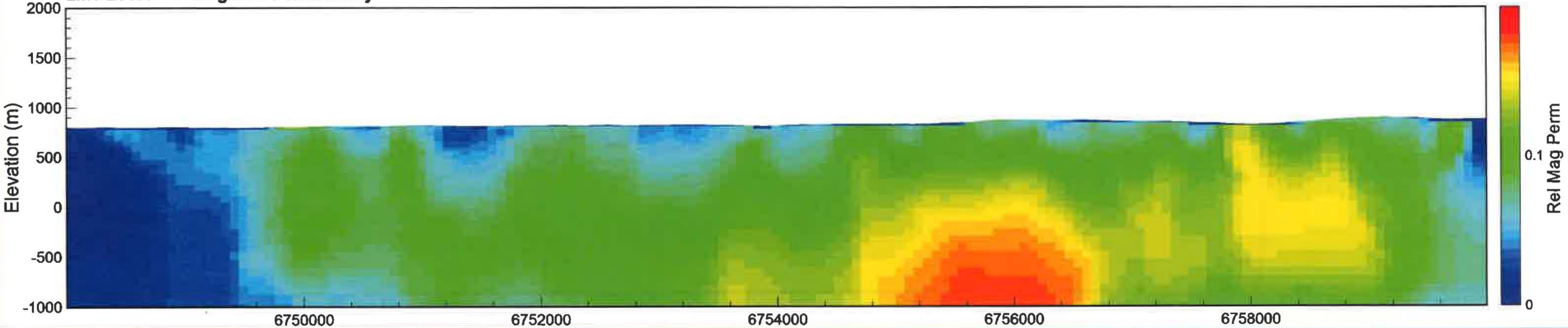
Line L1400 <<< Magnetic Permeability

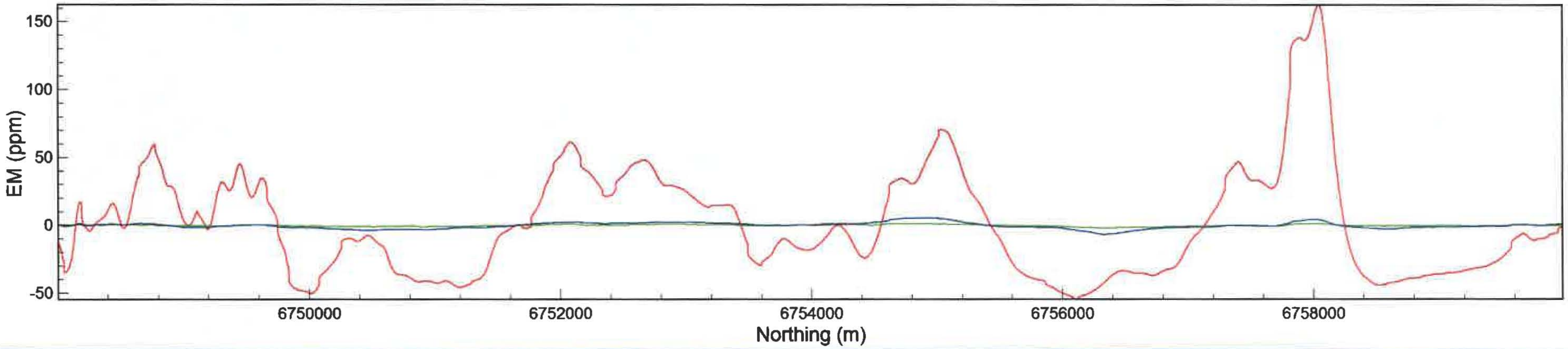

Line L1410 >>> IP-6.6 kHz red; 980 Hz; green; 880 Hz; blue

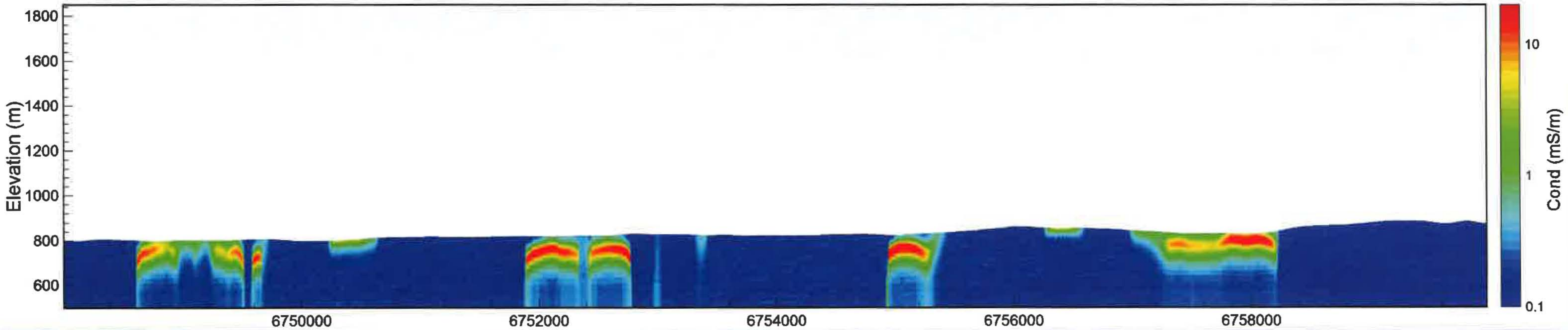

Line L1410 >>> LEI

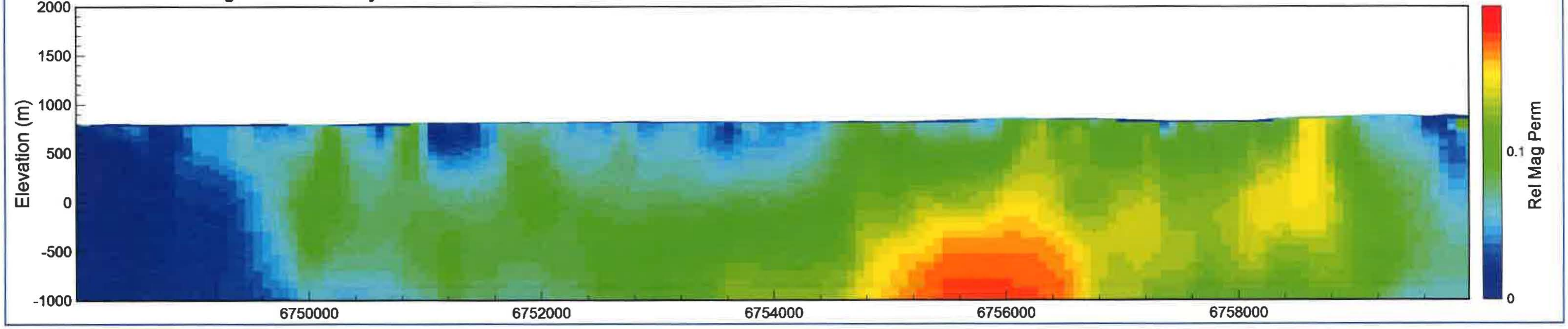

Line L1410 >>> Magnetic Permeability

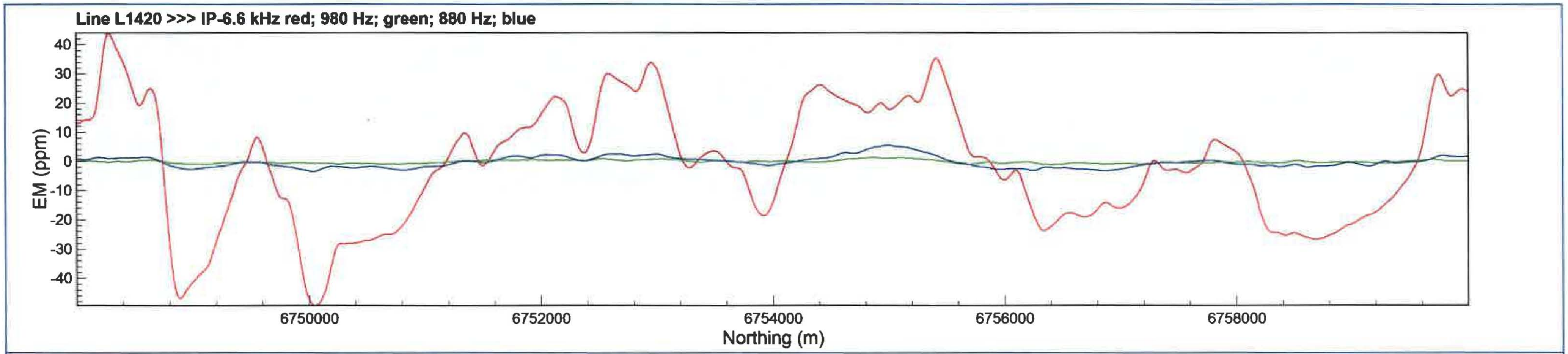
Line L1420 >>> IP-6.6 kHz red; 980 Hz; green; 880 Hz; blue

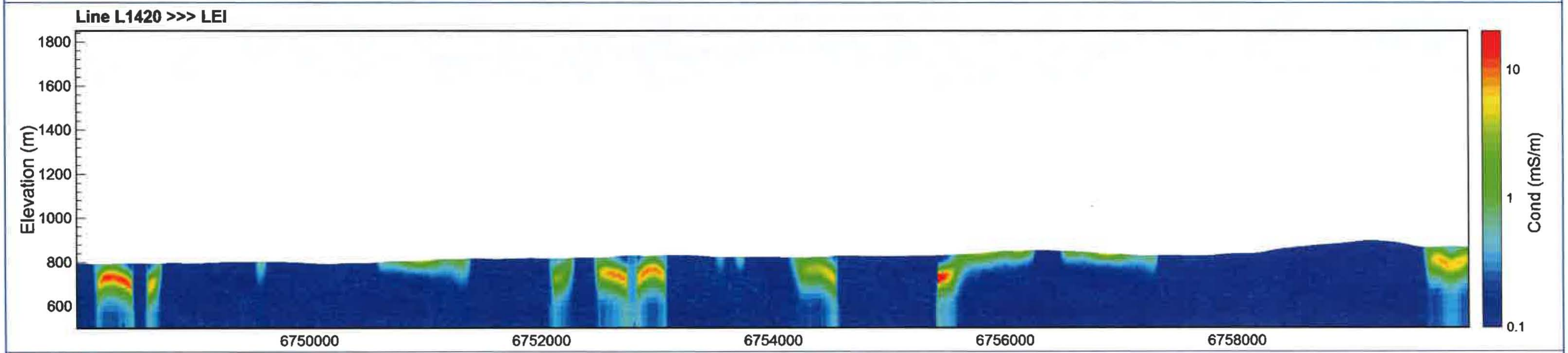
Line L1420 >>> LEI

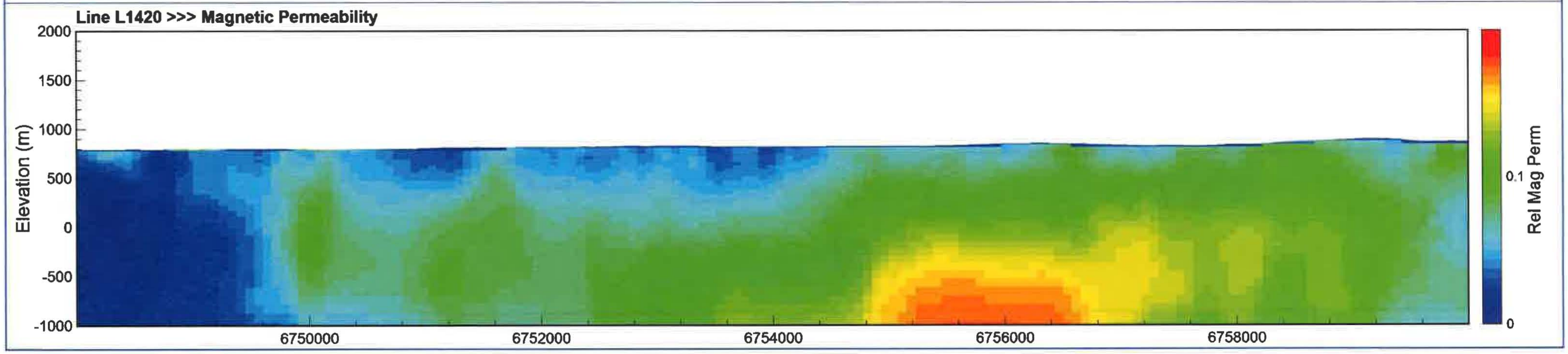
Line L1420 >>> Magnetic Permeability

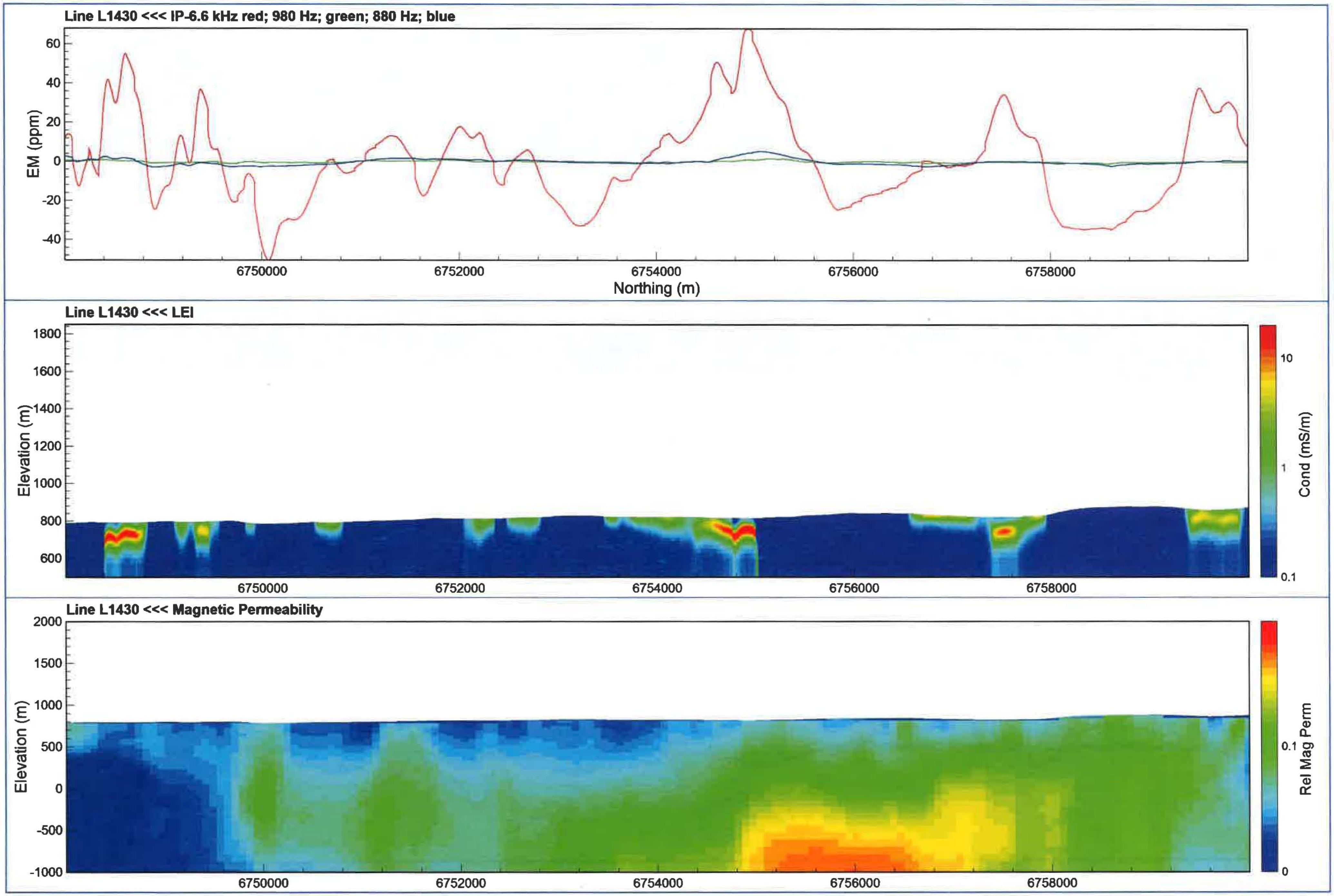

Line L1430 <<< IP-6.6 kHz red; 980 Hz; green; 880 Hz; blue

Line L1430 <<< LEI

Line L1430 <<< Magnetic Permeability

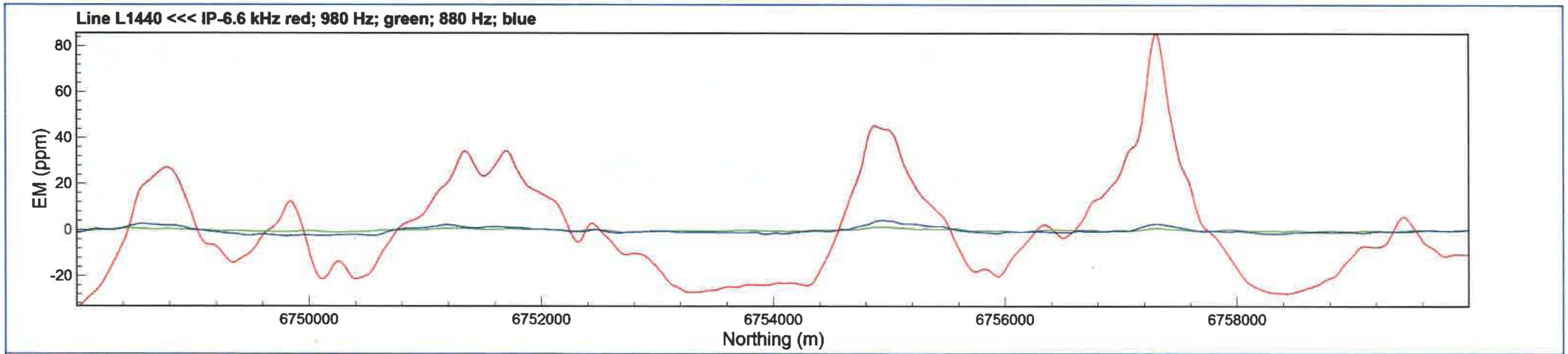

Line L1440 <<< IP-6.6 kHz red; 980 Hz; green; 880 Hz; blue

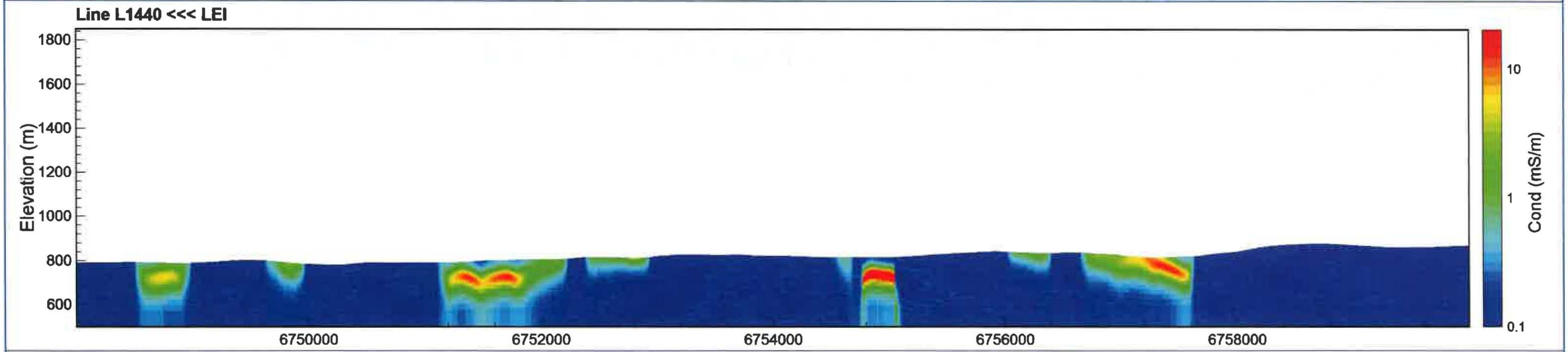

Line L1440 <<< LEI

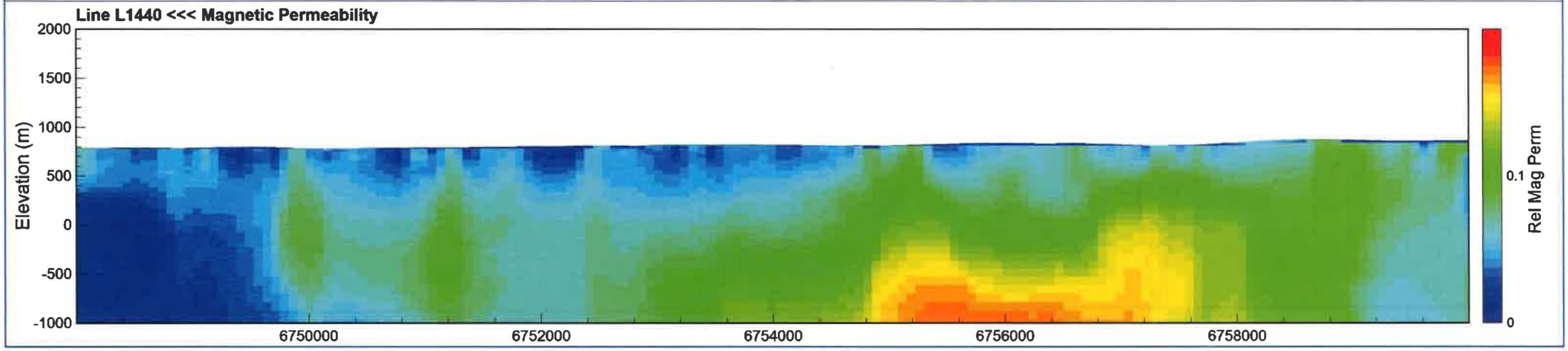

Line L1440 <<< Magnetic Permeability

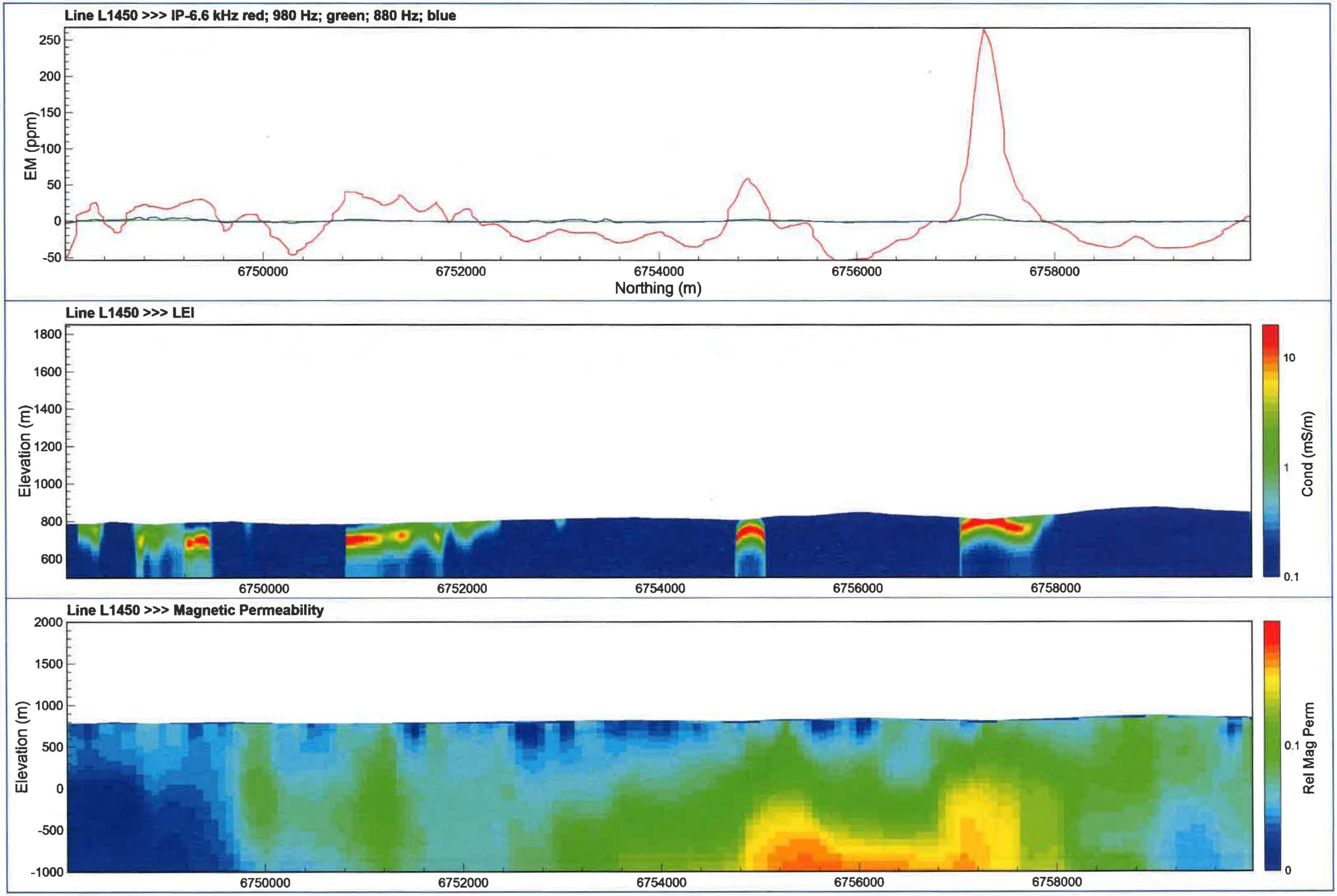
Line L1450 >>> IP-6.6 kHz red; 980 Hz; green; 880 Hz; blue
EM (ppm)
250
200
150
100
50
0
-50
6750000
6752000
6754000
6756000
6758000
Northing (m)
Line L1450 >>> LEI
Elevation (m)
1800
1600
1400
1200
1000
800
600
6750000
6752000
6754000
6756000
6758000
Cond (mS/m)
10
1
0.1
Line L1450 >>> Magnetic Permeability
Elevation (m)
2000
1500
1000
500
0
-500
-1000
6750000
6752000
6754000
6756000
6758000
Rel Mag Perm
0.1
0

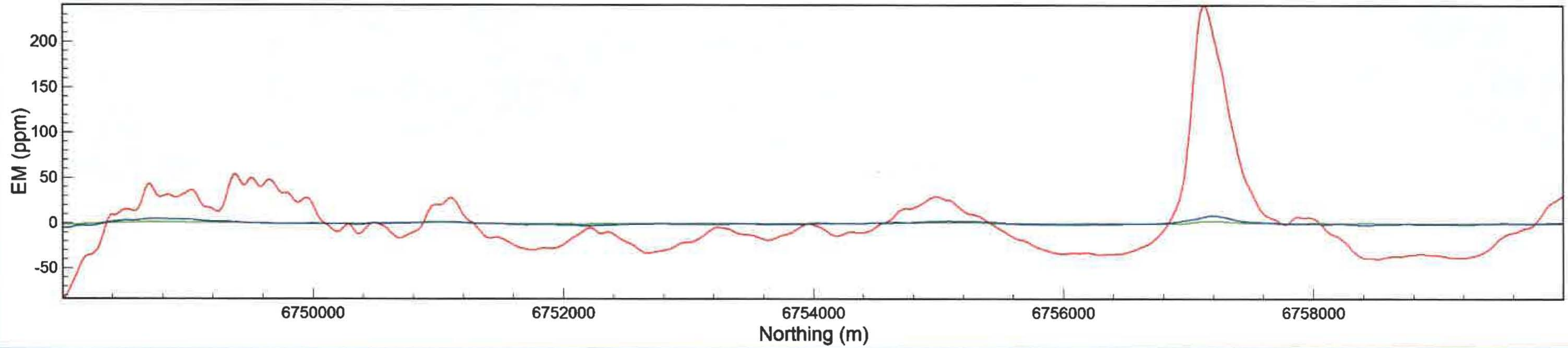

Line L1460 >>> IP-6.6 kHz red; 980 Hz; green; 880 Hz; blue

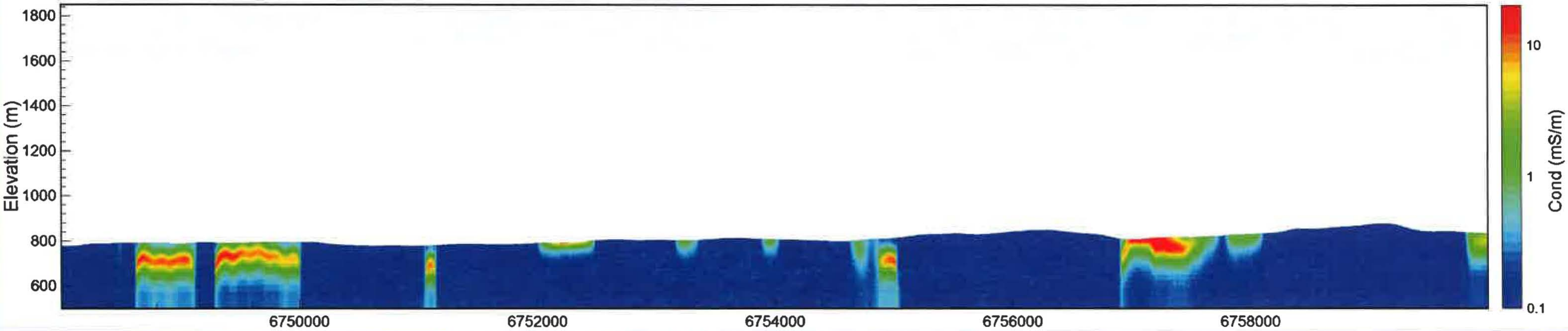

Line L1460 >>> LEI

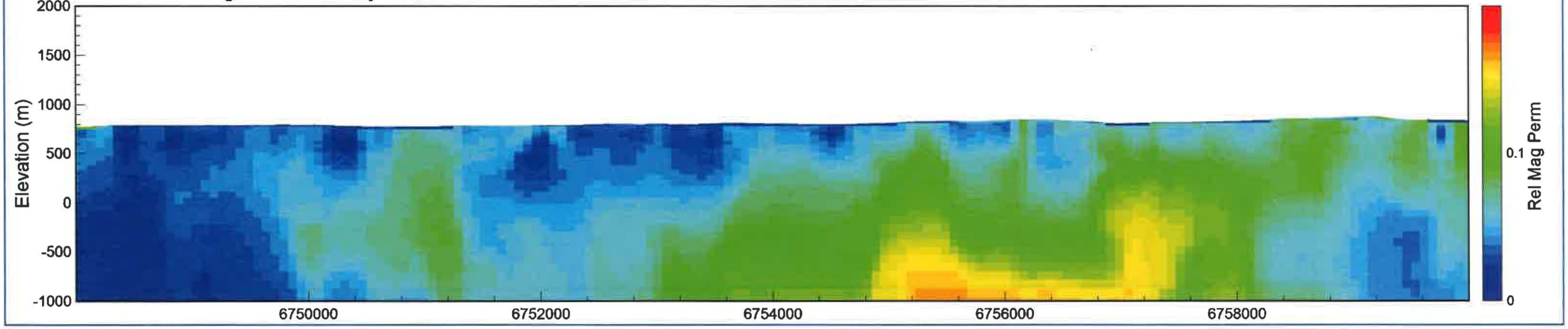

Line L1460 >>> Magnetic Permeability

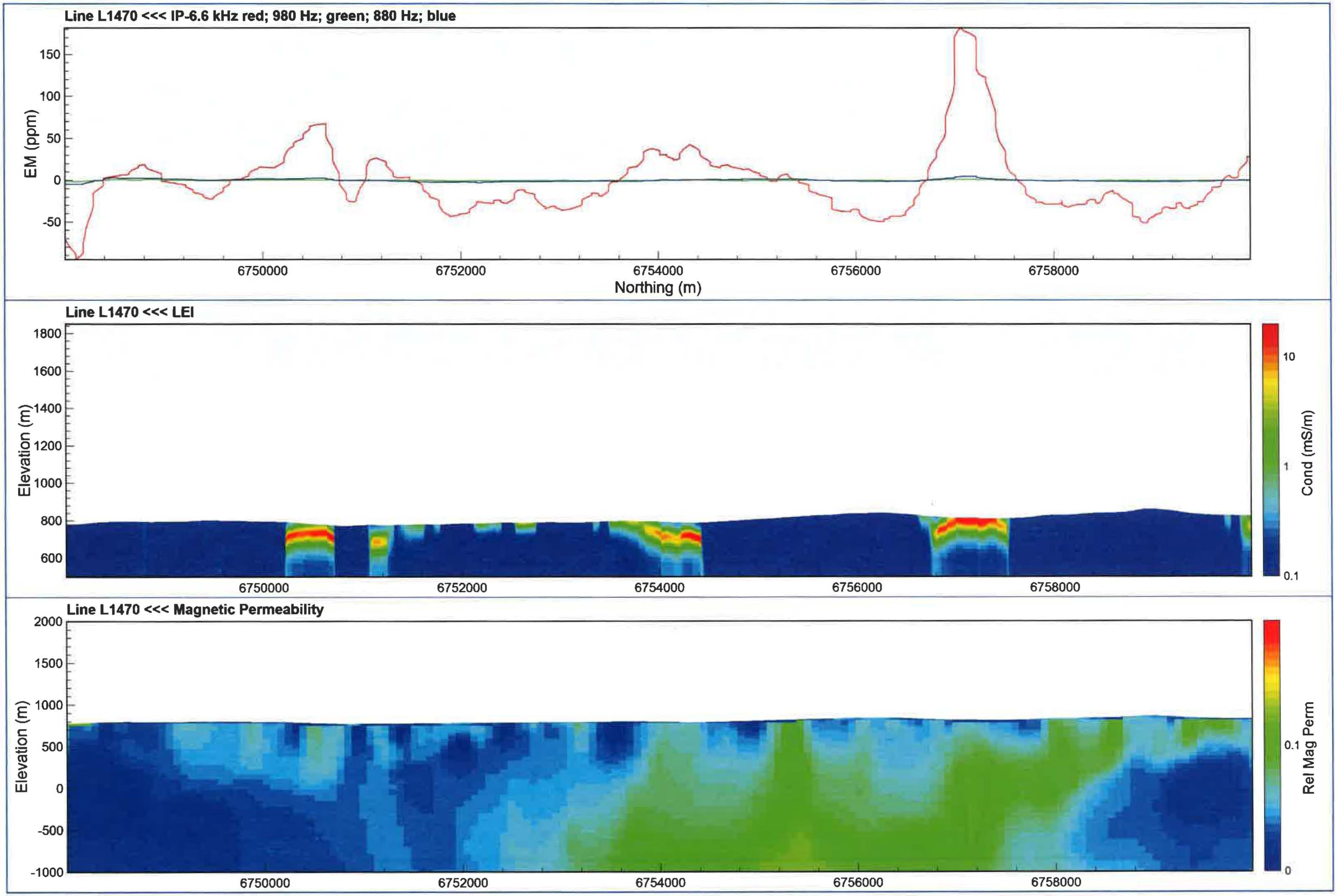
Line L1470 <<< IP-6.6 kHz red; 980 Hz; green; 880 Hz; blue
EM (ppm)
150
100
50
0
-50
6750000
6752000
6754000
6756000
6758000
Northing (m)
Line L1470 <<< LEI
Elevation (m)
1800
1600
1400
1200
1000
800
600
6750000
6752000
6754000
6756000
6758000
10
1
0.1
Cond (mS/m)
Line L1470 <<< Magnetic Permeability
Elevation (m)
2000
1500
1000
500
0
-500
-1000
6750000
6752000
6754000
6756000
6758000
0.1
0
Rel Mag Perm

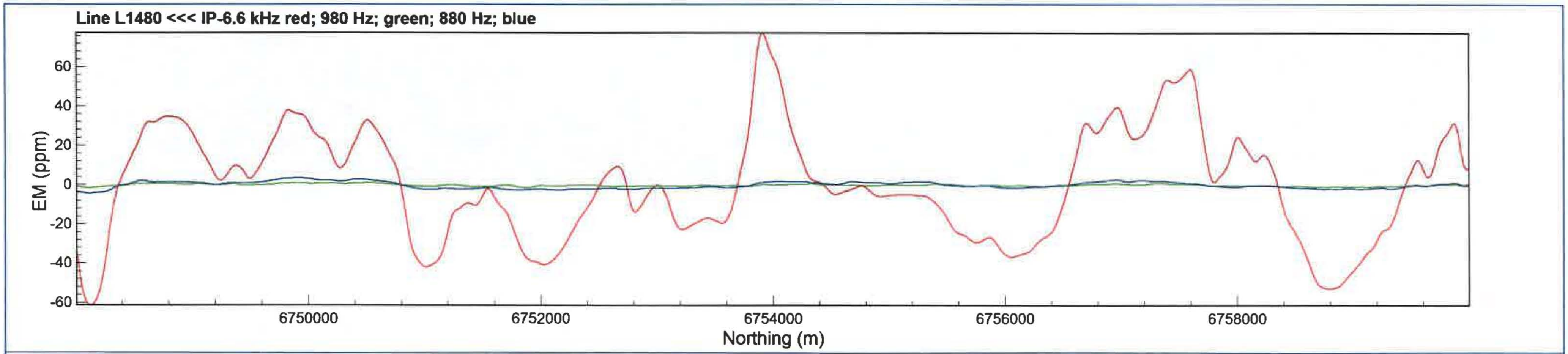
Line L1480 <<< IP-6.6 kHz red; 980 Hz; green; 880 Hz; blue

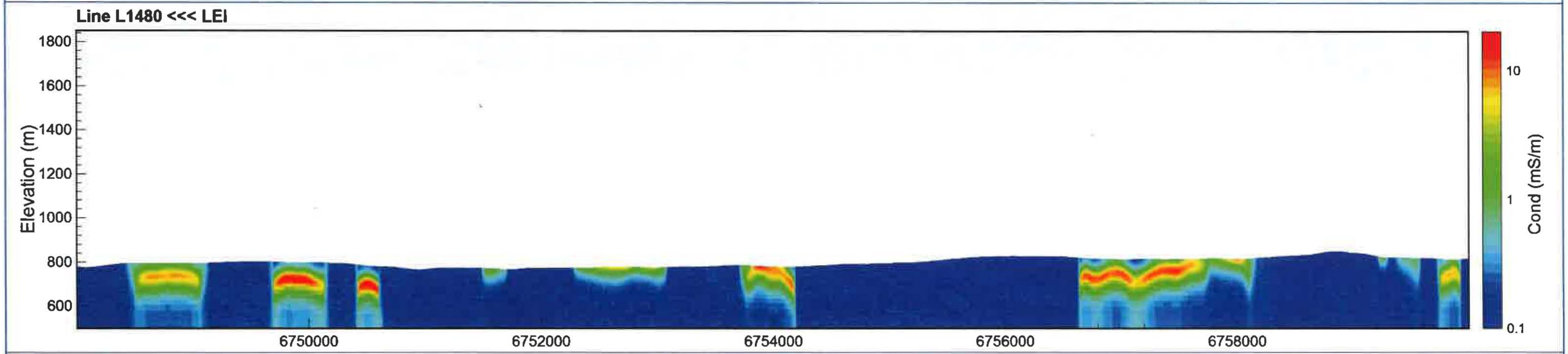
Line L1480 <<< LEI

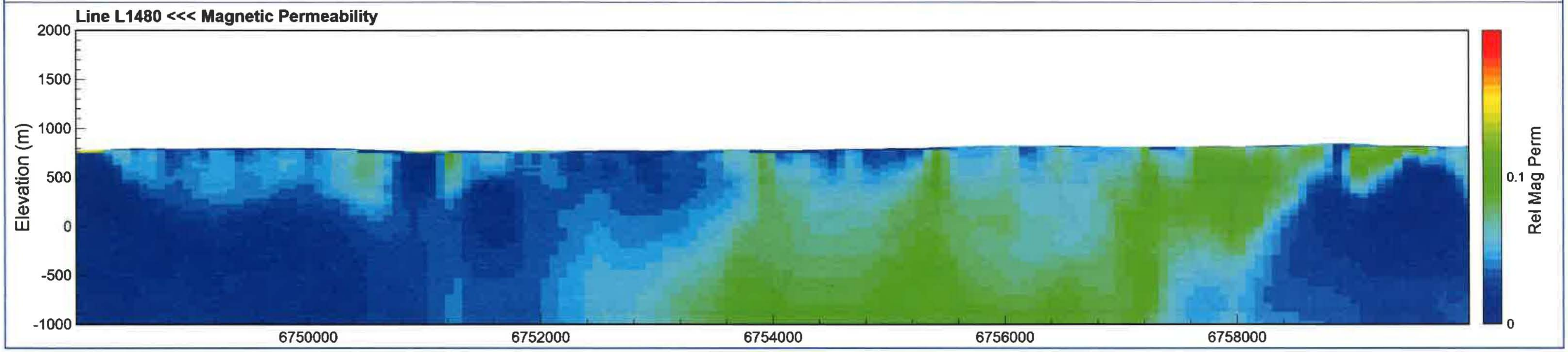
Line L1480 <<< Magnetic Permeability

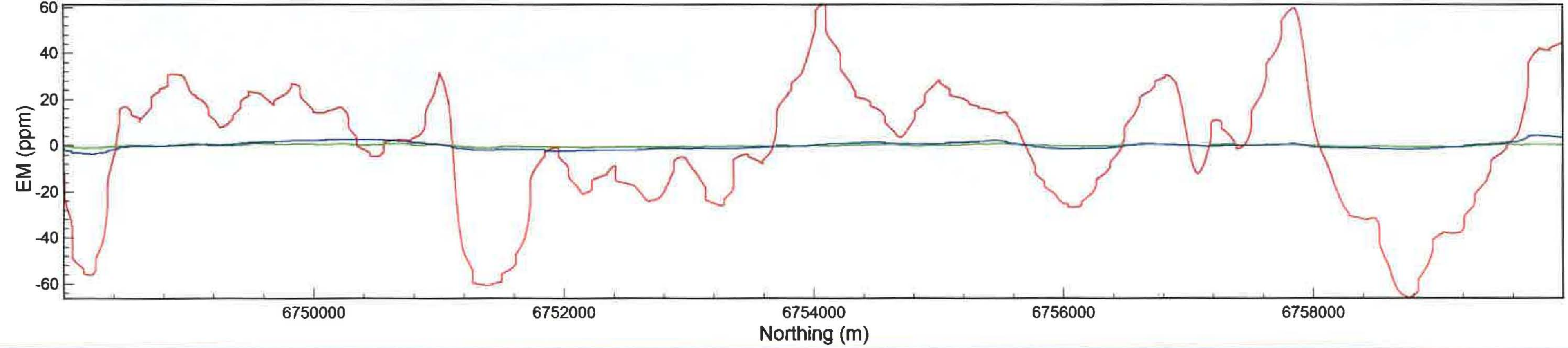

Line L1490 >>> IP-6.6 kHz red; 980 Hz; green; 880 Hz; blue

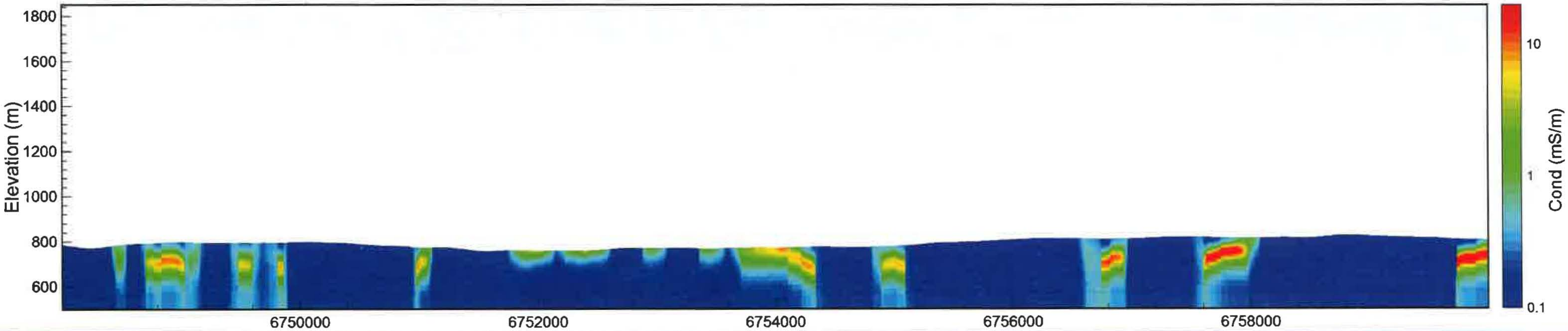

Line L1490 >>> LEI

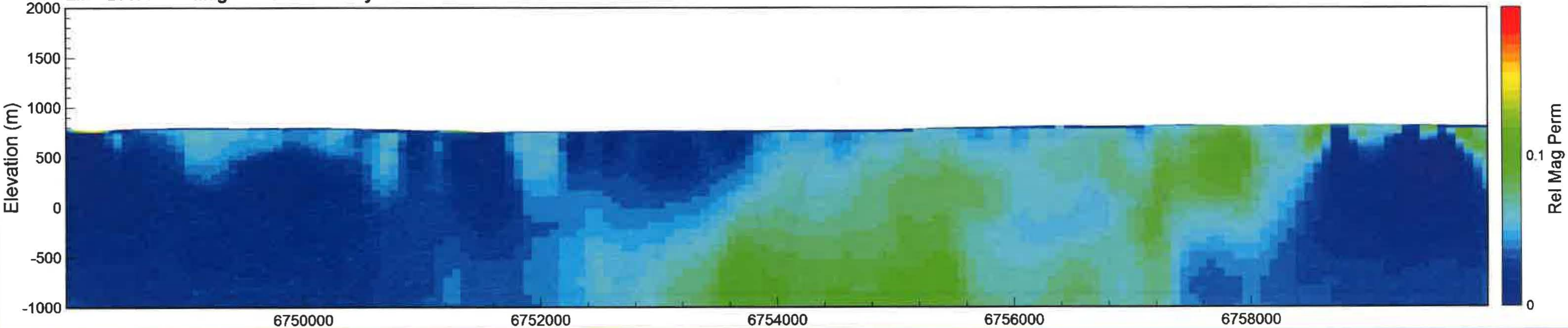

Line L1490 >>> Magnetic Permeability

Line L1500 >>> IP-6.6 kHz red; 980 Hz; green; 880 Hz; blue

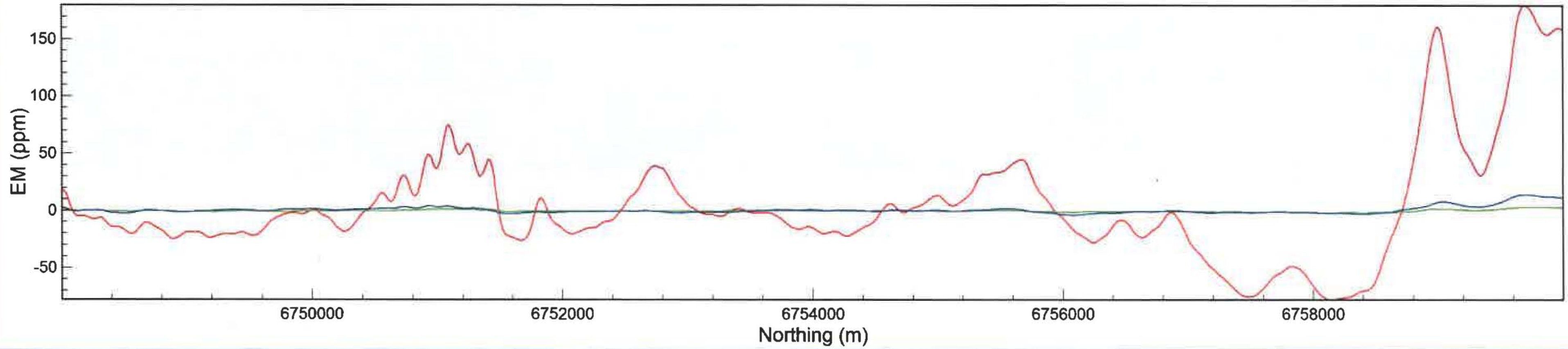

Line L1500 >>> LEI

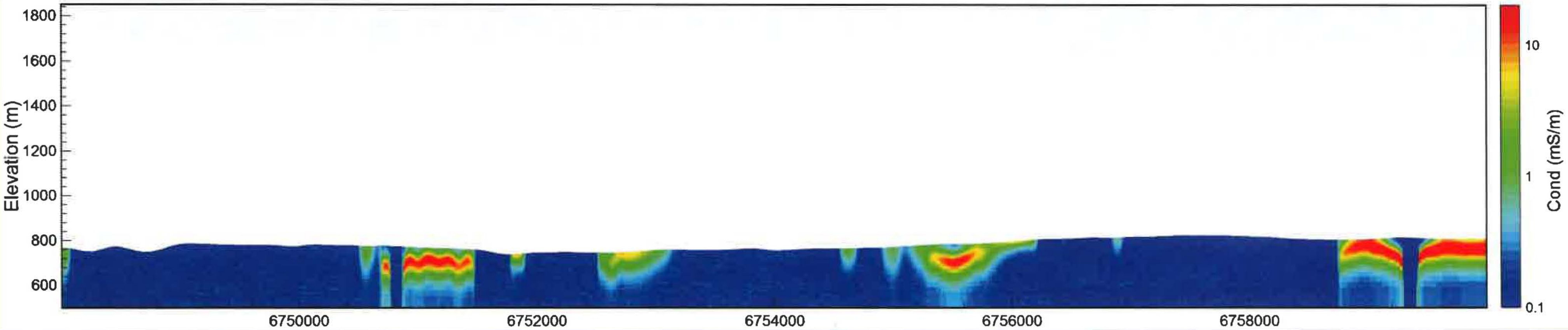

Line L1500 >>> Magnetic Permeability

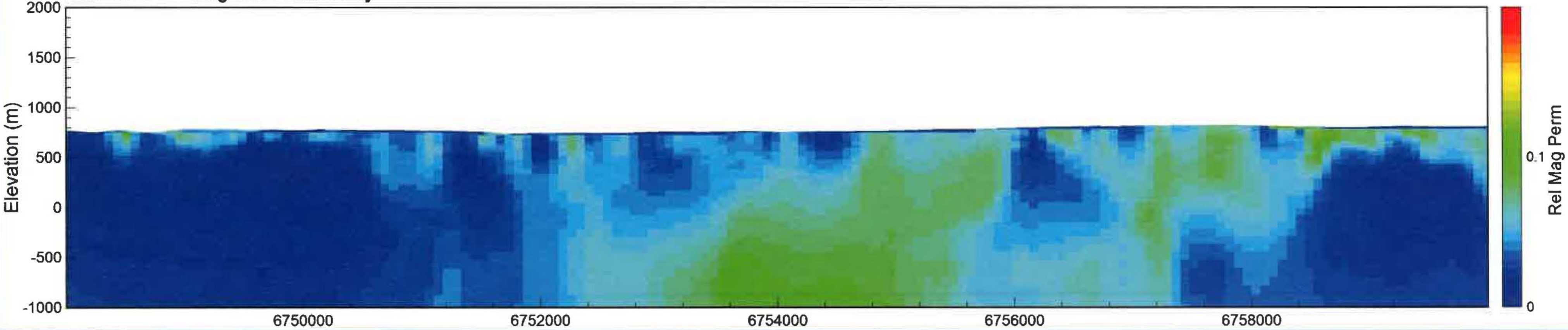

Line L1510 <<< IP-6.6 kHz red; 980 Hz; green; 880 Hz; blue

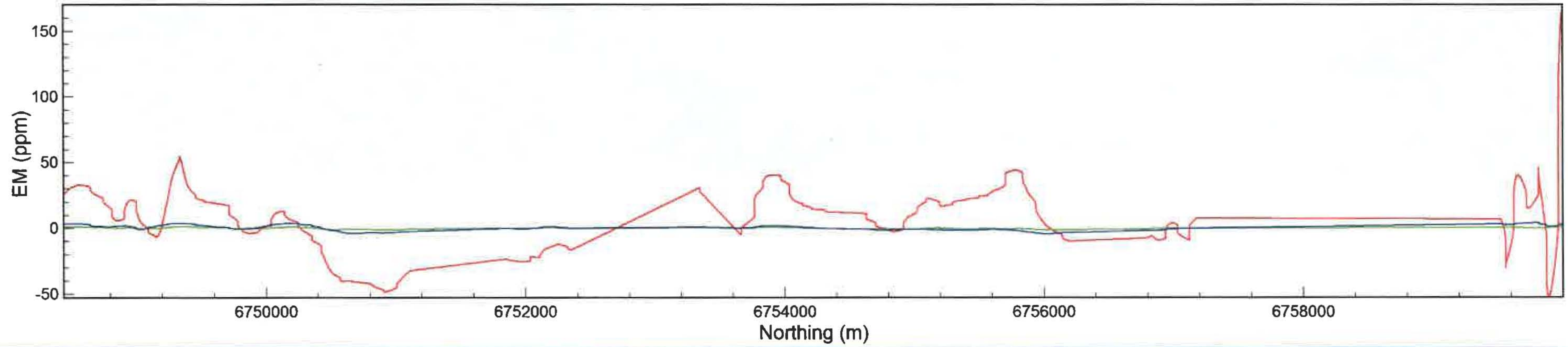

Line L1510 <<< LEI

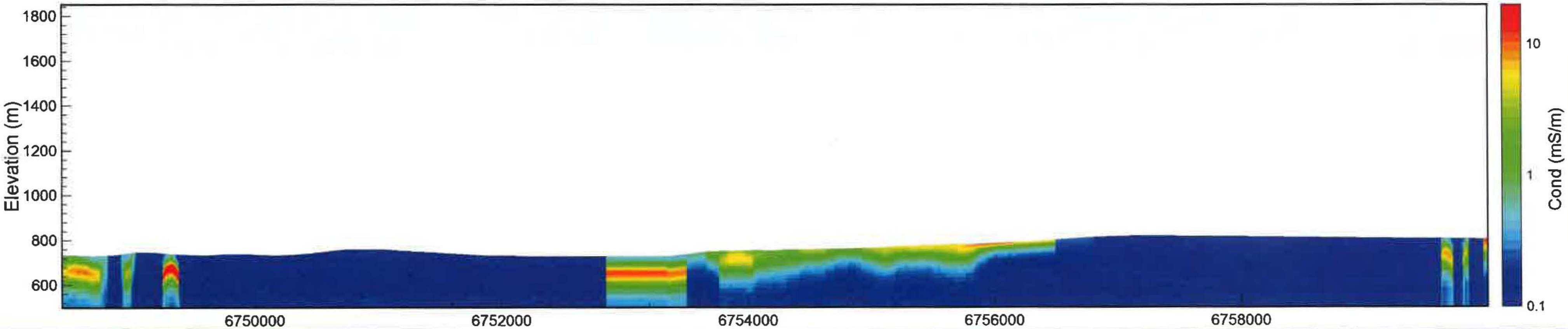

Line L1510 <<< Magnetic Permeability

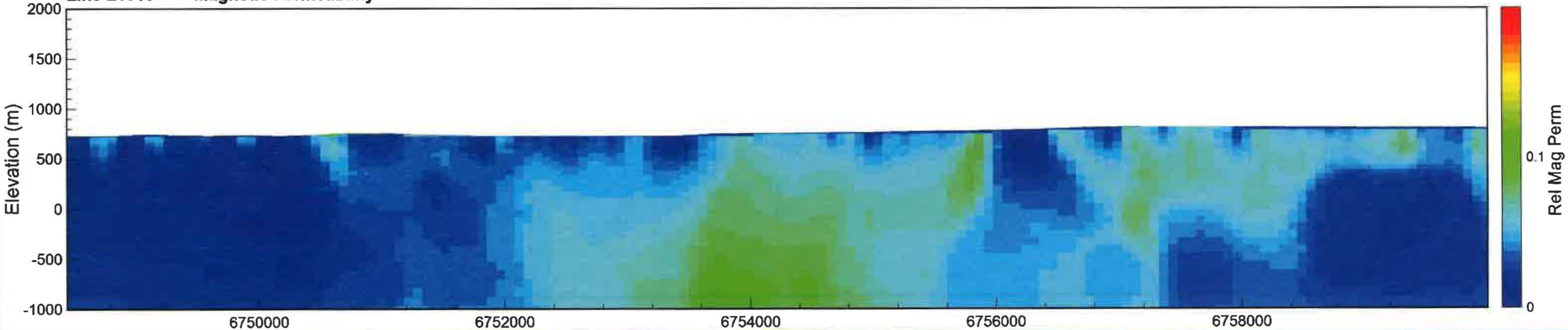

APPENDIX B Information on Data Processing

Magnetic Modeling in 3D

As part of Condor's *Tool Kit* approach to geophysical processing, we offer a suite of tools for the modeling magnetic data that allow us to draw upon the best solution to match each client's exploration problem.

QuickMag (ENCOM)

This application is a rapid means to undertake detailed modeling of complex discrete magnetic features such kimberlites or intrusives.

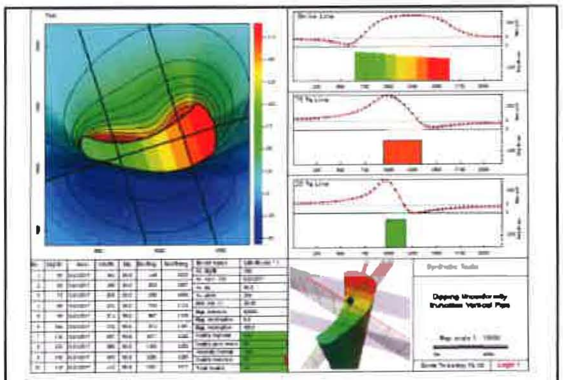

Keating Filter (GSC-GEOSOFT)

Designed initially by the GSC to allow for a rapid assessment of aeromagnetic data for kimberlites, Keating offers a very fast and robust means to assess even noisy magnetic data for circular intrusive bodies.

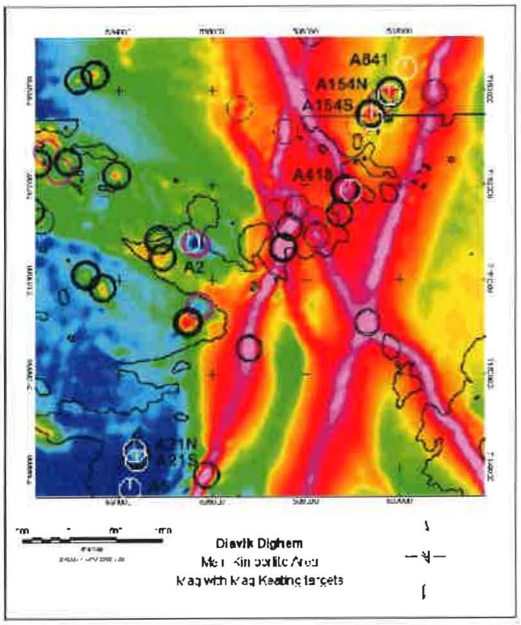

Model Vision Pro (ENCOM)

Model Vision is our work horse magnetic modeling program that allows for the rapid assessment of complex magnetic responses. Model Vision outcomes are often complementary to the more distributed voxel-style solutions of Mag3D and we frequently employ both approaches in order to full characterize the geometry of the magnetic data set.

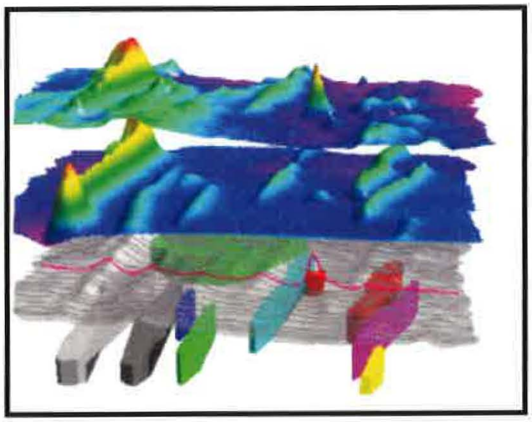

Mag3D

Also know as the UBC Mag3D, this code was developed in the 1990s by the University of British Colombia GIF team lead by Dr. Doug Oldenburg.

Mag3D provides for voxel-style model output to describe the distribution of susceptibility in the earth.

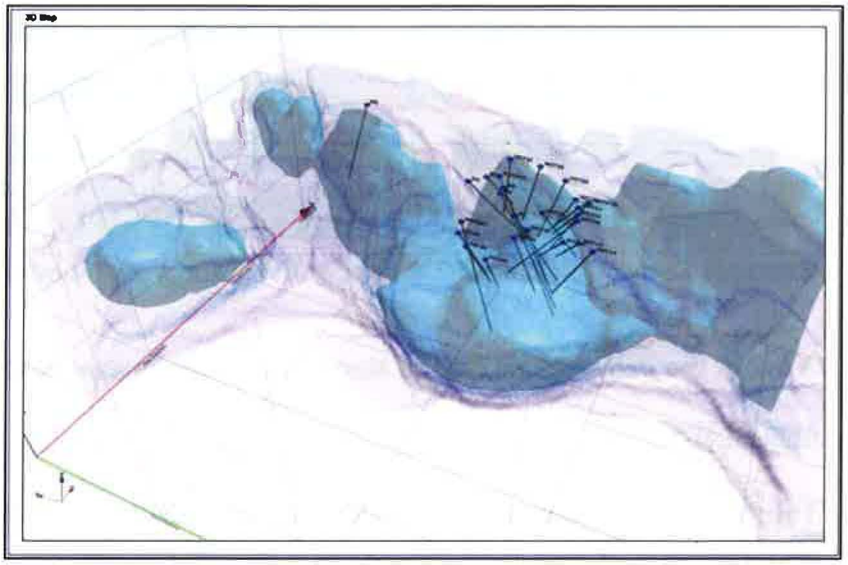

Cross-section of Mag3D model through layered intrusive

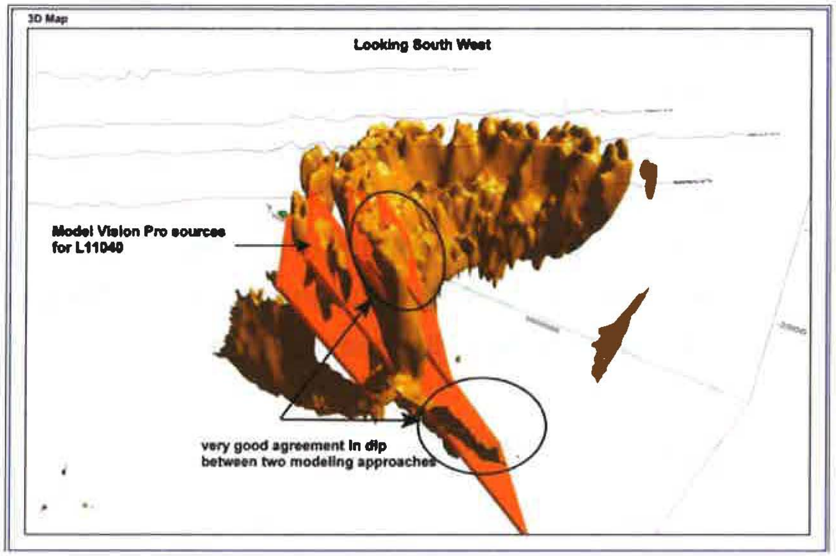

Example showing discrete body modeling (MVP) and Voxel model

Condor will work with our clients to produce the specific products that best highlight the outcomes of their 3D magnetic modeling including merging with client data, animations and export to other 3D graphics applications.

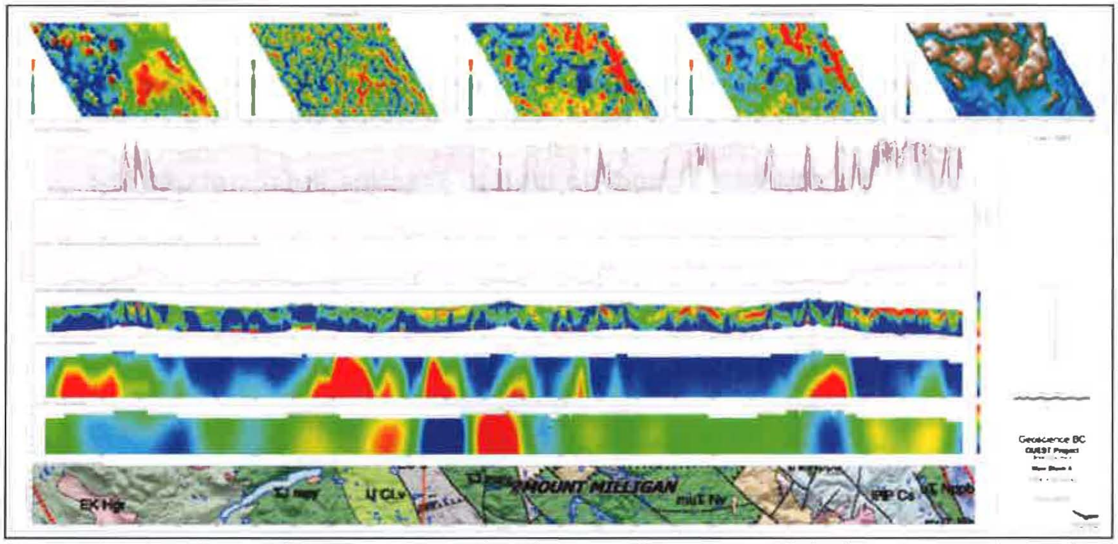

Example showing airborne EM conductivity and voxel models for mag and gravity.

A list of the deliverables for the Mag3D modeling is provided below.

<u>Mag3D Modeling</u>

The following products are provided as part of the Mag3D modeling. Some are stand-alone and some are imbedded with other products; the letters S and I are used to flag which; S= stand-alone and I =imbedded.

- **UBC mesh and sus files (S)**
- **Magnetic model X, Y and Z format (S)**
- **3D DXFs (S)**
- **Depth Slices: 50, 100 and 300 m (I-as TargetMaps)**
- **Depth Slices: 50, 100 and 300 m as Geosoft GRD files (S)**
- **Susceptibility Depth Section (I- in MultiPlots)**
- **AVI of model (S)**
- **Notes on processing (S)**

GEOPHYSICS, VOL. 61, NO. 2 (MARCH-APRIL 1996); P. 394-408, 18 FIGS.

3-D inversion of magnetic data

Yaoguo Li* and Douglas W. Oldenburg*

ABSTRACT

We present a method for inverting surface magnetic data to recover 3-D susceptibility models. To allow the maximum flexibility for the model to represent geologically realistic structures, we discretize the 3-D model region into a set of rectangular cells, each having a constant susceptibility. The number of cells is generally far greater than the number of the data available, and thus we solve an underdetermined problem. Solutions are obtained by minimizing a global objective function composed of the model objective function and data misfit. The algorithm can incorporate a priori information into the model objective function by using one or more appropriate weighting functions. The model for inversion can be either susceptibility or its logarithm. If susceptibility is chosen, a positivity constraint is imposed to reduce the nonuniqueness and to maintain physical realizability. Our algorithm assumes that there is no remanent magnetization and that the magnetic data are produced by induced magnetization only. All minimizations are carried out with a subspace approach where only a small number of search vectors is used at each iteration. This obviates the need to solve a large system of equations directly, and hence earth models with many cells can be solved on a deskside workstation. The algorithm is tested on synthetic examples and on a field data set.

INTRODUCTION

Magnetic surveying has been used widely over the years, resulting in a great amount of data with enormous areal coverage. Magnetic data have been used for mapping geological structures, especially in the reconnaissance stage of exploration, but when used in detailed prospecting, robust and efficient inversion algorithms must be used. However, a principal difficulty with the inversion of the potential data is the inherent nonuniqueness. By Gauss' theorem, if the field distribution is known only on a bounding surface, there are infinitely many equivalent source distributions inside the boundary that can produce the known field. Any magnetic field measured on the surface of the earth can be reproduced by an infinitesimally thin zone of magnetic dipoles beneath the surface. From a mathematical perspective, this means there is no depth resolution inherent in magnetic field data. A second source for nonuniqueness is the fact that magnetic observations are finite in number and are inaccurate. If there exists one model that reproduces the data, there are other models that will reproduce the data to the same degree of accuracy. The severity of the nonuniqueness problem for magnetic data is illustrated in Figures 1-3. (The gray scale in all figures indicates susceptibility in SI units for model sections and magnetic data in nT for data plots.) A 3-D dipping prism of uniform susceptibility in Figure 1 produces the surface magnetic field shown in Figure 2, which consists of 441 data. Slices of a 3-D susceptibility model that adequately reproduces the 441 data are shown in Figure 3. That result, however, bears little resemblance to the true model. Susceptibility is concentrated near the surface and displays zones of negative values. This mathematical model solution provides little information about the true structure that is useful.

Faced with this extreme nonuniqueness, previous authors have mainly taken two approaches in the inversion of magnetic data. The first is parametric inversion, where the parameters of a few geometrically simple bodies are sought in a nonlinear inversion and values are found by solving an overdetermined problem. This methodology is suited for anomalies known to be generated by simple causative bodies, but it requires a great deal of a priori knowledge about the source expressed in the form of an initial parameterization, an initial guess for parameter values, and limits on the susceptibility allowed (e.g., Bhattacharyya, 1980; Zeyen and Pous, 1991). Nonuniqueness is not generally an issue because only a small subset of possible models is considered due to the restrictive nature of the inversion algorithm. A related, but unique, approach in Wang and Hansen (1990) assumes polyhedronal causative bodies and

---

Presented at the 63rd Annual International Meeting, Society of Exploration Geophysicists. Manuscript received by the Editor May 2, 1994; revised manuscript received June 29, 1995.

*UBC-Geophysical Inversion Facility, Dept. of Geophysics and Astronomy, University of British Columbia, 129-2219 Main Mall, Vancouver, BC V6T 1Z4, Canada.

inverts for the position of the vertices of these bodies using the spectrum of the magnetic data. The method is general in principle but has difficulties both in constructing the causative bodies from the recovered vertices and in obtaining the susceptibility distribution.

In the second approach to inverting magnetic data, the earth is divided into a large number of cells of fixed size but of unknown susceptibility. Nonuniqueness of solution is recognized and the algorithm produces a single model by minimizing an objective function of the model subject to fitting the data. Green (1975) minimizes a weighted model norm with respect to a reference model, and this allows the interpreter to guide the inversion by varying the weighting according to the available information. Last and Kubik (1983) choose to minimize the total volume of the causative body so that the final model is compact and structurally simple. Guillen and Menichetti (1984) minimize the moment of inertia of the causative body with respect to the center of gravity or an axis passing through it. Their inversion result is guided by the estimate of the central depth and dip of the causative body. These approaches have merit but they are not flexible enough to handle problems we are concerned with. This is especially true of methods that attempt to collapse the anomalous susceptibility into a single body; such a solution is rarely an adequate representation of geologic structure.

In our inversion approach, we first make a decision about the variable in which the interpretation is to be made, that is, whether susceptibility, log susceptibility, or some function of susceptibility is sought. Next, we form a multicomponent objective function that has the flexibility to generate different types of models. The form of this objective function is such that it can correct for the undesirable aspects of the mathematically acceptable model in Figure 3, namely-the concentration of susceptibility near the surface, the excessive structure, and the existence of negative susceptibilities. Our objective function incorporates an optional reference model so that the constructed model is close to that. It penalizes roughness in three spatial directions, and it has a depth weighting designed to distribute the susceptibility with depth. Additional 3-D weighting functions in the objective function can be used to incorporate further information about the model. Such information might be available from other geophysical surveys, geological data, or the interpreter's qualitative or quantitative understanding of the geologic structure and its relation to the magnetic susceptibility. These 3-D weighting functions can also be used to answer questions about the existence of susceptibility features found from previous inversions. Negative susceptibilities are prevented by making a transformation of

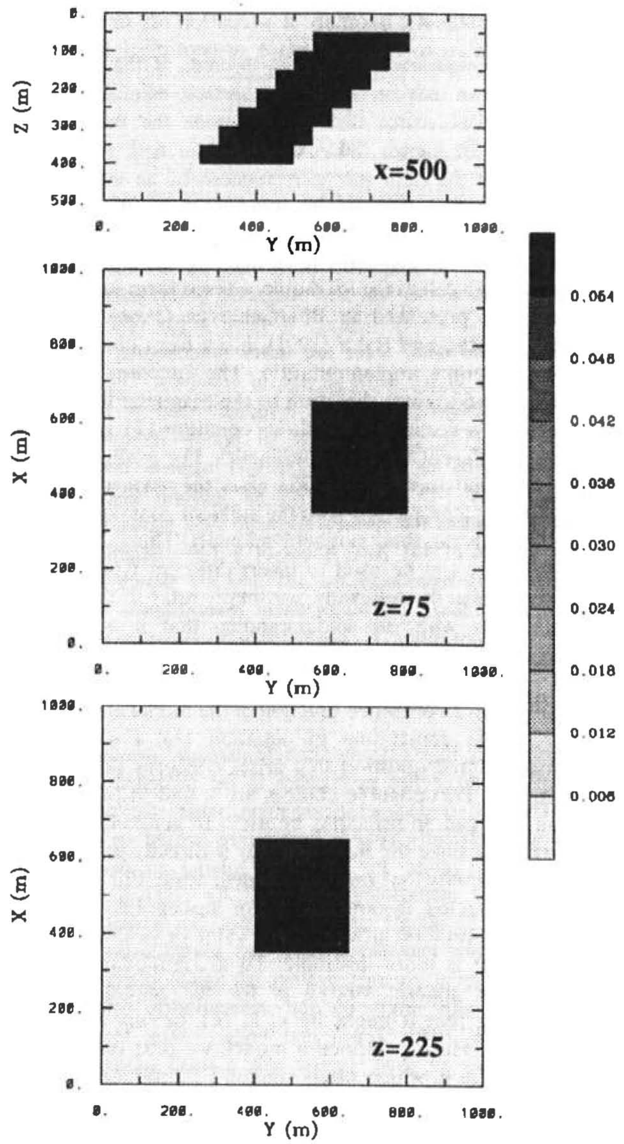

FIG. 1. Slices through a 3-D magnetic susceptibility model composed of a dipping slab in a nonsusceptible half-space. The slab is buried at a depth of 50 m and extends to 400-m depth at a dip angle of 45° . The gray scale indicates the value of magnetic susceptibility in SI units.

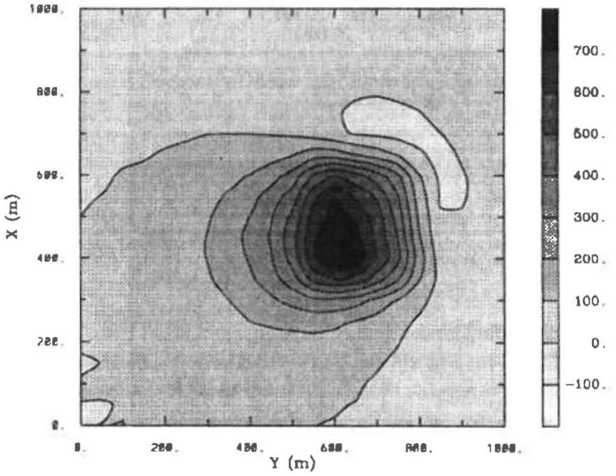

FIG. 2. The total field anomaly produced by the slab model in Figure 1. The inducing field has direction $I = 75°$ and $D = 25°$ and a strength of 50 000 nT. Uncorrelated Gaussian noise, with a standard deviation of 2% of the datum magnitude plus 1 nT, is added to the data. The gray scale indicates the magnetic anomaly in nT.

variables and solving a nonlinear inverse problem. The numerical solution for the inversion is accomplished by dividing the earth into a large number of cells so that relatively complex geologic bodies can be constructed. The computational difficulties often encountered in solving large matrix systems are avoided by working explicitly with a generalized subspace algorithm.

The paper begins by outlining our inversion methodology and empirically estimating parameters for the depth weighting based upon synthetic inversion of single 3-D prisms. Data from two synthetic models are then inverted. The paper concludes by inverting a field data set over a copper-gold porphyry deposit and a subsequent discussion.

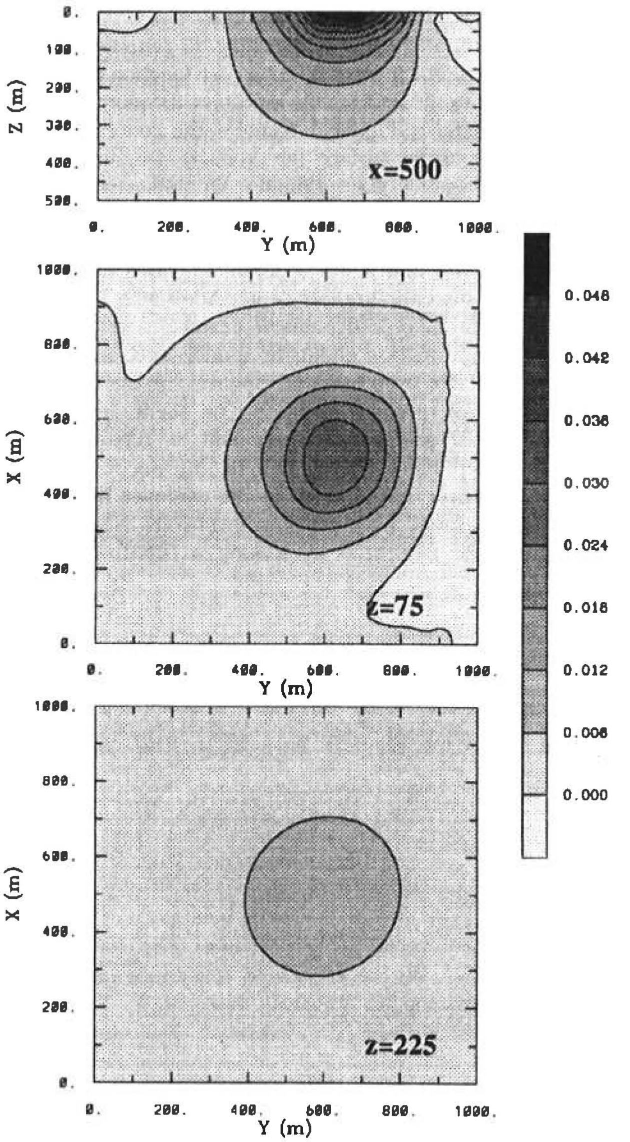

FIG. 3. The susceptibility model constructed by minimizing $\|\boldsymbol{\kappa}\|^2$ subject to fitting the data in Figure 2. As a mathematical solution, this model provides little, if any, information about the subsurface susceptibility distribution. It effectively illustrates the nonuniqueness inherent to the inversion of static magnetic field data.

INVERSION METHODOLOGY

Each magnetic anomaly datum observed above the surface can be evaluated by calculating the projection of the anomalous magnetic field onto a given direction. Let the source region be divided into a set of rectangular cells by an orthogonal 3-D mesh and assume a constant magnetic susceptibility value κ within each cell. Further we assume that there is no remanent magnetization and that the demagnetization effect is negligible. Thus only the induced magnetization is considered. This magnetization is uniform within each cell and is given by the product of the susceptibility and the inducing geomagnetic field $\underset{\sim}{\mathbf{H}}$. The magnetic anomaly at a location on, or above, the surface is related to the subsurface susceptibility by a linear relationship

$$\mathbf{d} = \underset{\sim}{\mathbf{G}}\boldsymbol{\kappa}, \tag{1}$$

where $\mathbf{d} = (d_1, \ldots, d_N)^T$ is the data vector and $\boldsymbol{\kappa} = (\kappa_1, \ldots, \kappa_M)^T$ is the susceptibility in the cells. The matrix $\underset{\sim}{\mathbf{G}}$ has as elements g_{ij}, which quantify the contribution of a unit susceptibility in thejth cell to the ith datum. Closed form solutions for g_{ij} were first presented in Bhattacharyya (1964) and later simplified in Rao and Babu (1991) into a form more suitable for fast computer implementation. The function g_{ij} is the projection onto a given direction of the magnetic field that is produced by a rectangular cell, so equation (1) is valid for computing different magnetic anomalies. For example, a projection onto the vertical direction gives the vertical magnetic anomaly while a projection onto the ambient geomagnetic field direction yields the total magnetic anomaly. Thus, the method presented here can be used to invert different types of magnetic data and in the following, we simply refer to them as the magnetic data with the understanding that it is direction specific.

Our inverse problem is formulated as an optimization problem where an objective function of the model is minimized subject to the constraints in equation (1). For magnetic inversion, the first question that arises concerns definition of the "model." Two possible choices are κ and $\ln(\kappa)$, but any function $g(\kappa)$ can, in principle, be used. In general, we prefer to invert for κ since the field anomaly is directly proportional to the susceptibility that varies on a linear scale. But depending upon the expected dynamic range of susceptibility and the physical interpretation attached to its value or variation, it may be that $\ln(\kappa)$ is more desirable. To accommodate this, we introduce the generic symbol m for the model with the understanding that it might be κ, $\ln(\kappa)$, or any monotonic function $g(\kappa)$. Having defined a model, we next construct an objective function, which when minimized, produces a model that is geophysically interpretable. The details of the objective function are problem dependent, but generally we need the flexibility to be close to a reference model m_0 and also require that the model be relatively smooth in three spatial directions. Here we adopt a right-handed Cartesian coordinate system with x positive north and z positive down. Let the model objective function be

$$\begin{aligned}\phi_m(m) = {} & \alpha_s \int_V w_s\{w(z)[m(\mathbf{r}) - m_0]\}^2\, dv \\ & + \alpha_x \int_V w_x \left\{\frac{\partial w(z)[m(\mathbf{r}) - m_0]}{\partial x}\right\}^2 dv \\ & + \alpha_y \int_V w_y \left\{\frac{\partial w(z)[m(\mathbf{r}) - m_0]}{\partial y}\right\}^2 dv \\ & + \alpha_z \int_V w_z \left\{\frac{\partial w(z)[m(\mathbf{r}) - m_0]}{\partial z}\right\}^2 dv, \end{aligned} \tag{2}$$

where functions w_s, w_x, w_y, and w_z are spatially dependent weighting functions while α_s, α_x, α_y, and α_z are coefficients that affect the relative importance of different components in the objective function. Here, $w(z)$ is a depth weighting function. It is convenient to write equation (2) as $\phi_m(m) = \phi_{ms} + \phi_{mv}$, where ϕ_{ms} refers to the first term in equation (2) and ϕ_{mv} refers collectively to the remaining three terms that involve variation of the model in three spatial directions.

The objective function in equation (2) has the flexibility of constructing many different models. The reference model m_0 may be a general background model that is estimated from previous investigations, or it could be the zero model. The reference model would generally be included in ϕ_{ms} but can be removed if desired from any of the remaining terms. Often we are more confident in specifying the value of the model at a particular point than in supplying an estimate of the gradient. The relative closeness of the final model to the reference model at any location is controlled by the function w,. For example, if the interpreter has high confidence in the reference model at a particular region, he or she can specify w_s to have increased amplitude there compared to other regions of the model. The weighting functions w_x, w_y, and w_z can be designed to enhance or attenuate structures in various regions in the model domain. If geology suggests a rapid transition zone in the model, then a decreased penalty for variation can be put there, and the constructed model will exhibit higher gradients provided that this feature does not contradict the data. Therefore, the reference model and four 3-D weighting functions allow for the incorporation into the inversion of additional information other than the magnetic data. The additional information can be from previous knowledge about the susceptibility, from other geophysical surveys, or from the interpreter's qualitative or quantitative understanding about the geologic structure and its relation to susceptibility. When this extra information is incorporated, the inversion derives a model that not only fits the data, but more importantly, also has a likelihood of representing the earth. From the viewpoint of magnetic inversion, such an approach allows one to construct a most-likely earth model that uses all available information, and it can also be used to explore the nonuniqueness. These two aspects form the foundation of a responsible interpretation.

The kernels (values of g_{ij}) for the surface magnetic data decay with depth. It is for this reason that an inversion that minimizes $\|m - m_0\|^2 = \int (m - m_0)^2\, dv$ subject to fitting the data will generate a susceptibility that is concentrated near the surface. To counteract the geometric decay of the kernels and to distribute susceptibility with depth, we introduce a weighting of the form $w(z) = (z + z_0)^{-\beta/2}$ into ϕ_{ms}, and optionally include it in ϕ_{mv}. The values of β and z_0 are investigated in the following section, but their choice essentially allows equal chance for cells at different depths to be nonzero.

The next step in setting up the inversion is to define a misfit measure. Here we use the 2-norm measure

$$\phi_d = \|\underline{\mathbf{W}}_d(\mathbf{d} - \mathbf{d}^{obs})\|_2^2, \tag{3}$$

and we assume that the contaminating noise on the data is independent and Gaussian with zero mean. Specifying $\underline{\mathbf{W}}_d$ to be a diagonal matrix whose ith element is $1/\sigma_i$ where σ_i is the standard deviation of the ith datum, makes ϕ_d a chi-squared variable distributed with N degrees of freedom. Accordingly $E[\chi^2] = N$ provides a target misfit for the inversion.

The inverse problem is solved by finding a model m that minimizes ϕ_m and misfits the data by a predetermined amount. This is accomplished by minimizing $\phi(m) = \phi_m + \lambda^{-1}(\phi_d - \phi_d^*)$, where ϕ_d^* is our target misfit and λ is a Lagrangian multiplier. To perform a numerical solution, we first discretize the objective function in equation (2) using a finite-difference approximation according to the mesh defining the susceptibility model. This yields

$$\begin{aligned}\phi_m(\mathbf{m}) &= \phi_{ms} + \phi_{mv} = (\mathbf{m} - \mathbf{m}_0)^T \underline{\mathbf{W}}_s^T \underline{\mathbf{W}}_s (\mathbf{m} - \mathbf{m}_0) + (\mathbf{m} - \mathbf{m}_0)^T (\underline{\mathbf{W}}_x^T \underline{\mathbf{W}}_x + \underline{\mathbf{W}}_y^T \underline{\mathbf{W}}_y + \underline{\mathbf{W}}_z^T \underline{\mathbf{W}}_z)(\mathbf{m} - \mathbf{m}_0) \\ &\equiv (\mathbf{m} - \mathbf{m}_0)^T \underline{\mathbf{W}}_m^T \underline{\mathbf{W}}_m (\mathbf{m} - \mathbf{m}_0) = \|\underline{\mathbf{W}}_m(\mathbf{m} - \mathbf{m}_0)\|^2, \end{aligned} \tag{4}$$

where $\mathbf{m}$ and $\mathbf{m}_0$ are M- length vectors. The individual matrices $\underline{\mathbf{W}}_s$, $\underline{\mathbf{W}}_x$, $\underline{\mathbf{W}}_y$, $\underline{\mathbf{W}}_z$ are calculated straightforwardly once the model mesh and the weighting functions w_s, w_x, w_y, w_z, and $w(z)$ are defined (see Appendix). The cumulative matrix $\underline{\mathbf{W}}_m^T \underline{\mathbf{W}}_m$ is then formed. For our formulation, the matrix $\underline{\mathbf{W}}_m$ is never computed explicitly but we shall use it to derive our final equations.

The inverse problem is solved by minimizing $\phi(\mathbf{m})$ with an appropriate minimization technique. To reduce computation and to invoke positivity, we use a subspace methodology. In its general form, the subspace technique allows the model parameter to be both positive and negative, and thus to ensure positive susceptibility, we may need to invoke a transformation of variables. Whether or not the transformation is required depends upon the relationship between m_i and κ_i. If $m_i = \ln(\kappa_i)$, so that interpretations are carried out in the logarithmic domain, then no further transformation is necessary since κ_i will be positive irrespective of the sign of m_i. However, if $m_i = \kappa_i$, or $m_i = g(\kappa_i)$, and $g(\kappa)$ is a positive function, then a transformation is required. All possibilities can be handled by introducing a new parameter p, such that $m_i = f(p_i)$, where $f(p)$ is a monotonic function whose inverse and first-order derivative exist. This mapping is then incorporated directly into the subspace minimization process.

Let $\mathbf{p}^{(n)}$ denote the parameter vector at the nth iteration and δp denote the sought perturbation. Performing a Taylor expansion of the perturbed model objective function about the point $\mathbf{p}^{(n)}$ yields

$$\phi_m(\mathbf{p}^{(n)} + \delta p) = \|\underset{\sim}{\mathbf{W}}_m \underset{\sim}{\mathbf{F}} \delta p + \underset{\sim}{\mathbf{W}}_m(\mathbf{m}^{(n)} - \mathbf{m}_0)\|^2, \tag{5}$$

where $\underset{\sim}{\mathbf{F}}$ is a diagonal matrix with elements

$$F_{ii} = \left.\frac{\partial f_i}{\partial p_i}\right|_{p^{(n)}} = \left.\frac{\partial m_i}{\partial p_i}\right|_{p^{(n)}}. \tag{6}$$

A similar Taylor expansion applied to the misfit objective functional $\phi_d(\mathbf{p}^{(n)} + \delta p)$ yields

$$\phi_d = \|\underset{\sim}{\mathbf{W}}_d \underset{\sim}{\mathbf{G}} \underset{\sim}{\mathbf{F}} \delta p + \underset{\sim}{\mathbf{W}}_d(\mathbf{d}(\mathbf{p}^{(n)}) - \mathbf{d}^{obs})\|^2. \tag{7}$$

At each iteration we desire a perturbation that minimizes equation (4) subject to generating a data misfit of $\phi_d = \phi_d^{*(n)}$, where $\phi_d^{*(n)}$ is the target misfit at the nth iteration. In the subspace technique we represent the perturbation as

$$\delta p = \sum_{i=1}^{q} \alpha_i \mathbf{v}_i \equiv \underset{\sim}{\mathbf{V}} \boldsymbol{\alpha}, \tag{8}$$

where the M-length vectors $\mathbf{v}_i$ $(i = 1, q)$ are as yet arbitrary. Writing the objective function to be minimized in terms of the coefficients $\boldsymbol{\alpha}$ yields

$$\begin{aligned}\phi(\boldsymbol{\alpha}) = {} & \|\underset{\sim}{\mathbf{W}}_m \underset{\sim}{\mathbf{F}} \underset{\sim}{\mathbf{V}} \boldsymbol{\alpha} + \underset{\sim}{\mathbf{W}}_m(\mathbf{m}^{(n)} - \mathbf{m}_0)\|^2 \\ & + \lambda^{-1}(\|\underset{\sim}{\mathbf{W}}_d \underset{\sim}{\mathbf{G}} \underset{\sim}{\mathbf{F}} \underset{\sim}{\mathbf{V}} \boldsymbol{\alpha} + \underset{\sim}{\mathbf{W}}_d(\mathbf{d}(\mathbf{p}^{(n)}) - \mathbf{d}^{obs})\|^2 - \phi_d^*).\end{aligned} \tag{9}$$

Differentiating with respect to the coefficients a yields the final equations

$$\begin{aligned}\underset{\sim}{\mathbf{B}} \boldsymbol{\alpha} &= \mathbf{b}, \\ \underset{\sim}{\mathbf{B}} &= \underset{\sim}{\mathbf{V}}^T \underset{\sim}{\mathbf{F}}^T(\underset{\sim}{\mathbf{G}}^T \underset{\sim}{\mathbf{W}}_d^T \underset{\sim}{\mathbf{W}}_d \underset{\sim}{\mathbf{G}} + \lambda \underset{\sim}{\mathbf{W}}_m^T \underset{\sim}{\mathbf{W}}_m) \underset{\sim}{\mathbf{F}} \underset{\sim}{\mathbf{V}}, \\ \mathbf{b} &= -\underset{\sim}{\mathbf{V}}^T \underset{\sim}{\mathbf{F}}^T \underset{\sim}{\mathbf{G}}^T \underset{\sim}{\mathbf{W}}_d^T \underset{\sim}{\mathbf{W}}_d(\mathbf{d}^{(n)} - \mathbf{d}^{obs}) \\ &\quad - \lambda \underset{\sim}{\mathbf{V}}^T \underset{\sim}{\mathbf{F}}^T \underset{\sim}{\mathbf{W}}_m^T \underset{\sim}{\mathbf{W}}_m(\mathbf{m}^{(n)} - \mathbf{m}_0).\end{aligned} \tag{10}$$

We note that the matrix $\underset{\sim}{\mathbf{B}}$ is q x q and therefore the system of equations is easily solved if q is small. At each iteration, we search for a value of λ that yields the target misfit for that iteration. If the target misfit cannot be reached, then the value of λ that achieves the smallest misfit is taken. The search is usually accomplished by solving equation (10) a number of times using different λ values. Once the optimum value of λ is found, the system is solved again to obtain the coefficients $\boldsymbol{\alpha}$ and the model perturbation. This iterative process is continued until the final expected data misfit is achieved and the model objective function undergoes no significant decrease with successive iterations. Subspace vectors $\mathbf{v}_i$ are generated mainly from the gradients of the data and model objective functions. The data are grouped to form subobjective functions of misfit, and a steepest descent vector corresponding to each subobjective function is used as a subspace vector. Partitioning of the data can be formed by grouping data that are spatially close, or by grouping data such that each group has approximately the same contribution to the total data misfit. Both approaches have worked well. The model objective function is partitioned and the gradient vector associated with each of the four components in the model objective function provides additional subspace vectors. In addition, a constant vector is always included, and the selected subspace vectors are orthonormalized before being used in the search. More details on the implementation of the subspace method for the linear inverse problem can be found in Oldenburg and Li (1994).

The final item of practical importance is the specification of the mapping needed to ensure positivity of susceptibility. The positivity is required since we are dealing only with induced magnetization, and the presence of negative susceptibility is negligible in practical geophysical applications. Although our formalism permits the minimization of $m = g(\kappa)$, the two most common situations are $m = \ln(\kappa)$ and $m = \kappa$. When $m = \ln(\kappa)$, we set $p = m$ and hence the matrix $\underset{\sim}{\mathbf{F}}$ in equation (10) is the identity matrix. If $m = \kappa$, we use the two-stage mapping proposed in Oldenburg and Li (1994). It is composed of an exponential segment and a straight line. The two segments are joined together such that the mapping and its first derivative are both continuous. The mapping is given by

$$\kappa = \begin{cases} 0 & p < p_b \\ e^p - \kappa_b & p_b \le p \le p_1, \\ (p - p_1 + 1)e^{p_1} - \kappa_b & p > p_1 \end{cases} \tag{11}$$

where $p = p_1$ is the transition point between exponential and linear segments, and κ_b is selected to be small enough such that susceptibilities smaller than κ_b are not significantly different from zero when the final interpretation is carried out. Here, κ_1 and hence p_1 are chosen so that the ratio $(\kappa_1 + \kappa_b)/\kappa_b$ does not exceed about two orders of magnitude. This prevents the elements F_{ii} from becoming too disparate. We note that the ith row of $\underset{\sim}{\mathbf{V}}$ is multiplied by F_{ii}, and if this value is too small, the ith row of $\underset{\sim}{\mathbf{V}}$ is essentially annihilated and there will be no possibility of adjusting the value of the ith cell. However, if the ratio is too small, the flexibility in the mapping will be restricted and this affects the convergence rate of the algorithm. In the limit that $\kappa_b \rightarrow \kappa_1$, the nonlinear mapping degenerates into a linear truncation and the inversion will not converge. However, between the above two extremes, there is a wide range of values for the ratio that can yield a good mapping. Based upon numerical experiments (Oldenburg and Li, 1994), we have chosen a value of 50.0 for this ratio for the examples throughout this paper.

DEPTH WEIGHTING

It is well known that static magnetic data have no inherent depth resolution. For instance, when minimizing $\|m\|_2^2 = \int m^2\, dv$, structures tend to concentrate near the surface regardless of the true depth of the causative bodies. In terms of model construction, this is a direct manifestation of the nature of the kernels whose amplitudes rapidly diminish with depth. The tendency to put structure at the surface can be overcome by introducing a depth weighting to counteract this natural decay. Intuitively, a weighting that approximately compensates for the decay gives cells at different depths equal probability to enter into the solution with a nonzero susceptibility. Before proceeding with the details of the weighting function for magnetic inversion, we illustrate the necessity, and effectiveness, of such a weighting function using a simple 1-D problem.

Consider a set of data $\mathbf{d} = (d_1, , \ldots, d_N)^T$ generated from the equation

$$d_i = \int_0^1 g_i(z) m(z)\, dz, \qquad i = 0, \ldots, N, \tag{12}$$

where the kernels are

$$g_i(z) = e^{-az} \cos(2\pi i z).$$

The decay factor e^{-az} causes the constructed model m,(z) to have structure concentrating toward the region of small z in the classic model construction that minimizes $\|m\|^2$, since the model will be a linear combination of the kernels, i.e.,

$$m_c(z) = \sum_{i=0}^{N} \alpha_i e^{-az} \cos(2\pi i z). \tag{13}$$

This is shown in Figure 4a and 4b for two different models. These models are constructed from five data (i = 0,4) to which noise has been added. It is apparent that the constructed model is shifted toward small z where the amplitude of kernels is relatively large. One way to counteract the bias is to seek a solution in model space that is spanned by the nondecaying portion of the kernels, in this case just the cosine functions. The desired model would have the form

$$m_c(z) = \sum_{i=0}^{N} \tilde{\alpha}_i \cos(2\pi i z), \tag{14}$$

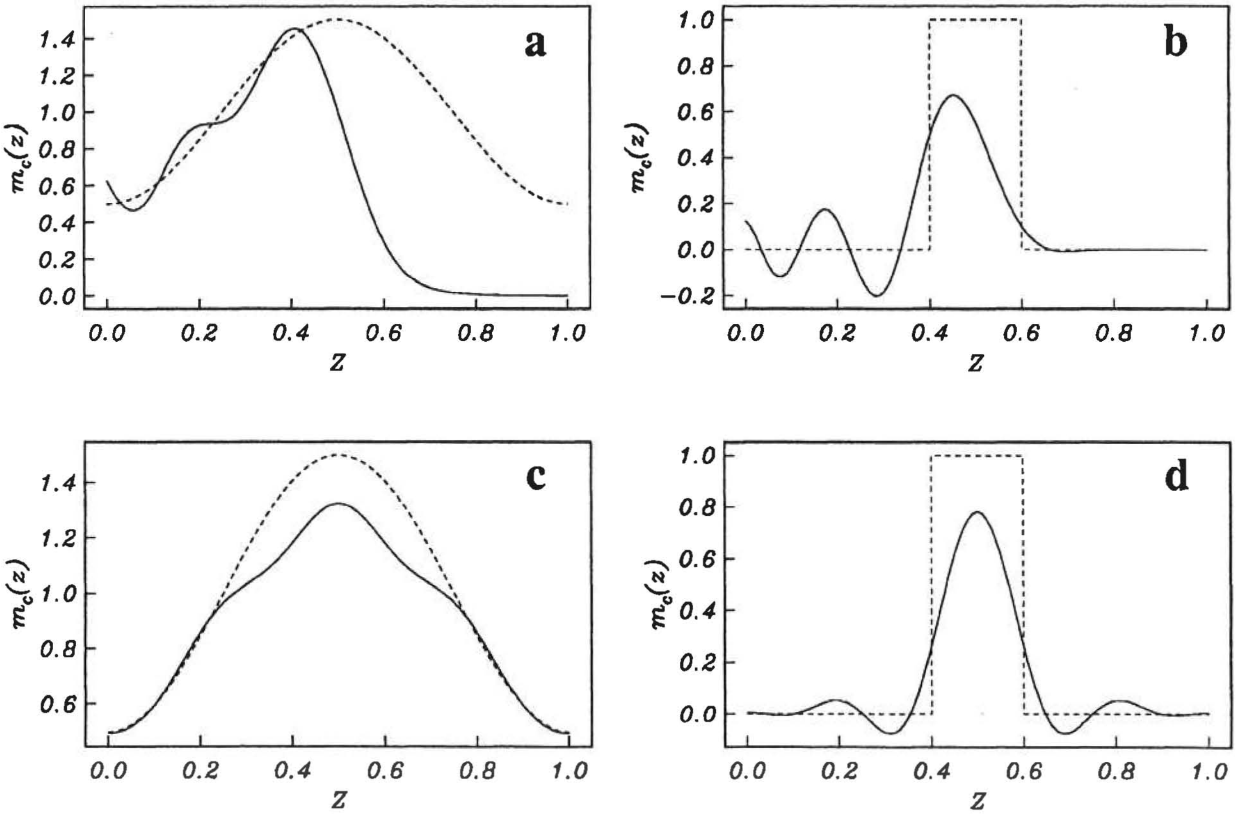

FIG. 4. A 1-D example showing the use of a weighting function in the inversion procedures to counteract the natural decay in the kernel function. In all panels the dashed line shows the true model. Panels (a) and (b) show, for the two different true models, respectively, the model constructed using the original kernel functions with the decaying factor e^{-az}. Notice the shift of the recovered model towards the small z region. Panels (c) and (d) show the weighted models recovered by applying a weighting function $w(z) = e^{az/2}$. They are better representations of the true model.

where $\tilde{\alpha}_i$ are coefficients. Free from the influence from the decay factor, a model constructed from this set of basic functions should have a better chance of having significantly high values at depth.

We accomplish this by finding an appropriate weighting function $w(z)$. We first rewrite the data equation as

$$d_i = \int_0^1 \frac{g_i(z)}{w(z)} * w(z)m(z)\,dv \equiv \int_0^1 g_i^w(z)m^w(z)\,dv, \quad (15)$$

where $g_i^w(z)$ are the weighted kernels and $m^w(z)$ is the weighted model. Then the inverse problem is solved by minimizing $\|m^w(z)\|^2$ and the solution is given by

$$m_c^w(z) = \sum_{i=0}^{N} \tilde{\alpha}_i g_i^w(z). \quad (16)$$

Dividing $m_c^w(z)$ by the weighting function and substituting in $g_i^w(z)$ yields

$$m_c(z) = \sum_{i=0}^{N} \tilde{\alpha}_i \frac{g_i(z)}{w^2(z)} = \sum_{i=0}^{N} \tilde{\alpha}_i \frac{e^{-az} \cos(2\pi i z)}{w^2(z)}. \quad (17)$$

This equation can be made identical to equation (14) by choosing $w(z) = e^{-az/2}$. Carrying out the weighted inversion for the above two data sets produces models shown in Figures 4c and 4d. They are much better representations of true models.

This methodology is then applied to the inversion of surface magnetic data by finding the appropriate weighting function that counteracts the depth decay of the data kernels. There is no distinct separable factor defining the decay in the kernel, therefore we resort to an empirical estimate. Since the decay rate depends upon the observation height as well as the size and aspect ratios of the cells making up the 3-D model, such estimates are expected to be problem dependent. Numerical experiments indicate that the function of the form $(z + z_0)^{-3}$ closely approximates the kernel's decay directly under the observation point, given a correctly chosen value of z_0. This is consistent with the fact that, to first order, a cubic-shaped cell acts like a dipole source whose magnetic field decays by inverse distance cubed. The value of z_0 can be obtained by matching the function $(z + z_0)^{-3}$ with the kernel function beneath the observation point. Thus, a reasonable candidate for the depth weighting function is given by

$$w(z) = \frac{1}{(z + z_0)^{3/2}}. \quad (18)$$

The susceptibility model constructed by minimizing a model objective function consisting of only ϕ_{ms}, i.e.,

$$\phi_m(m) = \int_V (w(z)m(x, y, z))^2\,dv, \quad (19)$$

subject to fitting the data should place the recovered anomaly at approximately the depth of the causative body. This hypothesis is tested by inverting surface data produced by a susceptible cubic body at three different, depths. The cube is 200 m on a side. Data are calculated over a 21 X 21 grid of 50-m spacing in both directions, and 2% Gaussian noise is then added. The observation is assumed to be 1 m above the surface and the inducing field has $I = 75°$, $D = 25°$. The region directly beneath the data grid is taken as the model domain and discretized into 4000 cells (20 cells in each horizontal direction and 10 along depth) of 50 m on a side.

Given the stated data parameters and model discretization, the estimated value of z_0 in the depth weighting function is 25 m. Figure 5 shows the comparison of the kernel beneath a datum point and the function $w^2(z)$. This weighting function is used to invert surface data caused by the susceptible prism, and the results of minimizing ϕ_{ms} are shown in Figure 6. Each panel in the figure is the cross-section through the center of the model obtained by inverting the data set produced by a cube at a different depth. They are rather good recoveries in terms of source depth, which is indicated by the superimposed outline of the true body in each section.

In the above analysis we have established a practical way for estimating an appropriate depth weighting function that distributes the susceptibility more uniformly with depth. The weighting is valid when the model objective function consists only of ϕ_{ms}. In general, we like to include a penalty against roughness and thereby produce a model that is smooth. To incorporate the above weighting scheme in the spatial variations, we make the following argument. Since minimizing ϕ_{ms} tends to provide a reasonable depth distribution, we wish only to improve the model's smoothness while maintaining the depth characteristic. A conceptually consistent approach would be to apply the roughness measures to the weighted model. We form a generic model objective function

$$\phi_m(m) = \alpha_s \int_V w_s\{w(z)[m(\mathbf{r}) - m_0]\}^2\,dv$$
$$+ \alpha_x \int_V w_x \left\{\frac{\partial w(z)[m(\mathbf{r}) - m_0]}{\partial x}\right\}^2 dv$$
$$+ \alpha_y \int_V w_y \left\{\frac{\partial w(z)[m(\mathbf{r}) - m_0]}{\partial y}\right\}^2 dv$$

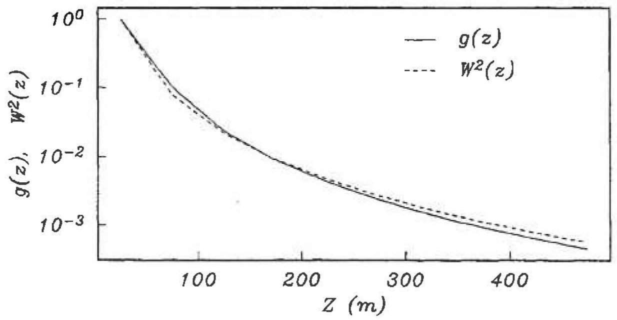

FIG. 5. Comparison of the kernel function (solid) directly beneath the observation point with the estimated curve (dashed) given by $w^2(z) = (z + z_0)^{-3}$ with $z_0 = 25$ m. The source cell is a cube of 50 m on a side. Here, z denotes the depth to the center of the cell. Both curves are normalized for comparison.

$$+ \alpha_z \int_V w_z \left\{ \frac{\partial w(z)[m(\mathbf{r}) - m_0]}{\partial z} \right\}^2 dv, \qquad (20)$$

where the depth weighting is applied inside the derivatives of the roughness components and the reference model m_0 can be removed from any term if desired. This type of depth weighting has proven to work satisfactorily on a number of synthetic examples and is the default choice in our algorithm. The examples to be presented in the following sections all use this depth weighting function.

Before proceeding further, we remark that the above weighting represents only one possibility. One could potentially design a different weighting by incorporating the depth weighting in the usual 3-D weighting functions w_s, w_x, w_y, w_z. Such an approach applies the depth weighting outside the derivative operators directly. However, the decay rate of the depth weighting for each component will be different, and it is difficult to establish a consistent rule for the choice of the different weightings. In addition, the extra set of parameters required by such a weighting scheme introduces more subjectivity into the inversion process. We have not explored this approach in detail; however, it is observed that straightforward inclusion of the depth weighting derived above into the 3-D weighting function in the form of $\int_V w_z w^2(z)\{\partial[m(\mathbf{r}) - m_0]/\partial z\}^2\, dv$ can yield reasonable results.

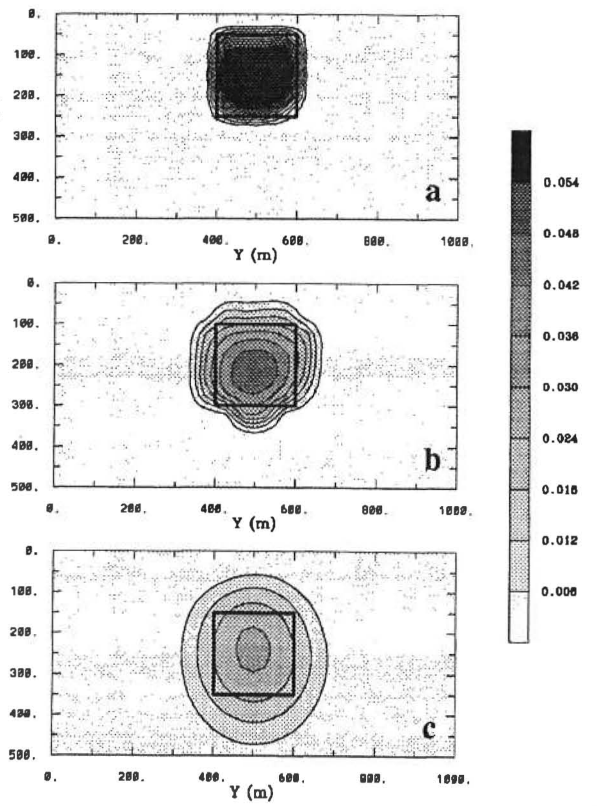

FIG. 6. Cross-sections through the center of the recovered model for a cube at a central depth of 150,200, and 250 m. The cube is 200 m on a side. The inversion uses the weighting function derived from the kernel decay estimated in Figure 5. The true position of the cube is outlined in each cross-section. As the true source depth increases and, as a result, the high-frequency content in the data decreases, the recovered model becomes increasingly smooth and attains a smaller amplitude. However, the depth of the recovered model is close to the true value.

PRACTICAL ASPECTS OF DATA PREPARATION

The data used in the inversion are the residual data obtained by subtracting a regional field from the initial observation. The inversion algorithm has been developed under the assumptions that the surface magnetic anomaly is produced by the induced magnetization only and that there are no remanent magnetization or demagnetization effects present. Incorrect removal of regional field, or any deviation from the above assumptions, is expected to cause a deterioration in the inversion results. Furthermore, the susceptibility distribution is mathematically represented by a piece-wise constant function defined on a user-specified grid of cells. Magnetic sources, however, have a wide range of physical sizes. In some cases, source dimensions will be significantly smaller than the size of cells in the mathematical model. If measurements are taken close to such a source, the resulting anomaly will have a width that is significantly smaller than that produced by a single cell in the mathematical model and this may produce artifacts. We ameliorate this problem by inverting data that have been upward continued to a height approximately equal to the width of the surface cells in the model. We arrive at this conclusion from a numerical experiment. We first generate the magnetic field H_ℓ from a small localized surface source that is assumed to be a cube of width ℓ. At each height h above the surface, a one-parameter inverse problem is carried out to find a uniform susceptibility of a large surface cube that has a width of L and shares a common horizontal center with the small cube. If H_L is the field of the large cell that best reproduces H_ℓ then the misfit functional,

$$r(h) = \frac{\int_{\Delta S} (H_\ell - H_L)^2\, ds}{\int_{\Delta S} H_\ell^2\, ds}, \qquad (21)$$

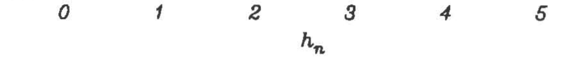

FIG. 7. The misfit between magnetic field as a result of a small cubic source and the field as a result of a larger cubic model cell having a best fitting susceptibility. The numbers indicate the ratio of the cell width. The misfit is plotted as a function of the observation height normalized by the width of the model cell. Note that the misfit decreases rapidly until the height is approximately equal to the width of the model cell, and that it changes slowly thereafter.

can be computed, where ΔS is the surface area of the data map. Figure 7 shows the misfit function $r(h)$ for trial values of $\ell/L = 0.1, 0.2, 0.4$. We note that $r(h)$ decreases rapidly until $h \approx L$, and that it changes slowly thereafter. Since the above misfit analysis is a worst case scenario because the contaminating body is located at the surface, the suggestion of upward continuing the data to a height approximately equal to the width of surface cells may be somewhat conservative, and inversionists may want to vary this. However, in many field surveys, magnetically susceptible small bodies exist close to the surface and hence upward continuing the data prior to inversion is prudent.

SYNTHETIC EXAMPLES

As the first example, we invert the total field anomaly data given in the Introduction. The model consists of a 3-D dipping slab buried in a nonsusceptible half-space (slab model). Figure 1 shows three slices through the slab model. The susceptibility of the slab is 0.06 (SI unit). Under an inducing field with a strength of 50 000 nT and a direction at $I = 75°$ and $D = 25°$, the slab model produces the surface total magnetic anomaly shown in Figure 2, which consists of 441 data over a 21 **X** 21 grid of 50-m spacing. The data have independent Gaussian noise added whose standard deviation is equal to 2% of the accurate datum magnitude plus 1 nT. We invert these 441 noise-contaminated data to recover the susceptibility of an earth model parametrized by 4000 cells of 50 m on a side (20 cells in each horizontal direction and 10 in depth).

The data are partitioned into 49 groups to provide 49 search vectors for the subspace algorithm. In addition, each component in the model objective function provides one basis vector, and a constant vector is included. For the depth weighting, the value of z_0 is estimated as 25 m. The additional 3-D weightings in the objective function are all set to unity. The reference susceptibility model is set to zero. For the nonlinear mapping, we choose $\kappa_b = 0.0002$ and $\kappa_1 = 0.01$.

First, we invert the data by minimizing an objective function composed only of the ϕ_{ms} and using $m = \kappa$ as the model parameter. A total of 51 subspace vectors are used at each iteration. The inversion reaches the expected misfit in 13 iterations but a few extra iterations are performed in an attempt to further reduce the value of the model objective function while keeping the misfit at the target value. By iteration 18, the objective function is decreasing by less than 1% per iteration, and the process is terminated. The constructed susceptibility model is shown in Figure 8 and can be compared with the true model in Figure 1. The tabular shape of the anomaly and its dipping structure are clear, and the depth extent is reasonably recovered. The amplitude of the recovered model is slightly higher than the true value, but the dip angle inferred from the recovered model is close to the true value. We point out that the model sections should be plotted using gray shading for each cell to reflect the piece-wise constant nature of the model. However, when the model has only a small number of cells in each spatial direction, the structural trends are more readily shown when contours are used. For this reason, we have contoured the model sections.

Next, the same data are inverted using a model objective function that includes penalty terms on spatial roughness, ϕ_{mv}. The depth weighting is applied to all terms, as in equation (20). The inversion uses 54 subspace vectors and achieves the expected misfit in 13 iterations. The recovered model is shown in Figure 9. It is smoother, has a slightly lower amplitude than the model in Figure 8, and it recovers the essential features of the true model such as the depth and dip angle.

It is observed, in this example and in other synthetic and field test examples, that minimizing either the first term in the model objective function in equation (20), ϕ_{ms}, or using all four terms, generates models that are reasonable representations of the true structure. In the absence of prior information, both models can provide useful information about the subsurface susceptibility distribution. However, the model minimizing ϕ_{ms} can be obtained at less computational cost. Further-

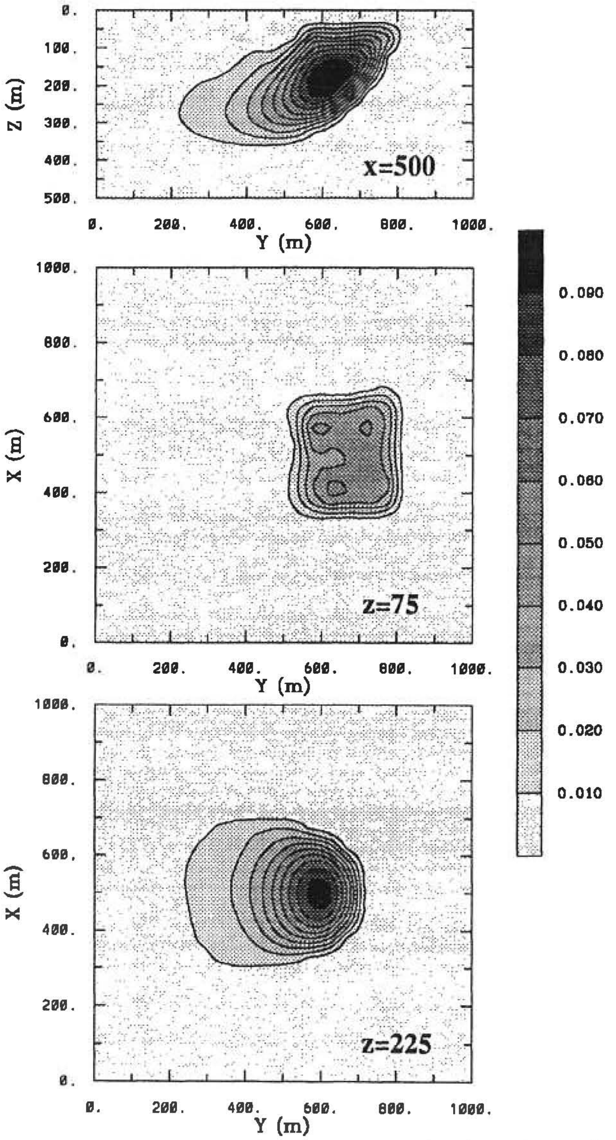

FIG. 8. Model obtained from inverting the data shown in Figure 2 by minimizing only ϕ_{ms}, which has the depth weighting applied. This is to be compared with the true model in Figure 1. The major features in the true model, such as dip angle and depth extent, are evident in the recovered model.

more, the depth weighting in this case is rather well supported by mathematical analysis whereas it is an argued extension for the three roughness components. Therefore, a reasonable approach to inverting field data might be a two-step process. The data can be inverted first by minimizing ϕ_{ms}, and the resultant model may be used in the interpretation as a preliminary result. If there are interesting features present and if one desires to refine the model by incorporating prior information to enhance or attenuate the structural complexity in different regions, a second inversion can be carried out using an objective function consisting of both ϕ_{ms} and ϕ_{mv}. The model obtained by minimizing ϕ_{ms} can then be used in this inversion as an initial model. The available prior information can be incorporated into the second inversion by forming a reference model and 3-D weighting functions, w_s, w_x, w_y, w_z.

We now invert the same data by using $m = \ln(\kappa)$ as the model. It is not possible to incorporate a zero susceptibility as the reference model, so we minimize an objective function consisting of ϕ_{mv} with the reference model removed. The same depth weighting is applied to all terms of ϕ_{mv}. Since $\kappa = e^m$, the positivity of the susceptibility is ensured without invoking the transformation of variables. The result is shown in Figure 10a. This is a cross-section at $x = 500$ m and plotted on a logarithmic scale in accordance with the model used in the inversion. The inverted susceptibility shows the presence of the dipping anomaly as a broad region of high susceptibility. However, the interpretation based upon such a model can be complicated by the variations of susceptibility that are small and have little effect on the surface data. We have replotted the cross-section on a linear scale in Figure 10b and the anomalous region is now delineated more clearly. Its top portion indicates the tabular body and defines the depth to the

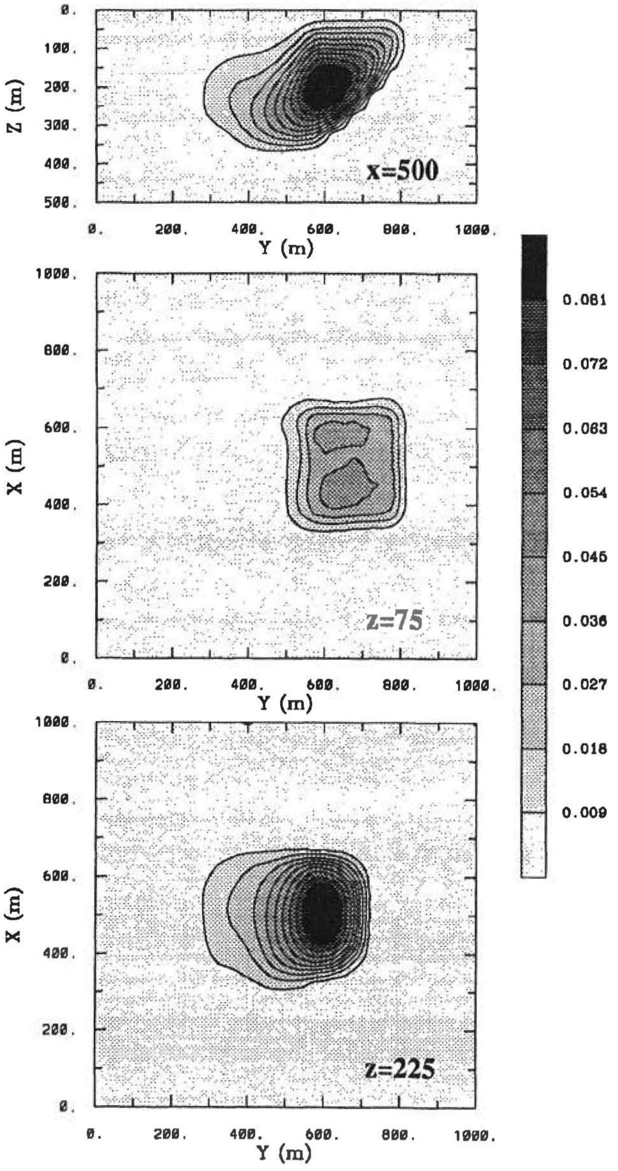

FIG. 9. The model derived from inverting the slab model data in Figure 2 by minimizing the model objective function having both ϕ_{ms} and ϕ_{mv}. The same depth weighting is used. This model appears to be smoother and has a smaller amplitude than that in Figure 8.

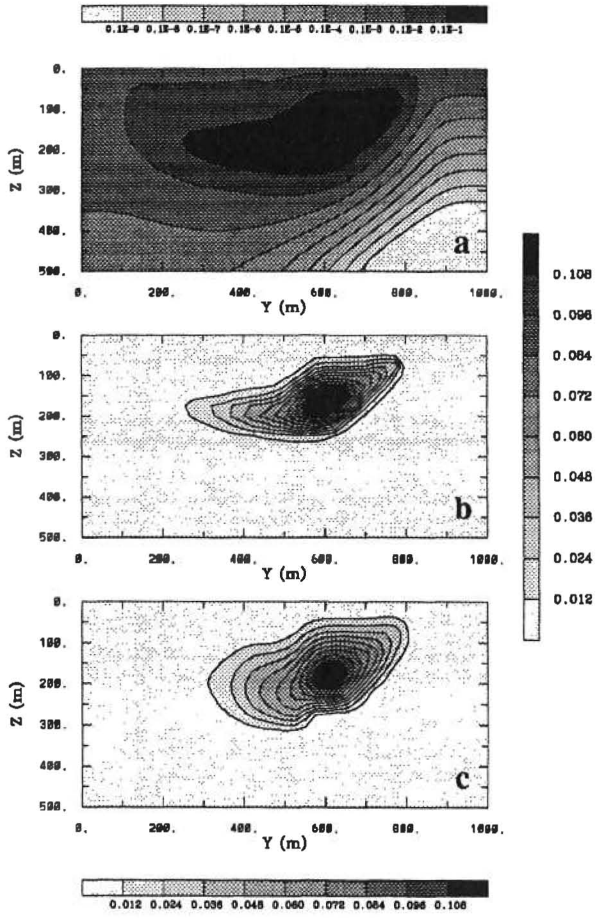

FIG. 10. The model obtained from inverting the data shown in Figure 2 by using $m = \ln(\kappa)$ as the model and minimizing ϕ_{mv} with the reference model removed. The inverted logarithmic susceptibility in cross-section at $x = 500$ m is shown in (a) and it is replotted on a linear scale in (b). As a comparison, the result obtained by using $m = \kappa$, and the same objective function is shown in (c).

top and dipping angle. The anomaly terminates at a shallower depth than the true model and has a nearly horizontal extension to the left. As an exact comparison, Figure 10c is the susceptibility model obtained by minimizing ϕ_{mv}, but using $m = \kappa$ as model and invoking the positivity. This is a smoother model and exhibits more gradual changes in the susceptibility. It has a slightly deeper extent than the model in Figure 10b. With the exception of details toward the bottom, however, both models provide almost the same information about the anomalous susceptibility region. It might be concluded that inversion using either linear or logarithmic susceptibility is viable for practical applications. However, we note that the presentation in Figure 10b is inconsistent with the model used in the inversion. Since the inverted susceptibility is easier to interpret on a linear scale as demonstrated here, and since the magnetic data are linearly related to the susceptibility, we generally prefer to work with the susceptibility κ as the model in the inversion.

As the second example we invert the total field anomaly data produced by a slightly more complicated model and with two different inducing field directions. The true model is shown in Figure 11 in the same format as before. It is a dipping slab having its top and bottom portions offset to simulate the result of a normal faulting. The faulted slab strikes north. The data from this model, when the inducing field has a direction of $I = 45°$ and $D = 45°$, are shown in Figure 12. Again Gaussian noise has been added to the data. The inversion minimizes an objective function consisting of ϕ_{ms} and ϕ_{mv} that have the same depth weighting and nonlinear mapping as used to produce the results in Figure 9. Figure 13 displays the recovered model in three slices. It shows two distinct anomalous regions of susceptibility that correspond to those in the true model. The dipping structure is evident from the top block. On plan view, the strike direction and the strike length of the anomaly are also well recovered.

When the inducing field direction is $I = 0°$ and $D = 45°$, the surface anomaly with added Gaussian noise is that shown in Figure 14. Carrying out the inversion using an identical model objective function generates the model shown in Figure 15. It is similar to the model shown in Figure 13, which is recovered under an inducing field at 45° inclination. Again, the two separate blocks, the dipping direction, and the length and direction of the strike, are all reasonably recovered. This is a positive result in that, although the surface anomalies have very different expressions under different inducing field directions, the inversion algorithm is able to consistently recover the source structure. Moreover, the algorithm had no difficulty in inverting data generated from an inducing field having zero inclination; such data often pose problems in interpretations that include a reduction to pole.

We emphasize that positivity has played a pivotal role in all the inversions. Magnetic data generally have regions of nega-

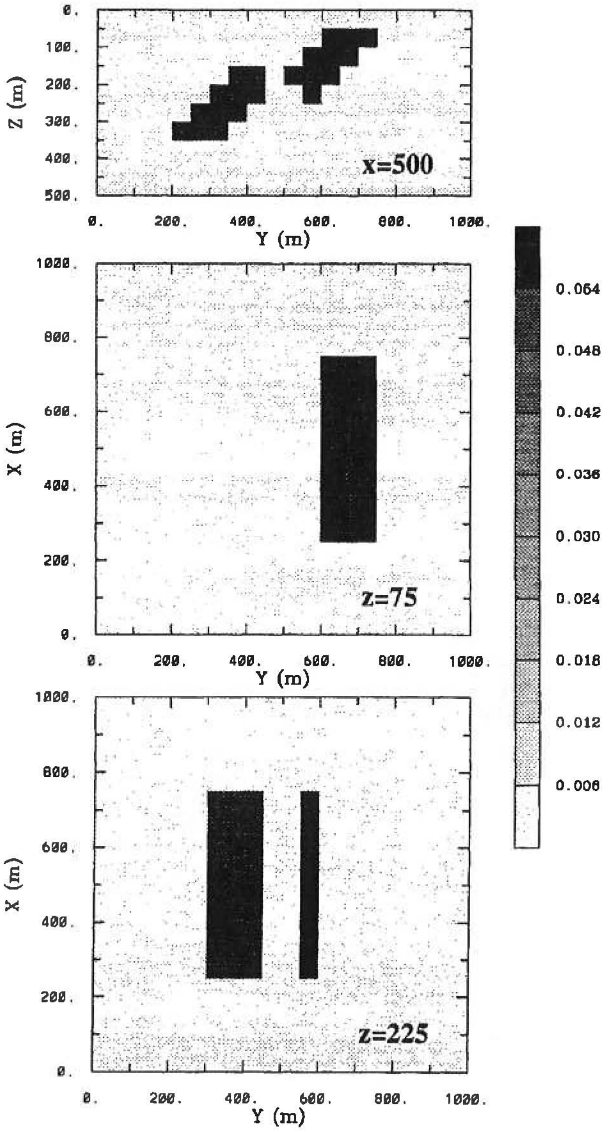

FIG. 11. The second synthetic test example. The top and bottom portions of the anomalous susceptibility are offset to simulate a norm fault structure. It also has a large strike length in the north direction.

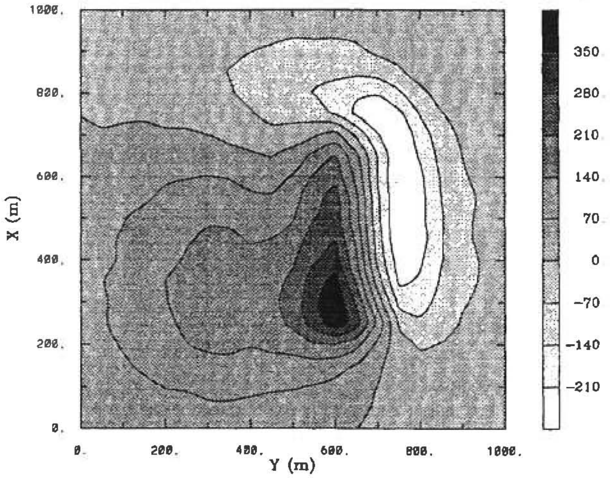

FIG. 12. The surface total field anomaly produced by the faulted slab in Figure 11, under an inducing field at $I = 45°$ and $D = 45°$. Uncorrelated Gaussian noise is again added to the data.

tive values that result from dipping bodies or inclined inducing field, or both. Without positivity, the constructed susceptibility is often negative and the dipping bodies appear more vertical. Recovery of correct dip and, to some extent, depth to the top of the anomalous body, are often the result of invoking positivity. Once the positivity is imposed, it is no longer true that an equivalent stratum that reproduces the data exists at any depth. Therefore, cells of anomalous susceptibility cannot be placed arbitrarily close to the surface, and no equivalent source can be constructed with negative susceptibilities. This restricts the class of admissible models and, consequently, reduces the nonuniqueness.

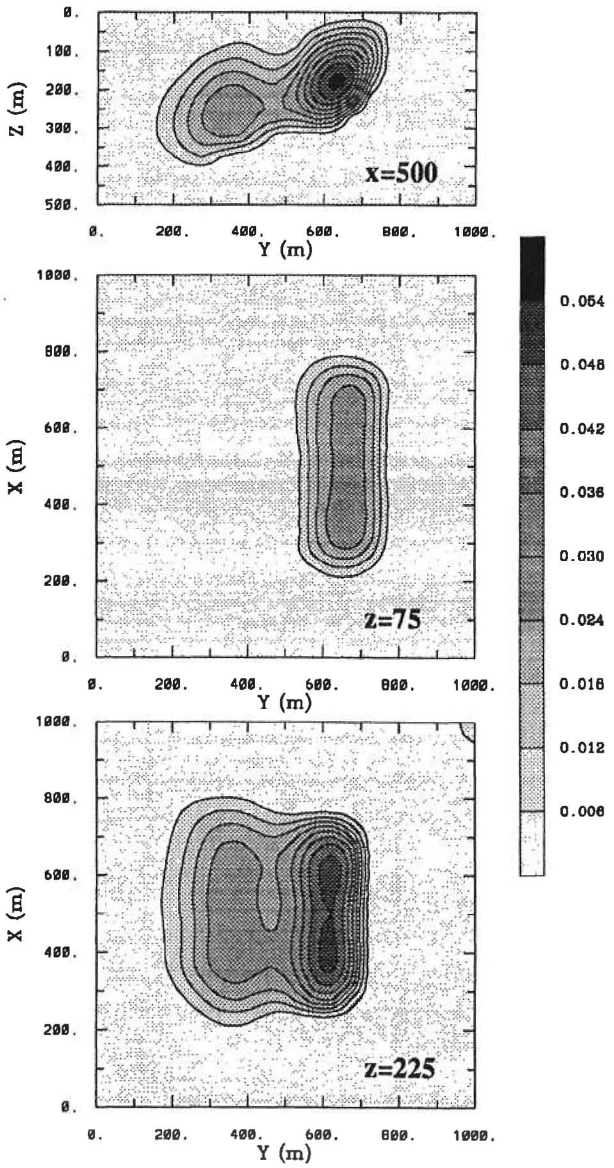

FIG. 13. The susceptibility model recovered from the data shown in Figure 12. It is seen that both the top and bottom block of the true model are recovered and the strike direction and length are well defined.

FIELD EXAMPLE

As the final example, we invert field data taken over a copper-gold porphyry deposit at Mt. Milligan in central British Columbia. The host rocks for the deposit are early Mesozoic volcanic and sedimentary rocks and contain intrusive monzonitic rocks that have accessory magnetite. Porphyry-style alteration and copper-gold mineralization are contemporaneous with the intrusive events. The copper and gold are known to be concentrated in the potassic alteration assemblage, which is mainly around the contact of the monzonite intrusions and may extend outward and into fractured volcanic rocks. Among other minerals, magnetite is one of the strong indicators of the potassic alteration. Ground magnetic data are acquired in the region at 12.5-m spacing along lines in the east direction and spaced 50 m apart. Our study of the data set has focused on a 1.2 km x 1 km area, which covers a large monzonite body known as the MBX stock and contains a reasonably isolated set of magnetic anomalies. Fairly detailed information about the geology is available through a major drilling program, but no susceptibility logs were available.

Magnetic data from a larger area were first upward continued to 20 m. A regional field was then defined and removed from the upward continued data. The continuation operation suppresses the noise in the data and also facilitates the discretization of the topographic surface for the model so that all observation points remain above the discretized surface. Although the original data were collected at 12.5-m spacing, we use the data at 25-m spacing. This yields 1029 data points at varying elevations. Figure 16 shows the data contoured according to their horizontal locations. The direction of the inducing field is $I = 75°$ and $D = 25.73°$. Several major magnetic highs are observed in the map. However, the influence of anomalies adjacent to the map is also visible along the edges. We choose a model domain that is horizontally larger than the data area, coincides at the top with the highest point on the topographic surface, and extends to 450-m depth. The model is discretized horizontally at a 25-m interval beneath the area of data. In the

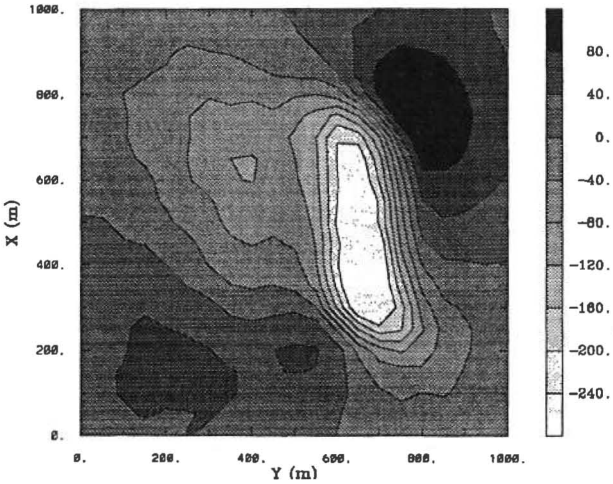

FIG. 14. The surface total field anomaly produced by the faulted slab in Figure 11 under an inducing field at $I = 0°$ and $D = 45°$. Uncorrelated Gaussian noise is added to the data.

vertical direction, the first 100 m is divided at a 12.5-m interval so that the surface can be adequately discretized onto the model mesh. Below the depth of 100 m, an interval of 25 m is used. This results in a mesh with 52 x 44 x 22 cells. Once the mesh is defined, the topography is discretized onto it. The 43 428 cells below this surface define the susceptibility model, and the inverse problem is therefore formalized by inverting 1029 data to recover the susceptibilities in those cells. The depth weighting is referenced to the top of the model domain. Each datum is assumed to have an error whose standard deviation is equal to 5% of its magnitude plus 10 nT. The error estimate includes not only the repeatability of the instrument reading but also the geological noise and errors introduced by the inaccurate recording position and by separating the anomalous field from the initial total field measurements. One hundred subspace vectors generated by dividing the data map into small subareas are used in the inversion. We use a nonlinear mapping with $\kappa_b = 0.0002$ and $\kappa_l = 0.02$. The recovered model is shown in Figure 17 as one plan-section and three cross-sections. From the plan-section, two concentrated susceptibility highs are observed in the central region. Surrounding them are three linear anomalies trending northeast. In the cross-sections, the major anomalies are seen at moderate depths but there is considerable variation in the depth to the top. There are also smaller anomalies extending to the surface. In general, there are more detailed structures near the surface and the model becomes increasingly smooth at greater depths. As required by the objective function, there is no excessive structure associated with each unit of high susceptibility region. Comparison with drill logs indicates that the recovered magnetic susceptibility highs are mostly associated with the monzonite intrusions and with faults or fracture zones. Figure 18 compares the recovered susceptibility model with the geology (Cam DeLong, personal communication) in the cross-section at x = 600 m. The large susceptibility high is spatially well-correlated with the MBX stock and reflects the initial magnetite content in the intrusion. Two smaller susceptibility highs are present east of the stock. The high at y = 650 m coincides with the boundary of stock and porous trachytic units while the high at y = 900 m coincides with the upper portion of the Rainbow dyke. These are locations of the most intensive potassic alterations and the susceptibility highs are indicative of the magnetite produced by the alteration process. Over all, this is a rather encouraging result.

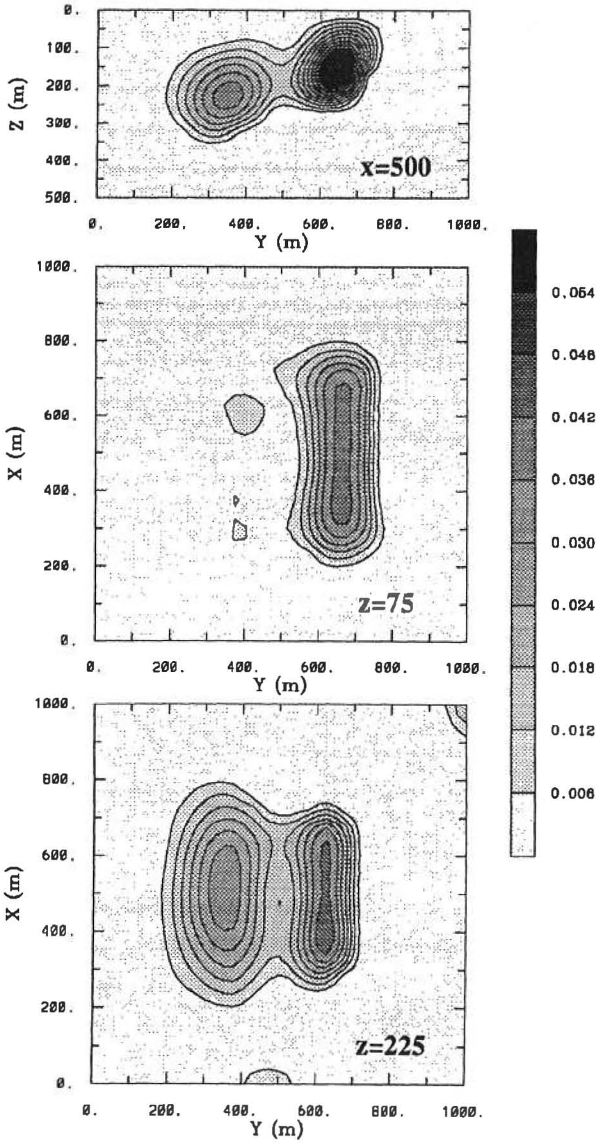

FIG. 15. The susceptibility model recovered from the data shown in Figure 14. This model is similar to that shown in Figure 13.

CONCLUSION

We have developed an algorithm to invert surface magnetic data for general 3-D susceptibility distributions. Although we have illustrated the algorithm using examples on the scale pertinent to mining applications, the method is general and applicable to problems on different scales ranging from environmental to regional investigations. To overcome the inherent nonuniqueness, we obtain the solution by minimizing a

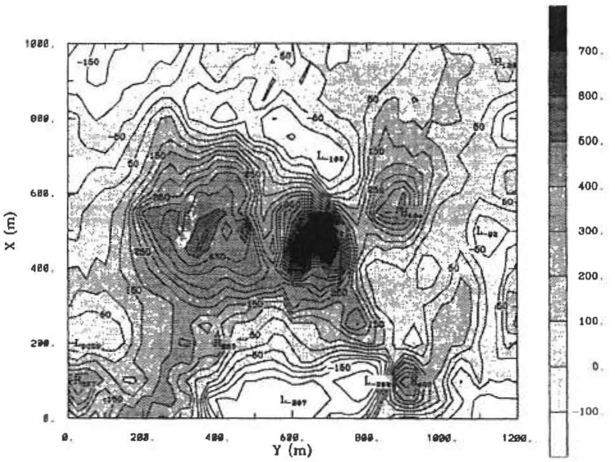

FIG. 16. The extracted total field anomaly from ground magnetic data at Mt. Milligan Copper-gold porphyry deposit. The data are contoured according to their horizontal locations in this map, although thev are at different elevations.

specific objective function of the model. Our model objective function has the ability to incorporate prior information into the inversion via a reference model and 3-D weighting functions. A crucial feature of the objective function is a depth weighting function that counteracts the natural decay of the kernel functions. The parameters of the depth weighting depend upon the discretization of the model but are easily calculated. The minimization is carried out using a subspace technique that reduces the computational effort and allows the positivity constraint of susceptibility to be incorporated. Both susceptibility and logarithmic susceptibility can potentially be used as the model in the inversion. Since the data are linearly related to susceptibility, and since usually absolute values of susceptibility are required for interpretation rather than relative values, especially in regions of very low susceptibility, we have generally chosen to work with susceptibility. To suppress the noise from small magnetic bodies near the surface, we recommend in general that the data be upward continued to a height comparable with the width of the surface cell before inversion.

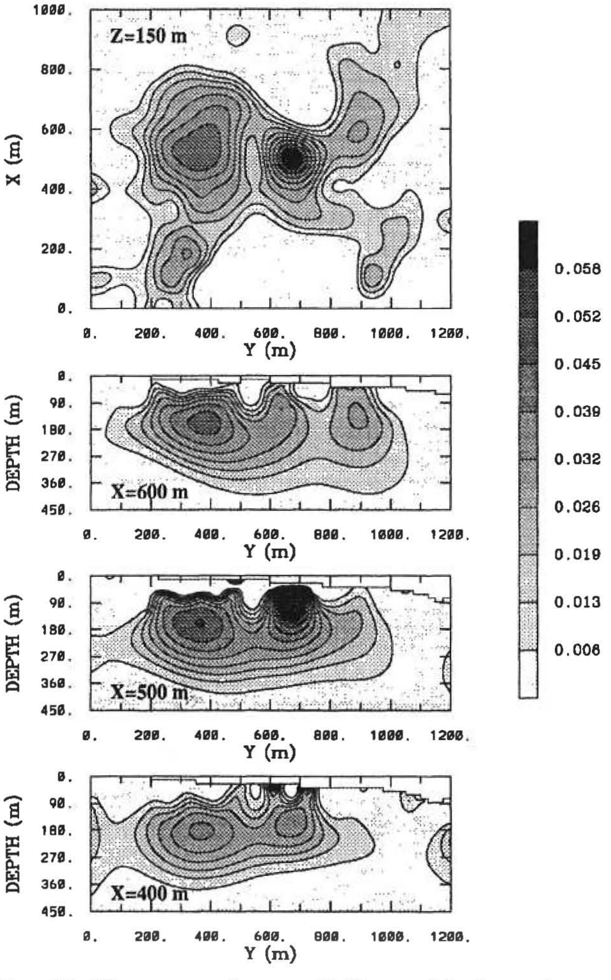

FIG. 17. The recovered susceptibility model shown in one plan-section and three cross-sections. The plan-section is at the depth of 150 m and the three cross-sections are at x = 600,500, and 400 m, respectively.

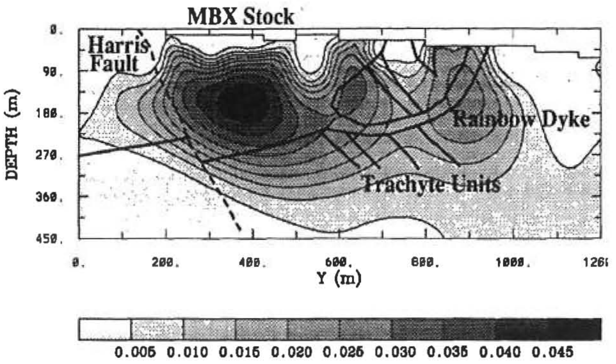

FIG. 18. Comparison of the recovered susceptibility model in a cross-section (x = 600) with the geology for the Mt. Milligan deposit. The susceptibility high within the MBX stock reflects the initial magnetite in the intrusive while the susceptibility highs near the Rainbow dyke are related to the magnetite produced by potassic alteration.

Applications of our inversion to synthetic data sets have produced models representative of the true structures and demonstrated the ability of the algorithm to construct consistent models at different magnetic latitudes. Inversion of field data has produced a susceptibility model that is consistent with the known geology and mineralization information. These results represent an encouraging conclusion: although the inversion of magnetic data seems impossibly nonunique when one has a large number of cells, inversions using a properly designed model objective function can produce susceptibility distributions that yield meaningful geologic information.

ACKNOWLEDGMENTS

This work was supported by an NSERC IOR grant and an industry consortium "Joint and Cooperative Inversion of Geophysical and Geological Data." Participating companies are Placer Dome, BHP Minerals, Noranda Exploration, Cominco Exploration, Falconbridge, INCO Exploration & Technical Services, Hudson Bay Exploration and Development, Kennecott Exploration Company, Newmont Gold Company, Western Mining Corporation, and CRA Exploration Pty.

REFERENCES

Bhattacharyya, B. K., 1964, Magnetic anomalies due to prism-shaped bodies with arbitrary magnetization: Geophysics, **29**, 517-531.

——— 1980, A generalized multibody model for inversion of magnetic anomalies: Geophysics, **45**, 255-270.

Green, W. R., 1975, Inversion of gravity profiles by use of a Backus-Gilbert approach: Geophysics, **40**, 763-772.

Guillen, A., and Menichetti, V., 1984, Gravity and magnetic inversion with minimization of a specific functional: Geophysics, **49**, 1354-1360.

Last, B. J., and Kubik, K., 1983, Compact gravity inversion: Geophysics, **48**, 713-721.

Oldenburg, D. W., and Li, Y., 1994, Subspace linear inversion methods, Inverse Problems, **10**, 915-935.

Rao, D. B., and Babu, N. R., 1991, A rapid methods for three-dimensional modeling of magnetic anomalies: Geophysics, **56**, 1729-1737.

Wang, X., and Hansen, R. O., 1990, Inversion for magnetic anomalies of arbitrary three-dimensional bodies: Geophysics, **55**, 1321-1326.

Zeyen, H., and Pous, J., 1991, A new 3-D inversion algorithm for magnetic total field anomalies: Geophys. J. Int., **104**, 583-591.

APPENDIX

MODEL OBJECTIVE FUNCTION

Our inversion method uses a model objective function of the form

$$\phi_m(m) = \alpha_s \int_V w_s\{w(z)[m(\mathbf{r}) - m_0]\}^2\, dv$$

$$+ \alpha_x \int_V w_x\left\{\frac{\partial w(z)[m(\mathbf{r}) - m_0]}{\partial x}\right\}^2 dv$$

$$+ \alpha_y \int_V w_y\left\{\frac{\partial w(z)[m(\mathbf{r}) - m_0]}{\partial y}\right\}^2 dv$$

$$+ \alpha_z \int_V w_z\left\{\frac{\partial w(z)[m(\mathbf{r}) - m_0]}{\partial z}\right\}^2 dv. \qquad \text{(A-1)}$$

The numerical evaluation of this functional is carried out by introducing the model mesh and evaluating all terms using a finite-difference approximation. The discretized model objective function has the form

$$\phi_m(\mathbf{m}) = (\mathbf{m} - \mathbf{m}_0)^T(\underset{\sim}{\mathbf{W}}_s^T\underset{\sim}{\mathbf{W}}_s + \underset{\sim}{\mathbf{W}}_x^T\underset{\sim}{\mathbf{W}}_x + \underset{\sim}{\mathbf{W}}_y^T\underset{\sim}{\mathbf{W}}_y$$

$$+ \underset{\sim}{\mathbf{W}}_z^T\underset{\sim}{\mathbf{W}}_z)(\mathbf{m} - \mathbf{m}_0)$$

$$\equiv (\mathbf{m} - \mathbf{m}_0)^T\underset{\sim}{\mathbf{W}}_m^T\underset{\sim}{\mathbf{W}}_m(\mathbf{m} - \mathbf{m}_0) \qquad \text{(A-2)}$$

Each component matrix can be written as the product of three individual matrices and one oefficient. That is,

$$\underset{\sim}{\mathbf{W}}_i = \alpha_i \underset{\sim}{\mathbf{S}}_i \underset{\sim}{\mathbf{D}}_i \underset{\sim}{\mathbf{Z}}, \qquad i = s, x, y, z, \qquad \text{(A-3)}$$

where $\underset{\sim}{\mathbf{S}}_i$ are diagonal matrices representing the spatially dependent 3-D weighting functions, $\underset{\sim}{\mathbf{D}}_i$ are the finite-difference operators for each component, and $\underset{\sim}{\mathbf{Z}}$ is a diagonal matrix representing the discretized form of depth weighting function $w(z)$.

The elements of $\underset{\sim}{\mathbf{S}}_i$ are given by $\sqrt{w_i}$. They are defined over each cell for $\underset{\sim}{\mathbf{S}}_s$, and over each interface between adjacent cells in the respective directions for $\underset{\sim}{\mathbf{S}}_x$, $\underset{\sim}{\mathbf{S}}_y$, and $\underset{\sim}{\mathbf{S}}_z$. $\underset{\sim}{\mathbf{D}}_s$ has elements $\sqrt{\Delta x \Delta y \Delta z}$ on its diagonal, where Ax, Ay, and Δz are the cell width. The matrix $\underset{\sim}{\mathbf{D}}_x$ has two elements $\pm\sqrt{\Delta y \Delta z/\delta x}$ in each row, where δx is the distance between the centers of cells adjacent in the x - direction. Similarly, $\underset{\sim}{\mathbf{D}}_y$ and $\underset{\sim}{\mathbf{D}}_z$ have elements $\pm\sqrt{\Delta x \Delta z/\delta y}$ and $\pm\sqrt{\Delta x \Delta y/\delta z}$, respectively, where δy and δz are the distances between centers of adjacent cells in the y- and z - directions. Once the mesh is defined and all weighting functions, w_s, w_x, w_y , w_z, and $w(z)$ are chosen, equation (A-3) is evaluated straightforwardly and $\underset{\sim}{\mathbf{W}}_m^T\underset{\sim}{\mathbf{W}}_m$ is formed.

Conductivity Depth Imaging

Introduction

Condor Consulting, Inc.

Conductivity Depth Imaging or CDI of airborne EM (AEM) data is the term applied to the mathematical transformation of the EM response recorded in the measuring instrument of the survey aircraft that is the transformed into a conductivity distribution of the earth. The accuracy or resolution of the outcomes of CDI is dependent on a number of factors including the type of EM system employed, the quality of the data the system produces, the terrain covered by the system and methodology of the CDI approach. Basically all CDI approaches in commercial use involve what is termed a 1D approximation of the earth. This means that the mathematical model being fit to the data can only capture changes in conductivity vertically in the earth. Displays of CDI outcomes in 2D (sections along lines) and 3D (gridding between lines) all rely on outcomes that are derived from initial 1D processing.

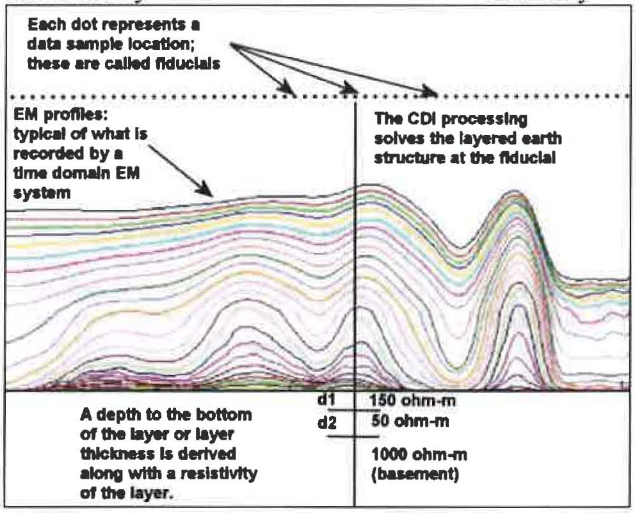

Imaging vs. Inversion: CDI processing can in turn be broken down into two major approaches in the mathematical process involved in solving the sub-surface conductivity structure; this being what is termed either imaging or inversion methodology. Both approaches are in use by survey contractor and consultants and each technique has advantages and draw backs depending on two primary factors; the EM system which acquired the data and the geological problem. Condor uses both approaches but prefers the inversion approach in most applications.

Off-time vs. Bfield: A derived Bfield outcome is now commonly delivered by the major contractors along with the traditional pure off-time data. Condor will routinely process both data streams and then assess which provides the superior outcome for subsequent use specific project assessment. Condor has found this dual processing approach is required as it is very difficult before hand to assess what data stream will provide the best outcome.

In the next several pages, examples of CDI processing will be presented which illustrate the role it can play in modern AEM interpretation. The color section showing a CDI is termed a Conductivity Depth Section or CDS.

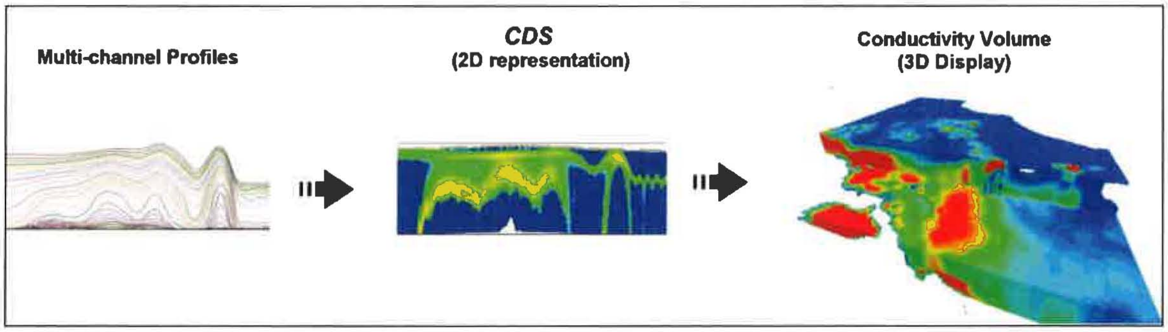

Historically, AEM was used primarily for fairly simple detect of discrete high conductance features which could represent deposits of massive sulfides such as VMS or Ni-Cu. There was little interest in extracting more information other than the X, Y location of the feature and some basic idea of the quality of the conductor. Ground follow-up for location validation and drill hole spotting was always done.

In modern exploration however, there is a far greater range of targets being sought after and in a much wider variety of settings. Even in traditional areas where AEM has been used are now deemed 'mature' explorers are expecting that more sophisticated acquisition and processing techniques will be required to make new discoveries.

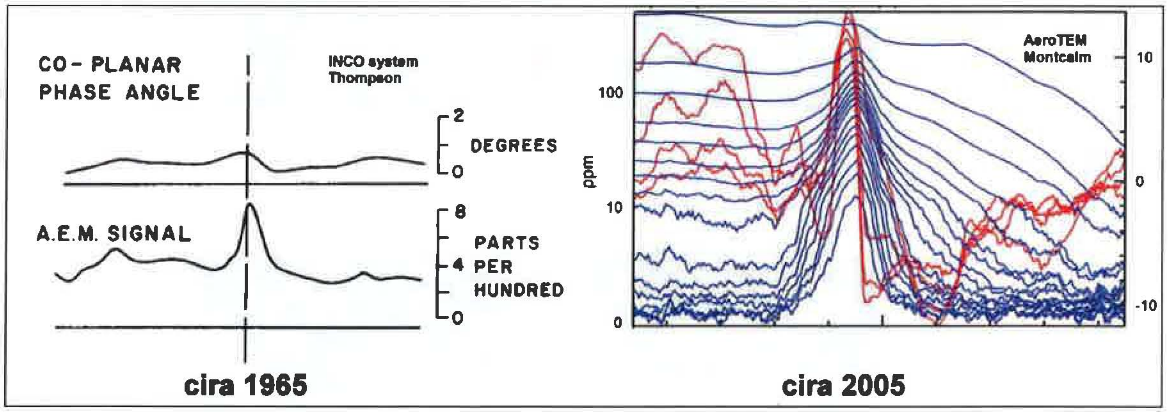

In the CDI process (this applies to either imaging or inversion approaches), those elements of the geology that are dominantly horizontal in nature can be modeled quite well whereas narrow steeply dipping features most often appear with a 'comet-like' shape the depth of which does not necessarily correspond all that well to the actual depth within earth. While this may seem like a major draw back to using these outcomes, a combination of experience, local calibration and access to alternate means to model the data allow the seasoned interpreter to define the subsurface geology quite well. The CDI processing at its best is a very useful means to provide a 3D conductivity "context" of the subsurface which can be extremely valuable in helping to recognize and define zones of interest.

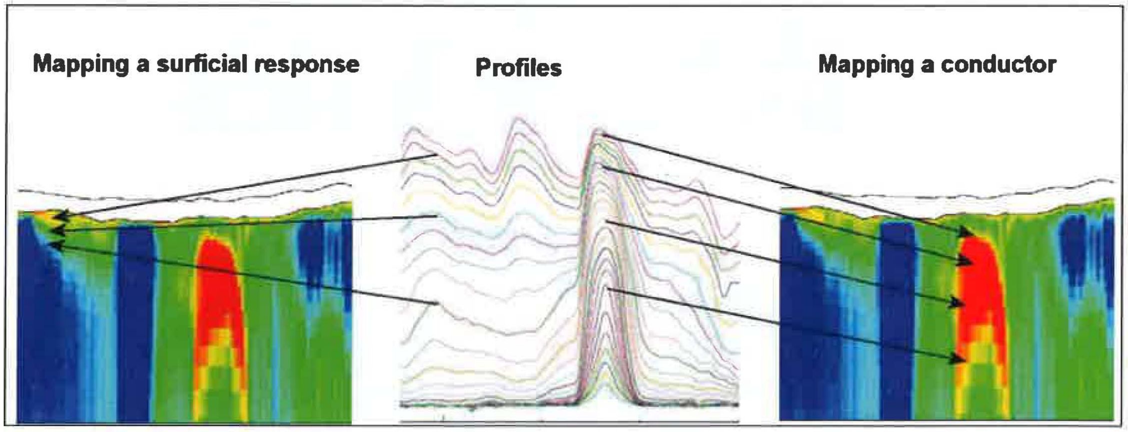

Differences between Imaging and Inversion

The image below shows the outcomes of an inversion program (termed Layered Earth Inversion or LEI) and a imaging program, in this case EMFlow. Three major differences are noted in this example (VTEM survey in the Athabasca Basin); first the depth to the major conductive zone appears deeper in the EMFlow outcome, second the topology of the basement conductor appears to be more rugged in the EMFlow outcome and third, the conductive horizon appears to end in the LEI outcome on the right hand side whereas the EMFlow result shows the zone continuing off the right and side of the image.

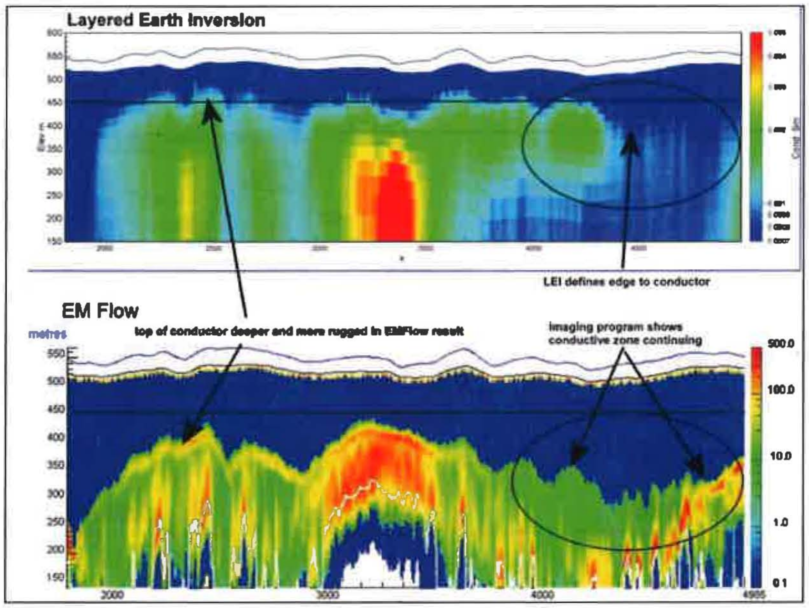

Differences between dB/dT and Bfield

The figure below shows the outcomes of LEI processing to the dB/dT and Bfield outcomes from a VTEM survey undertaken as part of a Ni-Cu search. These results are considered typical in that while the Bfield result shows a nominal greater sensitivity to higher conductance, the results are also somewhat nosier and appear to have slightly less high frequency content than the dB/dT results.

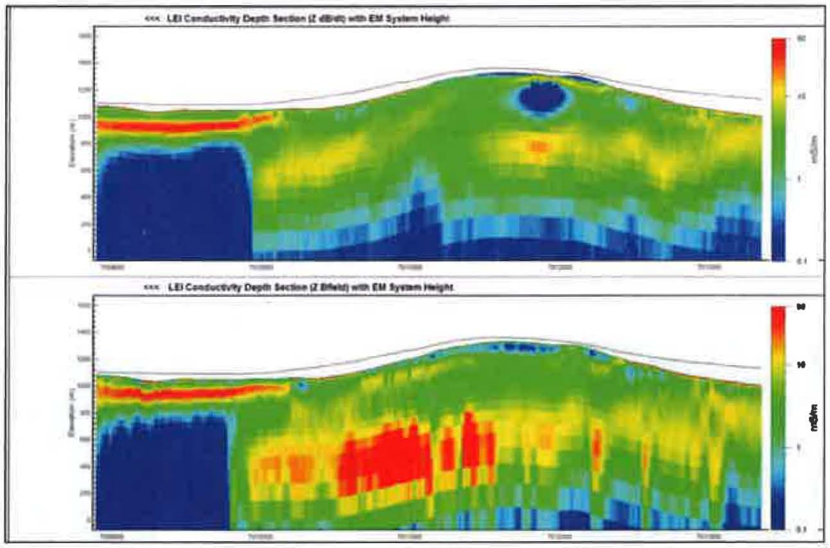

How CDI Helps Interpretation?

A major benefit of having a CDI outcome to interpret is that it coveys a far more geological "feel" to the EM data than profiles along. This is sometimes termed "mapping" with target detection and discrimination a sub-set of this larger interpretive activity.

Using the previous image as an example, the dB/dT CDS has been annotated with what Condor terms Wide Zones. These are zones of broad conductivity in the CDS which are felt to characterize different parts of the geological section. In this case WZ-1 is a thin shallow near surface that could represent lake sediments or a in a weathered terrain, part of a distinctive weather profile over a mafic rock. The WZ-2 features are "in the earth" sources that represent zones of increased conductivity which could represent different rock units or alteration of a specific unit.

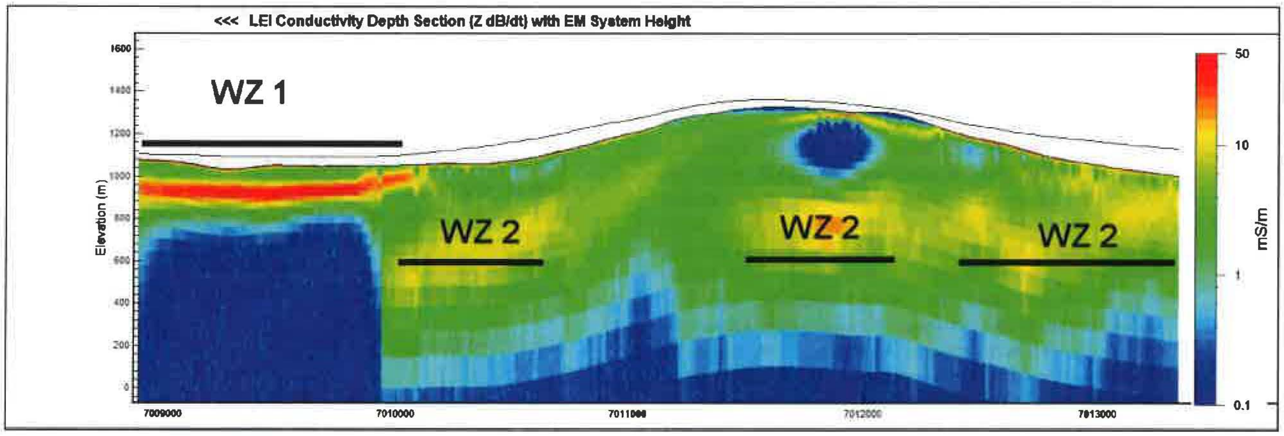

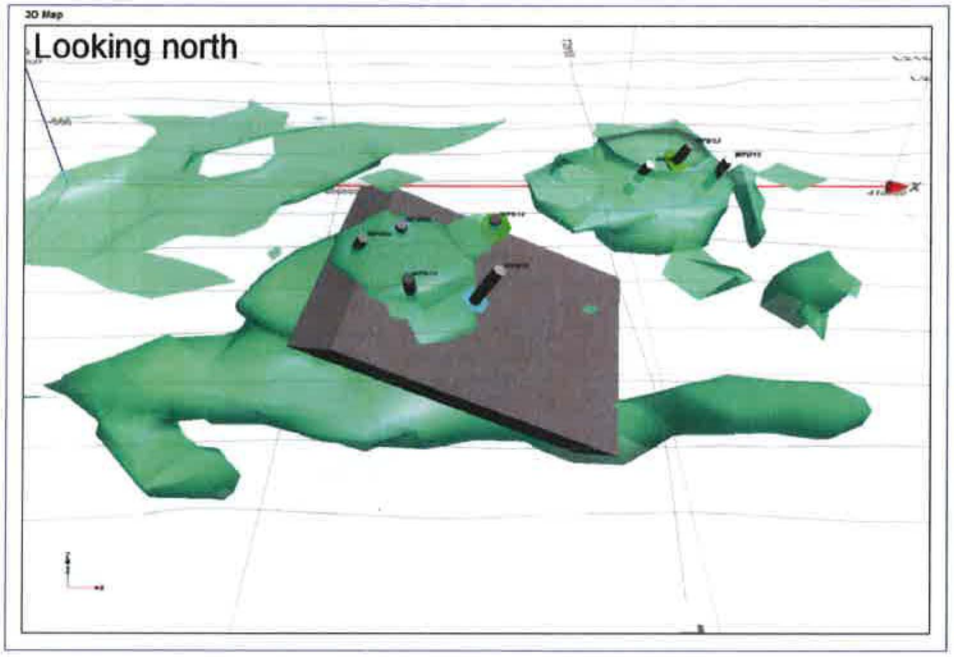

Another benefit of the CDI processing is that it in turn allows for the creation of 3D voxel models of the EM outcomes. This is often an excellent means to capture in a holistic sense the sub-surface conductivity distribution either as a stand-alone model or as part of the integrated geoscience model (referred to as a Common Earth Model). An example of such a conductivity model combined with parametric models of specific anomalies (produced using Maxwell) and drill holes is shown in the figure to the left.

Analysing frequency-domain EM data for highly conductive targets

Daniel Sattel
EM Solutions LLC
Golden, CO, USA
dsattel@earthlink.net

Ken Witherly
Condor Consulting, Inc.
Lakewood, CO, USA
ken@condorconsult.com

SUMMARY

The sensitivity of RESOLVE data to highly conductive targets is examined. Modelling results from synthetic data across horizontal plates suggest that RESOLVE data detect highly conductive structures, but don't resolve their conductances and time-constants if those values exceed 500 S and 8 ms, respectively.

A RESOLVE data set flown initially for kimberlite exploration has been re-analysed for nickel sulphides. Since the latter are highly conductive, the standard processing products such as apparent resistivity grids, deemed useful for mapping kimberlites, did not provide the optimum resolution for data analysis. The survey area is characterized by strong magnetic and EM responses due to the presence of banded-iron formations and pyrrhotite-rich massive sulphides. In order to determine the strongest conductors, time-constants and apparent conductivities were derived from the RESOLVE survey data. Due to the strong magnetic response, correction of the RESOLVE data for magnetic permeability resulted in better-resolved time-constants. This was achieved by inverting the data for the conductivity σ and magnetic permeability μ_r of a layered-earth, followed by the forward modelling of the layer conductivities with $\mu_r=1$. A comparison of independently derived time-constants and apparent conductances suggests that reliable values do not exceed 0.5 ms and 200 S, respectively. Conductors with values above 200 S / 0.5 ms are detectable, but not resolvable.

Key words: Airborne EM, inversion, nickel sulphides, RESOLVE.

INTRODUCTION

Highly conductive nickel sulphides present a challenging target to airborne EM exploration. Nickel mineralizations can be too conductive for most time-domain EM systems, due to their flexible/uncertain system geometries, or too deep for frequency-domain EM systems. A successful survey of the DIGHEM system across a highly conductive, shallow nickel body at Voisey's Bay is described by Witherly *et al.* (2003).

After a brief discussion of synthetic frequency-domain EM responses as a function of subsurface conductance for the RESOLVE system (Fraser and Hodges, 2007), a RESOLVE survey flown in 2004 is analysed for highly conductive targets. The standard processing products such as apparent resistivity grids did not provide the optimum data resolution for nickel exploration. In order to improve resolution at higher conductivities, time-constants were derived from the EM data. The derived time-constants allowed for the prioritisation of exploration targets.

SYNTHETIC DATA

Figure 1 shows the RESOLVE responses above the centre of a horizontal plate (100m by 100m) as a function of plate conductance. At high conductances, the EM response is purely in-phase with the transmitted primary EM response. The in-phase responses $A_{ip}(f)$ asymptote toward the inductive limit *IL*, which is a function of the system and plate geometry. Due to the successful removal of the primary field, the RESOLVE system detects highly conductive material. However, the resolution of conductivities is limited by the noise level of the system. This is illustrated in Figure 2, where

$$\Delta A_{ip}(f) = IL - A_{ip}(f) \qquad (1)$$

In order to resolve a certain conductance, the noise level has to be equal or better than the corresponding $\Delta A_{ip}(f)$ value. Figure 2 suggests that, assuming a noise level of 10 ppm for all frequencies, maximum resolvable conductances range from 1.2 S for the 140 kHz response to 500 S for the 400 Hz response.

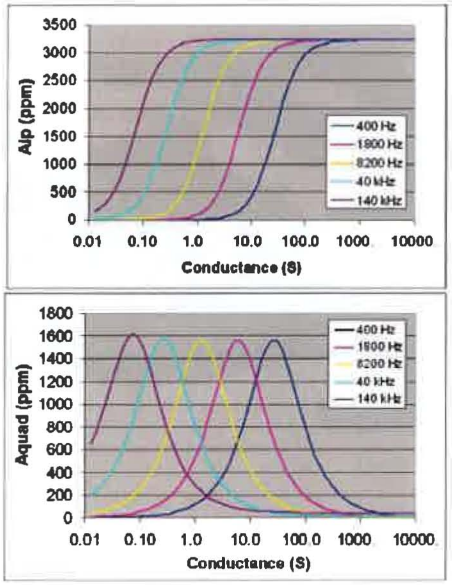

Figure 1. RESOLVE in-phase (top) and quadrature (bottom) responses as a function of plate conductance and frequency.

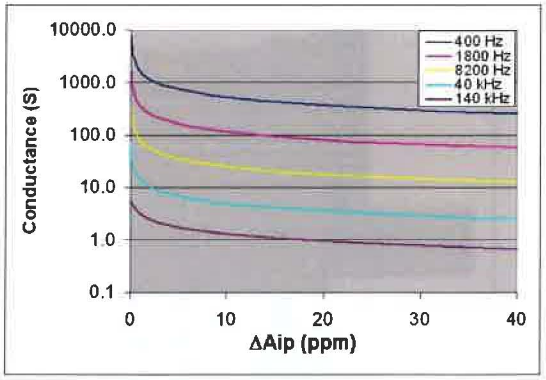

Figure 2. The in-phase data from figure 1 are replotted as conductance vs $\Delta A_{ip}(f)$. For a given noise level and frequency, conductance resolution is limited to below the conductance at the equivalent value of $\Delta A_{ip}(f)$.

TIME-CONSTANTS

Grant and West (1965) and Macnae *et al.* (1998) show that the frequency-domain response of an isolated conductor can be expressed as:

$$A(\omega) = \sum_i A_i \frac{j\omega\tau_i + \omega^2\tau_i^2}{1+\omega^2\tau_i^2} \qquad (2)$$

From equation (2) it can be shown that for each of the recorded RESOLVE frequencies f_i, a time-constant can be derived from the observed in-phase and quadrature responses $A_{ip}(f)$ and $A_{quad}(f)$:

$$\tau_i = \frac{A_{ip}(f_i)}{\omega_i A_{quad}(f_i)} \qquad (3)$$

The time-constants derived from the data in Figure 1 are shown in Figure 3 as a function of $\Delta A_{ip}(f)$. Assuming a noise level of 10 ppm for all frequencies, maximum resolvable time-constants range from 0.015 ms for the 140 kHz response to 8 ms for the 400 Hz response.

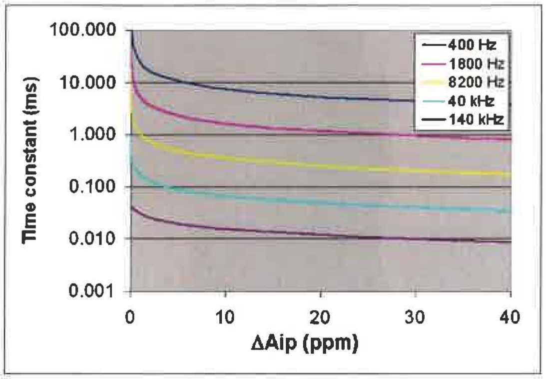

Figure 3. The in-phase data from figure 1 are replotted as time-constant vs $\Delta A_{ip}(f)$. For a given noise level and frequency, time-constant resolution is limited to below the time-constant at the equivalent $\Delta A_{ip}(f)$.

FIELD DATA ANALYSIS

A RESOLVE survey was flown for GGL Diamond Corp. (GGLD) in 2004 initially for kimberlite exploration, and recorded EM responses in the range 400 Hz – 135 kHz. Subsequently the data were re-analysed for highly conductive nickel-sulphides. EM and magnetic profiles are shown with derived products in Figure 4.

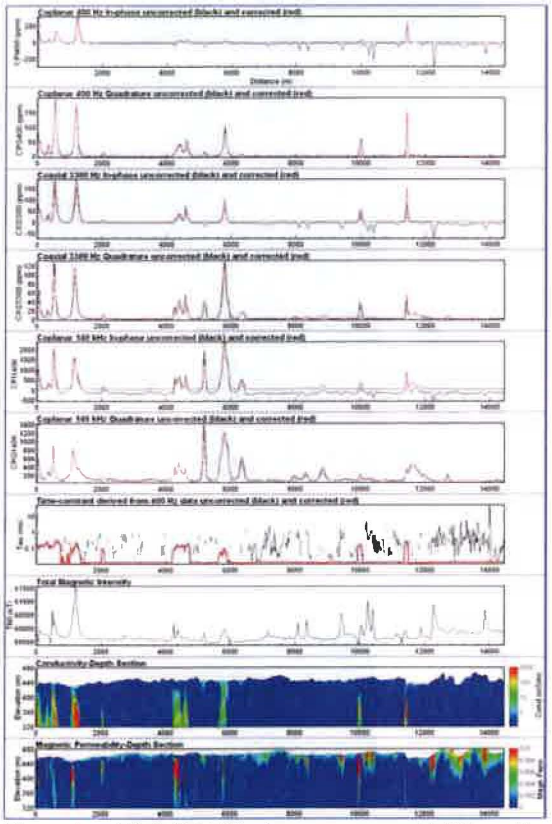

Figure 4. RESOLVE EM, time-constant and TMI profiles with derived conductivity-depth and magnetic permeability-depth sections. EM and time-constant profiles corrected for magnetic permeability are shown in red, uncorrected profiles in black.

The profiles of figure 4 show that negative 400 Hz in-phase responses correlate with magnetic highs. An image of the time-constant derived using equation (3) is shown in Figure 5. The time-constant profile shown in Figure 4 indicates that time-constants cannot be determined reliably in the presence of magnetic anomalies. Next, the data were corrected for magnetic permeabilities before deriving time-constants. For that, data were inverted for the conductivity σ and magnetic permeability μ_r of a layered-earth using EM1DFM (Farquharson *et al.*, 2003), followed by the forward modelling of the conductivity structures with μ_r=1. Results of the latter are shown in Figures 4 and 6. The correction resulted in time-constant profiles being more continuous and grids showing a higher resolution at lower time-constant values.

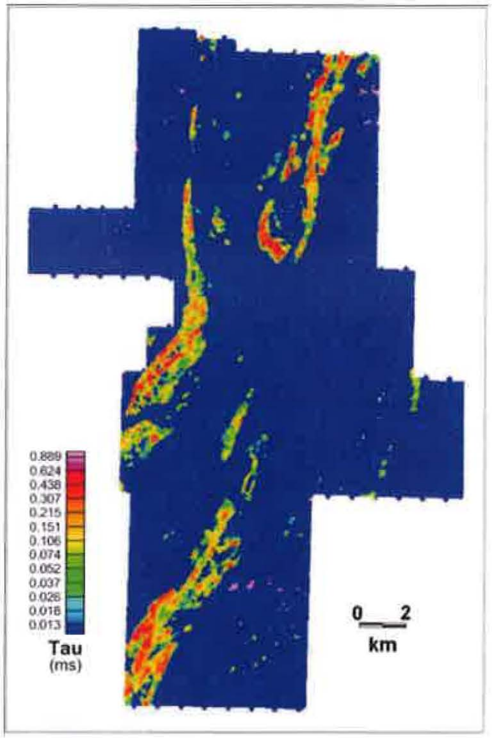

Figure 5. Time-constant image derived from 400 Hz inphase and quadrature responses using equation 1.

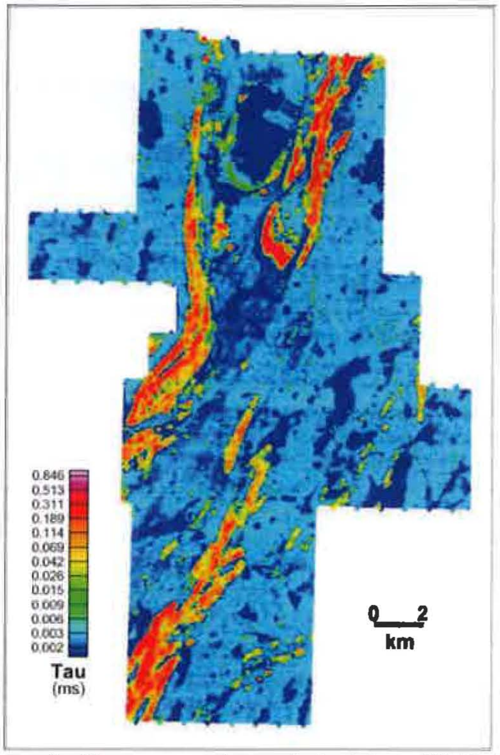

Figure 6. Time-constant image derived from 400 Hz inphase and quadrature response corrected for magnetic permeability.

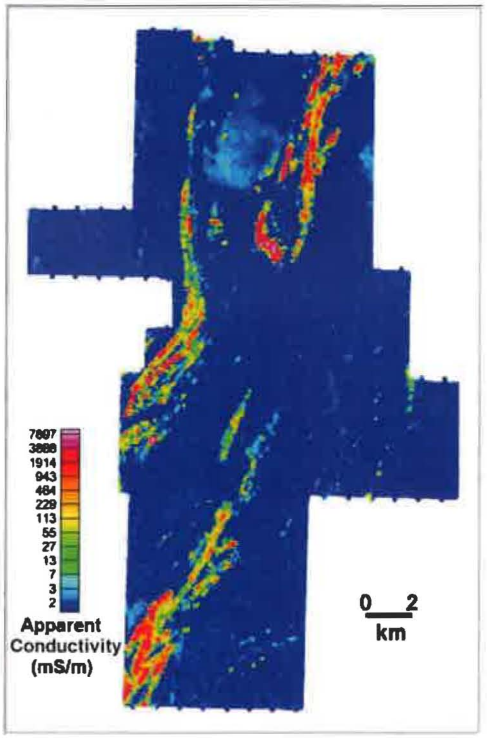

Figure 7. Apparent conductivity of 400 Hz response, corrected for magnetic permeability and dielectric permittivity.

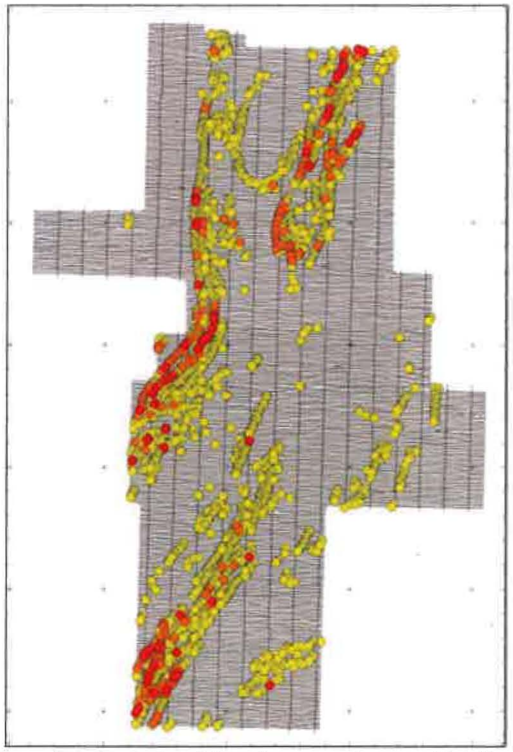

Figure 8. Anomaly picks of survey data on flightlines. Anomalies are ranked from high (red) to low (yellow), according to their associated time-constants as illustrated in Figure 9.

An image of the 400 Hz apparent conductivity image is shown in Figure 7. The shown apparent conductivities were derived from the apparent resistivities provided by Fugro Airborne Surveys, who used an algorithm described by Huang and Fraser (2001), which corrects for magnetic permeability and dielectric permittivity. Though derived with completely different approaches, the images of Figures 5 and 6 are quite similar to Figure 7.

The interpretation of the data set included manual anomaly picking, which made use of the derived conductivity-depth sections, EM and magnetic profiles. The final anomaly picks are shown in Figure 8. These anomalies were ranked as a function of their time-constants from 1 (high) to 3 (low), with the ranking scheme shown in Figure 9. Figure 9 also indicates that time-constants of picked anomalies do not exceed 0.5 ms. Higher time-constants as indicated in Figures 5 and 6 have not been determined at anomaly centres and correspond to edge effects. A ground EM survey is currently in progress to examine the areas of the highest time-constants.

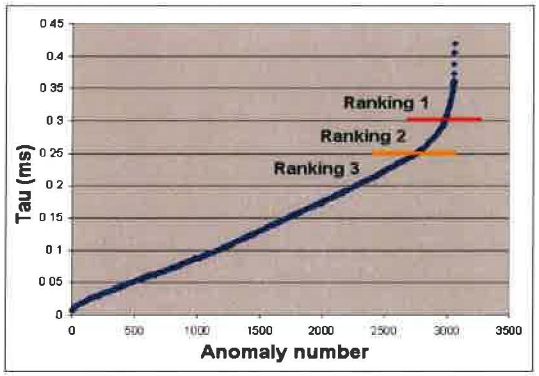

Figure 9. Anomaly picks sorted by their associated time-constants and ranking applied in Figure 8. Anomalies were ranked 1, 2 and 3 for tau > 0.3, 0.25 < tau < 0.3 and tau < 0.25, respectively.

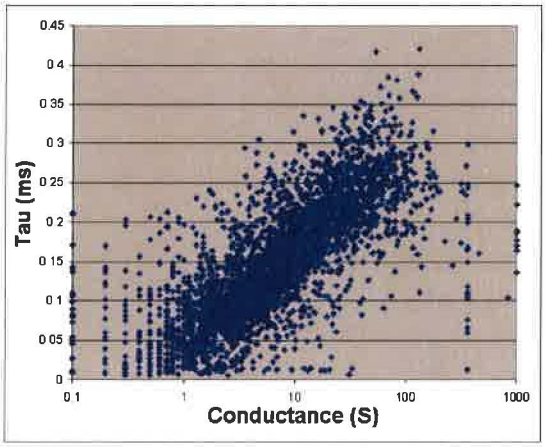

Figure 10. Vertical plate conductances vs time-constants for RESOLVE survey data.

Finally, Figure 10 shows a comparison for a survey-data subset between time-constants and conductances determined by Fugro Airborne Surveys using a vertical plate model. Besides showing a close relationship between the two parameters, Figure 10 also suggests that conductances above 200 S and time-constants above 0.4 ms are unlikely to be resolved reliably from the data.

CONCLUSIONS

Synthetic data suggest that conductances above 500 S and time-constants above 8 ms cannot be determined reliably from RESOLVE data. Field data indicate that conductance and time-constant resolution is limited to below 200 S and 0.4 ms, respectively. Material of higher conductances is detected, but the conductances are too high to be resolvable.

Removing the effects of magnetic permeability allowed for the continuous determination of time-constants in a survey area characterized by negative in-phase responses related to strong magnetic anomalies. The derived time-constants agree well with the apparent conductivities and were used to prioritise exploration targets.

ACKNOWLEDGMENTS

The authors are thankful to GGL Diamond Corp. for the release of the survey data and modelling results shown.

REFERENCES

Farquharson, C.G, Oldenburg, D.W., and Routh, P.S., 2003, Simultaneous 1D inversion of loop-loop electromagnetic data for both magnetic susceptibility and electrical conductivity: Geophysics 68, 1857-1869.

Fraser, D.C., and Hodges, G., 2007, Induction-response functions for frequency-domain electromagnetic mapping system for airborne and ground configurations: Geophysics 72, F35-F44.

Grant, F.S., and West, G.F., 1965, Interpretation Theory in Applied Geophysics: McGraw Hill.

Huang, H., and Fraser, D.C., 2001, Mapping of the resistivity, susceptibility and permittivity of the earth using a helicopter-borne EM system: Geophysics 66, 148-157.

Macnae, J., King, A., Stolz, N., Osmakoff, A., and Blaha, A., 1998, Fast AEM data processing and inversion: Exploration Geophysics 29, 163-169.

Witherly, K.E., Irvine, R.J., and Raiche, A., 2003, The application of airborne electromagnetics to the search of high conductance targets: 16th Geophysical Conference and Exhibition, ASEG, Expanded Abstracts.

Quartz Claims - Canol Project

Grant #	Claim	Owner Name	Recorded date
YC29864	MIKLIN 210	Mark Lindsay - 50%, Mike Mickey - 50%	6/7/2004
YC29825	MIKLIN 171	Mark Lindsay - 50%, Mike Mickey - 50%	6/7/2004
YD106014	KING 14	Daniel Brent Mackenzie - 100%	3/2/2011
YD35473	TCR 17	Nokuyukon Holdings Ltd. - 50%, Glacier Drilling Ltd. - 50%	5/18/2011
YD35475	TCR 19	Nokuyukon Holdings Ltd. - 50%, Glacier Drilling Ltd. - 50%	5/18/2011
YD106112	DOME 2	Guillaume Pedneault - 100%	3/2/2011
YD106079	HUNTER 23	Daniel Brent Mackenzie - 100%	3/2/2011
YD35471	TCR 15	Nokuyukon Holdings Ltd. - 50%, Glacier Drilling Ltd. - 50%	5/18/2011
YC26900	MIKLIN 146	Mark Lindsay - 50%, Mike Mickey - 50%	6/7/2004
YD106023	KING 23	Guillaume Pedneault - 100%	3/2/2011
YD106008	KING 8	Shane Johnson - 100%	3/2/2011
YD106026	KING 26	Guillaume Pedneault - 100%	3/2/2011
YD106039	KING 39	Stephan Ruest - 100%	3/2/2011
YD106034	KING 34	Guillaume Pedneault - 100%	3/2/2011
YD106041	KING 41	Stephan Ruest - 100%	3/2/2011
YD106043	KING 43	Stephan Ruest - 100%	3/2/2011
YD106032	KING 32	Guillaume Pedneault - 100%	3/2/2011
YD106062	HUNTER 6	Shane Johnson - 100%	3/2/2011
YC99848	JOE 26	Joanne McDougall - 50%, Nokuyukon Holdings Ltd. - 50%	11/1/2011
YC99823	JOE 1	Joanne McDougall - 50%, Nokuyukon Holdings Ltd. - 50%	11/1/2011
YC99844	JOE 22	Joanne McDougall - 50%, Nokuyukon Holdings Ltd. - 50%	11/1/2011
YD35463	TCR 7	Nokuyukon Holdings Ltd. - 50%, Glacier Drilling Ltd. - 50%	5/18/2011
YD118707	TCR 25	Nokuyukon Holdings Ltd. - 50%, Glacier Drilling Ltd. - 50%	5/18/2011
YD118708	TCR 26	Nokuyukon Holdings Ltd. - 50%, Glacier Drilling Ltd. - 50%	5/18/2011
YD118706	TCR 24	Nokuyukon Holdings Ltd. - 50%, Glacier Drilling Ltd. - 50%	5/18/2011
YD35462	TCR 6	Nokuyukon Holdings Ltd. - 50%, Glacier Drilling Ltd. - 50%	5/18/2011
YD35461	TCR 5	Nokuyukon Holdings Ltd. - 50%, Glacier Drilling Ltd. - 50%	5/18/2011
YD118710	TCR 28	Nokuyukon Holdings Ltd. - 50%, Glacier Drilling Ltd. - 50%	5/18/2011
YC29858	MIKLIN 204	Mark Lindsay - 50%, Mike Mickey - 50%	6/7/2004
YD106072	HUNTER 16	Stephan Ruest - 100%	3/2/2011
YD106068	HUNTER 12	Stephan Ruest - 100%	3/2/2011
YD106113	DOME 3	Guillaume Pedneault - 100%	3/2/2011
YD35470	TCR 14	Nokuyukon Holdings Ltd. - 50%, Glacier Drilling Ltd. - 50%	5/18/2011
YD106097	RJL 11	Stephan Ruest - 100%	3/2/2011
YD106115	DOME 5	Guillaume Pedneault - 100%	3/2/2011
YD106075	HUNTER 19	Stephan Ruest - 100%	3/2/2011
YD106104	RJL 18	Guillaume Pedneault - 100%	3/2/2011
YC26886	MIKLIN 132	Mark Lindsay - 50%, Mike Mickey - 50%	6/7/2004
YD106091	RJL 5	Stephan Ruest - 100%	3/2/2011
YD106073	HUNTER 17	Stephan Ruest - 100%	3/2/2011
YD106085	HUNTER 29	Daniel Brent Mackenzie - 100%	3/2/2011
YD106122	DOME 12	Shane Johnson - 100%	3/2/2011
YD106088	RJL 2	Stephan Ruest - 100%	3/2/2011
YD106116	DOME 6	Guillaume Pedneault - 100%	3/2/2011
YC29820	MIKLIN 166	Mark Lindsay - 50%, Mike Mickey - 50%	6/7/2004
YC26853	MIKLIN 99	Mark Lindsay - 50%, Mike Mickey - 50%	6/7/2004

Quartz Claims - Canol Project

YD106067	HUNTER 11	Stephan Ruest - 100%	3/2/2011
YC29856	MIKLIN 202	Mark Lindsay - 50%, Mike Mickey - 50%	6/7/2004
YD35458	TCR 2	Nokuyukon Holdings Ltd. - 50%, Glacier Drilling Ltd. - 50%	5/18/2011
YD106095	RJL 9	Stephan Ruest - 100%	3/2/2011
YD106025	KING 25	Guillaume Pedneault - 100%	3/2/2011
YD106044	KING 44	Stephan Ruest - 100%	3/2/2011
YD106007	KING 7	Shane Johnson - 100%	3/2/2011
YD106051	KING 51	Daniel Brent Mackenzie - 100%	3/2/2011
YD106048	KING 48	Daniel Brent Mackenzie - 100%	3/2/2011
YD106054	KING 54	Daniel Brent Mackenzie - 100%	3/2/2011
YD106033	KING 33	Guillaume Pedneault - 100%	3/2/2011
YD106037	KING 37	Stephan Ruest - 100%	3/2/2011
YD152425	BLACKJACK 4	Daniel Brent Mackenzie - 100%	2/12/2011
YD152423	BLACKJACK 2	Daniel Brent Mackenzie - 100%	2/12/2011
YC99832	JOE 10	Joanne McDougall - 50%, Nokuyukon Holdings Ltd. - 50%	11/1/2011
YC99845	JOE 23	Joanne McDougall - 50%, Nokuyukon Holdings Ltd. - 50%	11/1/2011
YC99839	JOE 17	Joanne McDougall - 50%, Nokuyukon Holdings Ltd. - 50%	11/1/2011
YC99847	JOE 25	Joanne McDougall - 50%, Nokuyukon Holdings Ltd. - 50%	11/1/2011
YC29854	MIKLIN 200	Mark Lindsay - 50%, Mike Mickey - 50%	6/7/2004
YD106090	RJL 4	Stephan Ruest - 100%	3/2/2011
YD106099	RJL 13	Guillaume Pedneault - 100%	3/2/2011
YD106124	DOME 14	Shane Johnson - 100%	3/2/2011
YC26885	MIKLIN 131	Mark Lindsay - 50%, Mike Mickey - 50%	6/7/2004
YC99840	JOE 18	Joanne McDougall - 50%, Nokuyukon Holdings Ltd. - 50%	11/1/2011
YC29822	MIKLIN 168	Mark Lindsay - 50%, Mike Mickey - 50%	6/7/2004
YD106081	HUNTER 25	Daniel Brent Mackenzie - 100%	3/2/2011
YC26895	MIKLIN 141	Mark Lindsay - 50%, Mike Mickey - 50%	6/7/2004
YC99841	JOE 19	Joanne McDougall - 50%, Nokuyukon Holdings Ltd. - 50%	11/1/2011
YC99830	JOE 8	Joanne McDougall - 50%, Nokuyukon Holdings Ltd. - 50%	11/1/2011
YD114502	KING 2	Shane Johnson - 100%	3/2/2011
YD106013	KING 13	Daniel Brent Mackenzie - 100%	3/2/2011
YD106018	KING 18	Daniel Brent Mackenzie - 100%	3/2/2011
YC29817	MIKLIN 163	Mark Lindsay - 50%, Mike Mickey - 50%	6/7/2004
YC99835	JOE 13	Joanne McDougall - 50%, Nokuyukon Holdings Ltd. - 50%	11/1/2011
YD106027	KING 27	Guillaume Pedneault - 100%	3/2/2011
YD106006	KING 6	Shane Johnson - 100%	3/2/2011
YD106046	KING 46	Daniel Brent Mackenzie - 100%	3/2/2011
YD106074	HUNTER 18	Stephan Ruest - 100%	3/2/2011
YC29834	MIKLIN 180	Mark Lindsay - 50%, Mike Mickey - 50%	6/7/2004
YC29826	MIKLIN 172	Mark Lindsay - 50%, Mike Mickey - 50%	6/7/2004
YC99838	JOE 16	Joanne McDougall - 50%, Nokuyukon Holdings Ltd. - 50%	11/1/2011
YD106071	HUNTER 15	Stephan Ruest - 100%	3/2/2011
YD106106	RJL 20	Guillaume Pedneault - 100%	3/2/2011
YC99827	JOE 5	Joanne McDougall - 50%, Nokuyukon Holdings Ltd. - 50%	11/1/2011
YC99850	JOE 28	Joanne McDougall - 50%, Nokuyukon Holdings Ltd. - 50%	11/1/2011
YD106052	KING 52	Daniel Brent Mackenzie - 100%	3/2/2011
YD106029	KING 29	Guillaume Pedneault - 100%	3/2/2011

Quartz Claims - Canol Project

YC99836	JOE 14	Joanne McDougall - 50%, Nokuyukon Holdings Ltd. - 50%	11/1/2011
YD106031	KING 31	Guillaume Pedneault - 100%	3/2/2011
YD106010	KING 10	Shane Johnson - 100%	3/2/2011
YC99837	JOE 15	Joanne McDougall - 50%, Nokuyukon Holdings Ltd. - 50%	11/1/2011
YD106093	RJL 7	Stephan Ruest - 100%	3/2/2011
YC26898	MIKLIN 144	Mark Lindsay - 50%, Mike Mickey - 50%	6/7/2004
YC29821	MIKLIN 167	Mark Lindsay - 50%, Mike Mickey - 50%	6/7/2004
YD35474	TCR 18	Nokuyukon Holdings Ltd. - 50%, Glacier Drilling Ltd. - 50%	5/18/2011
YD106069	HUNTER 13	Stephan Ruest - 100%	3/2/2011
YD05489	QUEEN 2	Shane Johnson - 100%	3/2/2011
YC26863	MIKLIN 109	Mark Lindsay - 50%, Mike Mickey - 50%	6/7/2004
YD106049	KING 49	Daniel Brent Mackenzie - 100%	3/2/2011
YD106119	DOME 9	Shane Johnson - 100%	3/2/2011
YD106103	RJL 17	Guillaume Pedneault - 100%	3/2/2011
YD106123	DOME 13	Shane Johnson - 100%	3/2/2011
YC99826	JOE 4	Joanne McDougall - 50%, Nokuyukon Holdings Ltd. - 50%	11/1/2011
YC29866	MIKLIN 212	Mark Lindsay - 50%, Mike Mickey - 50%	6/7/2004
YD35464	TCR 8	Nokuyukon Holdings Ltd. - 50%, Glacier Drilling Ltd. - 50%	5/18/2011
YD118709	TCR 27	Nokuyukon Holdings Ltd. - 50%, Glacier Drilling Ltd. - 50%	5/18/2011
YD106050	KING 50	Daniel Brent Mackenzie - 100%	3/2/2011
YD106024	KING 24	Guillaume Pedneault - 100%	3/2/2011
YC99843	JOE 21	Joanne McDougall - 50%, Nokuyukon Holdings Ltd. - 50%	11/1/2011
YC29818	MIKLIN 164	Mark Lindsay - 50%, Mike Mickey - 50%	6/7/2004
YC29830	MIKLIN 176	Mark Lindsay - 50%, Mike Mickey - 50%	6/7/2004
YD106059	HUNTER 3	Shane Johnson - 100%	3/2/2011
YC29850	MIKLIN 196	Mark Lindsay - 50%, Mike Mickey - 50%	6/7/2004
YC29801	MIKLIN 147	Mark Lindsay - 50%, Mike Mickey - 50%	6/7/2004
YD106096	RJL 10	Stephan Ruest - 100%	3/2/2011
YD35459	TCR 3	Nokuyukon Holdings Ltd. - 50%, Glacier Drilling Ltd. - 50%	5/18/2011
YD35466	TCR 10	Nokuyukon Holdings Ltd. - 50%, Glacier Drilling Ltd. - 50%	5/18/2011
YD106105	RJL 19	Guillaume Pedneault - 100%	3/2/2011
YC26857	MIKLIN 103	Mark Lindsay - 50%, Mike Mickey - 50%	6/7/2004
YD106121	DOME 11	Shane Johnson - 100%	3/2/2011
YC29862	MIKLIN 208	Mark Lindsay - 50%, Mike Mickey - 50%	6/7/2004
YD106042	KING 42	Stephan Ruest - 100%	3/2/2011
YD106009	KING 9	Shane Johnson - 100%	3/2/2011
YC26894	MIKLIN 140	Mark Lindsay - 50%, Mike Mickey - 50%	6/7/2004
YC26897	MIKLIN 143	Mark Lindsay - 50%, Mike Mickey - 50%	6/7/2004
YC99846	JOE 24	Joanne McDougall - 50%, Nokuyukon Holdings Ltd. - 50%	11/1/2011
YC99831	JOE 9	Joanne McDougall - 50%, Nokuyukon Holdings Ltd. - 50%	11/1/2011
YD106030	KING 30	Guillaume Pedneault - 100%	3/2/2011
YD106036	KING 36	Stephan Ruest - 100%	3/2/2011
YD118703	TCR 21	Nokuyukon Holdings Ltd. - 50%, Glacier Drilling Ltd. - 50%	5/18/2011
YD106098	RJL 12	Stephan Ruest - 100%	3/2/2011
YD106017	KING 17	Daniel Brent Mackenzie - 100%	3/2/2011
YD106019	KING 19	Daniel Brent Mackenzie - 100%	3/2/2011
YD106058	HUNTER 2	Shane Johnson - 100%	3/2/2011

Quartz Claims - Canol Project

YD106094	RJL 8	Stephan Ruest - 100%	3/2/2011
YC99828	JOE 6	Joanne McDougall - 50%, Nokuyukon Holdings Ltd. - 50%	11/1/2011
YC99829	JOE 7	Joanne McDougall - 50%, Nokuyukon Holdings Ltd. - 50%	11/1/2011
YD05488	QUEEN 1	Shane Johnson - 100%	3/2/2011
YD106082	HUNTER 26	Daniel Brent Mackenzie - 100%	3/2/2011
YD106120	DOME 10	Shane Johnson - 100%	3/2/2011
YD106080	HUNTER 24	Daniel Brent Mackenzie - 100%	3/2/2011
YD106004	KING 4	Shane Johnson - 100%	3/2/2011
YD106015	KING 15	Daniel Brent Mackenzie - 100%	3/2/2011
YD106047	KING 47	Daniel Brent Mackenzie - 100%	3/2/2011
YC26893	MIKLIN 139	Mark Lindsay - 50%, Mike Mickey - 50%	6/7/2004
YC26896	MIKLIN 142	Mark Lindsay - 50%, Mike Mickey - 50%	6/7/2004
YC26855	MIKLIN 101	Mark Lindsay - 50%, Mike Mickey - 50%	6/7/2004
YD106100	RJL 14	Guillaume Pedneault - 100%	3/2/2011
YD106066	HUNTER 10	Shane Johnson - 100%	3/2/2011
YD106064	HUNTER 8	Shane Johnson - 100%	3/2/2011
YC29819	MIKLIN 165	Mark Lindsay - 50%, Mike Mickey - 50%	6/7/2004
YC99834	JOE 12	Joanne McDougall - 50%, Nokuyukon Holdings Ltd. - 50%	11/1/2011
YC26891	MIKLIN 137	Mark Lindsay - 50%, Mike Mickey - 50%	6/7/2004
YC29852	MIKLIN 198	Mark Lindsay - 50%, Mike Mickey - 50%	6/7/2004
YD106117	DOME 7	Shane Johnson - 100%	3/2/2011
YD106087	RJL 1	Stephan Ruest - 100%	3/2/2011
YC29860	MIKLIN 206	Mark Lindsay - 50%, Mike Mickey - 50%	6/7/2004
YD106118	DOME 8	Shane Johnson - 100%	3/2/2011
YC99842	JOE 20	Joanne McDougall - 50%, Nokuyukon Holdings Ltd. - 50%	11/1/2011
YD114501	KING 1	Shane Johnson - 100%	3/2/2011
YD106108	RJL 22	Guillaume Pedneault - 100%	3/2/2011
YD106038	KING 38	Stephan Ruest - 100%	3/2/2011
YD106056	KING 56	Daniel Brent Mackenzie - 100%	3/2/2011
YD106055	KING 55	Daniel Brent Mackenzie - 100%	3/2/2011
YD35465	TCR 9	Nokuyukon Holdings Ltd. - 50%, Glacier Drilling Ltd. - 50%	5/18/2011
YD106021	KING 21	Daniel Brent Mackenzie - 100%	3/2/2011
YD106016	KING 16	Daniel Brent Mackenzie - 100%	3/2/2011
YD106005	KING 5	Shane Johnson - 100%	3/2/2011
YD35469	TCR 13	Nokuyukon Holdings Ltd. - 50%, Glacier Drilling Ltd. - 50%	5/18/2011
YD106061	HUNTER 5	Shane Johnson - 100%	3/2/2011
YD106083	HUNTER 27	Daniel Brent Mackenzie - 100%	3/2/2011
YD106107	RJL 21	Guillaume Pedneault - 100%	3/2/2011
YC29823	MIKLIN 169	Mark Lindsay - 50%, Mike Mickey - 50%	6/7/2004
YC29829	MIKLIN 175	Mark Lindsay - 50%, Mike Mickey - 50%	6/7/2004
YC99833	JOE 11	Joanne McDougall - 50%, Nokuyukon Holdings Ltd. - 50%	11/1/2011
YC29828	MIKLIN 174	Mark Lindsay - 50%, Mike Mickey - 50%	6/7/2004
YC26890	MIKLIN 136	Mark Lindsay - 50%, Mike Mickey - 50%	6/7/2004
YC26861	MIKLIN 107	Mark Lindsay - 50%, Mike Mickey - 50%	6/7/2004
YD106077	HUNTER 21	Daniel Brent Mackenzie - 100%	3/2/2011
YD152422	BLACKJACK 1	Daniel Brent Mackenzie - 100%	2/12/2011
YC26887	MIKLIN 133	Mark Lindsay - 50%, Mike Mickey - 50%	6/7/2004

Quartz Claims - Canol Project

YD106076	HUNTER 20	Stephan Ruest - 100%	3/2/2011
YC29802	MIKLIN 148	Mark Lindsay - 50%, Mike Mickey - 50%	6/7/2004
YD106092	RJL 6	Stephan Ruest - 100%	3/2/2011
YC29833	MIKLIN 179	Mark Lindsay - 50%, Mike Mickey - 50%	6/7/2004
YD35457	TCR 1	Nokuyukon Holdings Ltd. - 50%, Glacier Drilling Ltd. - 50%	5/18/2011
YD106086	HUNTER 30	Daniel Brent Mackenzie - 100%	3/2/2011
YC99849	JOE 27	Joanne McDougall - 50%, Nokuyukon Holdings Ltd. - 50%	11/1/2011
YC29832	MIKLIN 178	Mark Lindsay - 50%, Mike Mickey - 50%	6/7/2004
YC26899	MIKLIN 145	Mark Lindsay - 50%, Mike Mickey - 50%	6/7/2004
YD106022	KING 22	Daniel Brent Mackenzie - 100%	3/2/2011
YC26892	MIKLIN 138	Mark Lindsay - 50%, Mike Mickey - 50%	6/7/2004
YD106111	DOME 1	Guillaume Pedneault - 100%	3/2/2011
YD106040	KING 40	Stephan Ruest - 100%	3/2/2011
YD106045	KING 45	Daniel Brent Mackenzie - 100%	3/2/2011
YD106035	KING 35	Stephan Ruest - 100%	3/2/2011
YD106078	HUNTER 22	Daniel Brent Mackenzie - 100%	3/2/2011
YC26889	MIKLIN 135	Mark Lindsay - 50%, Mike Mickey - 50%	6/7/2004
YC26859	MIKLIN 105	Mark Lindsay - 50%, Mike Mickey - 50%	6/7/2004
YD106053	KING 53	Daniel Brent Mackenzie - 100%	3/2/2011
YD152424	BLACKJACK 3	Daniel Brent Mackenzie - 100%	2/12/2011
YD106089	RJL 3	Stephan Ruest - 100%	3/2/2011
YD106101	RJL 15	Guillaume Pedneault - 100%	3/2/2011
YD106110	RJL 24	Guillaume Pedneault - 100%	3/2/2011
YD106102	RJL 16	Guillaume Pedneault - 100%	3/2/2011
YC29831	MIKLIN 177	Mark Lindsay - 50%, Mike Mickey - 50%	6/7/2004
YC29824	MIKLIN 170	Mark Lindsay - 50%, Mike Mickey - 50%	6/7/2004
YD106084	HUNTER 28	Daniel Brent Mackenzie - 100%	3/2/2011
YD106109	RJL 23	Guillaume Pedneault - 100%	3/2/2011
YD35460	TCR 4	Nokuyukon Holdings Ltd. - 50%, Glacier Drilling Ltd. - 50%	5/18/2011
YC99825	JOE 3	Joanne McDougall - 50%, Nokuyukon Holdings Ltd. - 50%	11/1/2011
YC26865	MIKLIN 111	Mark Lindsay - 50%, Mike Mickey - 50%	6/7/2004
YD106057	HUNTER 1	Shane Johnson - 100%	3/2/2011
YD35467	TCR 11	Nokuyukon Holdings Ltd. - 50%, Glacier Drilling Ltd. - 50%	5/18/2011
YC99824	JOE 2	Joanne McDougall - 50%, Nokuyukon Holdings Ltd. - 50%	11/1/2011
YD106060	HUNTER 4	Shane Johnson - 100%	3/2/2011
YD106070	HUNTER 14	Stephan Ruest - 100%	3/2/2011
YC29827	MIKLIN 173	Mark Lindsay - 50%, Mike Mickey - 50%	6/7/2004
YD106114	DOME 4	Guillaume Pedneault - 100%	3/2/2011
YD106028	KING 28	Guillaume Pedneault - 100%	3/2/2011
YD35476	TCR 20	Nokuyukon Holdings Ltd. - 50%, Glacier Drilling Ltd. - 50%	5/18/2011
YD118705	TCR 23	Nokuyukon Holdings Ltd. - 50%, Glacier Drilling Ltd. - 50%	5/18/2011
YD35472	TCR 16	Nokuyukon Holdings Ltd. - 50%, Glacier Drilling Ltd. - 50%	5/18/2011
YD106065	HUNTER 9	Shane Johnson - 100%	3/2/2011
YD106063	HUNTER 7	Shane Johnson - 100%	3/2/2011
YC26888	MIKLIN 134	Mark Lindsay - 50%, Mike Mickey - 50%	6/7/2004
YD35468	TCR 12	Nokuyukon Holdings Ltd. - 50%, Glacier Drilling Ltd. - 50%	5/18/2011
YD106012	KING 12	Daniel Brent Mackenzie - 100%	3/2/2011

Quartz Claims - Canol Project

YD106020	KING 20	Daniel Brent Mackenzie - 100%	3/2/2011
YD118704	TCR 22	Nokuyukon Holdings Ltd. - 50%, Glacier Drilling Ltd. - 50%	5/18/2011
YD106003	KING 3	Shane Johnson - 100%	3/2/2011
YD106011	KING 11	Daniel Brent Mackenzie - 100%	3/2/2011

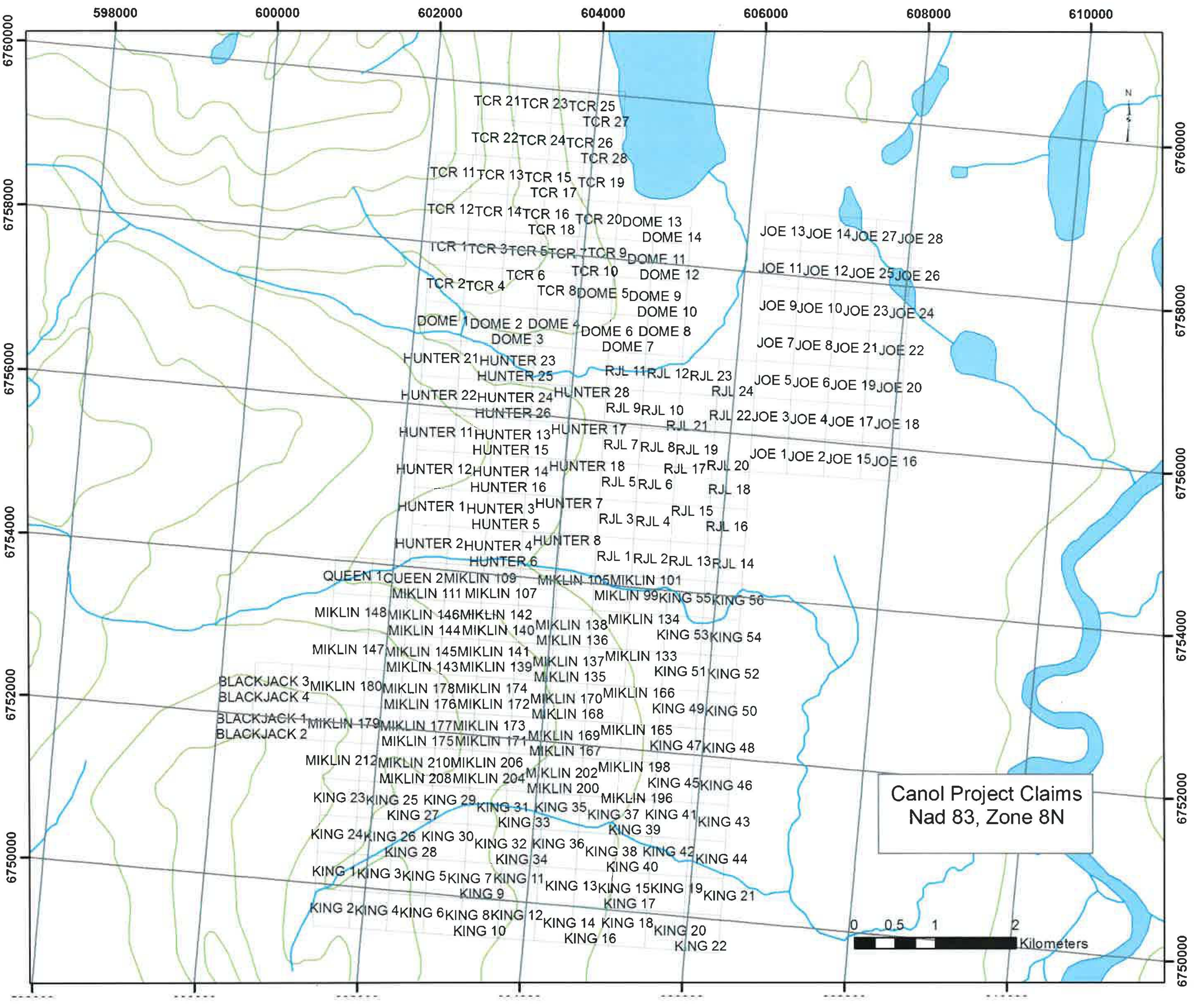
Canol Project Claims
Nad 83, Zone 8N